ISAS - INTERNATIONAL SCHOOL
FOR ADVANCED STUDIES

Reconstructing the Cosmic Density and Velocity Fields

Thesis submitted for the degree of
"Doctor Philosophiæ"

CANDIDATE   SUPERVISOR

Enzo Branchini   Prof. Dennis W. Sciama

October 1995

To Ilva and Gualtiero.........of course.

ACKNOWLEDGMENTS

Contents

List of Figures

List of Tables

PREFACE

This is a thesis about an exciting theme of modern Cosmology: the large scale structure and the dynamics of the universe.

Unlike other physical sciences, astronomy, and even more so Cosmology, does not allow one to directly interact with the subject of its research and thus it is impossible to carry out experiments in the classical sense. All one can do is to observe the content of the universe. The astrophysical analogous of setting up the experimental apparatus is the selection of a particular class of objects or phenomena. In other words one has to pick out those 'experiments' that the universe has already performed on his behalf to obtain a dataset analogous to the outcome of an ordinary experiment. Of course it is possible to carry out numerical simulations to study the evolutionary behaviour and the features of different cosmological models, but even in this case the observational data that the theoretical models should match are products of a unique realization. These data may be used for statistical analyses provided that their number is large enough and they have been acquired in a homogeneous way.

Such a peculiar condition makes observational data extremely valuable and explains why it is so important to increase efforts to obtain complete and statistically homogeneous data. Observational biases and intrinsic limitations do not allow us to gather such an ideal dataset. Nevertheless, one can try to improve their quality *a posteriori* by making theoretical assumptions to recover missed data or to account for biases. In practice one wants to restore the original information contained into a system (the observed universe) that has been degraded by some known physical process.

In this thesis we will be mainly interested on the reconstruction methods used in the study of the large scale structure of the universe. The layout of the thesis is as follows.

Chapter 1 provides the basic framework and definitions of background cosmology that we will be using for the rest of the thesis. We summarize there the fundamental concepts of the Standard Cosmology and its description of a homogeneous and isotropic universe. We stress the relevance of the cosmological information contained in the spatial distribution of density fluctuations and its link with the distribution of luminous objects. We also discuss the assumptions underlying the gravitational instability picture and we describe the growth of density fluctuations within this framework.

In Chapter 2 we review the main reconstruction methods that have been applied to the study of the large scale structure and dynamics of the universe. We discuss methods

that allow us to reconstruct the density field from the observed peculiar velocity field as well as those that allow us to recover the density field from the redshift space positions of luminous objects. The time reconstruction methods that predict the primordial density field from that presently observed are presented as well.

The main part of the thesis is divided in two Chapters containing original research contributions on two different reconstruction techniques; their implementation, reliability and application to real data. Chapter 3 describes an iterative method for reconstructing the density and the velocity field of galaxy clusters from their observed distribution. The study of the large scale dynamics have revealed that the knowledge of the mass distribution over very large scales is fundamental to properly understand the cosmic dynamics even on local scales. This is a strong motivation for extending the study of the density and velocity fields up to very large scales. For this reason we have decided to apply an iterative reconstruction technique to the cluster distribution since they allow us to trace the large scale density and velocity field. In Chapter 3 we discuss in detail the selection of a homogeneous subsample of clusters, the implementation and reliability of our method. The subsequent analysis of the density and velocity field allow us to constrain the value of the cosmic density parameter while the comparison with simulated data provides us with enough discriminatory power to rule out some cosmological models at a confidence level larger than $1-\sigma$.

Besides the exploration of the cosmic fields at the present epoch, it is also important to trace them back in time in order to understand the evolutionary processes that lead to the formation of the observed cosmic structures. This is the aim of the reconstruction technique we present in Chapter 4, which uses the least action principle to describe the growth of the density fluctuations assuming the gravitational instability picture. After reviewing the subject end discussing the relevance of the method as a cosmological test, we concentrate on its general reliability that we test using N–body techniques. The outcome of the analysis allow us to estimate the validity of the method in an Einstein–de Sitter universe and to define the limits within which the method can be reliably applied.

Chapter 1

BACKGROUND COSMOLOGY

In this Chapter we summarize the fundamental concepts of the Standard Hot Big Bang Cosmology. A complete treatment of the subject can be found in many excellent textbooks and reviews [Coles & Lucchin (1995), Kolb & Turner (1990), Lucchin (1990), Narlikar (1993), Padmamanabhan (1993), Peebles (1971, 1980, 1993), Primack (1984), Weinberg (1972), Zel'dovich & Novikov (1983)], here the aim is just to set up the fundamental tools that we will be using in this thesis.

In the first section we discuss the properties, the dynamics and thermal history of an expanding homogeneous and isotropic universe. In section (1.2) we discuss the inhomogeneities in the mass distribution and we develop those statistical tools that describe the spatial properties of the cosmic density field. In the last part we consider the evolution of the density fluctuations in the gravitational instability (GI hereafter) framework and their relation with the peculiar velocity field.

1.1   THE HOMOGENEOUS UNIVERSE

The Standard Hot Big Bang model relies on three basic assumptions:

- The observed universe is homogeneous and isotropic and therefore its geometrical and dynamical properties are well described by the Friedmann–Robertson–Walker (FRW) model.

- The evolution of the space–time can be described using General Relativity, although for many cosmological problems the Newtonian approximation is accurate enough.

- Homogeneity and isotropy hold on large scales. On scales smaller than our horizon the universe can be described by a perturbed FRW model in which metric fluctuations are small.

The Standard model is supported by three main observations:

1. During the thirties Hubble carried out a series of observations during which he discovered that galaxies are receding from us according to the simple linear relation

$$v_r \propto r, \tag{1.1}$$

where v_r is the recession velocity and r the distance of the galaxy (Hubble 1934, 1936). This systematic effect was interpreted as a geometrical space–time expansion.

2. An isotropically distributed electromagnetic radiation has been serendipitously detected by Penzias and Wilson (1965) in the microwave range. This cosmic microwave background (CMB) is interpreted as the relic blackbody radiation of an epoch in which the universe was very hot and dense. Subsequent measurements confirmed the original discovery founding that the CMB is fully consistent with the blackbody radiation having nearly constant temperature $T \simeq 2.73° \ K$ (Smoot et al. 1991) with fluctuations $\Delta T/T \sim 10^{-5}$ on a scale of 7° (Smoot et al. 1992).

3. The Standard model predicts the existence of an epoch in which the the universe was hot enough to allow the nucleosynthesis of the light elements (Wagoner 1973). The predicted abundances are in accordance with experimental determinations (c.f. Walker 1991)

1.1.1   The Cosmological Principle

The fundamental assumption of the Big–Bang Cosmology is the fact that on large scales the universe is homogeneous and isotropic. This statement, originally formulated by Einstein, constitutes the so called *Cosmological Principle*. A stronger version of this assumption is the Perfect Cosmological Principle stating that the universe is the same not only everywhere but also at all times. The Perfect Cosmological Principle constituted the basis of the now disfavoured Steady State Cosmology (Bondi & Gold 1948, Hoyle 1948) Attempts of justifying the Cosmological Principle have been made both on a philosophical basis and on more direct physical grounds (for a review on this subject see Barrow & Tipler 1986).

1.1.2 The Robertson–Walker Metric

Let us model the universe as a continuous fluid in which we label each element using three spatial comoving coordinates x^α ($\alpha = 1$, 2, 3). Each point in the–space time is then characterized by its comoving coordinates, x^α, and the proper time t measured by a clock moving with the fluid element. The metric

$$ds^2 = g_{ik}dx^i dx^k \qquad (i, k = 0, 1, 2, 3) \qquad (1.2)$$

represents the space–time interval between two points labelled by x^k and $x^k + dx^k$, and accounts for the geometrical properties of the space–time through the metric tensor g_{ik}. It can be shown that the most general space–time metric [called Robertson–Walker metric (R–W)] describing an homogeneous and isotropic universe is of the form

$$ds^2 = (cdt)^2 - dl^2 = (cdt)^2 - a(t)^2 \left[\frac{dr^2}{1 - Kr^2} + r^2(d\theta^2 + \sin^2\theta d\phi^2) \right], \qquad (1.3)$$

where dl is the spatial distance between two points measured at the same universal time t while (r, θ, ϕ) are comoving coordinates, $a(t)$ is the expansion parameter and K is the space curvature that can only take the values $(-1, 0, +1)$.

1.1.3 The Hubble Law

From the Cosmological Principle, which allows one to describe the geometrical structure of space–time with the R–W metric, follows that the space–time is expanding. This prediction has been experimentally verified by Hubble (1934). Let us introduce the proper distance, d_{pr}, of a point P from another point P_0 that is placed at the center of the coordinates (without loss of generality). The proper distance is defined as the distance measured by a chain of rulers held by a set of observes connecting P and P_0 at the same time t. According to this definition d_{pr} is the integral of dl along r:

$$d_{pr} = \int_0^r \frac{a d\tilde{r}}{(1 - K\tilde{r}^2)^{1/2}} = aF(r), \qquad (1.4)$$

where a is the expansion factor which depends on the universal time t. From eq. (1.4) we can notice that the proper distance changes with time and thus the source at P has a radial velocity

$$v_r = \frac{d(d_{pr})}{dt} = \dot{a}F(r) = \frac{\dot{a}}{a}d_{pr} \qquad (1.5)$$

with respect to P_0. Equation (1.5) is the so called Hubble law and the parameter

$$H(t) = \frac{\dot{a}}{a} \qquad (1.6)$$

is the famous Hubble parameter. Its value at the present–epoch H_o is loosely constrained by observations to be in the interval

$$30 \ km/sec \ h^{-1}\text{Mpc} \leq H_o \leq 100 \ km/sec \ h^{-1}\text{Mpc}$$

and is often expressed using the dimensionless parameter $h = H_o/(100 \ km/sec \ h^{-1}\text{Mpc})$. If galaxies have negligible proper velocities then eq. (1.5) predicts their systematic recession, as observed.

1.1.4   The Cosmological Redshift

To actually measure the velocity of a galaxy one takes advantage of the R–W metric properties which predict that a monocromatic wave emitted by a receding galaxy is systematically Doppler–shifted towards larger frequencies. Let us consider an electromagnetic wave emitted from a distant source at the time t_e with a wavelength λ_e. The redshift z of that source is defined as

$$z = \frac{\lambda_o - \lambda_e}{\lambda_e}, \qquad (1.7)$$

where λ_o is the wavelength of the radiation detected at t_o by an observer placed at the center of the coordinates (from now on the subscript $_o$ indicates the present–epoch). Since the light travels along null geodesic ($ds^2 = 0$), from equations (1.3) and (1.4) we obtain that for a light ray

$$\int_{t_e}^{t_o} \frac{cdt}{a} = F(r). \qquad (1.8)$$

Another wave emitted at $t_e + \delta t_e$ reaches the observer at $t_o + \delta t_o$. Since $F(r)$ is time independent we can write the analogous of eq. (1.8) for the second light ray and, by comparing the two relations, we obtain

$$\frac{\delta t_o}{a_o} = \frac{\delta t_e}{a_e} \qquad (1.9)$$

If, in particular, $\delta t_o \propto \lambda_o$ and $\delta t_e \propto \lambda_e$, we have

$$\frac{a_o}{\lambda_o} = \frac{a_e}{\lambda_e} \qquad (1.10)$$

and therefore

$$1 + z = \frac{a_o}{a_e}. \qquad (1.11)$$

Because of the one–to–one correspondence of the redshift and the expansion parameter, the former is commonly used as a label of a given epoch. For small z the redshift of a source is directly related to its recession velocity and to its comoving distance, provided that the source does not have a peculiar motion superimposed to its recession velocity.

1.1.5 The Cosmological Horizon

An important cosmological quantity for studying the evolution of the cosmic structures is the portion of the universe that has the possibility of being causally connected with which a generic observer at time t. This concept is quantified by the so called cosmological horizon (also called particle horizon) R_H, which is defined as the radius of the sphere containing all the points that could have communicated with the observer in the interval between $t = 0$ and t:

$$R_H(t) = a(t) \int_0^t \frac{c d\acute{t}}{a(\acute{t})}, \qquad (1.12)$$

where the observer has been places at the center of the coordinate system.

1.1.6 The Friedmann Equations

The Standard model uses General Relativity to relate the space–time geometry to the matter content of the universe. The link is given by the Einstein equations:

$$R_{ik} - \frac{1}{2}g_{ik}R - \Lambda g_{ik} = \frac{8\pi G}{c^4}T_{ik}, \qquad (1.13)$$

where Λ is the cosmological constant introduced by Einstein to allow static cosmological solutions, T_{ik} is the energy–momentum tensor, g_{ik} is the metric tensor, R_{ik} is the Ricci tensor, $R = g^{ik}R_{ik}$ is the Ricci scalar, G is the Newton's gravitational constant and c is the speed of the light. The energy–density tensor, of cosmological relevance, is that of a perfect fluid

$$T_{ij} = (p + \rho c^2)U_i U_j - p g_{ij}, \qquad (1.14)$$

where p is the pressure, ρc^2 is the energy density and $U_i = g_{ik}\frac{dx^k}{ds}$ is the four–velocity of the fluid. With the transformations:

$$p \longrightarrow p - \frac{\Lambda c^4}{8\pi G} \qquad \rho \longrightarrow \rho + \frac{\Lambda c^2}{8\pi G} \qquad (1.15)$$

we can formally recast eq. (1.13) in the standard form

$$R_{ik} - \frac{1}{2}g_{ik}R - = \frac{8\pi G}{c^4}T_{ik}. \qquad (1.16)$$

From the time–time component of eq. (1.16) one obtains

$$\ddot{a} = -\frac{4\pi}{3}G\left(\rho + 3\frac{p}{c^2}\right)a \qquad (1.17)$$

while substituting $\ddot{a}$ from eq. (1.17) in the space–space component on has

$$\dot{a}^2 + Kc^2 = \frac{8\pi G}{3}\rho a^2. \qquad (1.18)$$

Space–time components give the trivial relation 0=0. The relationships (1.17) and (1.18) are the so called Friedmann equations. They are not independent: eq. (1.18) can be obtained from eq. (1.17) if one assumes an adiabatic expansion of the universe:

$$d(\rho a^3) = -3\frac{p}{c^2}a^2 da \qquad (1.19)$$

The set of equations (1.17), (1.18) and (1.19) together with the equation of state $F(p, \rho) = 0$ allows, in principle, to compute the time evolution of the expansion parameter. The qualitative behaviour of $a(t)$ at $t < t_o$, however, can be already deduced by noticing that $\dot{a}_o > 0$ since the universe is expanding and that $\ddot{a} < 0$ at all times, provided that $\rho + 3\frac{p}{c^2} > 0$, a condition fulfilled at any time except during the so called inflationary epoch (during which $\ddot{a} > 0$). This means that the expansion parameter has a monotonically increasing behaviour in the time interval $[0, t_o]$. To predict the space time evolution at $t > t_o$, however, one has to solve the Friedmann equations.

The standard model assumes a perfect fluid with equation of state

$$p = w\rho c^2, \qquad (1.20)$$

where w lies in the 'Zel'dovich interval' $0 \leq w \leq 1$. In the case of dust (i.e. pressureless matter) $p = w = 0$, while for a non–degenerate relativistic fluid in thermal equilibrium (e.g. photons) $w = 1/3$. Substituting eq. (1.20) into eq. (1.19) allows to relate the density, ρ, to the expansion factor, a, by

$$\rho a^{3(1+w)} = constant \qquad (1.21)$$

so that for $a \to 0$ (which occurs for $t \to 0$) the density diverges. The explicit solution, $a(t)$, depends both on w and on the value of the density parameter at the present–epoch:

$$\Omega_o \equiv \frac{\rho_o}{\rho_{ocr}} = \frac{\rho_o 8\pi G}{3H_o^2} \qquad (1.22)$$

and can be obtained by integrating

$$\left(\frac{\dot{a}}{a_o}\right)^2 = H_o^2 \left[\Omega_o \left(\frac{a_o}{a}\right)^{(1+3w)} + (1 - \Omega_o)\right], \qquad (1.23)$$

that can be easily obtained from eq. (1.18). Simple solutions of eq. (1.23) exist for $\Omega_o = 1$, i.e. for the so called Einstein–de Sitter model:

$$a \propto t^{2/3} \qquad for \qquad w = 0 \qquad (1.24)$$

and

$$a \propto t^{1/2} \qquad for \qquad w = 1/3 \qquad (1.25)$$

At the present–epoch $w = 0$ since the universe is dominated by matter because the matter density, ρ_{om}, is much higher than the energy density associate to the CMB, ρ_{or}:

$$\frac{\rho_{om}}{\rho_{or}} \sim 4 \times 10^4 \; \Omega_o h^2. \tag{1.26}$$

For $t < t_o$ the expansion factor is an increasing function of t and thus, according to eq. (1.21), the CMB energy–density has decreased faster than the matter density. This means that an earlier epoch existed with $\rho_r > \rho_m$, which then means that the universe has been dominated by radiation in the early stages. The epoch in which the two densities are equal is called *equivalence epoch*. From eq. (1.21) and (1.26) it turns out that *equivalence* occurred at $z = 4.3 \times 10^4 \; \Omega_o h^2$.

Since the CMB has a nearly perfect blackbody spectrum, the energy density and the temperature of the radiation are linked by the Stefan–Boltzmann law:

$$\rho_{or} = \frac{\sigma T_{or}^4}{c^2}, \tag{1.27}$$

where σ is the so called blackbody constant and T_r is the radiation temperature. From equations (1.21) and (1.27) one sees that the temperature of the radiation scales as

$$T_r(t) = T_{or} \left(\frac{a}{a_o} \right) \tag{1.28}$$

and thus it increases going back in time. Besides the equivalence epoch, there are two more important timescales in the thermal history of the universe: the *recombination* and the *decoupling* epochs.

Since the universe is cooling, there has been an early era in which the universe was hot enough to be fully ionized. The *recombination* time is defined as the epoch in which the temperature fell below $4000° \; K$ ($z \simeq 1500$), when 50 % of the matter gets in the form of neutral atoms.

The *decoupling* occurred when the collision time between photons and atoms became larger than the characteristic evolutionary timescale of the universe. In the cosmological situation the dominant mechanism of matter–radiation interaction is Thomson scattering by electrons while the universe timescale is the expansion time. Equalizing these two characteristic times one obtains that matter and radiation decoupled around $z \sim 300$.

1.2   THE INHOMOGENEOUS UNIVERSE

Up to now we have considered a homogeneous and isotropic universe. Observations, however, point at a different direction since the distribution of galaxies appears inhomoge-

neous and anisotropic. This implies that if galaxies are correlated to the mass distribution the cosmological principle is violated, at least on small scales. The Standard model, however, will still be valid provided that the metric fluctuation are small within our horizon, i.e. provided that we live in a perturbed FRW universe. Since requiring small metric fluctuations does not put stringent constraints on the amplitude of the density fluctuations on small scales, the basic hypotheses of the Standard model and its properties are consistent with the current observations of the galaxy distribution.

A complete theory should be able to describe the statistical spatial properties of the cosmic density field together with its evolution. In this section we describe the more common statistical tools employed to describe and to study the spatial features of the density field and its relation to the distribution of luminous objects.

1.2.1 The Density Fluctuations Field

It is convenient to define the density fluctuation field $\delta(\mathbf{x})$:

$$\delta(\mathbf{x}) = \frac{\rho(\mathbf{x}) - \langle \rho(\mathbf{x}) \rangle}{\langle \rho(\mathbf{x}) \rangle}. \tag{1.29}$$

In the statistical framework, $\delta(\mathbf{x})$ is treated as a random field, i.e. as a set of random variables, one for each point $\mathbf{x}$, so that our universe is a random realization 'picked up' from a statistical ensemble of universes. In this framework the average $\langle \cdot \rangle$ in eq. (1.29) is intended as an average over the ensemble.

The Cosmological Principle implies that $\delta(\mathbf{x})$ is a homogeneous and isotropic random process and that the average over the ensemble are invariant with respect to spatial translations and rotations. Furthermore, the *Ergodic Hypothesis* holds which states that ensemble averages coincide with spatial averages if one considers a single realization of the random field. This is essential since all the needed information is contained in a single $\delta(\mathbf{x})$ sample.

A convenient way of describing the density fluctuation field is to think of the perturbation, $\delta(\mathbf{x})$, as a superposition of monocromatic plane waves which, as we shall see, evolve independently when the fluctuations' amplitude is small. Let us consider a cubic volume $V = L^3$ larger than the maximum scale at which a significant density fluctuation can be detected. In this case V is a 'fair sample' of the universe. The density fluctuation field within the volume V can be expressed as a Fourier series:

$$\delta(\mathbf{x}) = \sum_{\mathbf{k}} \delta_{\mathbf{k}} \exp(i\mathbf{k} \cdot \mathbf{x}), \tag{1.30}$$

where **k** is the wavenumber that, because of the periodic boundary conditions

$$\delta(L, y, z) = \delta(0, y, z); \quad \delta(x, L, z) = \delta(x, 0, z); \quad \delta(x, y, L) = \delta(x, y, 0), \tag{1.31}$$

has components

$$k_\eta = n_\eta \frac{2\pi}{L} \quad \text{with} \quad \eta = x, \, y, \, z \tag{1.32}$$

where n_η are integers. The Fourier coefficients $\delta_\mathbf{k}$ are obviously obtained by Fourier transforming $\delta(\mathbf{x})$:

$$\delta_\mathbf{k} = \frac{1}{V} \int_V \delta(\mathbf{x}) \exp(-i\mathbf{k} \cdot \mathbf{x}) d\mathbf{x} \tag{1.33}$$

One can formally take the limit $V \to \infty$ in which case the Fourier coefficients become a continuous function of **k**, $\delta(\mathbf{k})$, that form a Fourier pair with $\delta(\mathbf{x})$:

$$\delta(\mathbf{x}) = \frac{1}{2\pi^3} \int_0^\infty \delta(\mathbf{k}) \exp(i\mathbf{k} \cdot \mathbf{x}) d\mathbf{k} \quad \leftrightarrow \quad \delta(\mathbf{k}) = \int_0^\infty \delta(\mathbf{x}) \exp(-i\mathbf{k} \cdot \mathbf{x}) d\mathbf{x} \tag{1.34}$$

1.2.2 Power Spectrum

Clearly, the expectation value of $\delta(\mathbf{x})$, $\langle \delta(\mathbf{x}) \rangle$, is null by construction while the variance $\sigma = \langle \delta^2(\mathbf{x}) \rangle$ is generally not. From the first of equations (1.34) it is straightforward to see that

$$\sigma^2 = \frac{1}{2\pi^2} \int_0^\infty \langle |\delta^2(\mathbf{k})| \rangle k^2 dk, \tag{1.35}$$

where the quantity $\langle |\delta^2(\mathbf{k})| \rangle = \langle |\delta_k^2| \rangle = P(k)$ is the power spectrum of the density fluctuations.

Together with the $P(k)$, which measures the amplitude of the Fourier coefficients as a function of **k**, to fully characterize $\delta(\mathbf{x})$ one needs to know the probability distribution of the fluctuations. For this purpose let us consider N realizations of $\delta(\mathbf{x})$ within different boxes with volumes V_1, V_2, ... V_N identical to the volume volume V and let us measure the probability distribution of the Fourier coefficients $\delta_\mathbf{k} = |\delta_\mathbf{k}| \exp(i\theta_\mathbf{k})$. If the phases are independent and randomly distributed in the interval $[0, 2\pi]$, as predicted by most of the popular mechanism of generating the primordial density fluctuations (like many inflationary models), then the $|\delta_\mathbf{k}|$ follow a Rayleigh distribution

$$\mathcal{P}(|\delta_\mathbf{k}|, \theta_\mathbf{k}) d|\delta_\mathbf{k}| d\theta_\mathbf{k} = \frac{|\delta_\mathbf{k}| V}{2\pi \langle |\delta_\mathbf{k}|^2 \rangle} \exp\left(-\frac{|\delta_\mathbf{k}|^2 V}{2\langle |\delta_\mathbf{k}|^2 \rangle} \right) d|\delta_\mathbf{k}| d\theta_\mathbf{k} \tag{1.36}$$

which represents the probability of having $|\delta_\mathbf{k}|$ in the interval $[|\delta_\mathbf{k}|, |\delta_\mathbf{k}| + d|\delta_\mathbf{k}|]$ and $\theta_\mathbf{k}$ in the interval $[\theta_\mathbf{k}, \theta_\mathbf{k} + d\theta_\mathbf{k}]$. In this case it is easy to show that the distribution $\mathcal{P}(\delta)$, which

represent the probability of measuring in the point x a fluctuation in the range $[\delta, \delta + d\delta]$, is Gaussian:

$$\mathcal{P}(\delta)d\delta = \frac{1}{(2\pi\sigma^2)^{1/2}} \exp\left(-\frac{\delta^2}{2\sigma^2}\right) d\delta \qquad (1.37)$$

and the fluctuation density field, $\delta(x)$, is called Gaussian as well.

It can be shown that for a Gaussian field the N–variate joint distribution of a set of $\delta(x_i)$, $\mathcal{P}(\delta(x_1), \delta(x_2)......\delta(x_N))$, can be written as a multi–variate Gaussian distribution which is a function of the $P(k)$ alone. Therefore *a Gaussian density fluctuations field is completely characterized by its $P(k)$.*

The variance σ^2 carries information about the amplitude of the density fluctuations but does not depend on their spatial distribution. In general eq. (1.35) does not converge and, in any case, it does not contain any information about the relative contribution to the fluctuations from different scales. Since the r.m.s. density fluctuation on a given scale is important for understanding the evolution of cosmic structures it is convenient to define the mass variance, σ_m^2, as the variance σ^2 measured within a spherical volume V_s. If $\langle M \rangle = V_s \langle \rho(x) \rangle = \frac{4}{3}\pi R^3 \langle \rho(x) \rangle$ is the average mass contained within V_s, then

$$\sigma_m^2 = \frac{\langle (M - \langle M \rangle)^2 \rangle}{\langle M \rangle^2}, \qquad (1.38)$$

where $\langle \cdot \rangle$ means spatial average within V_s. It can be shown that

$$\sigma_m^2 = \frac{1}{2\pi^2} \int_0^\infty P(k)W(kR)^2 k^2 dk, \qquad (1.39)$$

where

$$W(kR) = \frac{3[\sin(kR) - kR\cos(kR)]}{(kR)^3} \qquad (1.40)$$

is the window function that contain contributions to σ_m^2 from wavelengths $\lambda > R$. $W(kR)$ is the Fourier transform of the top hat filter

$$F(|x - \dot{x}|, R) = \frac{3}{4\pi R^3}\Theta\left(1 - \frac{|x - \dot{x}|}{R}\right), \qquad (1.41)$$

where Θ is the Heaviside function, that in real space delimitates the spherical volume V_s. Using a spherical window with sharp edges may cause problems since $W(kR)$ has an extended tail in the k–space and thus it can pick up undesired contribution from small k modes. To avoid this problem the Gaussian window is often used:

$$F(|x - \dot{x}|, R) = \frac{1}{(2\pi R^3)^{3/2}} \exp\left(-\frac{|x - \dot{x}|^2}{2R^2}\right) \qquad (1.42)$$

together with its Fourier transform

$$W(kR) = \exp\left[-\frac{(kR)^2}{2}\right]. \qquad (1.43)$$

1.2.3 The Correlation Function

A more complete description of the spatial properties of $\delta(\mathbf{x})$, besides the mass variance, can be obtained using the autocorrelation function (or covariance) of the the density field $\delta(\mathbf{x})$ which is defined as the expectation value of the two–point function:

$$\xi(\mathbf{r}) = \langle \delta(\mathbf{x})\delta(\mathbf{x}+\mathbf{r}) \rangle, \tag{1.44}$$

where the average is over all the points in the volume V. In a homogeneous and isotropic universe $\xi(\mathbf{r})$ does not depend on either the origin or the direction of $\mathbf{r}$ but only on its modulus $|\mathbf{r}| = r$ and thus $[\xi(\mathbf{r}) = \xi(r)]$.

Taking the limit $V \to \infty$ it is possible to show that $\xi(r)$ and $P(k)$ form a Fourier pair (Wiener–Kintchine theorem):

$$\xi(r) = \frac{1}{(2\pi)^3} \int_0^\infty P(k)\exp(-i\mathbf{k}\cdot\mathbf{r})dk = \frac{1}{2\pi^2} \int_0^\infty P(k)\frac{\sin(kr)}{kr}k^2 dk \tag{1.45}$$

and

$$P(k) = \int_0^\infty \xi(r)\exp(i\mathbf{k}\cdot\mathbf{r})dr = 4\pi \int_0^\infty \xi(r)\frac{\sin(kr)}{kr}r^2 dr. \tag{1.46}$$

The two–point autocorrelation function $\xi(r)$ can be generalized to define the auto-correlation function for $N > 2$ point. For example the three point autocorrelation function ζ is defined as

$$\zeta(r,s,t) = \langle \delta(\mathbf{x})\delta(\mathbf{x}+\mathbf{r})\delta(\mathbf{x}+\mathbf{s}) \rangle, \tag{1.47}$$

where the average is over all the points in the volume V and over all the directions of $\mathbf{r}$ and $\mathbf{s}$ such that $t = |\mathbf{r} - \mathbf{s}|$. The generalization to a larger number of points is straightforward.

Let us now consider a discrete distribution of masses within a volume V and with a number density n_V. The continuous density field can be formally expressed as

$$\rho(\mathbf{x}) = \sum_i m_i \delta_D(\mathbf{x} - \mathbf{x}_i), \tag{1.48}$$

where the sum extends to all the points found at $\mathbf{x}_i$ with masses m_i and δ_D is the Dirac function. If $m_i = m$ for each point then the average density is $\langle \rho \rangle = n_V m$ and the probability of finding a mass point in a randomly chosen infinitesimal volume δV is $\delta P = m^{-1}\rho(\mathbf{x})\delta V$. Analogously, the joint probability of finding a point mass in the volume δV_1 and a point mass in the volume δV_2 separated by a distance r is

$$\delta^2 P = \frac{\langle \rho(\mathbf{x})\rho(\mathbf{x}+\mathbf{r}) \rangle}{m^2}\delta V_1 \delta V_2 = n_V^2[1 + \xi(r)]\delta V_1 \delta V_2, \tag{1.49}$$

where $\xi(r)$ is the two–point correlation function. If the points were randomly distributed then $\xi(r) = 0$. Thus a positive correlation at a given scale r can be interpreted as an excess probability over random, while the anti–correlation, $-1 < \xi(r) < 0$, means a lack of probability with respect to the Poissonian case.

The different terminology used for $\xi(r)$ derives from its different meaning: in case of a continuous field the autocorrelation function measures the degree of spatial correlation of density fluctuations while in the discrete case $\xi(r)$ is defined in terms of conditional probability of founding discrete objects at specific points.

The two–point correlation function is the more popular statistical tool for describing the galaxy distribution together with its generalization to the N points case. Assuming that galaxies trace the mass, there is a one–to–one relation between the two–point spatial galaxy correlation function and the autocorrelation function of the underlying density field. We will discuss this point in the next section.

In the usual case of two–dimensional (projected) galaxy catalogues it is convenient to define the two–point angular correlation function $w(\theta)$:

$$\delta^2 P = n_\Omega^2 [1 + w(\theta)] d\Omega_1 d\Omega_2, \tag{1.50}$$

which represents the probability of finding two galaxies within the two infinitesimal solid angles $d\Omega_1$ and $d\Omega_2$ separated by the angle θ on sky; n_Ω is the number of galaxies per unit solid angle. $\xi(r)$ and $w(\theta)$ are connected trough the Limber equation. The relation between them is particularly simple in the case of power law behaviours:

$$\xi(r) \propto r^{-\gamma} \quad \longrightarrow \quad w(\theta) \propto \theta^{1-\gamma}. \tag{1.51}$$

Groth & Peebles (1977) computed the angular correlation function of the Shane–Wirtanen Lick galaxy counts and found that $w(\theta)$ is well fit by a power law of slope 0.77 for scales smaller than 2° with a sharp break on larger angular scales. More recently Maddox et al. (1990) computed the angular correlation function for APM galaxies and found that it matches the Lick one on small scales but its power law behaviour breaks at a somewhat larger scale. The spatial correlation function has been determined essentially from redshift surveys (Davis & Peebles 1983, Shanks et al. 1983, de Lapparent, Geller & Huchra 1988, Strauss et al. 1992 and Loveday et al. 1994). All the analyses agree that the galaxy–galaxy spatial correlation function, ξ_g, is well approximated by a power law in the range $0.1\,h^{-1}\text{Mpc} < r < 10\,h^{-1}\text{Mpc}$:

$$\xi_g(r) \simeq \left(\frac{r}{r_\circ}\right)^{-\gamma}, \tag{1.52}$$

with $\gamma \simeq 1.8$ and the correlation length $r_{\rm o} \simeq 5.4\,h^{-1}$Mpc which is consistent with the behaviour of $w(\theta)$.

Besides galaxies, the two–point correlation function has been measured also for other classes of objects. The spatial two–point correlation function of the Abell clusters of galaxies was found to be (cf. Bahcall & Soneira 1984, Klypin & Kopilov 1983, Plionis et al. 1991)

$$\xi_c(r) \simeq \left(\frac{r}{r_{\rm oc}}\right)^{-\gamma}, \tag{1.53}$$

where $12\,h^{-1}$Mpc $< r_{\rm oc} < 25\,h^{-1}$Mpc and $\gamma \simeq 1.8$ for separations in the range $5\,h^{-1}$Mpc $< r < 70\,h^{-1}$Mpc. The $r_{\rm oc}$ value is quite uncertain and varies with the cluster richness (the number of galaxies contained within the Abell radius of $\sim 1.5\,h^{-1}$Mpc). No correlation with cluster richness was found for the exponent γ which is remarkably close to that of galaxies.

1.2.4 The Bias Parameter

In order to link the matter density field to the observed galaxy distribution we have assumed that the density field is well traced by the discrete distribution of luminous objects. However, it is well known that most of the mass in the universe is in a dark form that can be revealed only through its dynamical influence and to fulfill the previous assumption all the matter should be concentrated in dark haloes surrounding the visible galaxies. Although there are good arguments to believe that the distribution of luminous objects trace the mass on scales larger than 5–10 h^{-1}Mpc, there is very little evidence that this is true also on smaller scales.

Because of our ignorance on the processes that lead to the formation of galaxies we do not have a physical model to relate the galaxy and mass distributions and one has to resort to simple statistical arguments. Kaiser (1984) suggested a model in which the galaxies form at the high–density peaks of the density field. In this case the galaxy distribution is said to be biased with respect to the matter. Kaiser (1984) was interested in studying the biasing of clusters relative to galaxies. It was soon realized that a similar mechanism can be extended to study the galaxy distribution with respect to the underlying density field, causing the clustering of the galaxies to be stronger than that of the mass. The *peak biasing* model introduced by Kaiser (1984) makes a definite prediction for the relation between the spatial two–point correlation functions of the biased and unbiased distribution, at least on large scales,

$$\xi_{biased}(r) \simeq b^2 \xi_{unbiased}(r), \tag{1.54}$$

where b is the *biasing parameter*, which is assumed constant, independent of scale and related to the threshold at which the objects are selected. In some sense the biasing factor parametrizes our ignorance about the formation of luminous objects. The peak biasing model naturally explains the fact that, as we have seen, ξ_c and ξ_g have the same shape but different amplitudes. Dekel & Rees (1987) proposed a physical mechanism to justify the Kaiser prescription (1984) although alternative biasing schemes have been proposed more recently (Babul & White 1991, Bower et al. 1993, Catelan et al. 1993).

In practice and in what follows we will assume the simple *linear biasing scheme*

$$\delta_{biased}(\mathbf{x}) = b\delta_{unbiased}(\mathbf{x}). \tag{1.55}$$

Equation (1.55) implies eq. (1.54) while the vice–versa is certainly not true. When $b > 1$ and the unbiased field refers to the mass density field, eq. (1.55) cannot be strictly correct since $\delta > -1$ always. To avoid this problem the scheme

$$1 + \delta_{biased}(\mathbf{x}) = [1 + \delta_{unbiased}(\mathbf{x})]^b \tag{1.56}$$

has been sometimes employed in the literature. It is worth stressing that the linear biasing model is just the simplest possible model for relating the density and the galaxy density fields but it would be surprising if there were not some kind of non–linear dependence at least on scales smaller than $5\,h^{-1}$Mpc (Coles 1986, Coles 1993).

1.3 THE EVOLVING UNIVERSE

There is one crucial observation that any evolutionary model has to explain: at the present–epoch the matter distribution is very clumpy and density fluctuations corresponding to visible galaxies are very large while the CMB isotropy suggests that at the recombination epoch the density field was highly homogeneous and the amplitude of density fluctuations was very small.

This constraint ruled out many models; among them one proposed in the sixties according to which galaxies were formed as a result of primordial cosmic turbulence. The standard GI scenario was proposed in the late sixties as an alternative model by several authors (Doroshkevich, Zel'dovich & Novikov, Peebles & Yu, Weinberg and Field among the others). The GI implements the gravitational Jeans instability theory in Cosmology and considers the adiabatic longitudinal solutions (while the cosmic turbulence considered the vortical modes of the Jeans theory) to describe the growth of initially small density

fluctuations. The GI is able to explain the high degree of isotropy in the CMB and the observed relationship between cosmic density and peculiar velocity fields. This success makes the GI the most popular scenario for understanding the LSS evolution, although some class of non GI models (e.g. some types of explosion scenarios) cannot be ruled out (c.f. Babul et al. 1994).

The simple idea underlying the Jeans theory is that small fluctuations in the density field develop via gravitational instability when the self gravitation of the overdensities becomes larger than the stabilizing effect of the pressure forces. In this case the density fluctuations grow until they eventually collapse. Jeans showed that the instability develops if the size of the fluctuation l exceeds a characteristic lengthscale (the so called Jeans length, λ_j) that depends on the local density and the sound velocity. Therefore if $l > \lambda_j$ the GI enhances the fluctuations otherwise the velocity dispersion dissipates them.

The growth of fluctuations within the Standard model is a much more complicated process in which, besides the phenomenon of the gravitational instability, one also needs to account for

- The expansion of the universe.

- The mass components of the universe. The simplest acceptable model is one of three components: baryonic material, non–baryonic material (made of one single type of particles) and photons. Moreover curvature adiabatic perturbations (in which all the three components are perturbed) are assumed.

- Physical processes that affect the growth of fluctuations during the radiation dominated era.

The net result of the evolutionary process mainly depends on the nature of the non baryonic mass component and can be divided in two categories:

- *Hot Dark Matter (HDM) Scenario*: In this case the universe is dominated by non–baryonic particles that were still relativistic when they decoupled from the other components. In this case the first structures to form are on large scales (having masses similar to that of clusters or superclusters of galaxies $\sim 10^{12} - 10^{14} \ M_\odot$). Galaxies form by successive collapse and fragmentation of these primordial structures. This is the so called *top down scenario*.

- *Cold Dark Matter (CDM) Scenario*: The universe is dominated by particles that decoupled when they were no longer relativistic or that have never been in thermal equilibrium with the other components. In this scenario structures form by aggregation of smaller overdensities ($\sim 10^6$ $M_\odot$) that cluster under the effect of gravity (*hierarchical clustering*). For this reason the CDM scenario is also called *bottom up* scenario.

Here we will not discuss in detail the growth of density fluctuations and we will mainly concentrate on the so called 'linear approximation', that describes their GI evolution when $\delta \ll 1$, and on the possible generalization to the non–linear regime. An overview of the growth of density perturbation will be given at the end of the section.

1.3.1 Linear solutions

Let us consider a density perturbation field, generated somehow in the early stages of the universe, that starts growing when the non–relativistic matter begin to dominate the density of the universe (any relativistic component is thought to give a negligible contribution). We also assume the existence of post–recombination density fluctuations in the non–relativisitic components of the matter. Here we treat the matter as a pressureless ideal fluid. The equations of the motion for the matter fluid are the classical Poisson equation (which states that density fluctuations originate by metric perturbation given by the Newtonian potential ϕ), the continuity and the Euler equations (that state the conservation of the mass and of the momentum, respectively). In an expanding universe these equations can be written as

$$\frac{\partial \delta}{\partial t} + \frac{1}{a} \nabla \cdot (1 + \delta)\mathbf{v} = 0, \tag{1.57}$$

$$\frac{\partial \mathbf{v}}{\partial t} + \frac{1}{a}(\mathbf{v} \cdot \nabla)\mathbf{v} + \frac{\dot{a}}{a}\mathbf{v} = -\frac{1}{a}\nabla\phi, \tag{1.58}$$

$$\nabla^2 \phi = 4\pi G \langle \rho \rangle a^2 \delta, \tag{1.59}$$

where the peculiar velocity $\mathbf{v}$ and the density fluctuations δ are both functions of the comoving coordinates $\mathbf{x}$. Also the gravitational potential ϕ is a function of the comoving coordinates:

$$\phi(\mathbf{x}, t) = -Ga^2 \langle \rho \rangle \int \frac{\delta(\mathbf{\dot{x}}, t)}{|\mathbf{\dot{x}} - \mathbf{x}|} d\mathbf{\dot{x}} \tag{1.60}$$

as well as the peculiar gravitational field $\mathbf{g}$

$$\mathbf{g}(\mathbf{x}, t) = -\frac{\nabla\phi}{a} = Ga \langle \rho \rangle \int \frac{\delta(\mathbf{\dot{x}}, t)}{|\mathbf{\dot{x}} - \mathbf{x}|^3} d\mathbf{\dot{x}}. \tag{1.61}$$

Assuming small fluctuations ($\delta \ll 1$) and reducing to the case of fluctuations much larger than the Jeans length, we can recover the lowest order solutions to the equations of motion by linearizing the system of eq. (1.57), (1.58) and (1.59). It makes sense to look for linear solutions since at early stages $\delta \ll 1$ on all scales (as confirmed by the COBE results). The linear approximation is also valid at the present–epoch provided that $\delta(\mathbf{x})$ is smoothed on large enough scales.

Linear δ Solutions:

Combining eq. (1.57) and eq. (1.58) and linearizing allows to obtain the equation for $\delta(t)$ (Peebles 1980):

$$\frac{\partial^2 \delta}{\partial t^2} + 2\frac{\dot{a}}{a}\frac{\partial \delta}{\partial t} - 4\pi G \langle \rho \rangle \delta = 0. \tag{1.62}$$

The general solution has the form

$$\delta(\mathbf{x}, t) = \delta(\mathbf{x})[D(t) + \tilde{D}(t)], \tag{1.63}$$

where $D(t)$ is the growing mode and $\tilde{D}(t)$ is the decaying mode that, since it disappears rapidly, will not be considered in what follows. The solution (1.63) is self similar so that the initial density field retains its characteristic features and what changes is just the amplitude of the original fluctuations.

Substituting the growing mode of the solution (1.63) into eq. (1.62) gives

$$\ddot{D} + 2\frac{\dot{a}}{a}\dot{D} - 4\pi G \langle \rho \rangle D = 0. \tag{1.64}$$

In the case of an Einstein de Sitter universe $a(t) \propto t^{2/3}$ and $\rho \propto t^{-2}$, therefore eq. (1.64) becomes

$$\ddot{D} + 2\frac{4\dot{D}}{3t} = \frac{2D}{3t^2}, \tag{1.65}$$

that admits the solution

$$\delta(\mathbf{x}, t) = \delta(\mathbf{x})t^{2/3}. \tag{1.66}$$

Linear v Solutions:

The time behaviour of the Newtonian potential can be straightforwardly deduced from equations (1.60) and (1.63). To solve for $\mathbf{v}$ let us write the linearized analogue of the Euler and continuity equations:

$$\frac{\partial(a\mathbf{v})}{\partial t} = a\mathbf{g} \tag{1.67}$$

and

$$\nabla \cdot \mathbf{v} = -a \frac{\partial \delta}{\partial t}. \tag{1.68}$$

Equation (1.68) is particularly important since it returns $\delta(\mathbf{x})$ once $\mathbf{v}(\mathbf{x})$ is known. Introducing the quantity

$$f = \frac{d \log D}{d \log a} \tag{1.69}$$

eq. (1.68) can be rewritten in the standard form:

$$\delta(\mathbf{x}) = -\frac{\nabla \cdot \mathbf{v}}{aHf}. \tag{1.70}$$

The behaviour of f as a function of Ω_o is given quite accurately by the approximate relation $f \simeq \Omega_o^{0.6}$. Note that in the GI picture vortical modes decay with times so that the peculiar velocity field is curl–free and can be expressed as the gradient of a scalar function Φ_V called the velocity potential:

$$\mathbf{v} = -\frac{\nabla \Phi_V}{a}. \tag{1.71}$$

Substituting eq. (1.71) into eq. (1.70) gives

$$\nabla^2 \Phi_V = Hfa^2 \delta \tag{1.72}$$

that, compared with the Poisson equation (1.59), shows that $\phi \propto \Phi_V$ and thus $\mathbf{v} \propto \mathbf{g}$:

$$\mathbf{v} = \frac{2f}{3\Omega H} \mathbf{g}, \tag{1.73}$$

from which the time behaviour of $\mathbf{v}$ can be easily deduced. Equation (1.73) indicates that in the linear regime the peculiar velocity is proportional to the local gravitational acceleration. From eq. (1.73) one obtains

$$\mathbf{v}(\mathbf{x}) = \frac{aHf}{4\pi} \int \delta(\mathbf{x}) \frac{\acute{\mathbf{x}} - \mathbf{x}}{|\acute{\mathbf{x}} - \mathbf{x}|^3} d^3 \acute{x}, \tag{1.74}$$

a relationship that will be very useful in the rest of the thesis.

1.3.2   Beyond The Linear Regime

Linear theory allows us to predict the time behaviour of the density and peculiar velocity fields and it also relates the two fields through a simple, invertible formula. It should be kept in mind that linear relations are valid when $\delta \ll 1$ and therefore can lead to non negligible errors if they are used to describe what happens within the high density regions. Unlike the strong non–linear effects in virialized systems which tend to erase the

memory of the initial conditions, mildly non–linear effects can still carry crucial information about the large scale structure (LSS) of the universe. It is therefore very important to follow the growth of density fluctuations and the evolution of the peculiar velocity even in the quasi–linear regime (i.e. when $\delta \simeq 1$).

The first improvement over the simple linear theory should be attributed to Zel'dovich who proposed an ingenious extrapolation of linear GI into the non linear regime (Zel'dovich 1970). He expressed the displacement of particles from their initial, Lagrangian positions q to their Eulerian position, $\mathbf{x}(t)$ at time t as function of the peculiar velocities:

$$\mathbf{x}(\mathbf{q}, t) - \mathbf{q} = D(t)\nabla_{\mathbf{q}}\Phi(\mathbf{q}) = a(Hf)^{-1}\mathbf{v}, \qquad (1.75)$$

where the potential $\Phi(\mathbf{q})$ is proportional to the velocity potential and the gradient $\nabla_{\mathbf{q}}$ is taken with respect to Lagrangian coordinates. Under the hypothesis of no multi–streaming, relation (1.75) can be interpreted in the Eulerian space as:

$$\mathbf{q}(\mathbf{x}) = \mathbf{x} - (Hf)^{-1}a\mathbf{v}. \qquad (1.76)$$

Nusser et al. (1991) have shown that the solution of continuity equation yields

$$\delta(\mathbf{x}) = \left\| I - (fH)^{-1}\frac{\partial \mathbf{v}}{\partial \mathbf{x}} \right\|, \qquad (1.77)$$

where $\| \cdot \|$ is the Jacobian determinant and I is the unit matrix. This relation allows to compute the density field once the full 3D peculiar velocity field is known but it is difficult to invert to provide $\mathbf{v}$ when δ is given. For this purposed the following empirical approximation proved to be useful

$$\nabla \cdot \mathbf{v} = \frac{f\delta}{(1 + 0.18\delta)}. \qquad (1.78)$$

An even better approximation has been obtained by adding second order terms to the $(\mathbf{x} - \mathbf{q})$ Zel'dovich displacement and by truncating all the expressions to the second order. Using this strategy and solving the continuity equation Gramman (1993) obtained the following relation

$$\delta(\mathbf{x}) = -f^{-1}\nabla \cdot \mathbf{v} + 4/7f^{-2}\sum_i\sum_{j>i}\left(\frac{\partial v_i}{\partial x_i}\frac{\partial v_j}{\partial x_j} - \frac{\partial v_i}{\partial x_j}\frac{\partial v_j}{\partial x_i}\right) \qquad (1.79)$$

which can be inverted in second order to provide $\nabla \cdot \mathbf{v}$ given δ.

Another approximation has been obtained by Bernardeau (1992) assuming Gaussian fluctuations and vanishing variance:

$$\delta(\mathbf{x}) = \left[1 - \frac{2}{3}f^{-1}\nabla \cdot \mathbf{v}\right]^{3/2} - 1. \qquad (1.80)$$

that has been recently generalized to the case of non–vanishing variance (Dekel 1994).

Other non–linear methods, like those based on the least action principle will be presented in the next chapter.

1.3.3 Growth of Fluctuations: an Overview

As we have anticipated, the evolution of the density fluctuations is a quite complicated process. An evolutionary model should describe not only the growth of fluctuations under self gravity but also explain how primordial fluctuations form, how physical processes affect their evolution, how they evolve in the linear, mildly non–linear and highly non–linear regime. A complete discussion of this subject is beyond the scope of this thesis, here we will present briefly the evolution of density fluctuations by describing how their power spectrum gets modified which then allows us to characterize the evolution of the cosmic structures.

- *Primordial density fluctuations*: The common assumption is that overdensities are generated by quantum fluctuations at some very early epoch. Such fluctuations are naturally accounted for in the inflationary scenario that provides a physical model in which perturbations are generated during the epoch of vacuum energy domination, when $\ddot{a} > 0$, and the primordial scalar field, driving inflation, exhibits quantum fluctuations. Since inflation does not pick out any characteristic scale, these primordial fluctuations can be described by a scale–free primordial power spectrum

$$P_o(k) \propto k^n, \tag{1.81}$$

where n is the so called spectral index.

Before inflation, several authors attempted to justify the choice of a primordial scale invariant $P_o(k)$ and to specify the relative primordial index. Harrison (1970), Peebles & Yu (1970) and Zel'dovich (1972) proposed the so called *Cosmological White Noise* or *Harrison–Zel'dovich* spectrum which has $n = 1$ and predicts scale–independent fluctuations in the metric. Later on, inflation provided a justification for the Harrison–Zel'dovich spectrum which is not only predicted by many inflationary models (see Mukhanov, Feldman & Brandemberger 1992 and reference therein) but also by the cosmic strings scenario (Vilenkin 1981) and by the global textures model (Cen et al. 1991, Gooding et al. 1991). There are other models, however, which predict a different primordial spectrum like the power law inflation that allows for a tilting of the spectral slope (which means $n \neq 1$, Adams et al. 1993).

Furthermore, inflationary scenarios predict the shape of the PDF, which is expected to be Gaussian, and the nature of the density fluctuations, which are expected to be adiabatic. Isothermal initial conditions are quite unlike and seem to be ruled out since they predict temperature fluctuations in later stages comparable with those of the adiabatic perturbations (Mukhanov, Feldman & Brandemberger 1992).

- *Evolution outside the horizon*: The cosmological horizon at early times is very small so that all the fluctuations relevant for the structure formation are outside the horizon after the inflationary epoch. The amplitude of the density fluctuations outside the horizon grows according to linear law, $\delta(\mathbf{x}, t) = D(t)\delta(\mathbf{x})$, so that the super–horizon evolution does not modify the spectral shape. As time passes the horizon size increases and perturbations of larger and larger scale enter the horizon where they start interacting with the rest of the universe. At this point their evolution depends on the epoch in which they cross the horizon: fluctuations of small size enter first when the universe is dominated by radiation and thus they start interacting with the photon gas causing the power spectrum to get modified on sub–horizon scales. Large scale fluctuations enter the horizon later on when the universe is matter dominated and therefore they continue growing at the same rate via gravitational instability. As a consequence the power spectrum maintains its primordial shape on large scales.

- *Evolution during the radiation dominated epoch*: The details of the spectral bending during the radiation dominated epoch depend both on the cosmological parameters (h, Ω_o) and on the nature of the non–baryonic matter. Assuming a given set of cosmological parameters, and thus fixing the horizon scale at the epoch of equivalence between radiation and non–baryonic matter, there are two main modes in which the spectrum can be modified which correspond to the two evolutionary scenarios described in section (1.3):

- In the HDM scenario if a matter fluctuation crosses the horizon before the equivalence it starts suffering from the free streaming effect. The free streaming distance λ_{fs} is defined as the average distance covered by non–baryonic particles since they decouple until they become non–relativistic. Collisionless dark matter particles stream away and rapidly dissipate the fluctuations of size $< \lambda_{fs}$. HDM particles, like the neutrino, are characterized by a large value of λ_{fs} (of the order of $\sim 20\,h^{-1}\mathrm{Mpc}$). As a consequence the power spectrum at an epoch successive to the equivalence (the standard choice is to take the recombination as a reference epoch) shows a dramatic cutoff around λ_{fs}

and its overall shape is modified as follows:

$$\text{for } k > 1/\lambda_{fs} \rightarrow P(k) \sim 0$$

while

$$\text{for } k < 1/\lambda_{fs} \rightarrow P(k) =\sim P_\text{o}(k).$$

- In the CDM model λ_{fs} is much smaller than the size of cosmic structures and thus the free streaming is not important. There is, however, another relevant phenomenon that affects the growth of density fluctuations: when a perturbation enters the horizon and photons (which are the dominant component) and charged particles oscillate as an acoustic wave, the driving term for the growth of the associated CDM fluctuation disappears and the density fluctuation stops growing until equivalence. Even in this case the shape of the power spectrum gets modified: on scales larger than the horizon scale at the equivalence the spectral shape is unaltered while going towards smaller scales the amplitude of the spectrum decreases since those scales correspond to fluctuations of smaller size which spent most of their time within the horizon.

The scenarios sketched above are quite simplistic, there are other phenomena which have to be accounted for. The combined effect of the various processes affecting the growth of density fluctuations is usually described by the so called transfer function, $T(k)$, which is defined through the following expression:

$$P(k, t_f) = \left[\frac{D(t_f)}{D(t_i)} \right]^2 T^2(k, t_f) P(k, t_i), \tag{1.82}$$

where $P(k, t_i)$ is the processed spectrum at an arbitrary final epoch (usually the recombination), t_i is the initial epoch (the inflationary era) and the term $\frac{D(t_f)}{D(t_i)}$ parametrizes away the linear growth that the density fluctuations experience outside the horizon.

● *Evolution in the linear regime*:

After the recombination epoch density fluctuations grow via Jeans gravitational instability. Since at that epoch the amplitude of the fluctuations is very small on all the scales, we can describe the evolution of density fluctuations in the linear approximation, as we did in section (1.3.1). Equation (1.30) ensures that the linear evolution is self similar which means that, in the linear regime, the power spectrum maintains the shape it had at the recombination.

- *Evolution in the non–linear regime*: The linear approximation breaks down when the overdensities δ become of the order of unity, which first happens on small scales where the mass variance is larger. In this case one has to resort to nonlinear approximations which can account, however, only for the mildly–nonlinear regime (i.e. for $\delta \sim 1$). Following the growth of density fluctuations beyond this point is a non trivial task since the non–linear evolution, unlike the linear one, mixes up the different Fourier modes. The result is a scale dependent spectral bending which is more severe on small scales where the non–linear regime sets up earlier.

  An analytical, self consistent treatment of the problem does not exist. However Hamilton et al. (1991) and Peacok & Dodds (1994) have semi–empirically worked out an analytical formula which accounts for the nonlinear spectral bending and is valid in any regime. Their result relies on two hypotheses (a simple relation between the primordial and the evolved density contrast plus the assumption that the non–linear correlation function is a universal function of the linear one) whose validity has been tested using N–body simulations. Their method can describe the nonlinear evolution of the power spectrum but does not predict how the PDF is modified by the non–linear evolution.

Ideally, measuring the present–shape of the power spectrum and knowing the physical processes that modify $P(k)$, it is possible to trace its shape back to the recombination epoch, which then allows us to cast light on the nature of dark matter, to the primordial $P(k)$ shape, and to understand which mechanism generated the primordial density fluctuations. As we will see in the next chapter, this task is not so trivial since experimental uncertainties and our ignorance of galaxy formation reflect in serious uncertainties.

Chapter 2

THE RECONSTRUCTION METHODS

In this Chapter we present and discuss some of the reconstruction methods that have been used in the studies of the LSS.

The term reconstruction is used here in a broad sense: it indicates a phenomenological procedure by which, starting from the available noisy and incomplete observational data, one attempts to recover the true cosmic density and velocity fields using a theoretically justified reconstruction procedure, as displayed in the diagram below:

Observational Data $\longrightarrow$ Reconstruction Procedure $\longrightarrow$ $\delta(\mathbf{x})$, $\mathbf{v}(\mathbf{x})$

Clearly, to obtain $\delta(\mathbf{x})$ and $\mathbf{v}(\mathbf{x})$ one has to face two distinct problems related to the two entries of the diagram above:

2.0.4 Treatment of the Data

Experimental data need to be homogenized to avoid possible biases in the reconstruction procedure. In the LSS study one would ideally like to use all–sky catalogues of extragalactic objects selected with the same criteria and observed using a unique experimental apparatus. In practice this is not possible and very often one has to face the problem of properly merging several different catalogues to obtain an all–sky homogeneous sample. The samples available for studying the LSS can be grouped in two general categories:

1) All–sky redshift surveys containing thousands of objects which are already completed or will be available in the near future. From these surveys it is possible to extract

homogeneous catalogues of objects with a large sky coverage but with some small unsurveyed regions which are either due to galactic extinction (or cirrus emission) near the galactic plane or due to instrument limitations. The major drawback with redshift surveys is that peculiar motions cause the z–space density field, $\delta(\mathbf{s})$, to be systematically different from the true one, $\delta(\mathbf{x})$ ($\mathbf{s}$ is the redshif space position of a generic object). In what follows we will discuss some techniques aimed at correcting for this effect.

2) Galaxy catalogues with redshift–independent distance estimates, in which case the z–space distortions are unimportant. In this case, however, one has to face different and more severe problems. These catalogues are compiled by collecting several samples of galaxies with Tully–Fisher (Tully & Fisher 1977), D_n–σ (cf. Lynden–Bell et al. 1988) measurements, accumulated by different authors. Merging different catalogues in a self–consistent sample is not an easy task since the observers differ in their selection procedure, the quantity they measures, the calibration techniques and the recipes they use to correct for possible biases. Examples of homogenized merged sets are the Mark II catalogue compiled by D. Burstein and its updated version, the Mark III catalogue. Clearly, the resulting merged catalogue has neither an homogeneous nor an isotropic sky coverage and it is composed by a small number of objects. Finally, these catalogues are relatively shallow since the errors on the objects' distances increase with the distance itself which does not permit to extend their estimates to large distances.

2.0.5   Choosing the Reconstruction Algorithm

The second requirement is that of finding and implementing a reconstruction algorithm suited for the problem under study. Recovering the cosmic density and velocity fields at the generic time t is a particular case of the more general reconstruction problem in information theory. Roughly speaking, the problem consists in restoring the maximum amount of information of a system in which the original information has been degraded by some known process, or, vice–versa, to find the minimum amount of information needed to preserve those fundamental features that characterize the system itself.

This problem appears in many different astronomical contexts (the most popular example is the reconstruction of noisy pictures like those obtained by the Hubble Space Telescope before its restoring) and it has been faced using several different recipes, ranging from the very empirical ones (e.g. the methods for filling the unsurveyed regions) to the better theoretically grounded ones [e.g. the maximum–entropy algorithms of Gull & Daniel

(1978) or the fractal pixons restoration technique of Yahil (1995)].

The choice of the reconstruction method depends on the nature of the system to which it has to be applied and to the problem studied. For example for low density systems where non–linear effects are negligible one can design the reconstruction algorithm assuming a one–to–one correspondence between density and velocity fields while more sophisticated methods need to be implemented when the effects of the non–linear evolution cannot be neglected. For example, the shape of the $P(k)$ is nearly unaffected by non–linear evolution on scales $> 10\,h^{-1}\mathrm{Mpc}$; therefore we can recover the linear $P(k)$ by filtering the present–epoch density field on a proper scale. On the other end if one is interested in studying the linear probability distribution function ([PDF], that together with the linear $P(k)$ completely characterizes $\delta(\mathbf{x})$ as a random field) one need to trace $\delta(\mathbf{x})$ back in time since the PDF develops a strong skewness even in the mildly non–linear regime.

In this section we will review some of the most commonly used reconstruction methods aimed at studying the LSS of the universe.

We start by discussing the phenomenological reconstruction of the $P(k)$. This is a simple case in which, starting from different kind of observations one recover a statistical quantity (the $P(k)$) that contain all the information about the present–time density field provided it is Gaussian. In section (2.2) we present some methods for recovering $\delta(\mathbf{x})$ from observations. We discuss how to properly fill the unsurveyed regions, how to minimize the shot–noise, and how to eliminate redshift–space distortions. We also discuss the $POTENT$ method that allows to reconstruct the true density field from the observed peculiar velocities. Finally, in the last section we review the techniques used to trace the present–time density field back in time to the linear regime.

2.1 RECONSTRUCTING THE POWER SPECTRUM OF DENSITY FLUCTUATIONS

The $P(k)$ completely characterizes the density field in the linear regime if the phases are randomly distributed. Furthermore, since it is considerably easier to reconstruct than the whole density fluctuation field, it is not surprising that many authors have tried to directly recover the $P(k)$ from the available observations.

Direct measurements of $P(k)$ have been performed using a number of galaxy redshift surveys (Baumgart & Fry 1991, Peacock & Nicholson 1991, Park Gott & da Costa 1992,

Vogeley et al. 1992, Fisher et al. 1992, Feldman et al. 1994, Park et al. 1994, da Costa et al. 1994, Lin 1995). These studies allow to sample the $P(k)$ only up to a limiting depth of $\sim 100 \, h^{-1}$Mpc where it is subjected to significant z–space distortions and non–linear effects that modify its shape in a scale–dependent fashion. Furthermore, different authors utilize different catalogues ($IRAS$ galaxies, Optical galaxies, radiogalaxies, Abell/ACO clusters etc.) that are thought to trace the underlying density field in different ways.

To sample the shape of the $P(k)$ on a range of scales as wide as possible, several authors have derived empirical spectra by fitting various data sets. The general attitude is that of assuming an arbitrary shape for the $P(k)$ and fixing the free parameters of the model to match the available observations on small scales (to account for the clustering of luminous objects) and on very large scales (to recover the observed angular two–point correlation function, $w(\theta)$, or to fulfill the COBE constraints). For example, Peacock (1991) constrained his phenomenological spectrum using available redshift surveys of luminous galaxies and the APM angular two–point correlation function (Maddox et al. 1990). Padmamanabhan & Narashima (1993) extended that analysis by using the $IRAS$ and CfA redshift surveys data, the angular two–point correlation function from the APM survey, constraints from large scale streaming velocities and COBE data. Jing & Valdarnini (1993) computed their $P(k)$ from $IRAS$ galaxies and Abell/ACO clusters catalogue and constrained the tail of the $P(k)$ at small k using COBE observations. Similarly, the Torres, Fabbri & Ruffini (1994) $P(k)$ was derived by reproducing the shape of their generalized spatial two–point correlation function and by satisfying the COBE constraints.

To look closer to the procedure through which phenomenological power spectra are derived we describe here a novel analysis (presented also in Branchini, Guzzo & Valdarnini 1994) and the Peacock & Dodds (1994) [PD] analysis in more detail.

In the first case we build a model for $P(k)$ starting from general considerations on the present–time shape of the $\xi(r)$ computed from the CfA$_{15.5}$ and the Perseus–Pisces [PP] redshift surveys. More precisely, we show that the $1 + \xi(r)$ autocorrelation function can be approximated by a broken power law up to $\sim 30 \, h^{-1}$Mpc. We have interpreted the slope of $1 + \xi(r)$ at small scales as the outcome of the combined effect of non–linearity and of 'Fingers of God' z–distortions. Assuming that at large scales the power law behaviour of $1 + \xi(r)$ reflects its linear shape, we were able to constraint the $P(k)$ shape on small scales ($P(k) \propto k^{-2.2}$). To fix the large scale $P(k)$ shape, we adopt the simple functional form

$$P(k) = \frac{Ak^{\alpha}}{1 + (k/k_c)^{\alpha - n}}, \qquad (2.1)$$

where $\alpha = -2.2$ and $k_c = 0.08\,h^{-1}\mathrm{Mpc}$ from the consideration on the $\xi(r)$ shape while the normalization factor A depends both on the value of the bias factor for the luminous PP galaxies, b, and on the $P(k)$ amplitude enhancement generated by linear z–space distortions (Kaiser 1987). Using the rms temperature fluctuations at $10°$ measured by COBE and following two independent routes, we constrain the (n,b) pair in the range [0.75,1] and [1.4,1.9]. The resulting $P(k)$ matches extremely well the directly measured power spectra on scales smaller than $100\ h^{-1}\mathrm{Mpc}$. To check how our phenomenological $P(k)$ behaves when non–linear gravitational evolution set in, we perform N–body simulations of an Einstein–de Sitter universe with spectra given by eq. (2.1) with n in the allowed range. This also allows to better constrain the (n,b) pair: it turned out that the two–point correlation function of the simulated galaxy distribution matches the observed one for $(n,b) = (0.85, 1.8)$. N–body tests revealed that our power spectrum, which is very similar to a tilted CDM $P(k)$ with $n = 0.85$, allows us to obtain a small scale velocity dispersion in accordance with observation while a drawback in our model is that the angular two–point correlation function seems to lack some power on very large scales when compared to the APM data.

PD also performed a through phenomenological reconstruction. Their work extends those previously quoted by collecting information from a much larger set of data: the real space clustering of galaxies (by deprojecting the angular clustering of APM galaxies), the redshift–space galaxy clustering (QDOT and CfA surveys), the z–space clustering of the Abell/ACO clusters and the cross correlation between *IRAS* galaxies and Abell clusters or radiogalaxies. PD assume a scale–independent bias factors for the various population of objects. The power spectra they derive are normalized to that of *IRAS* galaxies, which then forces $b_{IRAS} = 1$. Furthermore they account for non–linear evolution on small scales by using the Hamilton et al. (1991) treatment. Furthermore, they account for z–space distortions by applying an analytical correction that account for both the large scale linear enhancement of the $P(k)$ amplitude (Kaiser 1987) and the small scales 'Fingers of God' effect (Peacock 1992). Finally, PD account for the rms CMB temperature fluctuations revealed by COBE. They obtain:

1. The bias factors of various populations of objects relative to the IRAS galaxies:

$$b_{Abell}\ :\ b_{Radio}\ :\ b_{Opt.}\ :\ b_{IRAS}\ =\ 4.5\ :\ 1.9\ :\ 1.3\ :\ 1$$

2. From the amount of redshift–space distortions, $\Omega_o^{0.6}/b_{IRAS} = 1.0 \pm 0.2$ while the amount of non–linear corrections required disfavour low Ω_o values.

3. The shape of $P(k)$ is extremely well described by a CDM transfer function

$$P(k) = \frac{Ak}{\left\{1 + \left[\left(\frac{6.4k}{\Gamma}\right) + \left(\frac{3.0k}{\Gamma}\right)^{3/2} + \left(\frac{1.7k}{\Gamma}\right)^2\right]^{1.13}\right\}^{2/1.13}}, \tag{2.2}$$

with a shape factor $\Gamma = 0.25$. Also, tilted models appear to be disfavoured by their lack of power at $\sim 100\, h^{-1}\mathrm{Mpc}$.

It seems difficult to reconcile our results with those of PD; generally similar contradictions arise when comparing the different empirical $P(k)$. These incongruities probably derive from having considered different datasets homogenized with different procedures, different recipes for correcting redshift–space and non–linear distortions and from adopting simplifying hypotheses (like the assumption of a linear biasing scale–independent scheme). Therefore a word of caution is due about the reliability of the phenomenological power spectra (c.f. Efstathiou 1995). However, this argument can be reversed: despite the simplistic assumptions, the use of inhomogeneous datasets and different data treatment it is quite surprising that most of the phenomenological models agree in predicting some fundamental features:

- There is more large scale power that predicted in the standard CDM model.

- The slope of $P(k)$ is steeper at small scales with respect to the SCDM.

- There is a peak around $k = 0.05\, h\, \mathrm{Mpc}^{-1}$.

2.2 RECONSTRUCTING THE COSMIC DENSITY FIELD

Discrete data can be transformed into a continuous density field $\hat{\delta}(\mathbf{x})$ by smoothing on a given scale under the assumption of linear biasing:

$$\hat{\delta}(\mathbf{x}) = \frac{1}{nb}\sum_i^N W(|\mathbf{x} - \mathbf{x}_i|)w(\mathbf{x}_i) - 1, \tag{2.3}$$

where n is the number density of objects, W is a window function characterized by a smoothing scale R_{sm} normalized to unit integral, b is the biasing factor and $w(\mathbf{x})$ is a weighting function that accounts for missed objects (e.g. in a magnitude or flux limited sample it is the inverse of the probability of finding an objects at a given position). Note that $\hat{\delta}(\mathbf{x})$

is different from the true density field, $\delta(\mathbf{x})$, since it is subject to errors from a number of sources:

- *Shot–Noise*: Galaxies sparsely sample the underlying density field. Having a limited number of mass tracers within each smoothed volume generates the so called shot–noise error that can be quantified as

$$\sigma_{sn} = \frac{1}{n} \left[\sum_i^N \left(W(|\mathbf{x} - \mathbf{x}_i|) w(\mathbf{x}) \right)^2 \right]^{1/2}. \tag{2.4}$$

Since the shot–noise increases with the sparsness of the sampling and with the incompleteness of the catalogue, it is particularly important for small and for magnitude or flux limited galaxy samples. A more complete discussion of the shot–noise error will be given in Chapter 3 and in Appendix.

- *Incomplete Sky Coverage*: All the extragalactic object samples, even the so called 'all–sky' surveys, are incomplete due to the extinction or cirrus emission near the galactic plane, a region of the sky called the zone of avoidance (ZoA).

- *Redshift Space Distortions*: The most complete and modern all–sky catalogues list the angular positions of the objects together with their observed redshifts. However, the presence of gravitationally driven peculiar velocities cause systematic distortions in the z–space mapping of the density field which need to be corrected for.

- *Non–linear Effects*: The non–linear evolution in high density regions spoils the simple one–to–one correspondence between density and peculiar velocity fields predicted by linear theory. Non–linear models can account for the distortions that would otherwise affect (a) the reconstruction of the density field from the observed peculiar velocity field and (b) the attempts to trace the present–time density field back in time.

In this section we review some methods for properly deriving the density field at the present–epoch, leaving to the next section the problem of reconstructing $\delta(\mathbf{x})$ at a generic time t.

2.2.1 Filling in the Zone of Avoidance

Extrapolating the density field to the ZoA is particularly important for dynamical studies since one needs to know the whole sky distribution of matter up to very large distances

to compute the peculiar velocity in a point. A number of filling techniques, either empirical or theoretically motivated, have been used for this purpose.

Not taking into account the unsurveyed regions will cause systematic errors in any dynamical modeling since such regions would act as a void, generating a systematic outflow. Filling the region with a random distribution of objects having the mean density estimated from the rest of the survey reduces the extent of the problem without however solving it completely. A better scheme is to interpolate the density field from higher latitude regions using cloning procedures (c.f. Lynden–Bell, Lahav & Burstein 1989) linear interpolation (Yahil et al. 1991) or a mixing of the two (Branchini & Plionis 1995). More sophisticated approaches expand the angular distribution of galaxies in spherical harmonics (cf. Yahil et al. 1986, Lahav 1987, Plionis 1988, Scharf et al. 1992) or combine the spherical harmonics decomposition to the Wiener filtering to reduce the shot–noise problem (Lahav et al. 1994). An example of such a filling procedure will be used in Chapter 3 as a part of a more general reconstruction algorithm. The best although extremely difficult alternative to such reconstructions is obviously to survey the zone of avoidance itself (see Balkowsky & Kraan–Kortweg 1994 for a review of this subject).

2.2.2 Reducing the Shot–Noise Using the Wiener Filter

The shot–noise problem can be minimized by properly filtering the data. If $\hat{\delta}(\mathbf{x})$ is the observed density field and σ_{SN} is the shot–noise then the true and the observed density fields are simply related by:

$$\hat{\delta}(\mathbf{x}) = \delta(\mathbf{x}) + \sigma_{SN}, \qquad (2.5)$$

where the shot–noise is assumed to be independent of the position. The Wiener filter $\mathcal{F}$ is defined so that the variance σ between the true and the measured density field is minimized (Rybicki & Press 1992). In practice one has to minimize the expression

$$\sigma = \int d^3\mathbf{x}[\delta(\mathbf{x}) - \mathcal{F}(\mathbf{x})\hat{\delta}(\mathbf{x})]^2 = \int d^3\mathbf{k}[\delta(\mathbf{k}) - \mathcal{F}(\mathbf{k})\hat{\delta}(\mathbf{k})]^2, \qquad (2.6)$$

with respect to $\mathcal{F}(\mathbf{k})$. The equality in eq. (2.6) follows by the Parseval's theorem. After minimizing one obtains the following expression for the Wiener filter:

$$\mathcal{F}(\mathbf{k}) = \frac{\langle \delta(\mathbf{k})^2 \rangle}{\langle \delta(\mathbf{k})^2 \rangle + N^2}, \qquad (2.7)$$

where $\langle \delta(\mathbf{k})^2 \rangle$ is proportional to the $P(k)$. Thus the Wiener filter $\mathcal{F}(\mathbf{k})$ requires a prior model for the $P(k)$.

The above minimization procedure defines the Wiener filter in the k-space but an expression for $\mathcal{F}(\mathbf{x})$ can be derived as well. Let us assume that the density field $\delta(\mathbf{x})$ is a linear functional of another field $u(\mathbf{x})$ (this holds for example in linear theory, where there is a one to one correspondence between the density field and the line-of-sight component of the peculiar velocity, u). Then, given noisy data u_i and an assumed prior model for $\delta(\mathbf{x})$ one obtain the optimal estimator for the density field δ_{opt}:

$$\delta_{opt}(\mathbf{x}) = \langle \delta(\mathbf{x})u_i \rangle \langle u_i u_j \rangle^{-1} u_j, \tag{2.8}$$

where the sum is over repeated indices (Hoffman 1994, Stebbins 1994). Assuming that the observed peculiar velocities can be written as $u_i = u(\mathbf{x}_i) + \epsilon_i$ with ϵ_i independent random errors with zero mean, then the autocorrelation matrix is $\langle u_i u_j \rangle = \langle u(\mathbf{x}_i)u(\mathbf{x}_j) \rangle + \epsilon_i^2 \delta_{ij}$. The matrix the $\langle u_i u_j \rangle$ has a large number of elements and its inversion is a nontrivial computational problem. From the first applications of this method (Zaroubi et al. 1994) different density fields came out from different priors producing fits with similar χ^2. This means that data are not sufficiently good to constrain the density field.

The major drawback of the Wiener filter is that it over-corrects the density field in the regions of poor data in which the filter returns the most likely value for the density field, i.e. $\delta = 0$. In other words the method filters the original field with a variable smoothing length that increases in the ill-sampled regions. To avoid this problem and to obtain a uniform smoothing a power-preserving filter defined as the square root of $\mathcal{F}$, which preserves the $P(k)$ of the original field has been recently proposed. Of course this filter does not share the minimum variance property of $\mathcal{F}$ but it has been shown that the difference between the true and the filtered field are always below the 10 % level.

The Wiener filter is also at the heart of the so called regularized multi-parameter models. As we have seen in the previous Chapter, the density field can be expanded in a discrete set of basis functions. A Fourier expansion similar to eq. (1.30) gives

$$\delta = \sum_{\mathbf{k}} [a_{\mathbf{k}} \sin(\mathbf{k} \cdot \mathbf{x}) + b_{\mathbf{k}} \cos(\mathbf{k} \cdot \mathbf{x})]. \tag{2.9}$$

Its analogous for the velocity field, assuming linear theory, is

$$\mathbf{v} = \frac{\mathbf{k}}{k} \sum_{\mathbf{k}} [a_{\mathbf{k}} \cos(\mathbf{k} \cdot \mathbf{x}) - b_{\mathbf{k}} \sin(\mathbf{k} \cdot \mathbf{x})]. \tag{2.10}$$

One can try to fix the parameters $a_{\mathbf{k}}$ and $b_{\mathbf{k}}$ by minimizing the likelihood, but the large number of coefficients involved wouldn't lead to believable results because noisy and sparse data would weakly constrain the coefficients. A regularization has been proposed by Kaiser &

Stebbins (1991) and Stebbins (1994) in which one maximizes the probability of parameters subjected to the data and assumes a prior model for the probability distribution of the Fourier coefficients. They assumed a Gaussian distribution with $P(k) = Ak^n = \langle a_k^2 \rangle = \langle b_k^2 \rangle$.

2.2.3 Recovering the $\delta(\mathbf{x})$ from the Observed $\delta(\mathbf{s})$

The efficient techniques for measuring redshifts have provided us with deep, dense and uniform all–sky redshift surveys. Assuming linear theory or some approximation to account for mildly non–linear evolution, it is possible to derive the real space density field from the z–space observed one. Strauss & Davis (1988) where the first who proposed and implemented an iterative method for recovering $\delta(\mathbf{x})$ from $\delta(\mathbf{s})$. In Chapter 3 we will apply a similar technique to recover the real space distribution and peculiar velocities of the Abell/ACO galaxy clusters, and we will describe the method with more details. Here we just sketch the general idea.

As we have seen in Chapter 1, if the velocity field is curl–free then linear theory predicts

$$\nabla \cdot \mathbf{v} = -f\delta, \tag{2.11}$$

that can be inverted to

$$\mathbf{v}(\mathbf{x}) = \frac{H_\circ f}{4\pi} \int \delta(\mathbf{x}) \frac{\dot{\mathbf{x}} - \mathbf{x}}{|\dot{\mathbf{x}} - \mathbf{x}|^3} d^3\dot{x}. \tag{2.12}$$

This relation returns the peculiar velocity at any given point given the density field $\delta(\mathbf{x})$. Assuming a linear biasing scheme $\delta_{obs} = b\delta$ the peculiar velocity can be computed from the observed density field that, in turns, can be obtained by smoothing the discrete distribution of luminous objects:

$$\mathbf{v}(\mathbf{x}) = \frac{H_\circ f(\Omega_\circ)}{4\pi b_{obs}} \int \delta_{obs}(\mathbf{x}) \frac{\dot{\mathbf{x}} - \mathbf{x}}{|\dot{\mathbf{x}} - \mathbf{x}|^3} W(|\dot{\mathbf{x}} - \mathbf{x}|) d^3\dot{x}. \tag{2.13}$$

Let us assume that we have obtained $\delta_{obs}(\mathbf{s})$ after smoothing, filtering and properly filling the unsurveyed regions of an all–sky distribution of luminous objects. The iterative reconstruction algorithm works as follows,

1. Assume $\delta_{obs}^{(0)}(\mathbf{x}_i) = \delta_{obs}(\mathbf{s})$, where (0) refers to the 0th iteration.

2. Compute $\mathbf{v}^{(0)}(\mathbf{x}_i)$ from eq. (2.13) at the objects' locations $\mathbf{x}_i$.

3. Compute the new object's distance r_i from the relation

$$H_\circ r_i = cz_i - \hat{\mathbf{x}}_i \cdot [\mathbf{v}(\mathbf{x}_i) - \mathbf{v}(0)], \tag{2.14}$$

where z_i is the redshift, $\hat{\mathbf{x}}_i$ is the unit position vector and $\mathbf{v}(0)$ is the peculiar velocity of the observer at the center of the coordinates.

4. Calculate the new density field $\delta^{(i+1)}(\mathbf{x})$ after smoothing the new distribution of objects.

5. Evaluate the difference between $\delta^{(i+1)}(\mathbf{x})$ and $\delta^{(i)}(\mathbf{x})$. If this is larger than a given tolerance level then go back to step 2.

Several authors have modified, improved and implemented similar iterative schemes [Yahil et al. 1991, Strauss et al. 1992, Hudson (1993), Freudling et al. (1994), Branchini & Plionis (1995) and for a review see Strauss & Willick (1995)] with the aim of reducing possible biases and source of errors. The previous iterative scheme assumes linear theory and thus cannot reconstruct the density field within the triple valued zones, i.e. in those high density regions in which a given redshift can correspond to three different locations. Although the smoothing procedure significantly reduces the extent of the problem, there remains a few regions in which it is necessary to introduce some local trick that allows to place the objects at the more plausible position among the three allowed (Yahil et al. 1991, Strauss & Willick 1995). Besides the few triple valued zones, the smoothed density field contains regions in which the volume averaged density contrast is of the order of unity, necessitating a quasi–linear treatment. One possible way out is to find an inverse δ–v relation of the sort $\nabla \cdot \mathbf{v} = F(\Omega, \delta_{obs})$ (Dekel 1994) in which a more physical non–linear biasing scheme may be included as well. The numerical action method, which will be discussed in Chapter 4, represents another possibility being a non–linear method that can be used to predict the present–time positions of the objects given their observed redshifts (c.f. Shaya, Peebles & Tully 1995).

A non–iterative method for removing redshift–space distortions has been proposed by Nusser & Davis (1994). They point out that, according to the Zel'dovich approximation [eq. (1.75)] , the difference between the real space and the z–space position of the objects is just proportional to the displacement of that object from $t = 0$ to the present. Starting from this observation and assuming irrotationality and conservation of the objects' number they obtain a differential equation for the velocity potential Φ_V. The peculiar velocity field can then be obtained by differentiation assuming linear theory. The major drawback of this method is that it does not account for triple valued regions.

A different non–iterative technique has been proposed by Fisher et al. (1994). The idea is to decompose the density field with spherical harmonics and spherical Bessel functions for the radial component. They notice that since redshift–space distortions do not couple

the different angular modes then the coupling matrix is analytic and can be inverted. The inverse matrix allows then to compute $\delta(\mathbf{x})$ directly from $\delta(\mathbf{s})$, one spherical harmonic at a time. Other authors have taken different approaches for recovering $\delta(\mathbf{x})$ from $\delta(\mathbf{s})$. Among them Kaiser et al. (1991), Taylor & Rowan–Robinson (1994) and Gramman (1993).

2.2.4 Recovering the $\delta(\mathbf{x})$ from the Observed $u(\mathbf{x})$

The true matter density field can be obtained directly from the observed radial peculiar velocity field assuming the GI picture. Bertshinger & Dekel (1989) noticed that if the gravitational instability holds then the peculiar velocity field is irrotational since initial vorticity decays in an expanding universe just as the initial peculiar velocities do. Furthermore the flow remains curl–free even in the quasi–linear regime as long as it is laminar. In this case the peculiar velocity field can be derived from a scalar potential Φ_V as $\mathbf{v}(\mathbf{x}) = -\nabla\Phi_V(\mathbf{x})$ and the radial velocity field $u(\mathbf{x})$ should contain enough information for reconstructing the whole peculiar velocity field.

The $POTENT$ procedure takes the discrete and noisy Mark II and, more recently, the Mark III radial velocity data u_i at $\mathbf{x}_i$ and first smooths them. Then, using the gravitational ansatz of potential flow, compute the scalar potential by integrating the smoothed radial velocity field $u(\mathbf{x})$ along radial trajectories:

$$\Phi_V(\mathbf{x}) = -\int_0^r u(\hat{r},\theta\phi)d\hat{r}. \qquad (2.15)$$

Once $\Phi_V(\mathbf{x})$ is known everywhere, tangential components of the peculiar velocity can be constructed by taking its gradient. Indeed, there is no need to choose radial paths of integration and the optimal ones, for recovering the potential, may depend on the field considered (Simmons et al. 1994). Finally, the $POTENT$ technique applies a quasi–linear approximation with an assumed value of Ω_o to reconstruct the true mass density field. The $POTENT$ as currently implemented uses a non–linear generalization of the linear approximation to GI [eq. (1.77)]

$$\delta_{POTENT}(\mathbf{x}) = \left\| I - (fH)^{-1}\frac{\partial\mathbf{v}}{\partial\mathbf{x}} \right\| - 1, \qquad (2.16)$$

that reduces to eq. (2.11) in the linear limits. I is the unit matrix and the bars denote the Jacobian determinant.

The nontrivial step in the $POTENT$ procedure is the smoothing of the discrete data into a continuous radial peculiar velocity field $u(\mathbf{x})$. The idea is that of reproducing the $u(\mathbf{x})$ that would have been obtained had the true $\mathbf{v}(\mathbf{x})$ been sampled densely and uniformly

and smoothed with a Gaussian window of radius R_{sm}. With the discrete data available, $u(\mathbf{x}_c)$ is taken to be the value at $\mathbf{x} = \mathbf{x}_c$ of an appropriate local parametric velocity model $\mathbf{v}(\alpha_k, \mathbf{x} - \mathbf{x}_c)$ obtained by minimizing

$$\sum_i W_i [u_i - \hat{\mathbf{x}}_i \cdot \mathbf{v}(\alpha_k, \mathbf{x}_i - \mathbf{x}_c)]^2, \qquad (2.17)$$

in terms of the parameters α_k, within an appropriate local window $W_i = W(\mathbf{x}_i, \mathbf{x}_c)$. The window function is chosen such that it reduces:

- The so called window bias (Dekel et al. 1994), coming from the fact that *POTENT* uses a tensor window smoothing coupled with a model for $\mathbf{v}(\alpha_k, \mathbf{x} - \mathbf{x}_c)$. The conical symmetry of the tensorial window may causes spurious flows if an improper velocity model is used.

- The statistical noise in the velocity field due to errors in the individual peculiar velocities.

- The sampling gradient bias which is due to the inhomogeneous sampling of the velocity field within the smoothing window.

POTENT is also subject to Malmquist bias, both homogeneous and inhomogeous (Strauss & Willick 1995, Dekel 1994), since it utilizes peculiar velocities obtained from 'forward' distance estimate. This problem can be solved using a Malmquist-free inverse–analysis in which one minimizes the analogous of eq. (2.17) both for the parametric velocity field model and for the parameters of the distance indicator relation.

Initial apparent inconsistencies between the mass density field obtained with the *POTENT* analysis (Dekel, Bertshinger & Faber 1990) and the IRAS galaxy density field have disappeared in a subsequent more careful analysis (Dekel et al. 1993). An even better similarity between the *POTENT* density field obtained from the Mark III catalogue and the optical galaxies density field, reconstructed using iterative techniques, has been recently obtained (Hudson et al. 1995). The similarity among the matter density field derived by *POTENT* and the density fields traced by optical and IRAS galaxies is the best evidence that the linear biasing prescription cannot be strongly violated on scales larger than $\sim 12\,h^{-1}\mathrm{Mpc}$ (i.e. the *POTENT* smoothing scale).

2.3 BACK IN TIME

The problem of reconstructing the density field back in time is strictly connected with that of removing non–linear effects that spoil the simple proportionality between the initial (e.g. at the recombination epoch) and the evolved density field. A large number methods for describing the non–linear gravitational clustering have been proposed in the recent past. Sahni & Coles (1995) have recently reviewed the state of the art of this subject.

Non–linear methods can be grouped in two general categories:

- Non–linear extensions of eq. (2.11) (Nusser et al. 1991, Bernardeau 1992, Gramman 1993, Giavalisco et al. 1993, Mancinelli et al. 1994)

- Non–linear schemes that allow to approximate the clustering in regions where the overdensity is of the order of unity (Peebles 1989, 1990, 1994, 1995, Weinberg 1991, Matarrese et al. 1992, Bagla & Padmanabhan 1994)

Tracing the evolution of the density field back in time in the GI framework is a mixed boundary value problem in which some conditions are specified at the present and some others at an earlier epoch. Reversing the evolution using an N–body simulation (i.e. using an initial value problem approach) has a negligible probability of recovering the quasi-homogeneous initial state characterized by very small peculiar velocities. The major problem is the presence of decaying modes that, having left no detectable trace at present. would amplify the noise in the backward integration.

One method of reconstructing the linear field, under the assumption that initial fluctuations were Gaussianly distributed, has been proposed by Weinberg (1989, 1991). This technique, called Gaussianization, assumes that both gravitational instability and biased galaxy formation preserve the rank order of density in cells. The idea is to reassign the density at different points under the constraint of preserving the rank density order to fit a Gaussian form. This procedure can be applied to z–survey data. One measures the $P(k)$ of the Gaussianized field then evolves this field using an N–body code and finally compute the final $P(k)$. The evolved and the measured $P(k)$ are then compared and the procedure is repeated until convergence. The method has been applied to the PP z–survey by the same author who found a $P(k)$ consistent with the standard CDM one. A bias factor $b = 2$ turned out to be necessary to reproduce the observed filamentary structure of the data.

An important reason for reconstructing the density field back in time is to check if the initial PDF was Gaussian, as predicted by common inflation. Non–linear evolution

causes the PDF to develop a positive skewness because peaks collapse to large densities while the density in voids cannot become negative; as a result the overall PDF shape becomes log-normal (Coles & Barrow 1987, Lucchin Matarrese & Vittorio 1988, Coles 1989, Coles & Jones 1991, Koffman et al. 1994). The observed PDF agrees with N-body evolution of an initial Gaussian field (Bouchet et al. 1993), but such a test has a limited discriminatory power since some class of non-Gaussian initial conditions can also develop a log-normal shape similar to the observed one (Messina et al. 1990, Messina et al. 1992, Moscardini et al. 1991, Matarrese et al. 1991, Weinberg & Cole 1992). It is therefore important to reconstruct the initial density field without assuming an initial Gaussian PDF, as the Gaussianization technique does. One possibility is the so called Zel'dovich time machine (Nusser & Dekel 1992), which eliminates the problem of the decaying modes. The authors express the Zel'dovich equation in Eulerian coordinates from which they obtain a first order equation for the velocity potential, ϕ_v, expressed in units of $a^2 \dot{D}$:

$$\dot{\phi}_v - \frac{\dot{D}}{2}(\nabla \phi_v)^2 = 0, \qquad (2.18)$$

which only allows for growing modes. Eq. (2.18) can be integrated backwards to obtain ϕ_v at early times. The initial density and velocity fields can be derived from ϕ_v assuming linear theory, while the boundary condition $\phi_v(t_o)$ can be extracted from observations of galaxy velocities and densities. Consideration of continuity in the context of the Zel'dovich equation has lead Gramman (1993) to insert a correction term, C_g in the right hand side of eq. (2.18):

$$\nabla^2 C_g = \sum_{i \neq j} \frac{\partial^2 \phi_g}{\partial x_i^2} \frac{\partial^2 \phi_g}{\partial x_j^2} - \left(\frac{\partial^2 \phi_g}{\partial x_i \partial x_j} \right)^2, \qquad (2.19)$$

where ϕ_g is the gravitational potential in the new units. N-body tests showed that solutions of eq. (2.19) matches the simulated data better than those of eq. (2.18) and that, in both cases, the solutions represent a considerable improvement over the simple linear approximation.

In another version of their time machine Nusser & Dekel (1993) use the full dynamical field. Assuming laminar flow they transform the tensor $\partial v_i / \partial x_j$ derived from $v(x)$ (which can be obtained from $POTENT$ reconstruction) in Lagrangian coordinates $q(x)$. Assuming linear theory they are able to relate the eignevalues of the transformation, $\partial v_i / \partial x_i$, to the initial density field:

$$\delta_{init.} = -D \sum_{i=1}^{3} \frac{\partial v_i / \partial x_i}{1 - (\partial v_i / \partial x_i)(H_o f(\Omega_o)}. \qquad (2.20)$$

The authors have applied this strategy to the $IRAS$ 1.936 Jy and recovered an initial density field fully consistent with Gaussian density fluctuations.

The natural way to deal with a mixed boundary value problem is given by the least action formalism. Peebles (1989) applied the least action principle to the gravitational growth of density fluctuation in an expanding universe. We will expand the subject in Chapter 4, here we just recall the general idea. Assuming that all the mass is associated to the visible galaxies and that they maintain their individuality at early times then it is possible to apply the principle of least action to reconstruct the orbits of the galaxies back in time provided that we can fulfill the boundary conditions. One bound is respected by specifying the position of the galaxies at the present–epoch the other is given by the GI which predicts negligible galaxy velocities at early times. Having satisfied the mixed boundary conditions we can reconstruct the galaxy orbits by minimizing the action of the system. In practice this step is done by parametrizing the galaxy orbits using arbitrary trial functions, specified by unknown coefficients. Minimizing the action allows us to determine the coefficients and thus the orbits. The form of the trial functions is quite arbitrary and a judicious choice should account for the problem studied. As pointed out by Giavilisco et al. (1993) a natural choice for the trial functions exists through which the numerical action method generalizes the Zel'dovich approximation.

The Least Action method has been mainly applied to study the local group's dynamics (Peebles 1989, 1990, 1994, 1995, Dunn & Laflamme 1993) and only recently it has been modified to be applied to a redshift sample of galaxies within $30\,h^{-1}\mathrm{Mpc}$ (Shaya, Peebles & Tully 1994, 1995). In this last implementation the least action method is used to recover the present density field $\delta(\mathbf{x})$ from the z–space galaxy positions and thus it represents a natural generalization of the iterative reconstruction method to the nonlinear case.

Chapter 3

RECONSTRUCTING POSITIONS AND PECULIAR VELOCITIES OF GALAXY CLUSTERS

In this Chapter we apply the linear iterative reconstruction method described in Chapter 2 to reconstruct the density and velocity fields traced by galaxy clusters within 20000 km/sec. This method relies on the GI pictures, on the linear biasing hypothesis and, in the present implementation, assumes also linear theory. As we have seen, to reconstruct the 3D objects' distribution we need to smooth the force field on scales large enough for linear theory to be valid. The natural smoothing length is the average separation of the objects, which for luminous galaxies is close to the typical scales where non–linear effects become important. Therefore, adopting linear theory to reconstruct the density field may lead to non negligible errors when high density regions are considered. One possible solution is to oversmooth the discrete galaxy distribution at the price of loosing a large amount of information. A better alternative is to improve the algorithm by using non–linear approximations or some *ad hoc* treatments of the high density regions. A further possibility is to consider objects characterized by large relative separations. Because of their low number density, clusters of galaxies are ideal candidates for applying the linear iterative reconstruction method (*[LIRM]* hereafter). Of course this advantage is associated to its complementary problem: clusters of galaxies sparsely sample the underlying density and velocity fields. In other words the price to pay for exploring the large scale density and velocity fields is a loss of resolution on small scales and an increase of the shot–noise error amplitude.

In this Chapter we show that volume limited subsamples of the Abell/ACO cluster

catalogue contain enough information to reconstruct the cosmic density and velocity fields on large scales, allowing not only to explore the large scale cosmography but also to perform quantitative studies of the large scale structure and dynamics. In fact, what we obtain at the end of the reconstruction procedure is an ideal all–sky catalogue of galaxy clusters endowed with redshifts, peculiar velocities and relative errors, complete up to a limiting depth of 20000 *km/sec* with which we can investigate:

- *The Dipole:* whether the large convergence depth of the cluster dipole found in Plionis & Valdarnini 1991 (PV91) and Scaramella et al. 1991 (SVZ91), its asymptotic amplitude and its alignment with the CMB dipole, are artifacts of redshift–space distortions.

- *The Peculiar Velocities:* those predicted from the clusters' distribution by using linear GI theory and their comparison with observations and cosmological models.

3.0.1 Dipole

If linear gravity is responsible for the observed peculiar velocities then according to the linear GI theory (cf. Peebles 1980) the peculiar gravitational acceleration should be aligned and proportional to the peculiar velocity; the constant of proportionality being a measure of the present–time growth rate of mass fluctuations and therefore a measure of the cosmological density parameter, Ω_o. The gravitational acceleration of any galaxy (or other extragalactic object) can be estimated by calculating the dipole moment of the distribution of mass surrounding it. Since, however, the latter is unknown one has to resort in estimating the dipole moment of the distribution of luminous extragalactic objects using some simplifying assumption about the relation between fluctuations in the matter and light distributions; which is non other than the *linear-biasing* assumption in which, as we have seen, galaxy fluctuations δ_g are related to those of the matter distribution δ by a constant factor $\delta_g = b\delta$.

Further difficulties arise from the fact that one can observe galaxies or other extragalactic objects limited in magnitude or flux, which then implies that distant contributions to the dipole could be missed if the characteristic depth of the galaxy catalogue is less than the convergence depth of the dipole. Moreover, most catalogues of extragalactic objects have also limited sky coverage which is usually due to light absorption near the Galactic plane.

Up to now the dipole of various populations of extragalactic objects has been determined: optical galaxies (Lahav 1987; Plionis 1988 1989; Lahav, Rowan-Robinson & Lynden-Bell 1988; Lynden-Bell, Lahav & Burstein 1989; Hudson 1993b), IRAS galaxies (Meiksin &

Davis 1986; Yahil, Walker & Rowan-Robinson 1986; Villumsen & Strauss 1987; Strauss & Davis 1988; Strauss et al. 1992; [hereafter SYDHF92] Rowan-Robinson et al. 1990; Plionis, Coles & Catelan 1993), X-ray active galactic nuclei (Miyaji & Boldt 1990); X-ray clusters (Lahav et al. 1989) and Abell clusters (Scaramella, Vettolani & Zamorani 1991; Plionis & Valdarnini 1991 and Scaramella, Vettolani & Zamorani 1994 [hereafter SVZ94]). In all cases the dipole moment was found to be quite well aligned with the CMB dipole suggesting that gravity is indeed responsible for the Local Group motion and that light traces mass.

An interesting historical fact, originating from these studies, is that the estimated dipole convergence depth has been a function of cosmic volume sampled; *the deeper the catalogue the larger the dipole convergence depth*: Lynden–bell et al. (1989) analysis, based on the shallow MarkII catalogue claimed that the mass fluctuations responsible for the local group (LG hereafter) motion are contained within $\sim 40\,h^{-1}$Mpc, i.e. the distance to the Great Attractor region. Subsequent analyses, based on the deeper $IRAS$ galaxy. sample, indicate that the dipole converges within $\sim 80 - 100\,h^{-1}$Mpc (Rowan–Robinson et al. 1990 and SYDHF92). Analyses based on the cluster distribution revealed that a significant contribution to the LG velocity comes from scales larger than 100 h^{-1}Mpc (PV91, SVZ91 and SVZ94); this requirement comes also from the smaller scale analysis of Shaya & Tully (1992) and Hudson 1994. According to SVZ91, SVZ94 and PV91 mass fluctuations beyond 100 h^{-1}Mpc contribute to ~ 20 % of the total LG velocity, and the final convergence depth for the cluster dipole, $R_{conv} \approx 17000\ km/sec$. This implies that the apparent dipole convergence of the shallower galaxy catalogues (being optical or IRAS) is probably artificial, determined by their limiting depth. In fact a careful investigation of the QDOT-$IRAS$ sample showed some evidence for a contribution to the dipole from scales comparable to the cluster R_{conv} (Plionis, Coles & Catelan 1993).

A further interesting outcome of the Abell/ACO cluster dipole analysis is the fact that there seems to be a *coherent* dipole anisotropy out to $\sim 17000\ km/sec$; i.e., the differential gravitational acceleration induced on the LG by the distribution of clusters in large equal-volume shells is roughly aligned with the CMB dipole in each shell (PV91).

The probability that these alignments may occur by chance is, in fact, very low: the random joint probability of having the cluster dipole, the optical and $IRAS$ galaxy dipoles aligned with the CMB dipole within a few degrees ($\sim 10°$, $\sim 10°$ and $\sim 25°$ respectively), assuming that they are independent, is $\leq 3 \times 10^{-6}$. Furthermore, as we discussed previously, PV91 found evidence for a coherent dipole anisotropy, in which the differential cluster dipole in each equal-volume shell roughly points towards the CMB dipole. In fact, the dipole in the

first shell ($R \lesssim 100\ h^{-1}$ Mpc) has $\delta\theta \lesssim 20°$ while in the most distant shell ($140 \lesssim R \lesssim 160\ h^{-1}$ Mpc), for which the dipole is aligned with the CMB, it has $\delta\theta \lesssim 10°$ and the distance between the centers of the two shells is $\sim 90\ h^{-1}$ Mpc, a distance at which $\xi_{cc}(r) \ll 1$, where ξ_{cc} is the spatial cluster–cluster correlation function (note that even the edges of the two shells are $\sim 43\ h^{-1}$ Mpc away). Therefore, these two volumes could be considered independent which would then decrease even further the probability of random alignment with the CMB dipole to $\lesssim 8 \times 10^{-8}$!

3.0.2 Peculiar Velocities

The study of the large scale cosmic flows is of great interest in Cosmology since it could provide clues about the origin and the evolution of the LSS of the universe and constrain the Ω_o value. We are now in the position to achieve this goal since technical advances in spectrographs and detectors in both visible and radio wavebands allowed in the last decade the large scale dynamics to become a mature scientific field in which observation and theory can be confronted in a quantitative way. An increasing number of reviews and books of this field is available, the most updated being those by Dekel (1994) and Strauss & Willick (1995); here we will just briefly recall the status of the art.

Two major developments seeded the study of the large scale dynamics. The first was the confirmation of the CMB dipole (Smoot et al. 1977), commonly regarded as a Doppler effect originated by a motion of $\sim 600\ km/sec$ of the LG with respect to the CMB frame. The second was the measurement of the radial peculiar velocities of galaxies using z–independent distant estimators like the Tully–Fisher (Tully & Fisher 1977) and the Faber–Jackson (Faber & Jackson 1976) relationships. Significant advances in observational techniques together with the introduction of improved versions of distance indicators allowed to compile catalogues containing several hundred objects endowed with peculiar velocities, in which distance errors are reduced to a level of 15–20 %. In the same period all–sky magnitude–limited redshift surveys containing several thousand of galaxies, like the CfA$_{14.5}$ (Huchra et al. 1983), CfA$_{15.5}$ (de Lapparent et al. 1986), PP (Giovanelli & Haynes 1991) SSRS (da Costa et al. 1991) and IRAS (Soifer et al. 1987, Strauss et al. 1990, Rowan–Robinson et al. 1990) ones, became available. As we have seen, redshift surveys can be use to infer the peculiar velocity field under the GI and linear biasing assumptions. The comparison between the observed and predicted velocity fields constitutes the heart of the large scale dynamics study. Amongst the many and sometimes contradictory results in this field, one of

the most generally accepted and particularly important for this thesis is the strong evidence for the existence of coherent large-scale galaxy flows in the local universe, extending from the Perseus-Pisces region on the one side to the Hydra-Centaurus/Great Attractor region on the other. These flows are well established both for elliptical (cf. Lynden-Bell et al. 1988) and spiral galaxies (cf. Rubin et al. 1976; Dressler & Faber 1990; Mould et al. 1991; Willick 1990; Han & Mould 1990; Courteau et al. 1993; Hudson 1994; Mathewson & Ford 1994) and point in the general direction of the CMB dipole. Although the extent of this volume may still be under debate the existence of the bulk flow seems to be certain. These results, together with the large-scale coherence of the cluster dipole, present a consistent picture in which the LG participates in a large-scale bulk motion induced by gravity, encompassing a large volume of radius $\sim 6000 - 15000 \ km/sec$.

As outlined by Babul et al. (1994) it is not possible to test the validity of the GI plus linear biasing picture by exploring the correlation between the the density field, traced by luminous objects and the velocity field. This limitation derives from the fact that the spatial properties of the GI equations are identical to a system of equations in which irrotationality and continuity are assumed. The only possibility to distinguish between a GI and a non-GI scenario is to look at the temporal behaviour of the equations, which in practice means that one should explore the correlation between CMB relic fluctuations and the present-time velocity field.

Although the velocity-density correlations do not constitute a GI test, it has to be stressed that such correlations are *consistent* with the GI + linear biasing scenario. This is the reason why the recent Lauer & Postman (1994) [LP] result represents a serious challenge to the standard picture. LP have extended the cosmic flow studies to very large scales, those traced by galaxy clusters, by using as a distance indicator the relationship between metric luminosities of the brightest cluster galaxies and the slope of their brightness profiles (Hoessel 1980). They find that the LG motion with respect to the frame defined by Abell/ACO clusters, within 15000 km/sec moves in a direction $\sim 80°$ away from that of the CMB dipole which then implies that, if the CMB dipole is a Doppler effect, the whole cluster frame is moving with respect to the CMB rest-frame with $\sim 700 \ km/sec$. Such a large velocity on such large scales is in contradiction with bulk flow velocities on smaller scales and it is difficult to reconcile with current models of structure formation (cf. Strauss et al. 1994; Feldman & Watkins 1994; but see Jaffe & Kaiser 1994).

If the alternative interpretation were true, i.e. if the CMB dipole were not Doppler in its origin, then it should be extremely difficult to understand why the LG peculiar accel-

eration should be aligned with the mass dipole (PV91; SVZ91; Branchini & Plionis 1995) as it is expected in the linear GI theory, while the Lauer & Postman LG peculiar velocity, with respect to the same sample of clusters, points $\sim 80°$ away. Understanding this apparent contradiction within the GI framework is an open challenge. Under the linear GI hypothesis our reconstruction procedure, which assumes that Abell/ACO clusters trace the mass, allows us to explore the dynamics on scales much larger than those probed by luminous galaxies. In other words we are in the position of estimating how likely the LP result is within the GI + linear biasing framework.

The relatively large smoothing we had to apply to the cluster distribution to reconstruct the underlying density field does not allow us to characterize the velocity field with a resolution comparable to that obtained from galaxy samples, but we are able to visualize the qualitative aspects and large scale features of the linear velocity field since the typical errors of the 1-D cluster peculiar velocities are ≤ 150 km/sec, within the sampled volume.

This Chapter is divided in three sections.

- In the first part we describe in detail the iterative reconstruction method and the tests we performed to asses its intrinsic reliability. Then we describe the Abell–ACO cluster subsample used, and the procedure we have adopted to obtain a statistically homogeneous all–sky cluster catalogue from it. Finally, we discuss from a cosmographic point of view the main features of the reconstructed density field and we compute the two–point spatial correlation function of the reconstructed cluster distribution.

- In the second part we concentrate on the cluster dipole. After discussing how the z–space distortions may affect the dipole amplitude, we discuss the techniques for measuring the dipole and the possible errors that affect its estimate. The dipole of the reconstructed Abell–ACO cluster distribution is then computed both in the z– and the 3D–space which allow us to estimate the Ω_o value. Finally, constraints on the various cosmological models are derived from the shape of the cumulative dipole.

- In the last section we analyse the Abell/ACO cluster velocity field and we compare it with the cluster velocity produced by numerical simulations. The simulated datasets are from Borgani et al. 1995 (B95, hereafter) and refers to several different cosmological models. We discuss the errors that affect both the reconstructed and the simulated velocity field. The analysis of these fields is then performed both from a qualitative and a quantitative point of view using low order statistics such as the bulk flow velocity,

the two–point velocity correlation function and the velocity probability distribution. Finally, we compare the reconstructed cluster velocities with the observed ones with the aim of constraining the value of the cosmological density parameter Ω_o.

3.1 THE ITERATIVE PROCEDURE & THE CLUSTER DENSITY FIELD

In this section we describe in detail the iterative algorithm, its reliability and the Abell/ACO cluster subsample to which the reconstruction procedure is applied. A cosmographic description of the cluster density field is given as well. The plan of this section is as follows: in section (3.1.1) we present an extended discussion of the two (Abell and ACO) cluster subsamples used, selection effects and homogenization procedures. In section (3.1.2) we present the reconstruction method and its reliability tests. In section (3.1.3) we present a qualitative analysis of the reconstructed cluster density field and in section (3.1.4) the spatial cluster–cluster correlation function is computed both in the redshift and 3D space.

3.1.1 The Cluster Sample

Our present analysis is based on a cluster sample extracted from the original Abell sample (Abell 1958) and from its southern extension, the ACO cluster catalogue (Abell, Corwin & Olowin 1989). The north declination limit of the ACO sample is $\delta = -17$, so that the two catalogues overlap in the strip $-27 \leq \delta \leq -17$. The overlapping region has been used by Abell, Corwin & Olowin (1989) to calibrate the J magnitudes of the ACO to the Abell magnitude system. However, systematic differences in the two calibrated catalogues have been noticed by ACO (1989), Batusky et al. (1989), Scaramella et al. (1990) and PV91 which cannot be ascribed to the suspected incompleteness of the richness class $R = 0$ clusters since the differences are evident, although less pronounced, even in the $R \geq 1$ samples (see PV91).

The problem of obtaining a composite and statistically homogeneous catalogue from the Abell and ACO samples, is particularly important in dipole studies since artificial systematic differences (density gradients or global density variations) can enhance or even produce a dipole signal. Although this issue has been addressed by a number of authors (cf. Scaramella et al. 1990 and PV91) we will also discuss it, following the PV91 line of reasoning.

Cluster distances, r, are estimated from redshifts using the standard relation:

$$r = \frac{c}{H_o q_o^2 (1+z)} \left[q_o z + (1-q_o)\left(1 - \sqrt{2 q_o z + 1} \right) \right], \qquad (3.1)$$

where c is the speed of the light and q_o the deceleration parameter at the present–epoch: $q_o = \ddot{a}(t_o) a_o / \dot{a}(t_o)$. The number of clusters within our subsample is not fixed since the distances slightly depend on q_o which we do not fix *a priori*. We also merge cluster pairs with relative distance $\leq 3\ h^{-1}$ Mpc into unique 'clusters' having as position their center of mass and as mass their combined total mass. We made this approximation to avoid non–linear effects on small scales for which our reconstruction method fails to account for. The combined subsample we consider is composed by:

1. Abell clusters of richness class $R \geq 0$ in the roughly volume–limited region $r \leq 250\ h^{-1}$ Mpc, $|b| \geq 13°$ and with $m_{10} < 17$. m_{10} is the magnitude of the tenth brightest galaxy in the cluster in the magnitude system corrected according to PV91. This sample is 100 % redshift complete. Note that the number of objects in this subsample varies between 269 and 276 for $q_o = 0.2$ and 0.5, respectively. Out of these we have merged 5 cluster pairs.

2. ACO clusters of richness class $R \geq 0$ with $r \leq 250\ h^{-1}$ Mpc, $|b| \geq 13°$ and $m_{10} < 17$. Among the 217 objects within the sample $\sim 77\%$ have measured redshift. For the remaining objects the redshift is determined using the $m_{10} - z$ relation used by PV91. Note that we have merged 7 cluster pairs.

Note that although Abell cautioned that the $R = 0$ cluster sample is not complete and therefore probably not suitable for statistical studies, many recent studies have been interestingly utilizing them (c.f. Tully 1987; Postman et al 1989; Huchra et al. 1990; Tully et al. 1992; Scaramella et al 1994). Furthermore, the density distributions and clustering properties of both the $R = 0$ and $R \geq 1$ Abell samples have been found to be similar out to $z \approx 0.2$ possibly indicating the weakness of such effects (Postman et al. 1992; but see Peacock & West 1992). In any case the stability of our main results as a function of cluster richness will be discussed in the relevant section.

The Selection Biases:

In order to obtain a statistically homogeneous all–sky sample of clusters we quantify separately the observational biases of the Abell and ACO subsamples and then we calibrate these subsamples by applying a homogenization procedure.

At low galactic latitudes, absorption of optical photons makes it unlikely to observe luminous objects. In the galactic strip $|b| \leq 20°$, to which we refer as the ZoA, there are only 20 clusters in our subsample. The galactic absorption outside the ZoA has been always found to be consistent with a cosecant law:

$$\log P(b) = \alpha(1 - \text{cosec}|b|), \tag{3.2}$$

where $P(b)$ gives the probability that a cluster in the range b to $b + \Delta b$ would have been included in the catalogue. There is no general agreement on the precise value of α. Bahcall & Soneira (1983) and Postman et al. (1989) found 0.3 for Abell clusters, Batuski et al. (1989) found $\alpha \sim 0.2$ for ACO clusters while LP94 found an even lower value ($\alpha \sim 0.15$) for both ACO and Abell clusters contained in a volume–limited 15000 km/sec sphere. To allow for this experimental uncertainty we will consider, in what follows, two different sets of values: $(\alpha, \alpha) = (0.3, 0.2)$, that better matches the behaviour of the number density of our cluster as a function of the galactic latitude and (0.2,0.2). The first value in each set refers to the Abell sample while the second to the ACO one.

The finite depth of the cluster sample was modeled with the redshift selection function that was estimated as in Postman et al. (1989). We modeled the probability that a cluster in the range z to $z + \Delta z$ would have been included in the cluster catalogue as:

$$P(z) = \begin{cases} 1 & \text{if } z \leq z_c \\ A \exp(-z/z_o) & \text{if } z > z_c \end{cases} \tag{3.3}$$

where z_c is the redshift up to which the space density of clusters remains constant (volume-limited regime). We obtain $z_c \sim 0.0787$ and 0.0664 for the Abell and ACO subsamples respectively. No appreciable declination dependence has been detected in the Abell/ACO subsample (but see Scaramella et al. 1990 for a possible zenithal dependence).

Homogenization of the Abell/ACO sample:

In this work we will follow the PV91 homogenization scheme, used to minimize the density variations of the Abell and ACO subsamples. The estimated observational biases allow us to assign the following weight to clusters:

$$w_i(z, b) = \frac{1}{P(z_i)P(b_i)}. \tag{3.4}$$

The individual number density of clusters of the two subsamples is therefore $n = V^{-1} \sum_i w_i(z, b)$, where the sum extends over all clusters within the sampled volume V. Since at low galactic

latitudes the patchy galactic absorption is not well described by eq. (3.2) we compute n above $|b| = 30°$. We divided V into equal volume shells with $\delta V \sim 2.6 \times 10^6 \ h^{-3} \ \mathrm{Mpc}^3$ in which we estimated the Abell and ACO cluster number densities separately. Due to the complex geometric boundaries, the volumes were computed by Montecarlo calculations.

Within $\sim 200 \ h^{-1}$ Mpc the space densities of the $R \geq 0$ Abell and ACO samples are constant $(P(z) = 1)$ with $n \sim 1.6 \pm 0.3 \times 10^{-5}$ and $\sim 2.7 \pm 0.3 \times 10^{-5} \ h^3 \ \mathrm{Mpc}^{-3}$, respectively, while the corresponding values for the $R \geq 1$ samples are $n \sim 8.2 \pm 1.3 \times 10^{-6}$ and $\sim 11 \pm 1.2 \times 10^{-6} \ h^3 \ \mathrm{Mpc}^{-3}$. The scatter was computed from the density fluctuations in the different bins. These values would be reduced by $\sim 18\%$ if no obscuration correction is applied (i.e., assuming $P(b) = 1$). Note that although the Abell-ACO density differences are reduced in the $R \geq 1$ sample they are still present, indicating that these density differences are not due to the possible incompleteness of the $R = 0$ clusters (see also Postman et al. 1990; PV91). This is also supported by the fact that the Abell-ACO density differences in the richest subsample $(R \geq 2)$ are a factor ~ 3 larger even than those of the $R \geq 0$ one.

An approximate homogenization of the two samples was then applied by equating the number density of the two catalogues in each equal volume shell. Assuming that the two catalogues are simply radially inhomogeneous, we computed the following weighting function:

$$\mathcal{W}_{rel}(r) = \begin{cases} 1 & \text{if } \delta \geq -17 \\ \frac{n(r_i, Abell)}{n(r_i, ACO)} & \text{if } \delta < -17 \end{cases} \qquad (3.5)$$

where r_i is the distance of the ith bin. No significant difference was found when using the two different sets of absorption coefficients. Note, however, that this is not the only possible homogenization scheme since we do not know *a priori* which is the true value of the cluster density. We could, therefore, homogenize the two samples by using the inverse of eq. (3.5), $\mathcal{W}_{rel}(r)^{-1}$. As we will show in what follows our main results remain stable on the choice of the homogenization scheme.

3.1.2 The Reconstruction Method

The whole reconstruction procedure can be schematically represented by the following diagram:

$$z_{obs} \quad \longrightarrow \quad z_{id} \quad \longrightarrow \quad 3\mathrm{D}_{obs}$$

Starting from the observed sky z–space distribution of galaxy cluster, z_{obs}, we generate a synthetic cluster distribution to account for unobserved clusters. This procedure allows us to

reconstruct the whole-sky cluster distribution in the z–space, z_{id}. An iterative reconstruction algorithm, similar to that proposed by Strauss & Davis (1988), is then applied to minimize the z–space distortion, allowing us to recover the real–space distribution of the observed clusters $3D_{obs}$ and therefore also their peculiar velocities. The *intrinsic* reliability of the entire procedure has been tested using a simulated catalogue of clusters kindly provided to us by S.Borgani.

z-Space reconstruction scheme:

To reconstruct the whole-sky z–space cluster distribution, z_{id}, we adopted a phenomenological approach. The basic idea is to fill the artificially (due to galactic absorption) low density regions of the surveyed volume with a synthetic cluster population having the same clustering properties as the distribution of the real clusters and then generate many Monte-Carlo realizations of this population. To this end we divide our procedure into two steps; one to reconstruct the cluster density field above $|b| = 20°$ and one to *fill* the ZoA.

$$|b| > 20°$$

The first step is to recover the cluster distribution for $|b| > 20°$. We divided our volume in two regions: an inner sphere with a radius of R_{in}=200 h^{-1} Mpc, which we consider as the region of reliable determination of the cluster density field, and an external region R_{in} $< r < 250$ h^{-1} Mpc.

In the inner part, in which $P(z) \simeq 1$, we used a Montecarlo rejection method to generate a population of synthetic clusters distributed according to the adopted $P(b)$ probability function and weighted them by $1/P(z)$ with the further constraint of being spatially clustered around the real clusters according to the observed spatial cluster–cluster correlation function (cf. Bahcall & Soneira 1983; Postman et al. 1992; Plionis, Valdarnini & Jing 1992). The following weights are then assigned both to real and mock clusters:

$$\tilde{w}_i(r) = \frac{\mathcal{W}_{rel}(r_i)}{P(z_i)}, \tag{3.6}$$

Finally, the total number of synthetic clusters outside the ZoA is determined by requiring the overall number density of clusters to be:

$$\tilde{n} = \frac{1}{V} \sum_i \tilde{w}_i(z, b), \tag{3.7}$$

where $\tilde{w}_i(z, b) = \mathcal{W}_{rel}(r_i) w_i(z, b)$. This requirement is fulfilled by imposing:

$$\sum_{real} \tilde{w}(z, b) = \sum_{real} \tilde{w}(r) + \sum_{synth} \tilde{w}(r), \tag{3.8}$$

where the first two sums extend over real clusters and the last one over synthetic objects. Beyond 200 h^{-1} Mpc the radial selection function, mainly for the ACO sample, falls below one roughly exponentially. Therefore weighting clusters that sparsely trace the density field with $1/P(z)$ can introduce non negligible shot–noise errors. To avoid this problem and keeping in mind that we will limit our analysis within R_{in} we reconstructed the cluster distribution in the external regions as following: the mock cluster distribution was Montecarlo generated to account for the $P(b)$ selection with no spatial correlation with real clusters; then the cluster redshift was determined according to $P(z)$ but, instead of weighting them by $1/P(z)$, we generated $1/P(z)$ synthetic clusters at the same b and z but with a randomly chosen l. Both real and synthetic clusters in this external region were simply weighted by $\mathcal{W}_{rel}(r)$ and their total number was determined by equating the local density with that of the central region.

Filling the ZoA

The second step is to fill the ZoA. Several different methods have been proposed and discussed in literature. As we have anticipated in section (2.2.1) and we have verified with Montecarlo simulations, the simple 'average mask' solution, i.e. filling the ZoA with a population of objects randomly distributed with the same number density as the real ones, is not satisfactory since it lowers the cluster dipole amplitude by $\sim 25\%$. We decided therefore to use a different method close to that proposed by S. Faber and used by Yahil et al. (1991). We divided the equatorial strip $-20° < b < +20°$ into 18 bins of 20° in longitude. In each bin we divided the distance range into bins of 2000 km/sec. The clusters were then sampled in the two northern and southern adjacent strips, defined so that their *joint* solid angle is equal to that of the ZoA. This requirement leads to the following limiting latitude for the strips:

$$|b_{lim}| = 90° - \cos^{-1}\left[2 \times \cos 70°\right] = 43.16° .$$

The number of synthetic clusters in each ZoA bin was then set equal to the sum of the clusters (real and synthetic) found in the two bins of the northern and southern, adjacent to the ZoA, strips; while their position, inside the ZoA bin, was randomly assigned. Finally, the real clusters in the range $13° < |b| < 20°$ are inserted and the total number of synthetic ZoA clusters is adjusted by subtracting a few at random until the average number density of real clusters is reached.

In what follows we will refer to the above 2-step z-reconstruction scheme as the *Randomized Standard Cloned Mask; [RSCM]*. At the end of the whole procedure nearly 50 % of the cluster population is composed by synthetic objects.

Variants of the RSCM

Other variants of the previously described method can be implemented as well. In the first one, which we call *Randomized Heavy Cloned Mask [RHCM]*, we fill independently the northern and southern parts of the ZoA by applying the *[RSCM]* to the northern and southern adjacent galactic strips ($20° \leq |b| \leq 43.16°$) separately. With this mask the randomization applies to smaller bins and the cloning effect is expected to be enhanced.

In the second variant, which we call (*Randomized Thin Cloned Mask [RTCM]*), we identify the ZoA with the equatorial strip $|b| < 13°$. Then we consider the two adjacent strips defined so that their *individual* solid angles are equal to that of the ZoA. The *[RSCM]* is then applied by half counting the number of clusters in the adjacent bins. The purpose of this scheme is to account for the spatial clustering on larger volumes.

Finally, we also use an alternative scheme to reconstruct the $r > 200 \ h^{-1}$ Mpc region which is based in extending the reconstruction technique used for the $r < 200 \ h^{-1}$ volume to the external region. The ZoA filling method used is the standard one, described in the previous subsection. We call this scheme *Modified Standard Scheme [MSS]*.

The z_{id} Cluster Distribution:

A typical z_{id} *RSCM* reconstruction is shown in panels (*a*) and (*c*) of Fig. (3.1). Black dots represent real clusters while open dots are synthetic objects. The figure displays the projection of the reconstructed cluster distributions onto the supergalactic plane (X_{sup}-Y_{sup} projection; panel *a*) and orthogonal to it (X_{sup}-Z_{sup} projection; panel *c*). A simple visual inspection reveals that the synthetic clusters fill the ZoA and smoothly reproduce the clustering observed in the two nearby galactic-latitude strips. Outside the ZoA, as expected, synthetic objects are clustered with the true ones and their density decreases towards the galactic poles.

However, since each cluster has a different weight a more relevant visualization of the z-space cluster distribution is presented as smoothed density maps in panels (*b*) and (*d*) where we have overlayed a 20×20 grid (each cell being 2000 *km/sec* wide) on the cluster distribution of panels (*a*) and (*c*) and smoothed the projected distribution using a 2D–Gaussian kernel with $R_{sm} = 1$ cell, while weighting each cluster by $\tilde{w}_i$. What, in fact, we present in these figures is the 'mean' smoothed density field; an average over 10 random realizations of the z-space reconstruction procedure. Note that in panels (*b*) and (*d*) the cell units used have 0 and 20 corresponding to the Cartesian supergalactic coordinate -20000 and 20000 (in units of *km/sec*) respectively. It is interesting to note in panel (*d*) [X_{sup}-Z_{sup} projection], the existence of a 'cross'-like structure with low-density cylindrical regions,
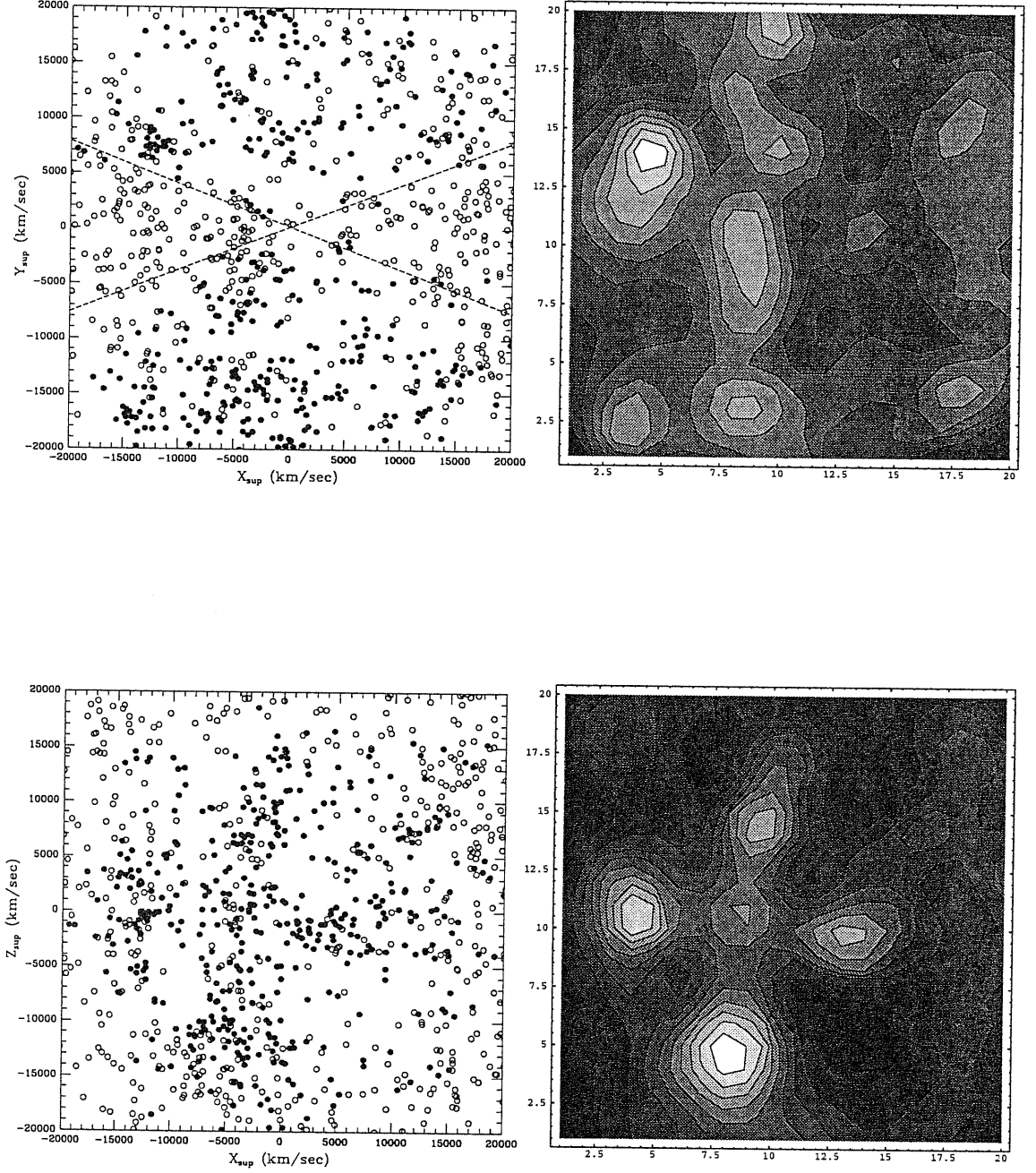
Figure 3.1: (a) and (c): The projected whole-sky z-space cluster distribution in Cartesian supergalactic coordinates. Filled symbols represent real Abell/ACO clusters while open symbols the synthetic objects. Short dashed lines delineate the $|b| \leq 20°$ region. (a) X_{sup}-Y_{sup} projection and (c) X_{sup}-Z_{sup} projection. (b) and (d): The projected smoothed whole-sky z-space cluster density field (of panels (a) and (c)). A 2–D Gaussian kernel was used with smoothing length $R_{sm} = 2000\ km/sec$. (b) X_{sup}-Y_{sup} projection and (d) X_{sup}-Z_{sup} projection. Note that cell units are used (see text for definitions).

passing through the cluster distribution and having a length of ~ 20000 km/sec. A more detailed discussion of the apparent structures will be presented in section (3.1.3).

3D–Space Reconstruction Scheme:

Our 3D reconstruction scheme is based on the assumption that the peculiar velocities of clusters are caused by gravitational instability and that linear perturbation theory applies on the scales relevant to the cluster distribution. The distribution of clusters in redshift–space differs from the true three–dimensional one by a non–linear term in the redshift–distance relationship:

$$cz_i = H_o r_i + \hat{\mathbf{x}}_i \cdot [\mathbf{v}(\mathbf{x}_i) - \mathbf{v}(0)], \qquad (3.9)$$

where $\mathbf{x}_i$ is the position of the ith cluster, $\mathbf{v}(\mathbf{x}_i)$ its peculiar velocity, $\mathbf{v}(0)$ the peculiar velocity of the observer placed at the centre of the coordinate system and H_o is the Hubble parameter.

Linear Theory

As we have seen in linear theory the peculiar velocities at the present epoch are proportional to the peculiar acceleration according to eq. (1.73)

$$\mathbf{v}(\mathbf{x}) = \frac{H_o f}{4\pi} \int \delta(\hat{\mathbf{x}}) \frac{\hat{\mathbf{x}} - \mathbf{x}}{|\hat{\mathbf{x}} - \mathbf{x}|^3} d^3 \hat{r} \ , \qquad (3.10)$$

where $\delta(\mathbf{x}) = [\rho(\mathbf{x}) - \rho_b]/\rho_b$ is the mass density fluctuation about the mean ρ_b and $a(t_o) = 1$. We assume that cluster density fluctuations are related to the mass fluctuations by a constant linear biasing factor:

$$\delta_c(\mathbf{x}) = b_c \delta(\mathbf{x}), \qquad (3.11)$$

where b_c is the bias parameter of clusters with respect to the mass. We can therefore replace $\delta(\mathbf{x})$ with $\delta_c(\mathbf{x})$ in eq.(3.10) provided that we substitute $f(\Omega_o)$ with $\Omega_o^{0.6}/b_c$ ($\equiv \beta_c$)

In order to apply linear theory we need to smooth the discrete cluster density field on an appropriate scale, where non-linear effects could be important. Since we are using galaxy clusters to probe the density and the peculiar velocity fields, a natural smoothing scale, large enough for linear theory to be valid, would be the cluster correlation length (i.e. the distance r_o at which the spatial cluster–cluster correlation function is unity). Recently Croft & Efstathiou (1994), analysing large N–body simulations, found that the velocity fields traced by galaxy clusters are non-linear below ~ 10 h^{-1} Mpc. Therefore we allow the smoothing radius to vary in the range $[10, 30]$ h^{-1} Mpc. Although, as we will see, the peculiar velocity field does depend on the choice of the smoothing length, the dipole parameters depend only weakly on its choice.

The discrete cluster distribution was smoothed with a top hat window function on a scale R_{sm} which is equivalent to smooth the peculiar acceleration with:

$$W(|\dot{\mathbf{x}} - \mathbf{x}|) = \begin{cases} \frac{|\dot{\mathbf{x}}-\mathbf{x}|}{R_{sm}^3} & \text{if } |\dot{\mathbf{x}} - \mathbf{x}| < R_{sm} \\ 1 & \text{if } |\dot{\mathbf{x}} - \mathbf{x}| \geq R_{sm} \end{cases} \tag{3.12}$$

where R_{sm} is the smoothing length. Since z_{id} is reconstructed up to $R_{max} = 250 h^{-1}$ Mpc, the integral in eq.(3.10) is converted into a sum over all the observed and synthetic clusters within R_{max}:

$$\mathbf{v}(\mathbf{x}) = \frac{\beta_c}{4\pi n_c} \sum_i \left(\frac{M_i}{M_C}\right) W(|\dot{\mathbf{x}} - \mathbf{x}|)\tilde{w}(\dot{\mathbf{x}}_i)\frac{\dot{\mathbf{x}}_i - \mathbf{x}}{|\dot{\mathbf{x}}_i - \mathbf{x}|^3} + \beta_c \frac{\mathbf{x}}{3} , \tag{3.13}$$

where distances $\mathbf{x}$ are measured in km/sec, i.e. we set that $h = 1$: an assumption that allows us to avoid problems related to the definition of distance and to the uncertainties on the Hubble constant and that will be valid throughout the rest of the Chapter. The average cluster density n_c is obtained by dividing the average cluster mass density ρ_c with M_C (mass of Coma cluster); ρ_c is given by:

$$\rho_c = \frac{1}{V} \sum_i M_i \tilde{w}(r_i) \tag{3.14}$$

where M_i is the mass of the generic cluster. As in PV91 and SVZ91 we assume that cluster masses are proportional to the the Abell–catalogue listed number of galaxies per cluster, $M_i \propto N_{A,i}$ (and $N_C = 106$); while the mass of the synthetic clusters was set equal to the average mass of the real clusters. The last term corrects for the net gravity of the homogeneous density background. The correction is necessary since the summation calculates the contribution from the density rather than from overdensity. Eq.(3.13) measures the true peculiar velocity only if density inhomogeneities outside the surveyed volume can be ignored.

As shown by Vittorio & Juskiewicz (1987) and Juskiewicz, Vittorio & Wyse (1990) in a multipole expansion of the external gravitational field the leading term is the dipole. Its effect is naturally removed if the peculiar velocities are evaluated in the LG frame because the dipole contribution is constant for all objects and does not affect the relative peculiar velocities. The only disadvantage of the LG frame is that the correction for the solar motion relative to its barycenter is uncertain by $\sim$ 50 - 100 km/sec (Yahil et al. 1977) which, as we will see, is smaller than the errors on the predicted LG velocity. For this reason we used eq.(13) to evaluate the cluster peculiar velocity in the LG frame. The higher order terms in the multipole expansion of the external gravitational field fall off faster than the dipole with distance and are generally negligible for distances smaller than $R_{max}/2$ (Yahil et al. 1991).

Possible systematic errors when computing peculiar velocities are therefore expected only at larger distances and should not appreciably affect the reconstruction reliability within 200 h^{-1} Mpc.

The Reconstruction Algorithm

To reconstruct the 3D density field we used a *LIRM* which is close to those described by Strauss & Davis (1988), Yahil et al. (1991) and Hudson (1993a) in which, starting from the observed z–space cluster distribution, one recovers the cluster true positions by iteratively computing their peculiar velocities according to eq. (3.10). As we already discussed in Chapter 2, this method is self consistent as long as the density fluctuations we are dealing with are linear, the clusters trace the mass and the mass fluctuations responsible for the peculiar motions of objects are within the volume sampled.

The general idea has been already discussed, here we describe our implementation. The steps of our iterative scheme are the following:

1. All the clusters are initially placed at their observed distance, $r^{(0)} = cz$, with no peculiar velocity and with an arbitrary value for the input β_c parameter. The index $^{(0)}$ refers to the 0th iteration.

2. The weighting function $w(\mathbf{x}_i)$ is computed and its value is kept constant in the subsequent iterations (i.e. the selection function is not upgraded). This speeds up the algorithm while it also does not lead to appreciable errors, since $P(z) \approx 1$ within 20000 km/sec.

3. The average density n_c within the sampled volume is computed and its value is updated.

4. The window function $W(|\mathbf{x}_i^{(k)} - \mathbf{x}^{(k)}|)$ is computed for each object.

5. The peculiar velocity of the ith cluster $\mathbf{v}^{(k)}(\mathbf{x}_i)$ is computed according to eq. (3.13) taking into account both, the clusters within R_{max} and those that during the iterations were placed beyond the volume limits (we will refer to these as 'passive' objects).

6. Radial positions of 'active' clusters are updated. Their new positions are given by

$$r^{(k+1)} = cz - \hat{\mathbf{x}}_i \cdot \left[\mathbf{v}(\mathbf{x}_i)^{(k)} - \mathbf{v}(0)^{(k)} \right]. \qquad (3.15)$$

Positions of 'passive' objects are not updated.

7. For each real active cluster we compute the difference of its position between the last two iterations. If the difference is larger than 0.5% r, then we jump back to step 3. The convergence is typically reached within 10 iterations.

Since the smoothing scheme treats clusters as spheres of radius R_{sm}, clusters in the spherical shell $|\mathbf{x} - R_{max}| < R_{sm}$ need to be weighted properly by computing how much of the sphere lies within R_{max}. But since we will estimate the dipole and the cluster velocity field only within 20000 km/sec and since we regard the cluster distribution beyond this radius as an improvement over a simple homogeneous distribution, we do not need to implement this correction.

Our iterative reconstruction algorithm can fail to recover the true 3D object position within high cluster density regions ('triple value regions') (cf. Yahil et al. 1991; Hudson 1993a). In our case, however, the objects are so sparsely distributed (which is the reason why the smoothing scale used is relatively large) that this problem is negligible. Obviously, the sparseness of the clusters introduces different problems, as we will discuss below.

3.1.3   Testing the Reconstruction Reliability

To test the *intrinsic* reliability of the whole reconstruction procedure and to optimize its performances we considered a catalogue of mock clusters extracted from a simulation performed by Borgani et al. (1994) in which the present–time cluster positions were determined by the Zel'dovich approximation in a standard CDM model Universe. The mock clusters were identified as peaks above a density threshold which was chosen so that their space density matches that of the observed clusters ($\sim 2 \times 10^{-5} h^3$ Mpc^{-3}). We considered a spherical volume centered around a LG–like observer (see B95). Each cluster peculiar velocity was determined according to linear theory after having computed the gravitational acceleration generated by all the clusters within the sampled volume. This ideal cluster distribution was then degraded by Montecarlo rejecting clusters according to the probability distributions $P(z)$ and $P(b)$ and by devoiding the ZoA. Finally, an artificial Gaussian distributed noise was added to the cluster velocity to mimic experimental errors in their measured redshifts. According to observational indications we used a variance of 200 km/sec (Strauss, Cen & Ostriker 1994). At this point we applied the *RSCM* together with the *LIRM* to recover the original object distribution and velocities.

Four different indicators were used to assess the *intrinsic* reliability of the reconstruction procedure:

- *The differences between reconstructed and true peculiar acceleration acting on the observer.*

To estimate these discrepancies we evaluate the true and the reconstructed peculiar

Radius h^{-1}Mpc	Δg	σg	$\Delta\theta$	$\sigma\theta$
100	8%	5%	6%	4%
150	4%	7%	2%	4%
200	3%	6%	2%	5%

Table 3.1: Dipole Errors: Per cent discrepancies and variances between the true and the reconstructed gravitational acceleration at different radii. Columns 2 and 3 refer to the amplitude discrepancy while column 4 and 5 list the average misalignment and its variance, respectively.

acceleration **g** at the observer's position from 10 different reconstructions. The reconstructed peculiar acceleration turned out to be very close to the original one: the per cent discrepancy between the amplitudes of the true and the reconstructed peculiar acceleration at the limiting depth of $200\,h^{-1}$Mpc was $3\pm6\%$ and the two vectors were misaligned by $2°\pm5°$, where the errors have been computed from the 10 independent realizations. Similar results are found when the analysis is restricted to smaller volumes: in Table (3.1) we list the difference in amplitude and the vectors misalignment (together with the relative variances) at different radii.

- *The volume averaged discrepancy between the true and the reconstructed position:*

$$\langle \epsilon_i \rangle = \langle |\mathbf{x}_{\text{true},i} - \mathbf{x}_{\text{rec},i}| / |\mathbf{x}_{\text{true},i}| \rangle$$

The most straightforward way to quantify the goodness of the reconstruction algorithm is that of computing the volume averaged discrepancy between the original cluster positions and the reconstructed ones based on 10 different Montecarlo reconstructions of the same distribution of synthetic clusters. In Fig. (3.2) we present the distribution of the ϵ_i values which peaks at $\lesssim 1\%$ and has a mean value of $\langle \epsilon_i \rangle \simeq 1.6\%$ (it is skewed towards large errors); while the probability of having $\epsilon_i > 3\%$ is quite low.

We also found, as expected, that ϵ_i depends on the initial displacement of the ith cluster with respect to its true position $|\mathbf{x}_{true,i} - \mathbf{x}^{(0)}|$. The reliability of the method greatly improves if clusters are initially placed close to their real positions, which would be possible if reliable z–independent distance measurements were available for some nearby clusters. We found that if the position of 30% of the objects where known then the previously quoted 1.6% error decreases to $\sim 1.1\%$.
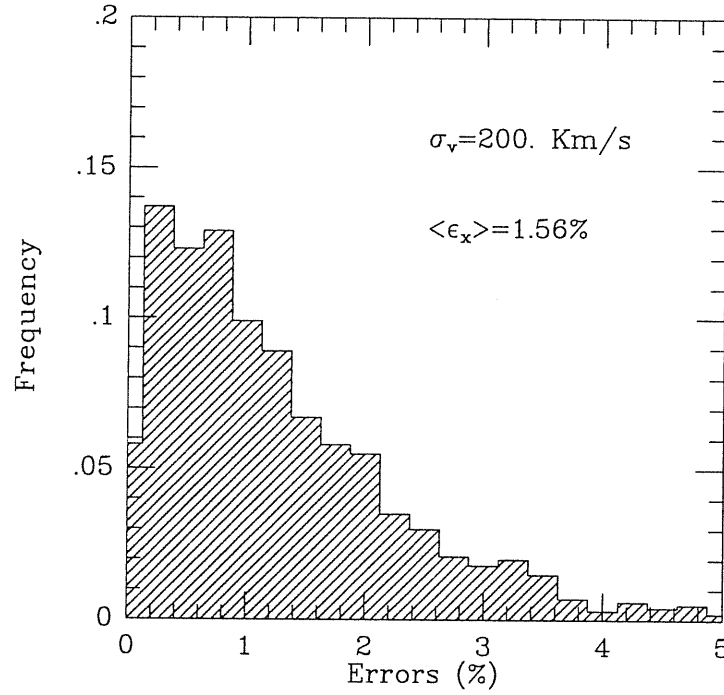
Figure 3.2: The distribution of relative percentage differences, ϵ_i, between the true and reconstructed positions of simulated clusters.

- *The spatial distribution of the ϵ_i.*

  More information on the reconstruction reliability can be obtained by exploring the spatial distribution of ϵ_i since there is no reason for the errors to be homogeneously and isotropically distributed. We have found that ϵ_i correlates with ϵ_r defined as: $|x_{true,i} - x_i^{(0)}|$ thus if the generic object is initially placed at its redshift distance, then ϵ_i is expected to be correlated with

$$\epsilon_r = \frac{|x_{true,i} - x_i^{(0)}|}{x_{true,i}} = \frac{[(v_p(x_i) - v_p(0))] \cdot \hat{x}_i}{H_o r_i}. \tag{3.16}$$

This means that the spatial distribution of errors is expected to be

  - anistotropic: ϵ_r is larger for objects placed along the direction of the observer's motion,

  - inhomogeneous: the ratio $\frac{(v_p(x) - v_p(0))}{H_o r}$ decreases with the distance,

Other sources of inhomogeneity in the errors distribution are the presence of a shear in the velocity field and selection effects. The present-analysis assumes a negligible shear while selections effects are already taken into account by the reconstruction procedure.

Radius h^{-1}Mpc	$\langle \epsilon_i \rangle$
100	2.6 %
150	1.6 %
150	1.2 %
250	1.0 %

Table 3.2: Radial reconstruction errors: Per cent discrepancies between the true and the reconstructed positions within different shells are listed as a function of the shell radius.

To directly appreciate the inhomogeneity of the errors distribution we computed ϵ_i averaged within shells of increasing radius. The results are quoted in Table (3.2) where we list the average per cent errors $\langle \epsilon_i \rangle$ within different regions of increasing radius. The average error within a 100 h^{-1}Mpc sphere is ~ 2.7 %. This value is larger than the volume averaged one but is smaller than the best experimental determination of the cluster distances based on redshift–independent distance indicators ($\sim 5\%$, see Jerjen & Tamman, 1993).

The radial dependence of the reconstruction errors is not the only expected spatial feature and thus we searched for other systematic effects. For this purpose we computed the variance of the reconstructed cluster position from the 10 different reconstructions:

$$\sigma_i = \langle (\mathbf{x}_i - \bar{\mathbf{x}}_i)^2 \rangle^{1/2}, \qquad (3.17)$$

where the average is intended over the different reconstruction, the index i refers to the ith cluster and $\bar{\mathbf{x}}_i$ is the average reconstructed position. To visualize the spatial distribution of σ_i we plot, in supergalactic Cartesian coordinates, the projected distribution of σ_i within a slice of 8000 km/sec wide centered on the supergalactic plan. [Fig. (3.3)]. The variance is smoothed with a 2D Gaussian filter with 500 km/sec radius and it is arbitrary normalized to unity.

Two distinct features can be noticed. Fist of all, comparing Fig. (3.3) with Fig. (3.6), σ_i appears to be larger in correspondence of the high density peaks, where the reconstruction procedure is expected to be less reliable. Superimposed to this pattern there is a second feature: the variance is large near the galactic plane (i. e. along the line connecting (X,Y)=(0,20) to (X,Y)=(0,40) and decreases when the galactic latitude increases, being nearly zero on the plane orthogonal to the galactic one [the (20,0)–(20,40) connecting line]. Again, this behaviour is not surprising since the reconstruction
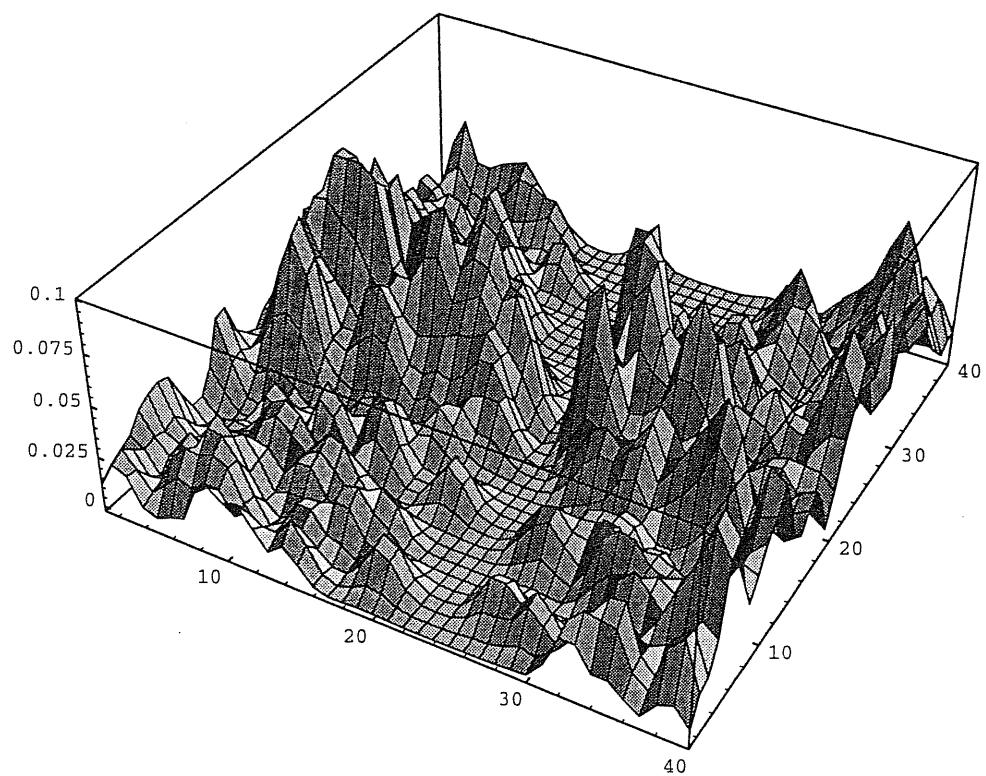
Figure 3.3: Surface plot visualization of the smoothed spatial distribution of σ_i within $-4000 < Z < 4000$ km/sec, projected onto the supergalactic plane.

within the ZoA strongly depends on the Montecarlo realization as the distribution of synthetic objects does.

- *The spatial cluster–cluster correlation function*

Using the standard procedure described in section (3.1.5) we computed the cluster–cluster spatial correlation function, ξ_{cc}, both for the redshift and real space distributions of the simulated clusters and we compared them to the analogous quantities computed from 10 different *LIRM*–reconstructed cluster distributions. Errorbars are intrinsic errors computed from the 10 different realizations.

Fig. (3.4a) shows the two–point correlation function for the simulated Z–space cluster distribution (open dots) and for the reconstructed one (starred symbols), the dashed line represents the function $\xi_{cc}(r) = (20/r)^{1.8}$, that fit the Abell and ACO cluster correlation function. Fig. (3.4b) displays an analogous plot for the 3D–space cluster distribution. The *RSCM* and the *LIRM* reproduce very well the original correlation functions over a wide range of scales.

We stress that the above tests are aimed at assessing the *intrinsic* reliability of the reconstruction method; cluster velocities are computed according to linear theory and no allowance for contribution from external gravitational fields is made (a set-up that needs not be true in the real universe). To get an estimate of the actual uncertainties in the whole procedure we need to account for several other effects, which will be quantified in the next section. The *intrinsic* uncertainty will be assumed to be independent from the other sources of errors and will be added in quadrature to compute the total uncertainty on the peculiar velocities.

The Reconstruction in the CMB–Frame:

As we have previously discussed, the reconstruction procedure naturally applies in the LG–frame. It is nevertheless interesting to check how well this method applies when it is used in the CMB–frame. The *LIRM* has been implemented under the assumption that external contributions to the acceleration of the generic object within the sampled volume can be modeled as a simple dipolar external field. If the strength of this dipolar field is large then systematic errors are expected if the reconstruction is performed in the CMB frame. This uncertainty originates from the fact that, if $v_{obs}(0)$ is the observed LG velocity with respect to the CMB and z is the redshift of a generic object as measured in the LG frame,
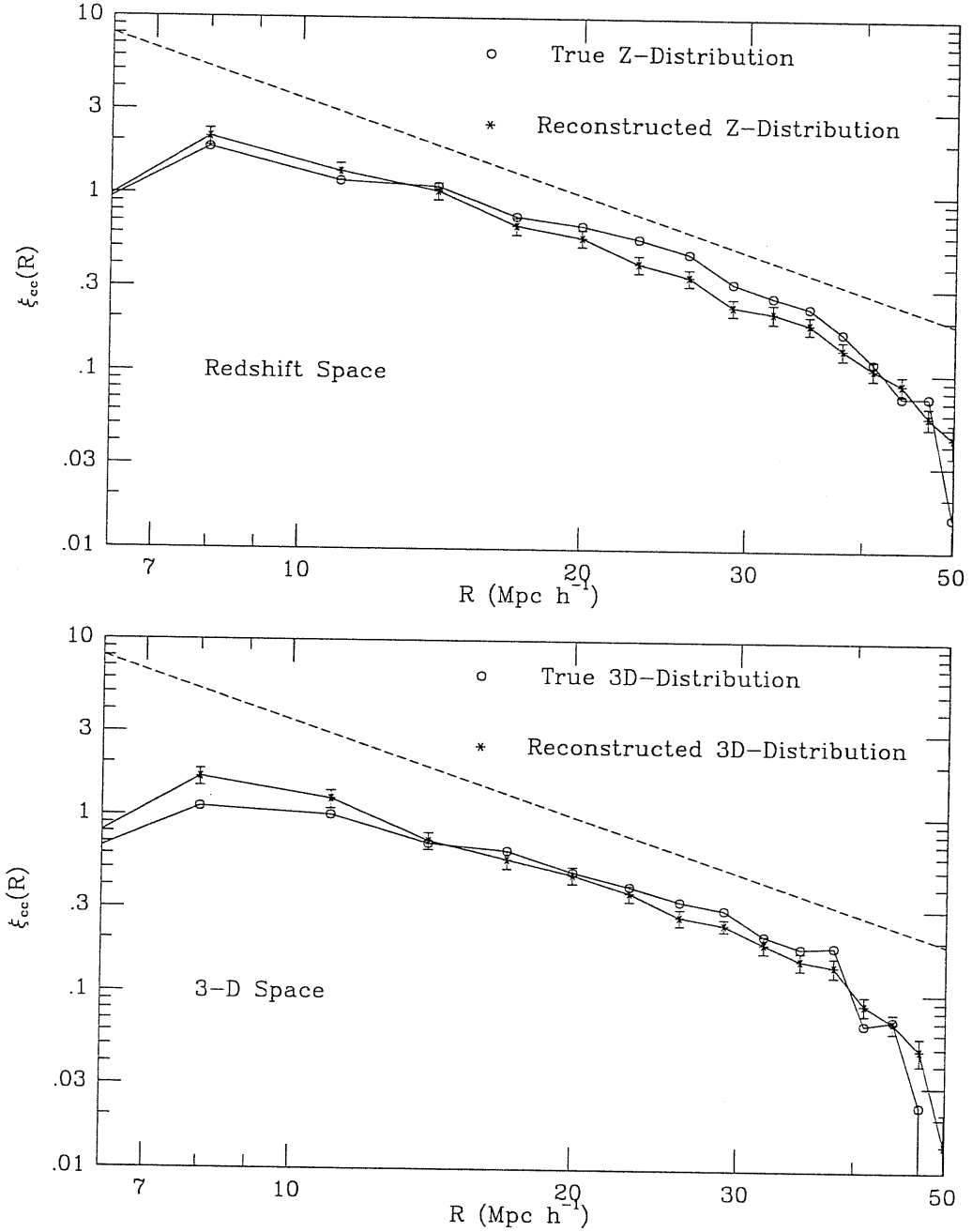
Figure 3.4: Spatial two-point correlation function of the simulated cluster distribution. Filled dots represents $\xi(r)$ of the simulated data and starred symbols refer to the reconstructed distribution. The experimental $\xi_{cc}(r) = (20/r)^{1.8}$ function is plotted as a dashed line. Fig. (a) refers to Z-space while Fig. (b) refers to the 3D distribution.

then the redshift in the CMB–frame, z_c is

$$cz_c = cz - \mathbf{v}_{obs}(0) \cdot \hat{\mathbf{x}}. \tag{3.18}$$

Therefore, when the reconstruction is applied to the CMB–frame cluster distribution, eq. (3.15) becomes

$$r_i^{(k+1)} = cz_i - \hat{\mathbf{x}}_i \cdot [\mathbf{v}(\mathbf{x}_i)^{(k)} - \mathbf{v}(0)^{(k)} + \mathbf{v}_{obs}(0)]. \tag{3.19}$$

Unless the external contributions are very small $\mathbf{v}(0)^{(k)} \neq \mathbf{v}_{obs}(0)$, leading to a systematic errors. Of course if $\mathbf{v}_{obs}(0)$ were generated by the mass distribution contained within 200 h^{-1}Mpc (i.e. there were non dipolar contribution from the external force field) then the CMB would be the best frame for reconstruction purposes since it would avoid the uncertainties deriving from the correction for the solar motion needed when working in the LG frame (Yahil et al. 1977). However, although the z–space cluster dipole flattens at $170\,h^{-1}$Mpc, it is impossible to *a priori* exclude further contributions from larger scales. To avoid these unpredictable uncertainties we have decided to perform the reconstruction in the LG frame also taking into account the fact that if the objects share a common bulk flow, as shown by experimental data, then their starting positions in the LG frame are very close to the true ones which minimizes the reconstruction errors.

3.1.4   Smoothed Cluster Density Maps in $z-$ and 3D–Space

In Fig. (3.5a) and (3.5b) we plot in supergalactic Cartesian coordinates the reconstructed whole-sky smoothed density field for a slice of 8000 *km/sec* wide, centered on the supergalactic plane, in z-space and in 3D space, respectively. Note that the same Gaussian smoothing and cell units are used as in Fig. (3.1b) and (3.1d). As also outlined by Scaramella (1994) who derived and discussed similar maps but only in z-space, the sparseness of the cluster distribution and the heavy smoothing could miss some features of the cosmic density field. Nevertheless, our reconstruction technique should reveal the main large–scale features of the 3D cosmic density field.

From these plots it is evident that eliminating the distortions due to peculiar velocities suppresses significantly the amplitude of the density peaks in 3D with respect to that in the z-space. This effect is particularly evident in the Virgo-Hydra-Centaurus (or else Great Attractor) region [centered at (X,Y) = (8.5,11)], in the Leo region [centered at (X,Y) = (11,14)] and around the Ursa-Major supercluster [centered at (X,Y)=(15,18)]. Interestingly, in the Perseus-Pegasus region [centered at (X,Y)=(13,10)] the opposite is true, ie.,
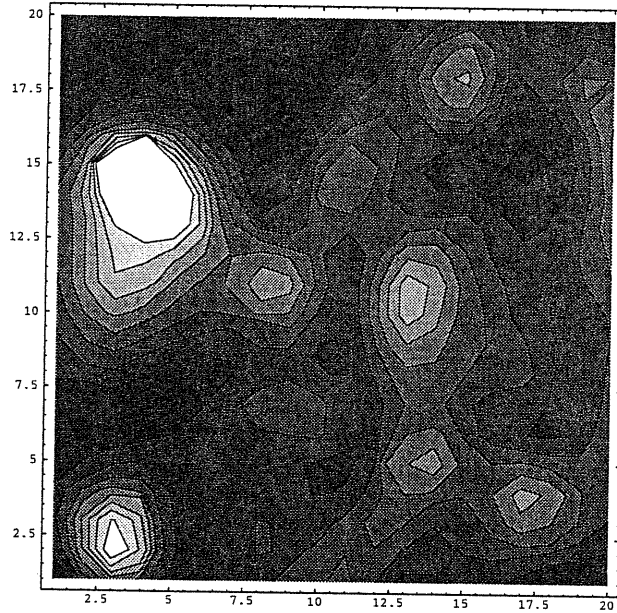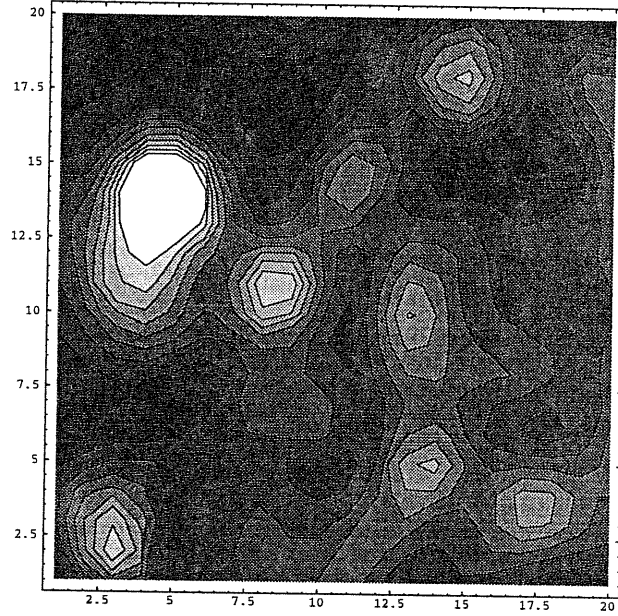
Figure 3.5: The projection onto the supergalactic plane of the smoothed cluster density field with $-4000 < Z_{sup} < 4000$ km/sec. Fig. (a) refers to z-space, while Fig. (b) to reconstructed 3D-space. The smoothing procedure is described in the text.

the 3D density amplitude is slightly higher than in the z-space case. This could be easily understood if there exists a coherent gradient of negative peculiar velocities, increasing in amplitude towards the near side of this structure (towards smaller X's, ie., towards the LG).

Also, the shape of the density peaks, in the 3D case, appears to be slightly elongated along the line of sight. This effect, which is mostly prominent in the Great Attractor and in the Shapley concentration [centered at (X,Y)=(3.5,14)], arises from the fact that in the linear regime the infall peculiar velocities within high density regions are coherent and tend to twist the isodensity contours along the line of sight.

A different representation of the cluster density in this slice is also presented in Fig. (3.6) where we plot a 3D surface-plot visualization of the density field (similar to that presented by Dekel 1994), again in both z-space (upper panel) and 3D (lower panel)

In Fig. (3.7) we present the 3D cluster density field for the four slices, each of 8000 km/sec width, above and below the supergalactic plane. Panel (a) and (b) correspond to the $4000 < Z < 12000\ km/sec$ and $12000 < Z < 20000\ km/sec$ slices respectively, while panel (c) and (d) represent the corresponding slices but for negative Z's. Our intention is not to present a detailed analysis of the structures evident in our contour plots (for such a task see Tully 1987 and Tully et al. 1992). However, we would like to emphasize the fact that, most structures found in the supergalactic plane extend not only to the first 8000 km/sec wide slice, above or below the supergalactic plane, but also to the second such slice. For example the overdensity corresponding to the Shapley concentration extends to both negative Z slices. Also the Great Attractor region is connected to the Lepus region [centered at (X,Y)=(8.5,10) in panel c] which seems to extend even further to the next slice (panel d) while a similar behaviour is found also for Perseus-Pegasus region. From panels (a) and (b) we see that the same is true for the Ursa Major supercluster, the Grus-Indus region [centered at (X,Y)=(3,2.5) in the supergalactic plane slice], the Leo region which seems to be connected with Hercules [centered at (X,Y)=(10,14) in the (a) and (b) slices] as well as the Pegasus-Pisces region [centered at (X,Y)=(17.5,4)] which is evident in the supergalactic plane and the two positive Z slices.

Comparison with Reconstructions on Smaller Scales:

Clusters of galaxies allow us to trace the density and velocity field on scales much larger than those possible when using galaxy samples. Clusters sparse sample the underlying density field and it is interesting to compare the cluster density field with that traced by galaxies which have a much higher resolution. A qualitative comparison is given in Fig. (3.8).
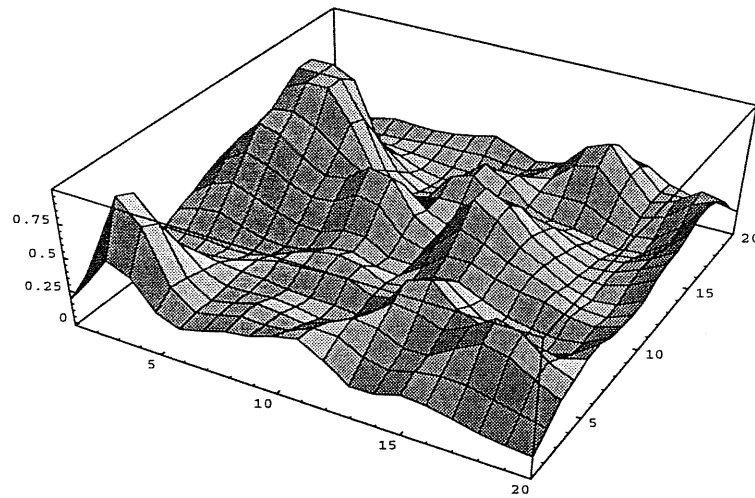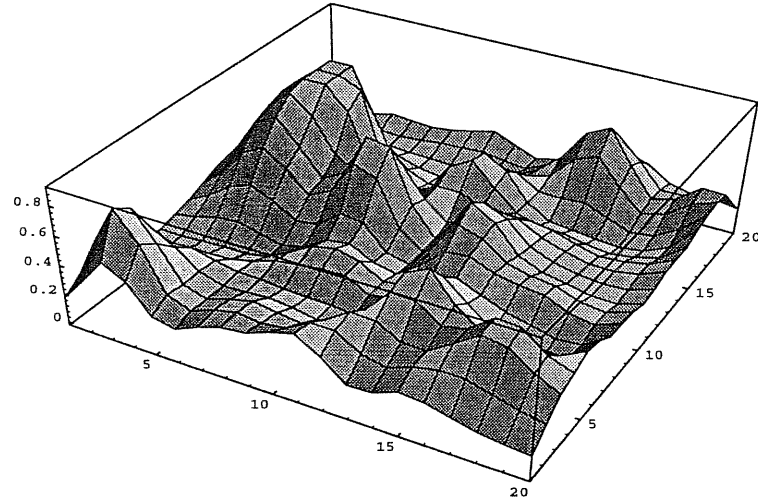
Figure 3.6: Surface-plot visualization of the density field of the slice $-4000 < Z_{sup} < 4000$ km/sec; the upper panel represents the density field in z-space and the lower panel the corresponding 3D-space density field.
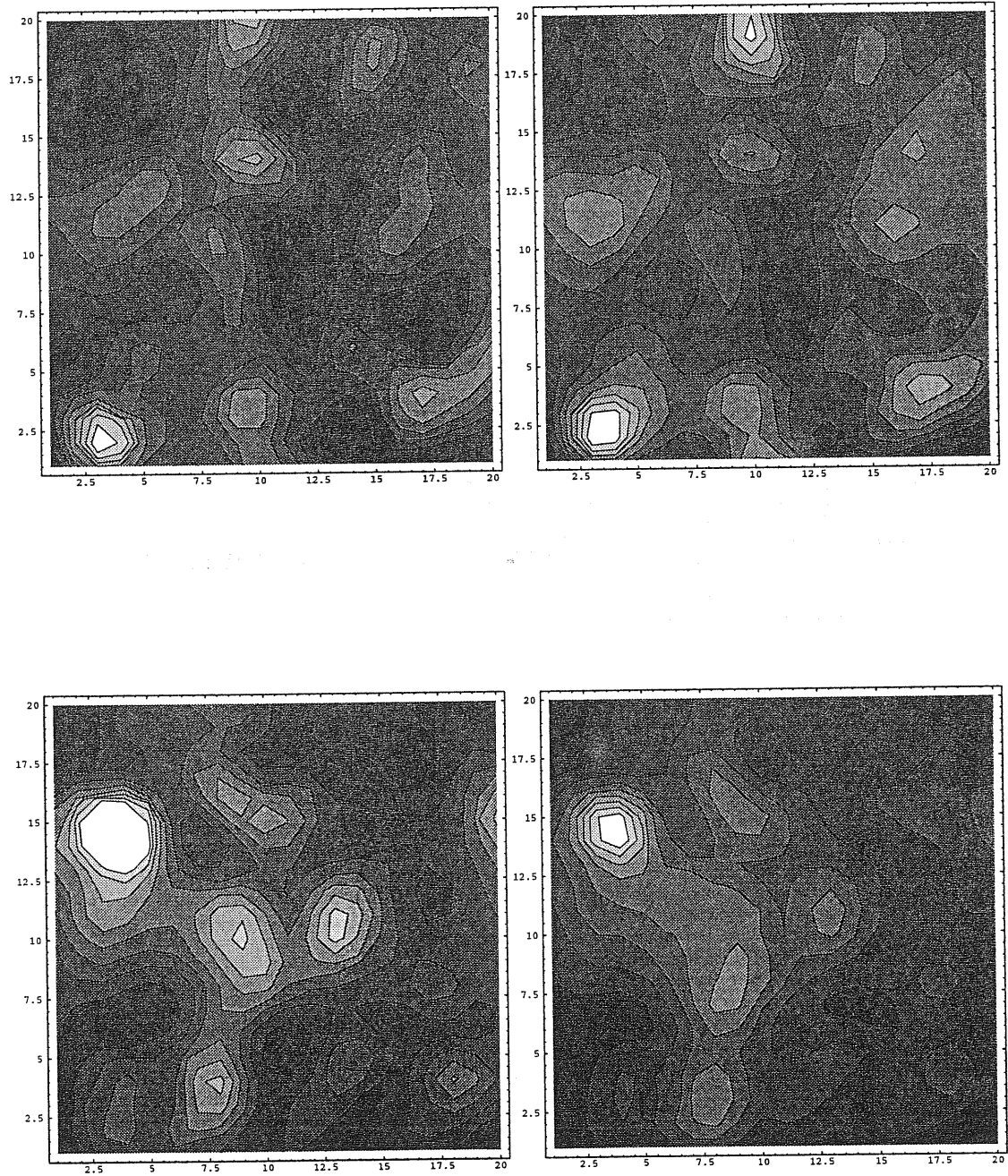
Figure 3.7: X_{sup}-Y_{sup} projections of the smoothed 3D-space cluster density field for 4 slices in Z_{sup}. (a) $4000 < Z_{sup} < 12000\ km/sec$. (b) $12000 < Z_{sup} < 20000\ km/sec$. (c) $-12000 < Z_{sup} < -4000\ km/sec$. (d) $-20000 < Z_{sup} < -12000\ km/sec$.

The plot on the bottom is the same of Fig. (3.6) while the two plots on the top show the results of two different reconstructions based on galaxy catalogues (from Fig. 2 of Hudson et al. 1995). The top left panel shows the outcome of a *POTENT* reconstruction based on MarkIII galaxies while the top right one displays the result of an iterative reconstruction applied to the Hudson's redshift catalogue of optical galaxies. In both cases a surface plot visualization of the reconstructed density field, projected onto the supergalactic plane is shown although with a smoothing and an orientation slightly different from those in Fig. (3.6). The area spanned by the two top plots has been delimitated, in the bottom panel, by a thick line. Although in the cluster density field small scales features have been washed out by the large smoothing, all the fundamental features can be recognized in all the three plots: the peaks in the Great Attractor, Coma and in the Perseus regions as well as the prominent local void (Dekel 1994). Interestingly, in both the cluster and the optical galaxy based reconstructed density fields, the amplitude of the Perseus–Pisces peak is larger than that of the Great Attractor.

3.1.5   The Cluster Two–Point Correlation Function

We computed the spatial two–point correlation function of the reconstructed Abell–ACO cluster distribution both in z– and in 3D space. Obviously, the reconstructed z–space correlation function is expected to match the observed one since synthetic clusters have been distributed with the constraint of reproducing the observed spatial two–point correlation function. However, comparing the redshift and the 3D space correlation functions allow in principle to determine the value of β_c.

The Z–Space Two–Point Correlation Function, ξ_z:

We computed the two–point correlation function separately for the Abell and ACO clusters subsamples. We used the standard estimator:

$$\xi_z(r) + 1 = \frac{N_{cc}(r) \cdot N_{CR}}{N_{cr}(r) \cdot N_{CC}}, \tag{3.20}$$

where $N_{cc}(r)$ is the number of cluster pairs in the interval $r - \delta r/2 \leq r \leq +\delta r/2$, $N_{cc}(r)$ is the number of cluster random pairs in the same interval, N_{CR} is the total number of cluster random pairs in the catalogue and N_{CC} is the number of cluster–cluster pairs. $\xi_z(r)$ has been evaluated in 19 logarithmic intervals in the range [4-200] h^{-1}Mpc. We generated the random population by fulfilling the real cluster sample's $P(b)$ and $P(z)$ selection functions

POTENT
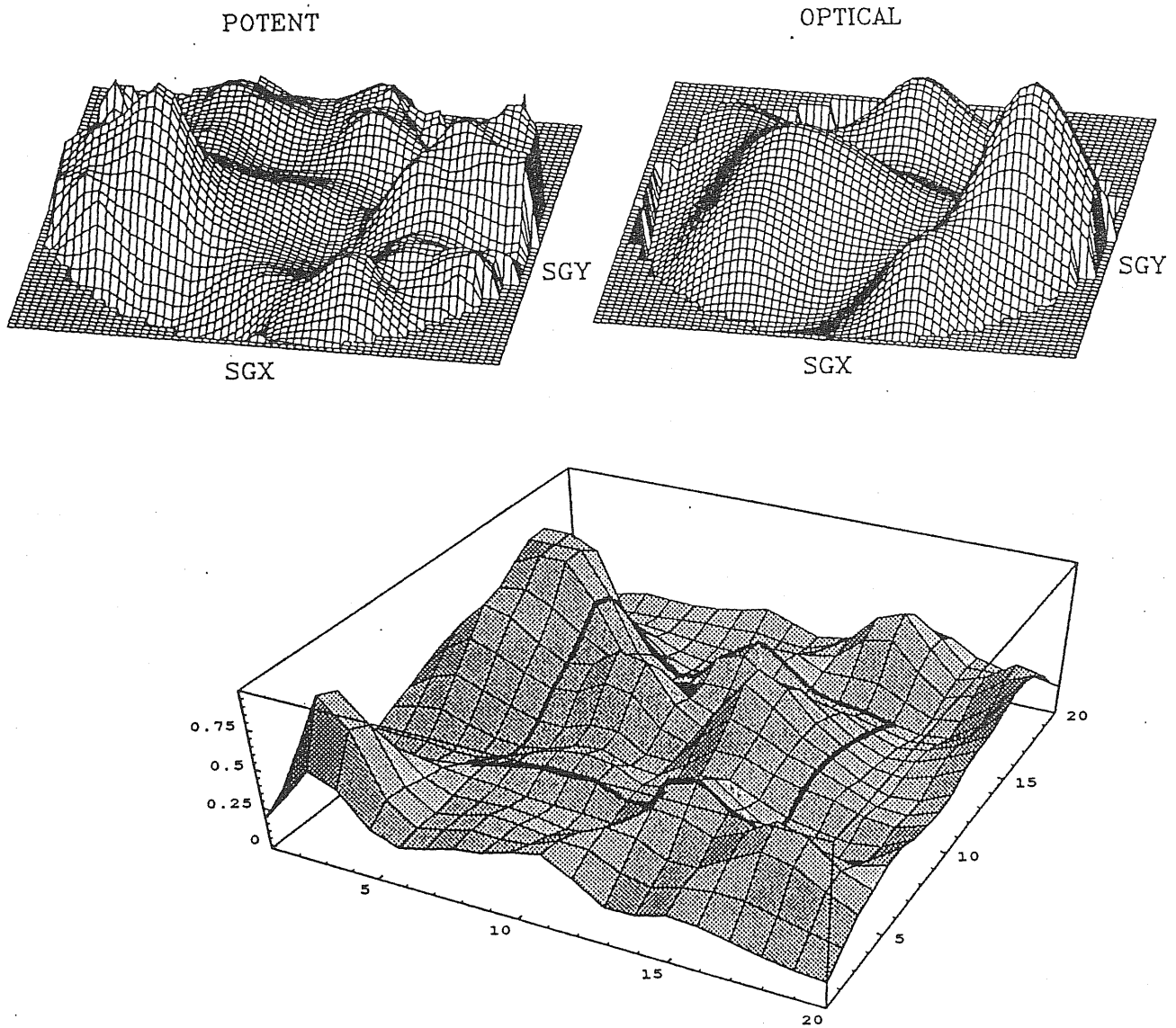
OPTICAL

Figure 3.8: Comparison between surface plots of the reconstructed density field traced by MARK III and optical galaxies (upper part) and by Abell/ACO clusters (lower part). The upper plots are from Hudson et al. (1995).

and in the same volume. Distances of the random clusters have been assigned using the Mattig relation [eq. (3.1)]. The two–point correlation function of the reconstructed z–space cluster distribution depends on (α, α), q_o and on the weighting scheme adopted. We therefore computed $\xi_z(r)$ for several different combinations of these free parameters and for each combination we performed 10 independent realizations of the random sample. The scatter between all the different correlation functions is used to estimate the *total* error. Final errors are computed by adding in quadrature the total errors to the bootstrap variance of ξ_z, σ_{ξ_z}, that, according to Mo, Jing and Börner (1992), can be analytically approximated by

$$\sigma^2_{\xi_z} \simeq 3 \times \sigma^2_{P_o}. \tag{3.21}$$

The Poissonian variance σ_{P_o} was estimated as

$$\sigma_{P_o} = \left(\frac{1 + \xi_z(r)}{N_{CC}} \right)^{1/2}. \tag{3.22}$$

In Fig. (3.9) we plot the Z–space correlation function estimated with the following choice of parameters: $(\alpha, \alpha) = (0.3, 0.2)$, $q_0 = 0.5$, $\beta_c = 0.25$, direct homogenization scheme [see section (3.2.2)] in which the relative Abell/ACO weights have been computed after dividing the 200 h^{-1} Mpc sphere into 10 equal volume shells. The plot on the top refers to the ACO clusters while the correlation of the Abell clusters are shown on the bottom.

For a more quantitative discussion, we characterized the $\xi_z(r)$ shape by the usual power law

$$\xi_z(r) = 10^A r^B = \left(\frac{r}{r_o} \right)^\gamma \tag{3.23}$$

The parameters A and B are derived by χ^2 minimizing the following expression

$$\chi^2 = \sum_{i=5}^{13} \left[\frac{\log \xi_i(r) - B \log r - A}{w_i} \right], \tag{3.24}$$

where $w_i = \sigma_i / \xi_i$. The sum is restricted to the distance range [9–70] h^{-1}Mpc to allow a useful comparison with the analogous parameters of the correlation function estimated in the real space. It turned out that for Abell clusters

$$A^z_{Ab} = 2.3 \pm 0.6 \quad \text{and} \quad B^z_{Ab} = -1.8 \pm 0.3$$

while for the ACO sample

$$A^z_{ACO} = 3.0 \pm 0.6 \quad \text{and} \quad B^z_{Ab} = -2.1 \pm 0.4.$$
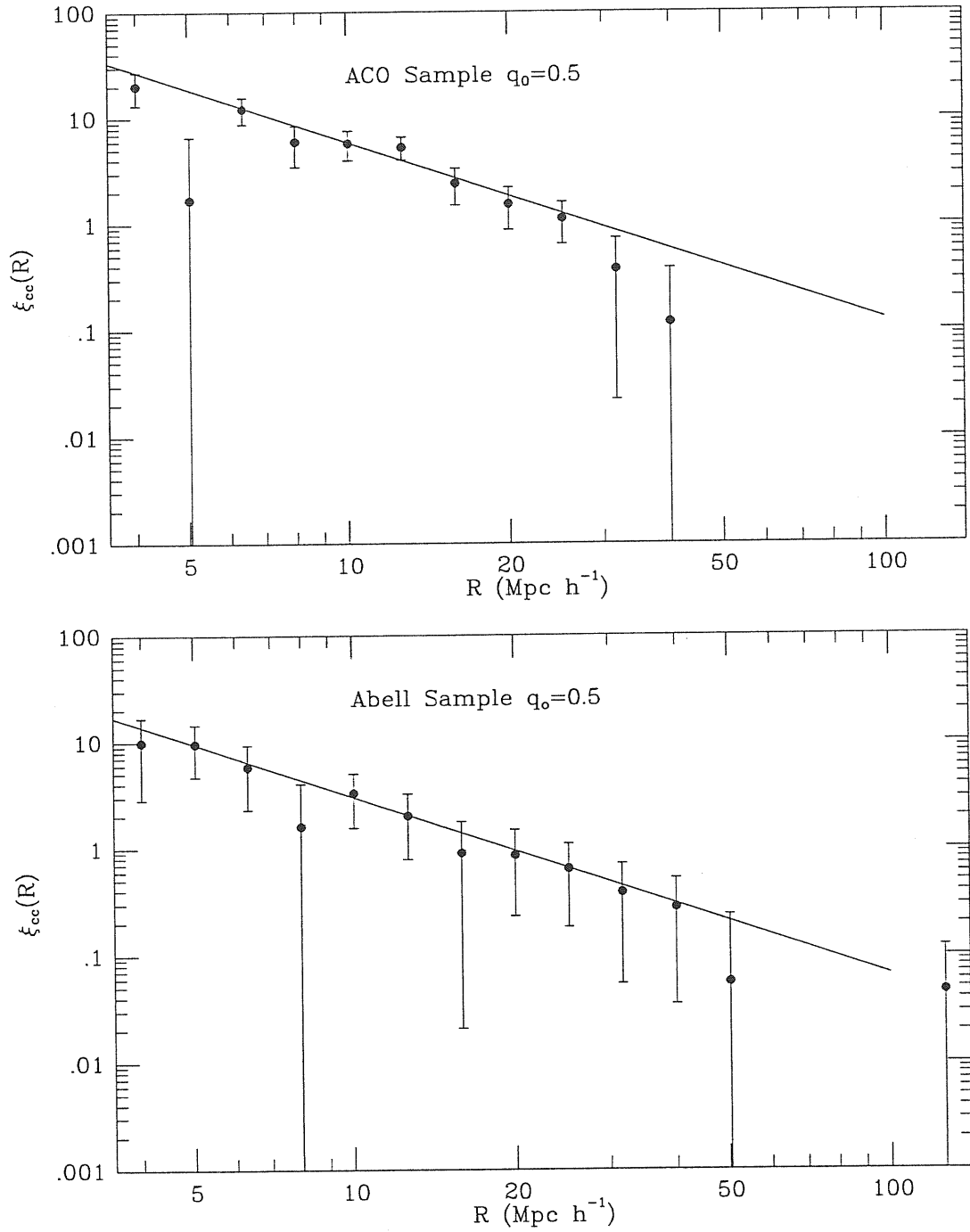
Figure 3.9: The z–space cluster–cluster spatial correlation functions for the ACO (Fig. (a)) and Abell clusters (Fig. (b)). The plot refers to the parameter choice specified in the text. The continuous line is the best fit to the data.

These values can be compared to those obtained by Plionis, Jing & Valdarnini (1991) who computed the correlation function for a slightly smaller although similar Abell/ACO sub-sample:

$$A^z_{Ab} = 2.4 \pm 0.5 \quad \text{and} \quad B^z_{Ab} = -1.8 \pm 0.2$$

and for the ACO sample

$$A^z_{ACO} = 2.6 \pm 0.5 \quad \text{and} \quad B^z_{Ab} = -1.8 \pm 0.2.$$

Although the parameters for the Abell sample are remarkably similar, the correlation slope of the reconstructed ACO cluster distribution is steeper that that of Plionis, Jing & Valdarnini (1991) with also a larger correlation length; note, however, that our sample has many more measure ACO redshifts. Because of the large uncertainties, however, the significance of the differences is below 1–σ level.

The 3D–Space Two–Point Correlation Function, $\xi_{3D}(r)$:

Using the same technique we computed the correlation function for the recon-structed 3D cluster distribution. Besides the free parameters used for the z–space recon-struction we also need to choose the smoothing radius that we allow to vary in a plausible range. We found that if the cluster distribution is smoothed on small scales ($< 10\,h^{-1}$Mpc) the correlation amplitude is severely depressed below 10 h^{-1}Mpc. This effect can be under-stood as follows: removing overestimated peculiar velocities unnaturally separates physically close cluster pairs and thus depresses the correlation on small scales. Applying the recon-struction algorithm with $R_{sm} < 10\,h^{-1}$Mpc, has the effect of separating most of the close cluster pairs. Since observations indicates that close clusters do exist, this effect provide us with one more argument, besides that of Croft & Efstathiou (1994) for preferring smoothing radii $\geq 10\,h^{-1}$Mpc. For this reason we computed A and B by minimizing the expression (2.25) in the interval [9–70] h^{-1}Mpc.

From the fitting procedure we obtain

$$A^{3D}_{Ab} = 2.25 \pm 0.6 \quad \text{and} \quad B^{3D}_{Ab} = -1.8 \pm 0.3$$

and

$$A^{3D}_{ACO} = 2.9 \pm 0.5 \quad \text{and} \quad B^{3D}_{Ab} = -2.2 \pm 0.3.$$

Constraining β_c Parameter:

The above results can be in principle used to constrain the density parameter since in the linear regime (which is the framework where we are working) the amplitude of the 3D correlation function is expected to be smaller than in the z–space according to the relationship

$$\xi_z(r) = \xi_{3D}(r) \left(1 + \frac{2\beta_c}{3} + \frac{\beta_c^2}{5} \right), \tag{3.25}$$

while the slope of the correlation function should remain the same (Kaiser 1987). This prediction turned out to be qualitatively correct and, using the average A and B values we obtain $\beta_c^{Ab} = 0.3$ and $\beta_c^{ACO} = 0.2$. The large uncertainties, however, do not allow us to strongly constrain the $\Omega_\circ$ parameter, although we do obtain central β_c values which are near the expected ones (PD) and also very similar to those we will obtain in what follows using completely different methods [see sections (3.2.5), (3.3.3), and (3.3.6)].

3.2 THE CLUSTER DIPOLE

3.2.1 The Cluster Dipole and its Redshift Space Distortions

The main scope of this section is to compare the cluster dipole as measured in z-space with the reconstructed one in 3D–space. A simple eye inspection of Fig. (3.5) and (3.6) reveals that for all but the PP high density regions the peaks of the true density field have a larger amplitude when observed in z–space [see discussion in section (3.1.3)]. To see how these distortions affect the estimate of the cluster dipole, requires a quantitative discussion. From a theoretical point of view the problem has already been addressed by Kaiser (1987). He showed that gravitationally driven peculiar velocities can have a large effect on the peculiar acceleration acting on an object. If D_r is the amplitude of the true dipole (which measures the peculiar acceleration) and D_z is the z-space dipole, then the relationship between D_r and D_z depends both on the selection function ϕ and on the power spectrum considered. Recalling the Fourier decomposition of the overdensity field we consider each power mode separately. The kth plane wave density perturbation is

$$\delta\rho/\rho(\mathbf{x}) = \Delta_o \cos(\mathbf{k} \cdot \mathbf{x} + \theta), \tag{3.26}$$

where Δ_o is related to the spectral amplitude and $\mathbf{k}$ is the wavenumber vector. In this case the peculiar gravitational acceleration is simply given by

$$D_r = -4\pi \frac{\Delta_o}{k} \sin(\theta). \tag{3.27}$$

In the limit $kR_{max} \gg 1$, Kaiser has shown that

$$D_z = D_r + \beta_c \left\{ \frac{D_r}{3} + 2\pi \frac{\Delta_o}{k} \int_{-1}^{+1} \mu^2 d\mu \int_0^{R_{MAX}} \frac{dr}{r} \left(2 + \frac{d\ln\phi}{d\ln r} \right) [\sin(\mu kr + \theta) - \sin(\theta)] \right\}, \tag{3.28}$$

where Δ_o is the amplitude of the generic k-mode and μ is the cosine of the angle between the wavevector $\mathbf{k}$ and the position vector $\mathbf{x}$. An approximate evaluation of eq. (3.28) gives

$$\frac{D_z - D_r}{D_r} = \frac{1}{3} \beta_c \left[1 + E(k) \right], \tag{3.29}$$

where

$$E(k) \simeq \log[(kR_{max})^2 \phi(R_{max})/\phi(k^{-1})] . \tag{3.30}$$

The sign of $E(k)$ depends on the selection function and on the sample's depth. Although a precise $E(k)$ evaluation requires an accurate determination of the selection function, we are confident that in our case $\phi(R_{max}) \simeq 1$ which then implies $E(k) > 0$. The final value

of $D_z - D_r$ can be obtained in the linear regime by combining each mode separately (for large k the non–linear evolution couple the different modes, and this approximation does not hold). To properly combine the different modes requires knowledge of the $P(k)$. However, unless one considers cosmological models with very large power on small scales, which are in conflict with observations, we expect that for our cluster sample $D_z - D_r > 0$.

Assuming naively a single mode fluctuation as being responsible for the cluster dipole, gives $E(k) \approx 3$, where we have used $k = \frac{2\pi}{R_{conv}}$, and thus

$$\frac{D_z - D_r}{D_r} \approx 1.33 \; \beta_c \; . \tag{3.31}$$

We will see further below that our estimate of β_c, derived by combining the resulting 3D cluster dipole and the LG peculiar velocity is roughly consistent with eq. (3.31), which provides also a further, although weak due to the naive assumption made, consistency test of our whole procedure. Having said that, we would like to point out, however, that the *coherence* of the dipole (see Plionis 1995 and references therein) on a scale comparable to k^{-1} indicates that this mode could dominate the cluster dipole, partially justifying the above assumption.

3.2.2   Dipole Estimation

The cluster dipole vector, for an observer placed at the center of the coordinate system, is defined as

$$\mathbf{D} = \frac{3}{4\pi} \int \rho_c(\mathbf{x}) \frac{\mathbf{x}}{|\mathbf{x}|^3} d\mathbf{x}, \tag{3.32}$$

which, in linear theory, is related to the peculiar velocity by

$$\mathbf{v} = \beta_c \frac{H_\circ \mathbf{D}}{3\langle \rho_c \rangle} \; . \tag{3.33}$$

For our discrete cluster field density field, smoothed with a top hat window, the dipole becomes:

$$\mathbf{D} = \frac{3M_C}{4\pi} \sum_i \left(\frac{M_i}{M_C} \right) w(r_i) W(r_i) \frac{\mathbf{x}_i}{|\mathbf{x}_i|^3} \tag{3.34}$$

The monopole of the smoothed field is defined as:

$$M = \frac{M_C}{4\pi} \sum_i \left(\frac{M_i}{M_C} \right) w(r_i) W(r_i) \frac{1}{|\mathbf{x}_i|^2} \tag{3.35}$$

Since the value of $\mathbf{D}/M$ has a smaller scatter than that of $\mathbf{D}$ (see PV91) it can be used to compute the LG peculiar velocity, assuming that the dipole has converged to its asymptotic

value within the volume sampled. In this case the relationship between the peculiar velocity and $\mathbf{D}/M$ is:

$$\mathbf{v}(r) = \frac{1}{3}\beta_c \mathbf{D}(r) \frac{H_o R_{conv}}{M(R_{conv})} \; . \tag{3.36}$$

However, based on Montecarlo experiments, we found that a better estimate of the peculiar velocity of the observer is obtained directly from eq. (3.13). The average 1σ scatter between $\mathbf{v}$, computed from eq. (3.36), and the true one is $\sim 12\%$ if 850 'clusters' are used, a number comparable to that of our cluster (true and synthetic) sample. The discrepancy originates from the fact that the monopole is a good estimator of the average density only in the limit of continuous density field. Using 8500 objects, for example, reduces the scatter to 7%. This effect could introduce a further uncertainty in the LG peculiar velocity computed via eq. (3.36).

Computing the dipole and the monopole separately is nevertheless important for assessing the effective convergence of the peculiar velocity vector since a necessary condition for final convergence is that while the dipole converges, the cumulative monopole continues to grow linearly with distance. This condition, however, is not sufficient to guarantee the final convergence of the dipole, which could still increase after having reached a *plateau* (cf. Plionis, Coles & Catelan 1993).

Possible Systematic Effects:

The reconstructed cluster distribution could depend on a number of free parameters that are only partially determined by observational constraints and theoretical requirements. We systematically explored the influence of the parameter choice by allowing each free parameter to vary within an experimentally plausible range. In practice the reconstructed cluster dipole, and therefore the predicted LG peculiar velocity, can be regarded as a function of many variables (the free parameters) that are listed in Table (3.3). Boldface quantities refer to what we call the *standard case*, defined by the following choice of parameters: $(\alpha, \alpha) = (0.3, 0.2)$, $R_{sm} = 20 \; h^{-1}$ Mpc, $q_o = 0.5$, $\beta_c = 0.25$, direct homogenization scheme (eq. 3.5) with the 200 h^{-1} Mpc sphere being divided into 10 equal volume shells. For each of the 48 possible combinations of the free parameters, to which we refer to as 'models', we performed 10 independent reconstructions and we computed the corresponding 3D dipole. To explore the influence of each variable on the predicted LG dipole separately we adopted the following procedure:

Galactic Absorption	(0.2,0.3)		(0.2,0.2)
Deceleration Parameter q_o	0.2		0.5
Smoothing length Mpc h^{-1}	10	20	30
$W_{rel}(r)$ Binning	10		15
Homogenization Scheme	Direct		Inverse

Table 3.3: Experimental Parameters: Each model explored is characterized by a different set of parameters. Boldface quantities represent the 'Standard Model' set.

Parameters	Δu	Δl	Δb
(0.2,0.3) vs. (0.2,0.2)	$-1 \pm 10\%$	$+3 \pm 5°$	$-2 \pm 4°$
$\beta_c = 0.25$ vs. $\beta_c = 0.114$	$-8 \pm 12\%$	$0 \pm 5°$	$-1 \pm 4°$
$R_{sm} = 20$ Mpc vs. $R_{sm} = 10$ Mpc	$-3 \pm 11\%$	$0 \pm 4°$	$+3 \pm 3°$
$R_{sm} = 20$ Mpc vs. $R_{sm} = 30$ Mpc	$-2 \pm 11\%$	$+1 \pm 4°$	$+1 \pm 4°$
bin = 10 vs. bin=15	$-4 \pm 11\%$	$+1 \pm 4°$	$0 \pm 4°$
Direct vs. Inverse	$+4 \pm 11\%$	$+1 \pm 4°$	$0 \pm 4°$

Table 3.4: Dipole Comparison: First column displays the parameters defining the two compared categories. Column 2 shows the % difference of the dipole amplitude at 170 h^{-1} Mpc together with the relative standard deviation. Columns 3 and 4 contain the average misalignment and its standard deviation at 170 h^{-1} Mpc along l and b, respectively.

- The parameter of interest is selected and models are divided according to the value chosen for that parameter (e.g. $q_o = 0.2$ or 0.5). Models having the same parameter values are grouped in the same category.

- The average dipole at 170 h^{-1} Mpc is computed for all the models in the same category and the same procedure is repeated for all different categories.

- The different average dipoles are compared. The differences in amplitude and the misalignment angles between different average dipoles are listed in Table (3.4).

It is evident from Table (3.4) that the only appreciable systematic effect comes from the choice of the β_c parameter. Varying the other experimental parameters (i.e. the galactic absorption coefficients, the smoothing radius and the homogenization procedure) generates systematic errors much smaller than the intrinsic uncertainties of the reconstruction.

To appreciate the influence of the β_c parameter on the reconstruction process we have to disentangle two different effects: the role of the deceleration parameter, q_o, that enters through eq. (3.1) in defining the outer limits of the sample, and that of the β_c factor, whose arbitrary initial value has to be specified for the LIRM to be applied. The first effect turned out to be much smaller than the second one.

The effect of varying the β_c parameter in the LIRM was explored by performing the reconstruction with the same q_o value but using two different β_c values (0.25 and 0.114). Although these values are different by a factor ~ 2, the asymptotic amplitudes of the reconstructed dipole are very similar, differing only by 8%, being smaller for the standard $\beta_c = 0.25$ case, while the direction does not change appreciably. The complete analysis was performed by exploring two different class of models having ($\beta_c = 0.25$, $q_o = 0.5$) and ($\beta_c = 0.114$, $q_o = 0.2$), respectively, confirmed the above results (see Table 3.4). It is therefore clear that there is a small, although systematic, effect related to the value of the β_c parameter which enters as an input in the reconstruction algorithm.

It is interesting to compare this result to that obtained by SYDHF92. The asymptotic amplitude of their reconstructed IRAS galaxy dipole on scales larger than ~ 100 h^{-1} Mpc strongly depends on the input β_c value. The origin of this effect, to which they refer as the 'Kaiser effect', was ascribed to z–space distortions that in their case are mainly due to the LG motion with respect to the distribution of distant galaxies. This problem has been theoretically addressed by Kaiser & Lahav (1988). Let us consider the mapping from real–space coordinates x to the z–space coordinates s:

$$s = x \left(1 + \frac{x \cdot (v(x) - v(0))}{|r|^2} \right), \tag{3.37}$$

where $h = 1$. Kaiser (1987) showed that the linearized apparent density fluctuation in the z–space is

$$\left(\frac{\delta \rho(x)}{\rho} \right)_s = \left(\frac{\delta \rho(x)}{\rho} \right)_r - \left(2 + \frac{dln(\phi)}{dln(r)} \right) \frac{x \cdot (v(x) - v(0))}{|r|^2} - \frac{x}{|r|} \cdot \frac{dv(x)}{dr}. \tag{3.38}$$

The apparent peculiar velocity vector for an object placed at the center of the coordinates is

$$v_s = \frac{\beta_c}{4\pi} \int \delta(s) \frac{s}{|s|^3} d^3 s, \tag{3.39}$$

that, using eq. (3.38), gives

$$v_s = \frac{\beta_c}{4\pi} \int_{s_{min}}^{s_{max}} d^3 r \frac{x}{|r|^3} \left(\frac{\delta \rho(x)}{\rho}_r - \left(2 + \frac{dln(\phi)}{dln(r)} \right) \frac{x \cdot (v(x) - v(0))}{|r|^2} - \frac{x}{|r|} \cdot \frac{dv(x)}{dr} \right). \tag{3.40}$$

This expression has general validity. In our case we are interested to distortions caused by the LG motion with respect to the distant masses that do not contribute to the LG motion. Thus the problem reduces to the case of a rocket–born observer who resides in a uniform universe at rest with respect to the CMB and its peculiar acceleration originates locally. In this idealized case the redshift–space distortions lead to a discrepancy between the true peculiar velocity induced by the mass distribution at the observer's location, $\mathbf{v}(0)$, and the peculiar velocity generated by the redshift–distorted mass distribution $\mathbf{v}_s$:

$$\mathbf{v}_s = \frac{\beta_c \mathbf{v}(0)}{3} \int \frac{dr}{r} \left(2 + \frac{d\ln\phi}{d\ln r} \right). \tag{3.41}$$

In the case of volume limited survey we have $\phi = 1$ within the sample and the Kaiser effect reduces to the z–space distortions caused by the locally generated observer motion and it can be easily removed by properly account for the local sources of acceleration. The situation is less trivial when the selection function falls below one well within the sample's depth as for the the $IRAS$ galaxy sample studied by SYDHF92, in which $\phi \ll 1$ well within 100 h^{-1} Mpc. In that case the Kaiser effect is mainly caused by the LG motion with respect to distant galaxies and has a dramatic effect when determining the scale of dipole convergence. Since the magnitude of the Kaiser effect depends on the amplitude of $\mathbf{v}(0)$, that in the reconstruction procedure is fixed by the input β_c parameter, the typical signature of the Kaiser effect is the dependence of the convergence depth on the β_c parameter used.

For our cluster sample $P(z)$ is close to unity within 200 h^{-1} Mpc and the Kaiser effect should be negligible, which is indeed the case as demonstrated by the stability of our dipole against the variations of β_c. A very different behaviour is found by SYDHF92 especially at large depths where the sensitivity to the input β_c parameter is manifested by large variations of the dipole amplitude shape as a function of β_c (cf. Fig. 6 of SYDHF92).

3.2.3   Error Estimate

To obtain a reliable error estimate of the reconstructed dipole we need to account for several different sources of errors. We estimate the *intrinsic* error, σ_i, in the reconstruction algorithm from the 10 independent reconstructions performed for each model explored. Other sources of errors, which will be described below, are the *observational* error σ_o and the *shot–noise* error σ_{sn}. In what follows we will assume that all these errors are independent so that the total uncertainty σ_T will be simply estimated by adding the errors in quadrature.

Observational Error:

We define as observational error the uncertainty derived from the different free parameter choice, listed in Table (3.3), whose separate influence on the reconstructed dipole was explored in the previous subsection. The reconstructed dipole can be therefore regarded as a function of the smoothing length, the homogenization scheme and its binning, parameters that we allowed to vary in a plausible range of values. The galactic absorption set and the β_c factor, instead, are considered fixed by observations to $(0.2, 0.3)$ and to $\beta_c = 0.25$, respectively. We chose $\beta_c = 0.25$ since, as we will see in section (3.2.4), this value is closer to that one derived from the comparison with the CMB dipole. We found that varying these parameters does not produce any systematic effect in the dipole determination and thus we can consider them as Gaussian variables and the dipole as a multivariate Gaussian function of the explored parameters. Following this argument we compute σ_o as the variance of the dipole obtained by averaging over all models having $(\alpha, \alpha) = (0.3, 0.2)$ and $\beta_c = 0.25$ (our standard case). The observational error at $170 \ h^{-1}$ Mpc produces an uncertainty of $\sim \pm 65 \ \beta_c^{-1} \ km/sec$ in the dipole amplitude and of $\pm 4°$ and $\pm 2°$ along b and l directions respectively.

Shot–Noise Error:

The usual shot–noise estimate assumes that luminous objects have been drawn by a Poisson process from the underlying density field while the reconstruction procedure relies on the hypothesis that clusters of galaxies are *biased* tracers the mass. A more meaningful and self–consistent estimate of the shot noise error has been proposed by SYDHF92 that accounts for two different effects:

- The Poissonian error due to the fact that luminous objects become random tracers of the density field when the selection function falls below unity.

- An uncertainty due to the fact that cluster masses are randomly taken from an underlying mass distribution. In our case we estimated the mass of real clusters from their Abell listed number of galaxies while for the synthetic clusters, which constitute $\sim 50\%$ of the whole cluster population, their mass was set equal to the average real cluster mass.

Using our formalism, the SYDHF92 shot–noise computed for the $\mathcal{W}_{rel} = 1$ case, reduces to (see in Appendix):

$$\sigma_{sn}^2 = \left(\frac{\beta_c}{4\pi n_c}\right)^2 \sum_i^{N_s} \frac{W(r_i)^2}{r_i^4} K\left[\tilde{w}(r_i) - 1\right],\tag{3.42}$$

where the sum extends only over the N_s synthetic clusters, n_c is the average cluster density defined from eq. (3.14), $K = \langle \mu_i^2 \rangle - 1$, with μ_i being the mass of the real clusters in units of average mass and ,from the real clusters mass variance, K=0.25. To compute the influence of the shot–noise on the amplitude and the direction of the dipole, we will assume that each component of the dipole is a Gaussian with zero mean and $\sigma_{sn,x} = \sigma_{sn,y} = \sigma_{sn,z}$. The 1-dimensional shot noise error at 170 h^{-1} Mpc reflects in an $\sim \pm 60 \; \beta_c^{-1} \; km/sec$ amplitude and a $\sim \pm 4°$ directional uncertainties.

3.2.4   The 3D Cluster Dipole

After reconstructing the cluster distribution with the *RSCM* and the *LIRM*, we computed the cluster dipole both in $z-$ and 3D–space. Figure (3.10) shows the amplitude of the peculiar velocity for the standard model, computed using eq. (3.13), as a function of distance. Open dots refer to the z-space dipole while filled symbols represent the reconstructed 3D cluster dipole. We also plotted, for reference, the dipole computed without any Abell/ACO homogenizing scheme (i.e. $\mathcal{W}_{rel} = 1$) in z-space (continuous line). Errorbars represent 1-σ total errors. Our main result is that the asymptotic value of the 3D dipole, D_r, is significantly less than the corresponding z-space one, D_z, as predicted by eq.(3.31). Removing z–space distortions erases the artificial redshift–space clustering, leading to $(D_r - D_z)/D_z \approx -0.23$ or else $(D_z - D_r)/D_r \approx 0.3$. Although the amplitude of the 3D dipole is significantly less than what previously found in cluster-dipole z-space studies (PV91; SVZ91), the qualitative dipole behaviour is similar in z-space and 3D–space: a 'bump' of the velocity amplitude around $50h^{-1}$ Mpc followed by a decrease due to the competing pull of the Great Attractor with the Perseus–Pegasus regions, a secondary increase after a *plateau* and an asymptotic convergence beyond $\sim 170 \; h^{-1}$ Mpc once that the Shapley concentration has entered into the sampled volume. The mass distribution beyond 60 h^{-1} Mpc is responsible for $\sim 30\%$ of the total LG peculiar acceleration. As already noticed from the qualitative analysis of the density field maps, the effect of eliminating the apparent z-space clustering is particularly important in local high density regions, such as the GA area, which is clearly responsible for the significant decrease of the $\sim 50 \; h^{-1}$ Mpc
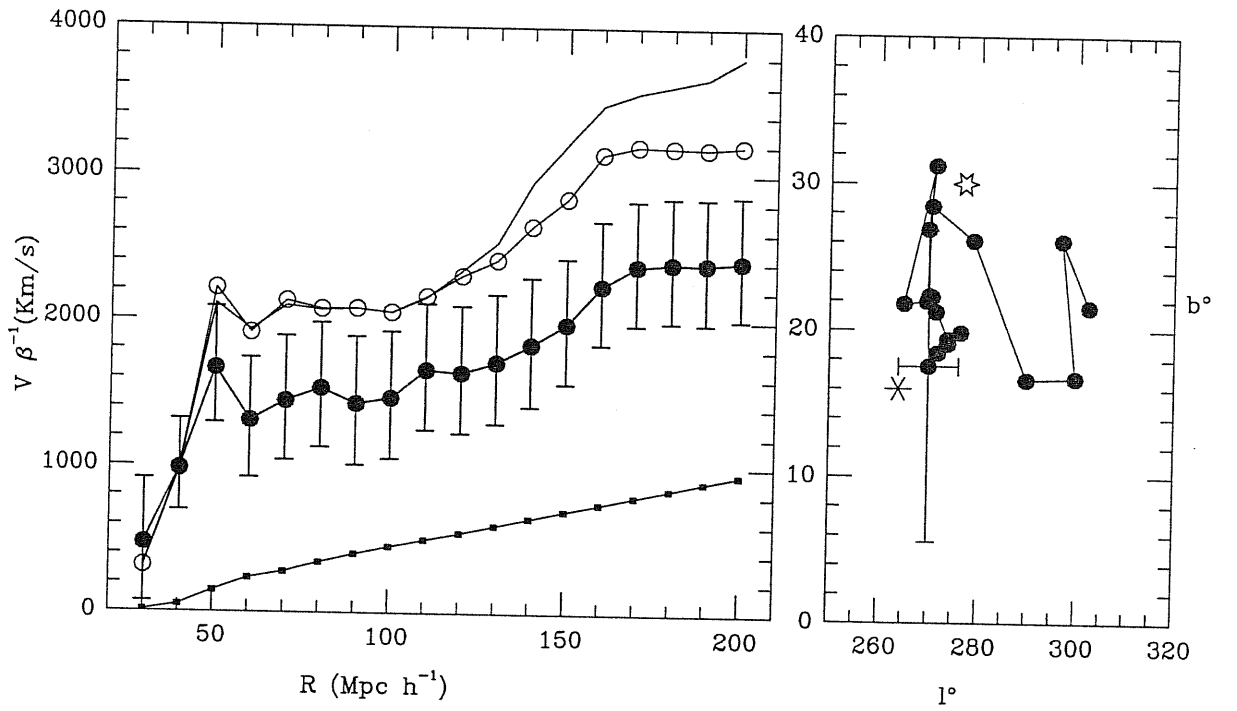
Figure 3.10: Left Panel (a) Dipole amplitude as a function of distance with open symbols representing the reconstructed whole-sky z-space dipole and filled ones the reconstructed 3D dipole. The continuous thin line refers to the z-space dipole without any Abell/ACO homogenizing scheme (i.e. $\mathcal{W}_{rel} = 1$). In arbitrary units, we plot also the 3D-space monopole (small filled squares). Right panel (b) Dipole cumulative direction as a function of the distance. The starred symbol indicates the CMB dipole apex, while the skeletal symbol represents the same but after correcting for a Virgocentric infall component of the LG motion, with an amplitude of 170 km/sec. Errorbars are 1–σ total uncertainty.

bump in the 3D cluster dipole case. In Fig. (3.10a) we also plot, in arbitrary units, the 3D space monopole term, which grows linearly out to the depths sampled which indicates that the dipole convergence at $\sim 170\ h^{-1}$ Mpc is not an artifact of ill sampling.

Figure (3.10b) displays the cumulative direction of the LG velocity. The starred symbol indicates the CMB dipole apex, while the skeletal symbol represents the CMB direction after correcting the LG for a Virgocentric infall of 170 km/sec. Errorbars represent the 1 σ total errors. Note that the relatively large error ($\leq 10°$) in the dipole direction, along b, is due to the uncertainty related to the amplitude of the Virgocentric infall (here we have used $V_{inf} \simeq 170 \pm 100\ km/sec$ from observations). The reconstructed 3D dipole points $\sim 10°$ away from the CMB apex when the Virgo infall is taken into account. No significant differences between the 3D and z-space dipole directions was found.

The Effect of Varying the Mask Model:

It is interesting to investigate the influence of the Mask model, adopted to reconstruct the whole sky z-space cluster distribution, on the reconstructed dipole. Here we compare the *RSCM* reconstructed standard dipole with the two obtained by using the same set of standard parameters but adopting the *RHCM* and *RTCM* mask models. In both cases there is a small increase of the dipole's amplitude, by $\sim 3\% - 4\%$, and the direction points $\sim 4 \pm 4°$ away from the original one (uncertainties refer to the intrinsic errors). We conclude that no significant dependance was found on the Mask choice, which is to be expected since all of them are based on a cloning scheme.

A more relevant comparison is probably between two conceptually different methods. For example between our *RSCM* and the spherical harmonic method (see PV91 for use of this method in the cluster dipole context). In Fig. (3.11) we compare our standard *RSCM* z-reconstructed dipole with that derived using the PV91 method for the same sample and the same set of parameters. In the insert we plot the relative velocity fluctuations, defined as $2 \times (v_{RSCM} - v_{SH})/(v_{RSCM} + v_{SH})$. It is evident that both methods give identical results, except in the inner volume ($\lesssim 50\ h^{-1}$ Mpc) where the number of clusters is extremely small and therefore shot–noise effects are large. This is quite extraordinary given the completely different methods used.

Finally, we explored the effect of using the *MSS* with which the reconstruction scheme adopted in the inner region ($\lesssim 200\ h^{-1}$ Mpc) is extended up to the limiting sample depth ($250\ h^{-1}$ Mpc). With the *MSS* the 3D dipole differs from the standard one only beyond 200 h^{-1} Mpc, where the amplitude monotonically increases (by $\sim 8\%$) and the
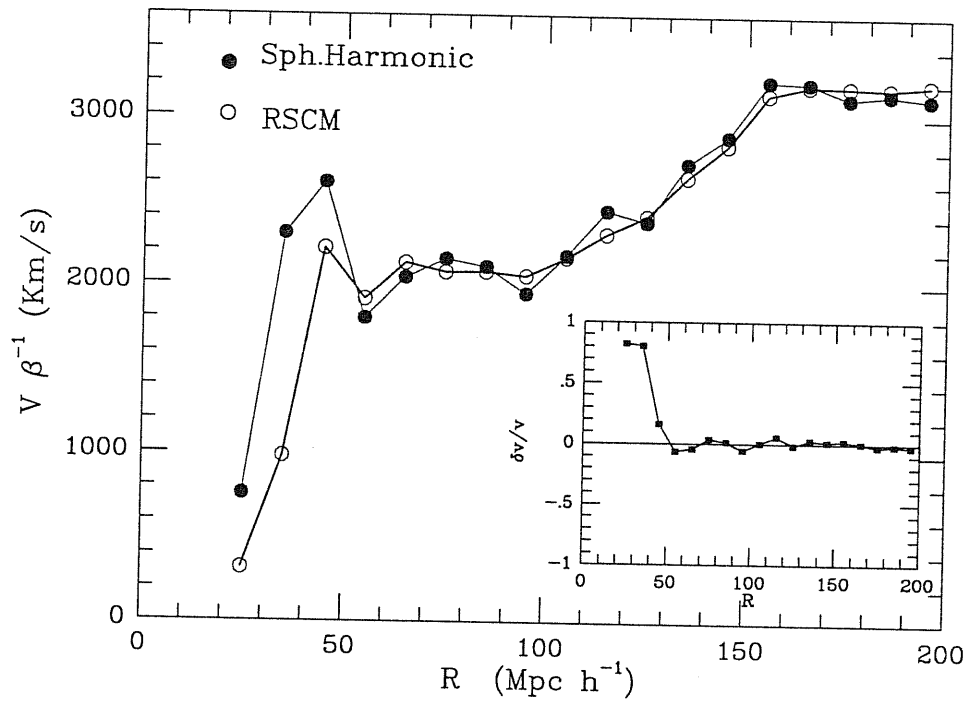
Figure 3.11: Comparison of the z-space dipole derived by using our standard *RSCM* method to reconstruct the whole-sky cluster distribution and that derived using the spherical harmonic method (cf. PV91) for the same sample and the same set of parameters. In the insert we plot the relative velocity fluctuations between the two determinations.

direction systematically drifts towards lower galactic latitudes. Using the *MSS* increases the shot–noise errors in a region where the selection function is significantly smaller than unity. The shot–noise errors are probably responsible for the drift in the dipole direction, while they also enhance the 'Kaiser Effect' which causes the dipole amplitude to increase.

Abell Richness Dependent Effect:

As discussed in section (3.1.1), our Abell/ACO sample includes also richness class $R = 0$ clusters which although suspect of being incomplete, such effect is not apparent within the volume considered in our analysis. However, we have tested, using the above mentioned Spherical Harmonic method, the effect of excluding them from our dipole analysis. Using $R \geq 1$ clusters we reduce our original sample by $\sim 57\%$ but we still find that their dipole has a similar overall shape with that of the $R \geq 0$ case; similar convergence depth (~ 170 h^{-1} Mpc) and CMB-alignment ($\delta\theta_{cmb} \lesssim 20°$) while their amplitude difference is $\delta v \sim -15\%$. We are therefore confident that the possible incompleteness of the $R = 0$ sample does not significantly affect the behaviour and asymptotic value of our cluster dipole and it probably becomes important only at distances considerably larger than the apparent cluster dipole convergence depth (see Postman et al. 1992).

We point out, however, that the $R \geq 1$ dipole increases initially in a much smoother fashion than the corresponding $R \geq 0$ one, which is due to the fact that 10 out of the 12 clusters within ~ 60 h^{-1} Mpc are $R = 0$ clusters and it is these clusters that constitute the large overdensities seen in the *Great Attractor* and Perseus-Pisces regions (see Fig 3.5), and thus responsible for the initial kick of the LG peculiar acceleration.

3.2.5 Cosmology from the Cluster Dipole

Constraints on the Value of β_c:

From the measured asymptotic value of the cluster dipole it is possible to constrain the value of β_c by matching it with the CMB dipole amplitude. An estimate of this parameter can be obtained by assuming that the cluster 3D dipole has converged to its final value at ~ 170 h^{-1} Mpc, in accordance with SVZ91 and PV91. We have, however, to take into account a zero-point offset in the cluster-dipole which originates from the fact that the Abell-like Virgo cluster, due to its proximity and thus low surface brightness, is not included in the Abell/ACO catalogue and therefore its contribution to the cluster dipole has been missed. A possible way to deal with this problem is to merge the cluster dipole with that of

some galaxy sample that trace more densely the local mass distribution (Scaramella et al. 1994). With this approach, however, the offset can be evaluated only assuming an *a priori* value of the cluster–galaxy relative bias, whose value is very uncertain (for a complementary approach see Plionis 1995). Instead we adopt a simpler phenomenological correction by identifying the zero point offset with the LG Virgocentric infall, the velocity of which we take to be $V_{inf} \approx 170 \; km/sec$. We choose this value to be the average of the traditional $\sim 260 \; km/sec$ value with the lower one of Faber & Burstein (1988) [$\sim 85 \; km/sec$].

Comparing the cluster dipole amplitude to the LG peculiar velocity (as inferred by the CMB dipole) via eq. (3.13), we then obtain:

$$\beta_c = 0.21(\pm0.03) \; f(V_{inf}) \, , \qquad f(V_{inf}) \equiv \left[\frac{622 - V_{inf} \cos \delta\vartheta}{622 - 170 \cos \delta\vartheta} \right] \qquad (3.43)$$

where the function $f(V_{inf})$ represents the parameterization of V_{inf} and $\delta\vartheta$ is the angle between the Virgo and CMB dipole directions ($\sim 45°$). If we erroneously did not account for the Virgo infall we would obtain $\beta_c \approx 0.26$ and similarly if the Virgocentric infall velocity is underestimated then a lower value of β_c can be obtained (for example if $V_{inf} = 260 \; km/sec$ then $\beta_c \approx 0.18$). The quoted uncertainty in eq.(3.43) comes from the total dipole scatter, as discussed in section (3.2.3), Although this uncertainty is quite wide, our estimate of the value of β_c is still more than $\sim 2\sigma$ larger that previous estimates based on the z-space cluster distribution (PV91, SVZ91 and SVZ94). Assuming $\Omega_o = 1$ we obtain a cluster bias parameter with respect to the underlying mass distribution of:

$$b_c = 4.8(\pm0.8).$$

According to the linear biasing prescriptions if b_A and b_B are the biasing factors of objects A and B with respect to the matter with $b_A > b_B$, the following relation holds: $b_{AB} \sim b_A/b_B$, where b_{AB} is the biasing factor of objects A with respect to objects B. If the biasing factor of Abell/ACO clusters with respect to IRAS galaxies is $b_{cI} \sim 4.5$ (cf. PD; Jing & Valdarnini 1993) we have that the above b_c value is consistent with a bias parameter of IRAS galaxies with respect to the mass of $b_I \sim 1.1^{+0.7}_{-0.3}$.

It is interesting to note that putting our derived β_c value in eq. (3.31) we get $(D_z - D_r)/D_r \approx 0.28$ which is in good agreement, taking into account the naive use of eq. (3.31), with the value of ~ 0.3 which we obtained directly by our reconstruction algorithm, thus providing an independent, albeit weak, consistency check of our whole procedure.

Although the dipole convergence at $\sim 170 \; h^{-1}$ Mpc is real, since at that distance the cluster monopole is still linearly increasing, it is impossible to prove that the dipole has

converged to its final value. The only way out is to evaluate the amplitude of the external contribution to the observed dipole using statistical methods.

Juskiewicz, Vittorio & Wyse (1990) computed the probability distribution of the peculiar velocity of a generic observer, constrained to be moving with a velocity of 620 km/sec with respect to the CMB, as a function of the sampled volume. From this distribution they computed the expectation value for the estimated LG velocity and its variance (their eq. 8a and 8b). The expectation value at 170 h^{-1} Mpc weakly depends on the cosmological model adopted. We explored a number of possible models ranging from the Standard CDM one to the phenomenological model proposed by Branchini et al. (1994) that resembles a tilted CDM with $n = 0.7$ and to the Peacock & Nicholson (1991) spectrum with more power on large scale. In all these cases the expectation value for the LG velocity, at 170 h^{-1} Mpc coincides with the true one. Also the variance slightly depends on the cosmological model, being larger in correspondence to the Peacock & Nicholson (1991) spectrum ($\sim 158 \, \beta_c^{-1} \, km/sec$ that, to be conservative, will be used as the typical cosmological variance). A probably better, although exaggerated, estimate of the β_c uncertainty can be therefore obtained by adding in quadrature the cosmological variance to the total error. The resulting β_c value is thus constrained into the range

$$\beta_c = 0.21^{+0.09}_{-0.11},$$

assuming a Virgo infall of 170 km/sec. Assuming $\Omega_o = 1$ we obtain a value for the cluster bias parameter

$$b_c = 4.8^{+3.5}_{-1.1}.$$

Constraining Dark Matter Models:

The observed cumulative acceleration acting on the LG can be used to discriminate between different cosmological models. Useful constraints can be imposed by requiring a cosmological model to reproduce the observed cumulative dipole. As outlined by SVZ94, the dipole increases beyond 80 h^{-1} Mpc which is a characteristic feature that can be used as a cosmological test. To quantify the constraint we consider the ratio of the peculiar velocity induced on an observer placed on the origin from fluctuations within a sphere of radius R_1 to that induced from fluctuations within a sphere of radius $R_2 > R_1$, $\chi_{(R_1,R_2)}$. Juskiewicz, Vittorio & Wyse (1990) computed the probability distribution for this ratio as a function of the cosmological model through the power spectrum $P(k)$ [their eq. (10)]. Here we compute the probability density distribution for ratio $\chi_{(R_1,R_2)}$ of the peculiar velocities
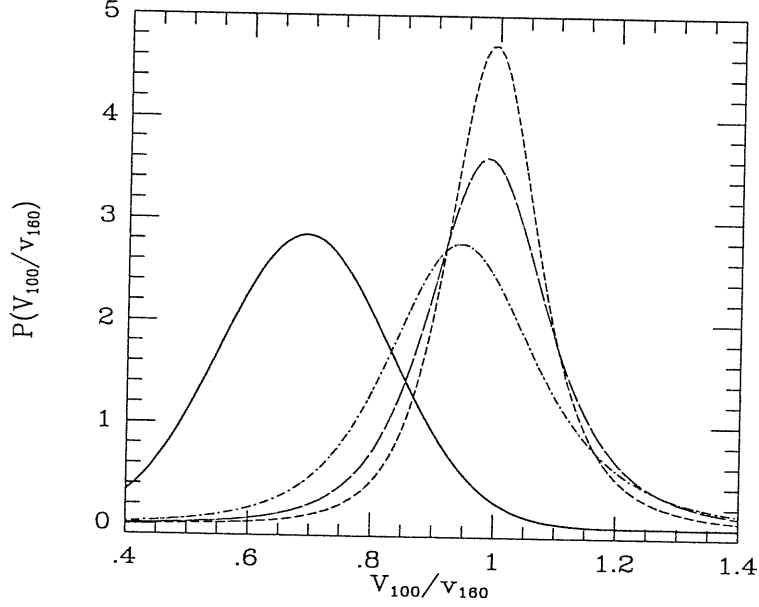
Figure 3.12: The probability density distribution for the dipole amplitude ratio between the two spheres with radii $R_1 = 100$ and $R_2 = 160$ h^{-1} Mpc.

generated within the two spheres of $R_1 = 100$ and $R_2 = 160$ h^{-1} Mpc. Thus we constrain a cosmological model to reproduce the observed ~ 20 % increase of the dipole amplitude in the $[100 - 160] \, h^{-1}$Mpc range. The probability distributions computed for the three cosmological models previously used, are displayed in Fig. (3.12). The continuous line represents the experimental values from the 3D standard dipole in Fig. (3.10a) assuming a Gaussian distributed total errors. Short dashed line represents the CDM standard model, long dashed line refers to the Branchini, Guzzo & Valdarnini (1994) phenomenological model while the Peacock and Nicholson (1991) model is displayed as a dot–dashed line. As already noticed by SVZ94, models with a large scale of coherence are preferred by the observed cluster dipole even when z–space distortions are removed. A detailed analysis, using large Zel'dovich simulations of the cluster distribution, on the constraints put by the cluster dipole on the different Dark Matter models is presented in Tini Brunozzi et al. (1995).

3.3 THE CLUSTER VELOCITY FIELD

In this section we analyse the reconstructed peculiar velocity of the Abell/ACO clusters. Since the errors are small enough, besides a qualitative description we have also performed a number of quantitative analyses and statistical tests that are presented and discussed in what follows.

3.3.1 A Qualitative Analysis

To qualitatively characterize the peculiar velocity field we have plotted the peculiar velocity of the objects versus their galactic coordinates.

In Fig. (3.13a) and (3.13b) (the two upper plots) the line of sight peculiar velocities of the objects averaged over all the models and over all the Montecarlo reconstructions, V_{1D}, are plotted versus the galactic longitude (on the left) and latitude (on the right). The empty region delimited by two vertical lines is the ZoA. While the behaviour of V_{1D} versus galactic latitude is featureless, apart for the presence of objects with high peculiar velocity that are found to reside within high density regions, the peculiar velocities show a typical dipolar structure when plotted versus galactic longitude, as outlined by the superimposed sinusoidal fit. A strong infall is visible at $l \simeq 260°$ while at $l \simeq 80°$ the majority of clusters is receding from the LG: the signature of the large scale bulk flow that we will discuss in section (3.3.4). The plot shows the $R_{sm} = 10\,h^{-1}\mathrm{Mpc}$ case but the same behaviour with an even smaller scatter is found for larger smoothing radii.

From a more cosmographic point of view we show in Fig. (3.14) the cluster peculiar velocity field for two smoothing radii ($R_{sm} = 10$ and $20\ h^{-1}$ Mpc) in a 8000 km/sec wide slice projected onto the supergalactic plane, where most prominent superclusters lie (Hydra-Centaurus, Coma, Shapley, Perseus-Pisces and Ursa-Major).

Open and filled dots refer to inflowing and outflowing objects, respectively while the length of each vector is proportional to the line of sight component of the peculiar velocity in the CMB frame projected onto the supergalactic plane. The small circle at the center represents the typical region spanned by dynamical analyses based on galaxy peculiar velocities (see Burstein 1990 and Dekel 1994 for comprehensive reviews), while the large circle represents the boundaries of the 20000 km/sec sphere.

The most prominent feature is a large coherent motion in the general direction of the CMB dipole towards the Shapley Concentration $(X, Y) = (-13000, +9000)$ km/s. It is interesting to note that as the smoothing radius increases the coherent bulk flow becomes
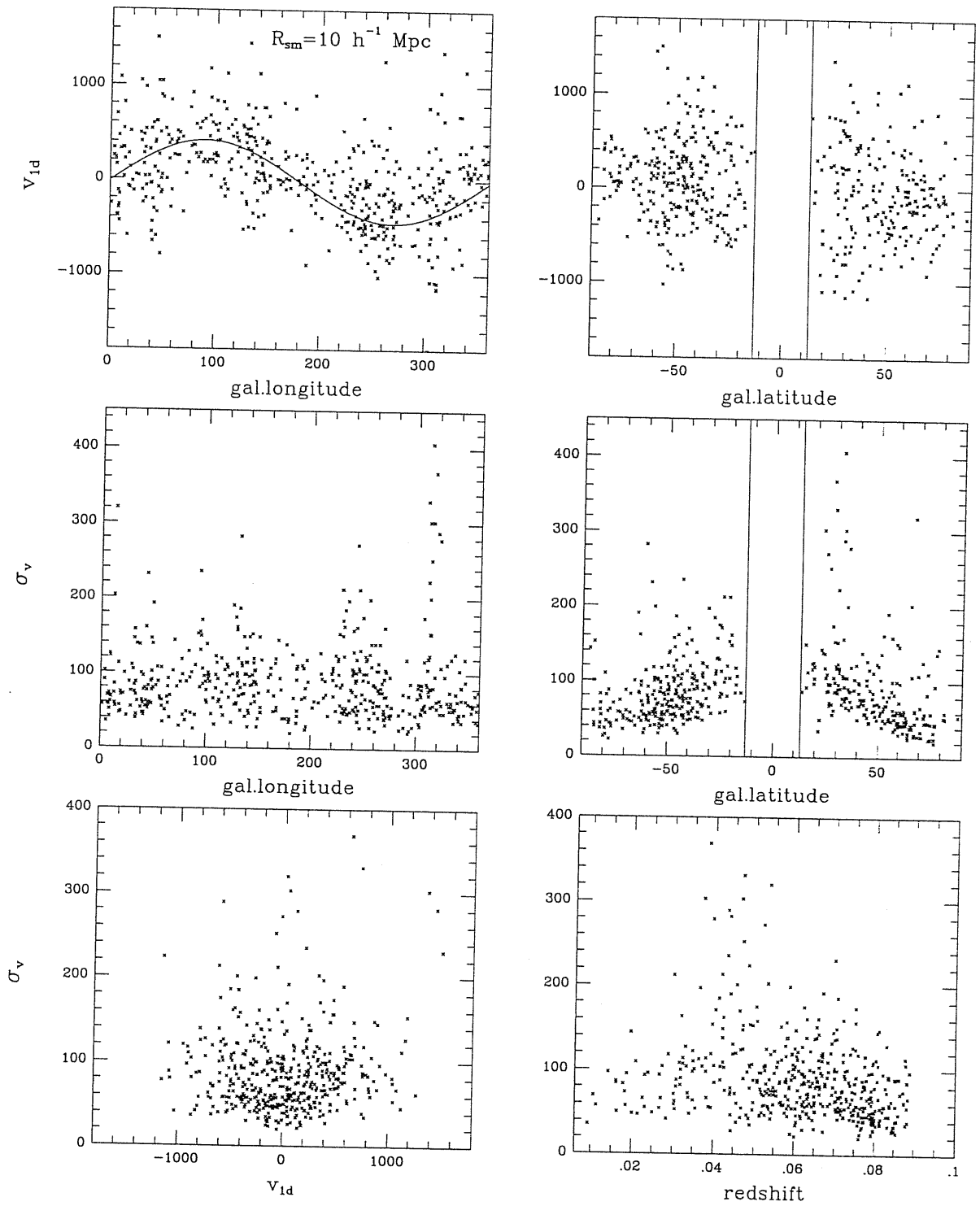
Figure 3.13: Average peculiar velocities and variances for the standard case. Their behaviour with respect to the relevant parameter of the cluster spatial distributions is shown.
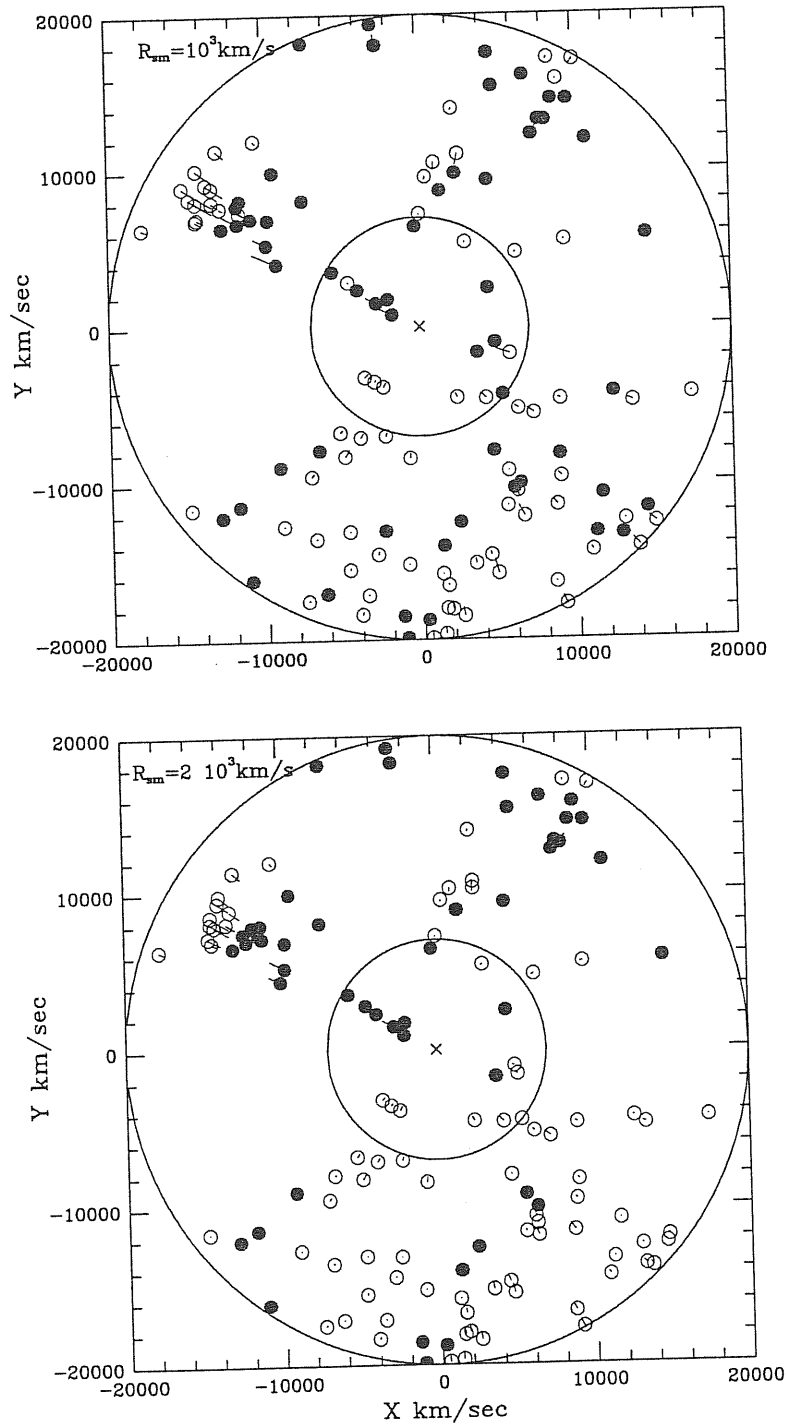
Figure 3.14: The cluster velocity field of a 8000 *km/sec* strip projected onto the super-galactic plane. Open dots are inflowing clusters while filled dots are outflowing ones.

more evident, since the local, small scale, gravitational effects get damped by the smoothing. Besides the extent of the bulk flow, other secondary features have been studied in the smaller scale galaxy analyses, like the presence of back infall in the Great Attractor region (Dressler & Faber 1991, Mattewson et al. 1992), the motions in the Perseus-Pisces region (Willick 1990) and the existence of a 'quiet' region around the Coma cluster (Courteau 1992). In our case, the coarness of the cluster sampling and the relatively large smoothing we have used does not allow to analyse such fine details of the peculiar velocity field. However, we have found, in agreement with galaxy studies, that the reconstructed line of sight peculiar velocities of clusters in the Coma region are consistent with ~ 0 km/sec for all the R_{sm} used. Again in agreement with galaxy studies, we have also found that the large-scale coherent motion does not have a constant amplitude; it is small in the Perseus-Pisces region $(X,Y)= (+8000, -4000)$ km/sec then rises in the Great Attractor zone $(X,Y)= (-4000, +500)$ km/sec while dropping on the backside of the Great Attractor. Furthermore, due to our large volume sampled we are able to identify other important features of the large-scale peculiar velocity field not previously studied. For example, it is evident that the bulk velocity rises again near the Shapley concentration where a large back infall is also apparent. Also in the Ursa-Major and Grus-Indus regions at $(X,Y)=(7000,14000)$ and $(X,Y)=(14000,-15000)$ km/sec, respectively a strong local infall is present (in accordance also with an analysis recently presented by Scaramella 1995 in which the large scale dynamics is probed by solving the Poisson equation where the source term is given by the cluster distribution but in z–space).

3.3.2   Error Analysis and Systematic Effects

We evaluate here the uncertainties of the peculiar velocities of clusters reconstructed using the *RSCM* and the *LIRM*, together with the systematic correlations between the velocity errors and the spatial distribution of clusters.

The Reconstructed Cluster Velocity Field:

As for the LG cluster dipole, we identified three major sources of uncertainty for the peculiar velocities: the intrinsic, the observational and the shot–noise errors. The meaning of the different errors is the same as in the discussion of the LG cluster dipole, the only difference being the definition of the shot–noise error. These errors are considered independent.

- Intrinsic Error (σ_i): The intrinsic error is defined as the variance of the generic cluster velocity based upon 10 different reconstructions of the same 'model'. This error

amounts, on average, to $\sim 100 \ km/sec$.

- Observational Error (σ_o): The observational error on the peculiar velocities is computed as the variance relative to different 'models' explored. Its amplitude $\sigma_o \sim 100 \ km/sec$ is similar to that of σ_i.

- Shot–Noise Error (σ_{sn}): In the case of cluster peculiar velocities it is not possible to use eq. (3.42) for the shot–noise error since the reconstructed cluster distribution is not symmetric about the generic cluster. To quantify the shot–noise effect we use the rough assumption that clusters are uncorrelated samplers of the velocity field. In this case the shot–noise for the peculiar velocity of a source at the position x relative to the LG is

$$\sigma_{sn}(\mathbf{x}) = \sigma_{sn}(\hat{\mathbf{x}} \cdot (\mathbf{v}(\mathbf{x}) - \mathbf{v}_{LG})) =$$
$$\frac{\beta_c}{4\pi n_c} \times \left(\sum_i \left(\frac{M_i}{M_C} \right)^2 \tilde{w}_i^2 \left\{ \hat{\mathbf{x}} \cdot \left[W(|\mathbf{x}_i - \mathbf{x}|) \frac{\mathbf{x}_i - \mathbf{x}}{|\mathbf{x}_i - \mathbf{x}|^3} - W(|\mathbf{x}_i|) \frac{\mathbf{x}_i}{|\mathbf{x}_i|^3} \right] \right\}^2 \right)^{1/2}. \quad (3.44)$$

The amplitude of this shot–noise error is nearly independent on x and its average value is $\sim 80 \ km/sec$, ranging from ~ 20 to $\sim 200 \ km/sec$. Eq. (3.44) overestimates the shot–noise error since, as we have discussed in section (3.2.2), theoretical arguments and observational evidences suggest that luminous objects are not random samplers but tracers of the underlying density field.

The total uncertainty of the cluster peculiar velocities is computed by adding σ_{sn}, σ_o and σ_i in quadrature. However, since our σ_{sn}, which is slightly smaller than σ_o and σ_i, overestimates the true shot–noise error we will not consider its contribution in what follows. The total error $\sigma_T^2 = \sigma_o^2 + \sigma_i^2$ represents therefore a reasonably close estimate of the actual reconstructed velocity variance. It turned out that 50 % of the clusters have a total velocity variance $< 100 \ km/sec.$ and that only 20% of the clusters have $\sigma_T > 160 \ km/sec.$

Besides a simple volume–averaged evaluation of the errors, it is also interesting to look for systematic effects by exploring the spatial distribution of the errors. The two central plots in Fig. (3.14) display the total errors (σ_V in the plots) versus galactic longitude (left panel) and latitude (right panel). There is an evident correlation between σ_T and the galactic latitude b as already found in section (3.1.3). This behavior depends on the fact that the number of real clusters is an increasing function of the galactic latitude and so is the reconstructed velocity. As displayed in the two plots on the top of the figure, no strong correlation is found either between σ_T and V_{1D} or between σ_T and the redshift of the objects.

r_{max}	R_{sm}	$|\mathbf{v}|_{LG}$ (km/sec)	l	b	$\tilde{\epsilon} \times 10^2$	$\delta\theta_{cmb}$	$\chi^2/d.f.$
100	5	265±100	284° ± 36°	30° ± 22°	−1.1 ± 0.9	6°	44/38
	10	**256± 95**	**283°± 39°**	**31°± 24°**	**-1.2±0.9**	**5°**	**42/38**
	20	302±80	280° ± 23°	22° ± 16°	−0.2 ± 0.9	9°	27/38
150	5	520±90	282° ± 15°	28° ± 10°	−1 ± 0.6	5°	217/115
	10	**470± 90**	**276°± 16°**	**28°± 11°**	**-0.7± 0.6**	**2°**	**202/115**
	20	440±65	277° ± 12°	28° ± 8°	−1.6 ± 0.5	2°	103/115
180	5	670±70	280° ± 9°	18° ± 6°	−0.2 ± 0.3	13°	445/167
	10	**635± 70**	**277°± 9°**	**18°± 6°**	**0±0.3**	**12°**	**337/167**
	20	592±55	276° ± 7°	19° ± 5°	−0.4 ± 0.3	11°	194/167

Table 3.5: Local Group motion with respect to the cluster frame within distance r_{max} and for 3 different smoothing radii (both in h^{-1} Mpc).

Finally, we found that the total uncertainties σ_T correlates with the local density: $\sigma_T \propto n_g^{0.8}$ where n_g is the number of neighbours within 1500 km/sec around the generic cluster.

3.3.3   The Local Group Velocity with Respect to the Clusters

Similarly to LP we compute the LG peculiar velocity with respect to the cluster frame, $\mathbf{v}_{LG}$, by using a χ^2-minimization of the real cluster peculiar velocities:

$$\chi^2 = \sum_{i=1}^{N} \left\{ \frac{[cz_i - d_i(1 + \tilde{\epsilon})] - \mathbf{v}_{LG} \cdot \hat{\mathbf{x}}_i}{\sigma_{T,i}} \right\}^2 , \qquad (3.45)$$

where d_i is the reconstructed 3-D cluster distance in the LG frame, $\hat{\mathbf{x}}_i$ the unit position vector and $\sigma_{T,i}$ is the total error computed by adding in quadrature $\sigma_{I,i}$, $\sigma_{o,i}$ and $\sigma_z(= 300$ $km/sec)$ which represents an uncertainty in cz_i. The quantities to be fitted by eq. (3.45) are the LG peculiar velocity vector, $\mathbf{v}_{LG}$, and the fractional error, $\tilde{\epsilon}$, in d_i.

In Table 3.5 we present the solution of eq. (3.45) for the $R_{sm} = 5$, 10 and 20 h^{-1}Mpc cases and for three limiting radii of the volume used for $\beta_c = 0.21$ (boldface quantities refer to our standard case). It is important to note that out to the limiting depth of the LP sample ($r_{LP} \sim 15000$ km/sec) our estimate of $|\mathbf{v}|_{LG}$ has not reached its asymptotic value. In fact we find $|\mathbf{v}|_{LG}(r_{LP}) \approx 470 \pm 90$ km/sec with a misalignment angle with respect to the CMB dipole apex of only $\delta\theta_{cmb} \approx 5°$ while its asymptotic value ($\approx 635 \pm 70$ km/sec) is reached at ~ 18000 km/sec. Our result, which is expected in the GI picture, is in strong
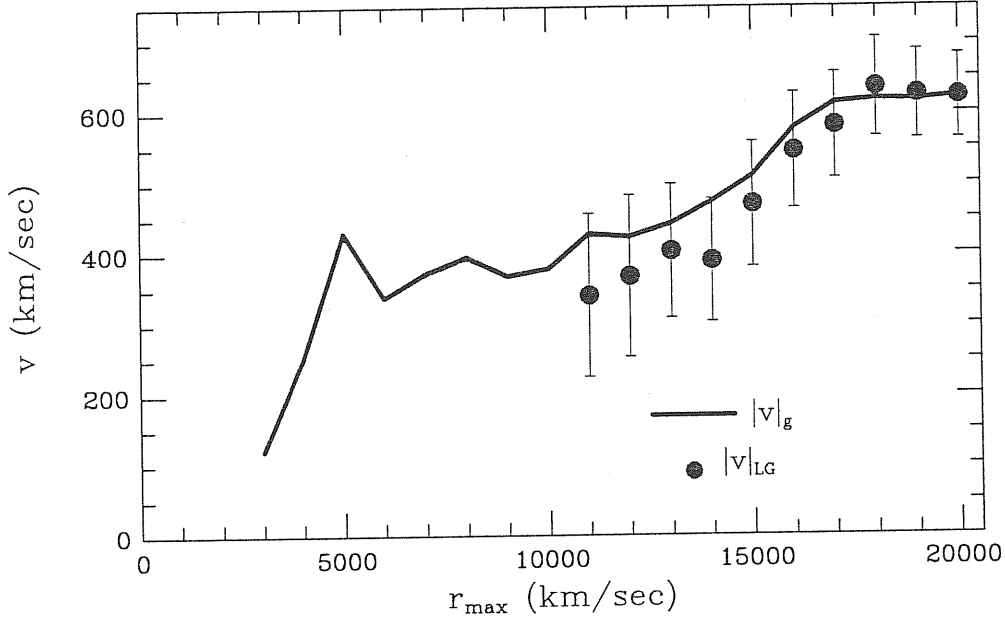
Figure 3.15: Comparison between the LG peculiar acceleration, $|v|_g$, as derived by the cluster dipole and the LG peculiar velocity, $|v|_{LG}$, for the $R_{sm} = 10^3$ km/sec case.

disagreement with LP who found $|v|_{LG}(r_{LP}) = 561 \pm 284$ km/sec but with $\delta\theta_{cmb} \approx 80°$. Figure (3.15) shows $|v|_{LG}$ computed within spheres of increasing radius together with the analogous quantity, $|v|_g$, obtained from the gravitational acceleration acting on the LG, after including a contribution of a ~ 170 km/sec Virgocentric infall and for (error bars indicate 1-σ total uncertainties). There is a good matching between the two quantities while their misalignment with the CMB dipole direction is $\lesssim 14°$ at the convergence depth. We stress that the v_{LG}-v_g matching constitutes a non–trivial demanding test of our reconstruction procedure. In fact v_g is estimated from the cluster dipole at the position of the LG while v_{LG}, is a nonlocal quantity in the sense that it requires knowledge of all the sample cluster peculiar velocities which are the outcome of our dynamical reconstruction algorithm. Furthermore, contrary to the $|v|_g$ case where we have a relative freedom to adjust its value according to what we believe is the Virgocentric infall velocity (see eq. 3.43), the $|v|_{LG}$ determination is independent of this 'zero point' uncertainty.

As discussed before there are different factors that could affect the estimate of v_{LG}. Increasing R_{sm} in the range [5–30] h^{-1}Mpc causes a weak but systematic decrease of $|v|_{LG}$ following the empirical law $|v|_{LG} \propto R_{sm}^{-\alpha}$ with $\alpha = 0.12 \pm 0.02$, shown in figure (3.16). Furthermore, the value of $|v|_{LG}$ scales linearly with β_c. Therefore we can write:

$$|v|_{LG} \approx 635 \; (\pm 70) \; \left(\frac{R_{sm}}{10^3 \; km/sec}\right)^{-\alpha} \frac{\beta_c}{0.21} \; km/sec \qquad (3.46)$$
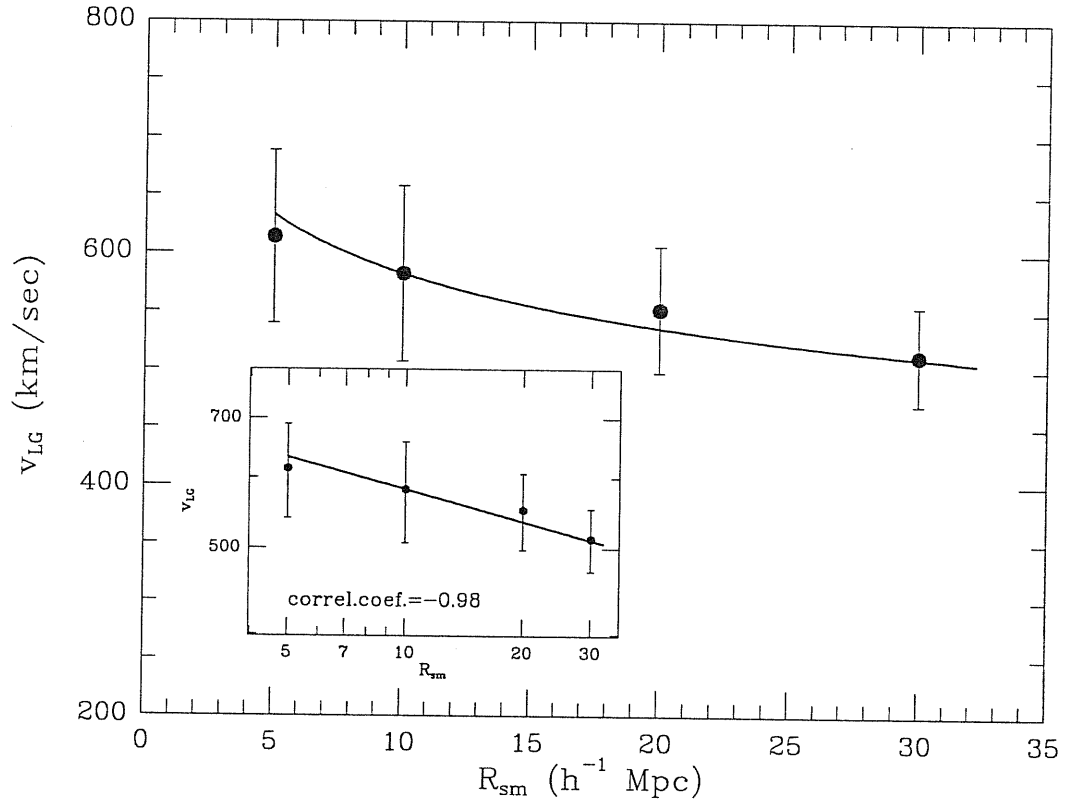
Figure 3.16: LG peculiar acceleration, v_{LG}, obtained by minimizing the velocity residuals versus smoothing radius R_{sm}. The points represent the V_{LG} averaged over all the models and the Montecarlo realization. Errorbars are 1-σ total uncertainties. The insert shows the same plot in logarithmic coordinates. The thick line is the best fit model, $v_{LG} \propto R_{sm}^{0.12}$

To obtain consistency with the CMB dipole, the peculiar acceleration, $|\mathbf{v}|_g$, induced on the LG of galaxies by the Abell/ACO cluster+Virgo distribution [which gives eq. (3.43)] and the LG velocity, $|\mathbf{v}|_{LG}$, with respect to the cluster frame [eq. (3.46)] while keeping in mind that $R_{sm} \gtrsim 0.3 \times 10^3$ km/sec (imposed by the expected strong non-linear effects below this radius) and that $V_{in} \gtrsim 100$ km/sec, we require:

$$0.18 \lesssim \beta_c \lesssim 0.23 \qquad (3.47)$$

(the lower limit is imposed by $R_{sm} \sim 0.3 \times 10^3$ km/sec, which then gives $V_{in} \approx 270$ km/sec and the upper limit by $R_{sm} \sim 2 \times 10^3$ km/sec, roughly corresponding to the cluster correlation length, which gives $V_{in} \approx 120$ km/sec). Eq. (3.47) implies that for $\Omega_o = 1$ the cluster biasing factor should satisfy $5.5 \lesssim b_c \lesssim 4.4$. A word of caution is due, however. This analysis is based on only one point in space (the LG) and it has been shown (Tini Brunozzi et al. 1995) that cosmic variance and sparse sampling of the density field by the clusters can introduce a quite large scatter in the estimated β_c parameter. In section (3.2.6) we will try to set more stringent constraints on β_c by correlating the reconstructed peculiar velocities with the observed ones.

3.3.4 Statistical Analysis of the Cluster Velocity Field

In what follows we will perform a more quantitative analysis of the velocity field traced by galaxy clusters. The small number of objects available (we limit our analysis within the central 20000 km/sec.) force the order of the statistic used to be low. We will compute the probability velocity function, the bulk velocity and the two point velocity correlation function of the reconstructed velocity field.

The Velocity Probability Function:

The 3D velocity probability function, $P(|v_{3D}|)$ is the probability of observing a peculiar velocity having an absolute value in the range $[|\mathbf{v}| \; ; \; |\mathbf{v}| + d|\mathbf{v}|]$ as well as the analogous distribution function for the line of sight peculiar velocity $v_{1d} = \mathbf{v} \cdot \hat{\mathbf{x}}$, $P(v_{1d})$. We only consider the reconstructed real cluster peculiar velocities (i.e. we do not consider synthetic clusters in the present–analysis, although, as we verified, including them does not significantly alter the final results). Three cases, corresponding to three different choices for the smoothing radius ($R_{sm} = 10, \; 20$ and $30 \, h^{-1} Mpc$) have been explored. The results are displayed in Fig. (3.17).

Since our iterative scheme is based on linear theory, each component of the reconstructed peculiar velocity should be Gaussian and the magnitude of the peculiar velocity
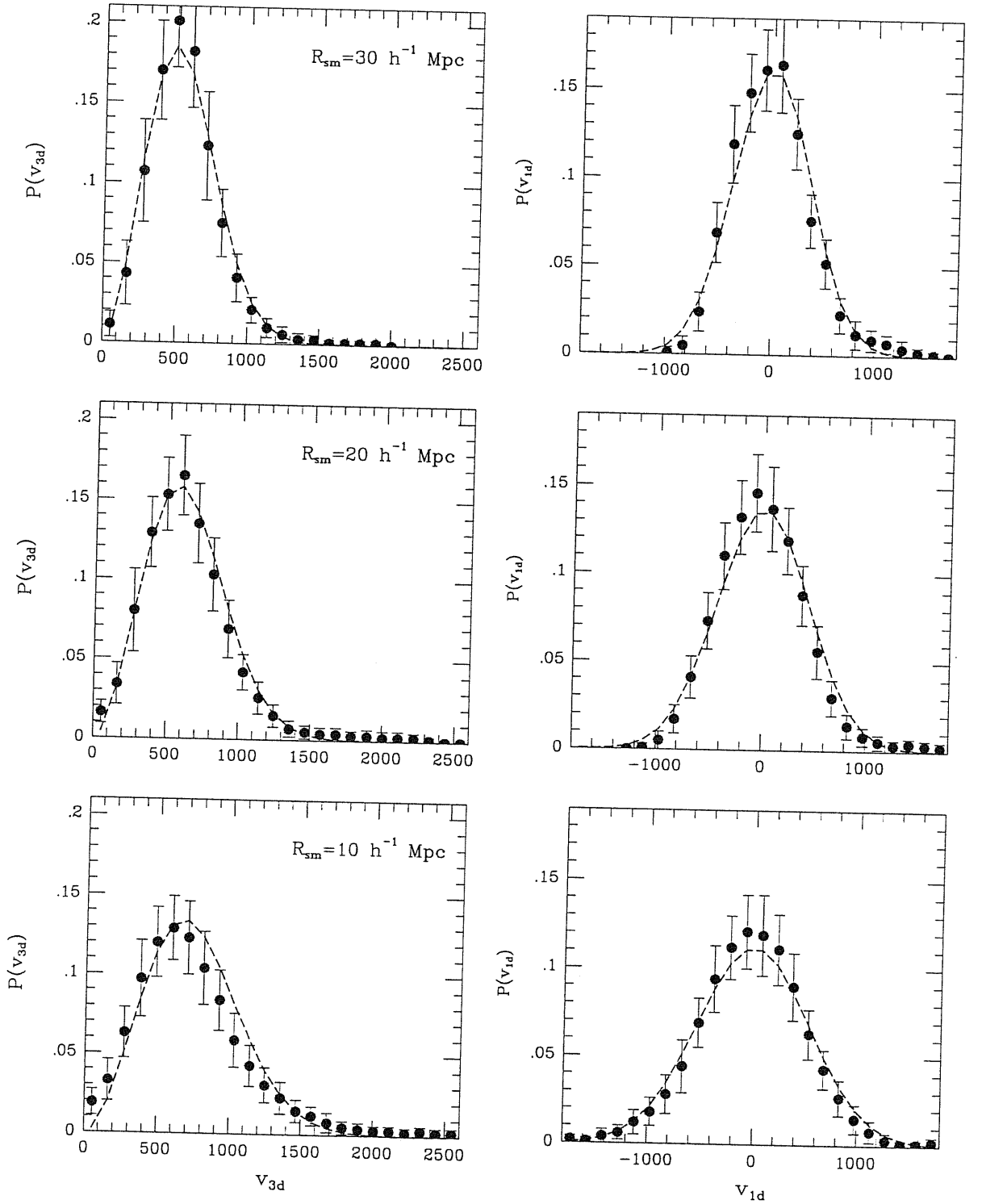
Figure 3.17: Differential velocity probability functions for the absolute value (v_{3d}) and the line of sight component (v_{1d}) of the cluster peculiar velocities. Three cases corresponding to three different choices for the smoothing length are shown. Errors represent 1-σ total uncertainties. The Maxwellian and Gaussian fits are shown as dashed lines.

will therefore possess a Maxwellian distribution. The results shown in Fig. (3.15) confirm this prediction and therefore constitute a check of consistency for the method. Using different smoothing radii results in a modification of shape of the probability distributions that, however, maintain their Maxwellian and Gaussian nature as confirmed by a goodness of fit analysis. Heavy smoothing peculiar velocities reduces the extent of the large velocity tail in the distributions, and, more generally decreases the magnitude of the peculiar velocities: their average values turned out to be $\langle|\mathbf{v}|\rangle = 756 \pm 405$, 640 ± 285 and 548 ± 219 for $R_{sm} = 10$, 20 and $30 \, h^{-1}\mathrm{Mpc}$, respectively.

A better way to check the consistency of the reconstruction procedure would be that of comparing the reconstructed velocity distribution with the observed ones. The best statistic to use in this case is the 1D cumulative peculiar velocity distribution function $P(> v_{1d})$, i.e. the probability of having a line of sight component of the peculiar velocity $> |v_{1d}|$, since it has a signal much more stable than that of the differential distribution function. However even the $P(> v_{1d})$ would not be very effective since the number of Abell/ACO clusters for which the measured peculiar velocity is available is very small. Moreover, comparing the true and the reconstructed peculiar velocities requires to select only isolated clusters for which non–linear effects are negligible, further reducing the size of the sample. Using such a small sample (that contains few Abell/ACO clusters) leads to large errors for the experimental $P(> v_{1d})$ making this test not useful.

The Bulk Velocity:

Given a selection function describing the observed region $\Psi(\mathbf{x})$, the bulk velocity is defined as the velocity of its center of mass $\mathbf{x}_o$. Its expected value is given by the integral of the peculiar velocities $\mathbf{v}(\mathbf{x})$ over the volume descibed by $\Psi(\mathbf{x})$:

$$\mathbf{V}_{3D}^{bulk}(\mathbf{x}_o) = \int \Psi(\mathbf{x}) \, \mathbf{v}(\mathbf{x}) \, \mathrm{d}\mathbf{x} = \int \nu_k e^{i\mathbf{kx}_o} \tilde{W}(k) \mathrm{d}\mathbf{k}, \qquad (3.48)$$

where the second relationship follows from the continuity equation that the generic k–mode in k–space and is

$$\mathbf{v}_k = -iH_o a f \frac{\mathbf{k}}{k^2} \delta_k = \hat{\mathbf{k}} \nu_k. \qquad (3.49)$$

For an isotropic $\Psi(\mathbf{x})$ the scalar window function $\tilde{W}(k)$ is simply the Fourier transform of $\Psi(\mathbf{x})$

$$\tilde{W}(k) = \int \Psi(\mathbf{x}) \, e^{i\mathbf{kx}} \, \mathrm{d}\mathbf{x}. \qquad (3.50)$$

In a homogeneous and isotropic universe the mean value of $\mathbf{V}_{3D}^{bulk}(\mathbf{x}_o)$ has to be zero, while its variance can be obtained from eq. (3.48) and (3.49):

$$\sigma_v^2 = \frac{(H_o f)^2}{2\pi^2} \int P(k) \tilde{W}(k)^2 \, dk. \tag{3.51}$$

If the density field is Gaussian so will be each component of $\mathbf{v}$ and thus $|\mathbf{v}|$ will have a Maxwellian distribution. As a consequence there will be a 90% probability of finding a measured bulk velocity within the range

$$\frac{\sigma_v}{3} \leq |\mathbf{V}_{3D}^{bulk}| \leq 1.6\sigma_v. \tag{3.52}$$

Because eq. (3.51) is weighted towards lower k than the analogous mass variance, which has an extra k^2 factor, bulk flows are potentially useful for probing large scales, and thus the linear regime of $P(k)$, beyond those which we can probe using the spatial clustering properties of galaxies. In general one deals with density and velocity fields smoothed over some suitable scale R_{sm} to remove unwanted non–linear effects. The smoothing is described, in the k-space, by a scalar window function $W'(k, R_{sm})$ and can be taken into account by simply substituting $\tilde{W}(k)$ with $\tilde{W}(k, R_{sm}) = W'(k, R_{sm})\tilde{W}(k)$ in the previous formulae.

All we can measure is the velocity of a discrete set of luminous objects (galaxies, clusters etc.) which we hope that trace the underlying velocity field without biases. In the discrete case eq. (3.48) modifies as

$$\mathbf{V}_{3D}^{bulk} = \frac{\sum_i \mathbf{v}_i w_i}{\sum_i w_i}, \tag{3.53}$$

where $\mathbf{v}_i$ is the smoothed velocity of the ith object, w_i is a weight that account for its mass (or for its spatial extension) and for selection effects in the sampling procedure.

Another way of defining the bulk flow is as the residual velocity of the whole cluster frame. Therefore an alternative estimator of the bulk velocity, which utilizes only the line of sight component of the real cluster peculiar velocities, which was also used by LP, is:

$$\mathbf{V}_{1D}^{bulk}(r) = \mathbf{C} - \mathbf{v}_{LG}(r) \tag{3.54}$$

where $\mathbf{C}$ is the CMB dipole vector and $\mathbf{v}_{LG}(r)$ is given by minimizing eq. (3.45).

Juszkievicz, Vittorio & Wyse (1990) have shown that $\mathbf{V}_{1D}^{bulk}$ and $\mathbf{V}_{3D}^{bulk}(r)$ does not coincide a priori and the following relationship holds:

$$\mathbf{V}_{1D}^{bulk}(r) = \mathbf{V}_{3D}^{bulk}(r) - \frac{H_o \Omega_o^{0.6}}{3} \mathbf{x}_{cm}, \tag{3.55}$$

where $\mathbf{x}_{cm}$ is the position of the center of mass of the sample. However, we have verified from our sample that for any meaningful choice of $H_{\circ}$ and $\Omega_{\circ}$, $\mathbf{V}_{1D}^{bulk}(r) \simeq \mathbf{V}_{3D}^{bulk}(r)$ since the center of mass of our real+synthetic cluster sample is very close to coordinate center (i.e. to the LG position). In the subsequent analyses both the estimators $\mathbf{V}_{1D}^{bulk}(r)$ and $\mathbf{V}_{3D}^{bulk}(r)$ have been employed.

To actually measure the bulk velocity, however, three major problems need to be faced.

- The fact that several different choices for the weighting scheme are possible. The simplest one is the number weighting, where $w_i = constant$. Its major drawback is that it ignores the effect of the errors in the peculiar velocity measurements. A second possibility is the inverse variance weighting, in which the weight is proportional to the inverse of the uncertainty in the measured velocity, giving more weight to the more reliable data. Dekel et al. (1990) have shown that this weighting scheme suffers from the so called 'sampling gradient bias', overestimating the contribution of the well sampled regions over those poorly sampled. To overcome this problem Dekel et al. (1990) proposed to multiply the inverse variance weighting by the distance of the ith object from its fourth nearest neighbour, giving more weight to isolated objects (see however Tormen et al. (1993) for problems associated to this scheme). In our case the set of reconstructed clusters ideally provides us with a perfectly sampled distribution for which the uncertainty over the reconstructed velocity is roughly the same for each object. This means that the inverse variance scheme reduces to a simple number weighting which we therefore decided to adopt. We have also implemented the mass weighting scheme in which $w_i \propto m_i$, where m_i the mass of the cluster assumed to be proportional to its number of Abell listed galaxies and we found very similar results to those obtained with the number weighting scheme.

- A second concern in handling observational data is that very often the volume sampled does not have sharp edges (e.g. in the case of a magnitude limited sample) and thus $\Psi(\mathbf{x})$ represents the probability of picking up an object at the position $\mathbf{x}$. As shown by Kaiser (1988) the use of non volume limited surveys coupled with the implementation of an inverse variance weighting scheme causes the window $\Psi(\mathbf{x})$ to shrink in a way difficult to model analytically. In our case this is not a problem since we deal with a nearly volume limited cluster sample and we use the number weighting scheme.

- Similarly, no significant problem arise, in our case, from observing only the line of sight

velocity component. As shown by Szalay (1988) and by Regös & Szalay (1989), the bulk flow of a galaxy distribution with peculiar velocities, can be defined through a least square fit of

$$(V_{3D}^{bulk})^\alpha = \frac{(M^{-1})^{\alpha\beta} \sum_i u_i^\beta w_i}{\sum_i w_i}, \tag{3.56}$$

where the sum over repeated indices is understood and $u_i^\alpha = (\mathbf{v}_i \cdot \hat{\mathbf{x}}_i)\hat{\mathbf{x}}_i^\alpha$ is the $\alpha = (1,2,3)$ component of the radial peculiar velocity. The weighted projection matrix

$$M^{\alpha\beta} = \frac{\sum_i w_i \hat{r}_i^\alpha \hat{r}_i^\beta}{\sum_i w_i} \tag{3.57}$$

takes into account the geometry of the sample. Even in the case of isotropic sampling, the use of line of sight peculiar velocities has a nonegligible effect, overestimating the expected r.m.s. velocity up to 25 %. This effect is further enhanced in the case of anisotropic sampling. This observational bias has a twofold effect: it modifies the bulk flow amplitude and causes a spurious alignment between the expected bulk velocity and the dipole moment of the objects' distribution. However, this bias does not affect our bulk flow estimate since the reconstruction procedure provides us with the full 3D velocity field.

Besides the previous theoretical arguments we obtained direct evidence of the robustness of our dipole estimate by noticing that both the independent estimators $\mathbf{V}_{3D}$ and $\mathbf{V}_{1D}$ give very similar results. Further evidence that our measurement is reliable has been obtained as follows: we computed the smoothed peculiar velocity generated by the cluster distribution on a $10 \times 10 \times 10$ grid with cell size of 20 h^{-1}Mpc and we verified that the bulk velocity computed from the velocity at the gridpoints is similar to that one computed using peculiar velocities at the cluster position.

To estimate the reconstructed cluster bulk velocity and the related errors we used the following procedure. We consider a single reconstruction and, by applying eq. (3.53) and eq. (3.54), we measure the cumulative bulk velocity within spheres of increasing radius around the LG. This procedure is repeated for each of the 10 reconstructions performed for one given 'model'. The 'model' bulk velocity is then computed by averaging over the different realizations, together with its intrinsic dispersion σ_i. The mean bulk flow is then obtained as an average among the 'model' bulk flows, which also allows us to compute the observational variance, σ_o. Finally, the total uncertainty in the bulk flow, σ_t, has been obtained by adding σ_i and σ_o in quadrature. Note that the amplitude of cluster bulk velocity has been fixed using $\beta_c = 0.21$, consistent with the cluster dipole analysis. It is also worth mentioning that

r_{max}/r_{eff}	R_{sm}	V_{1D}^{bulk} (km/sec)	l	b	$\delta\theta_{cmb}$
100/75	5	358	272°	30°	5°
	10	366	273°	29°	3°
	20	324	273°	37°	8°
150/113	5	113	248°	37°	25°
	10	152	280°	36°	7°
	20	182	277°	34°	4°

Table 3.6: Residual bulk motion of cluster frame within distance r.

our bulk flow estimate is not sensitive to the smoothing adopted: varying R_{sm} in the range $[1000\text{-}3000]km/s$ produces a variation of the bulk flow amplitude of $< 5\%$.

In Table (3.6) we present the average bulk flow estimated using eq. (3.54) as a function of sample limiting depth. Note that the bulk flow at r_{LP} has an amplitude of ~ 150 km/sec, much smaller than that found by LP (~ 700 km/sec) and thus in comfortable agreement with currently accepted cosmological models.

In Fig. (3.18) we plot, for $R_{sm} = 10^3$ km/sec, both estimators $\mathbf{V}_{3D}^{bulk}$ and $\mathbf{V}_{1D}^{bulk}$ as filled dots and starred symbols respectively, but now as a function of the *effective* depth ($r_{eff} \approx 3/4r_{max}$). Note that for the V_{1D} estimator we have used a limiting depth $r \geq 10000$ km/sec in order to have sufficient data for the χ^2 minimization to be stable. Error bars represent 1-σ total uncertainties. Although the two estimators are based on different velocities (V_{3D} is based on the full 3D velocities; while V_{1D} only on the line-of-sight components) and different total numbers of clusters (V_{3D} is based on real+synthetic objects while V_{1D} only on real ones) they provide a consistent estimate of the bulk velocity. We also plot as open dots the bulk velocity obtained by the *POTENT* reconstruction of the velocity field traced by Mark III galaxies (Dekel 1994) and as starred symbols the recent da Costa et al. (1995) bulk velocity. At the region where both the galaxy and cluster bulk velocity estimates overlap (at $r_{eff} \sim 40 - 60$ h^{-1}Mpc), they appear to be in very good agreement with each other.

The Velocity Correlation Function:

A full statistical description of the linear peculiar velocity field is given by the velocity correlation tensor, which is defined as

$$\Psi_{ij}(\mathbf{x}_1, \mathbf{x}_2) = \langle v_i(\mathbf{x}_1)v_j(\mathbf{x}_2)\rangle. \qquad (3.58)$$
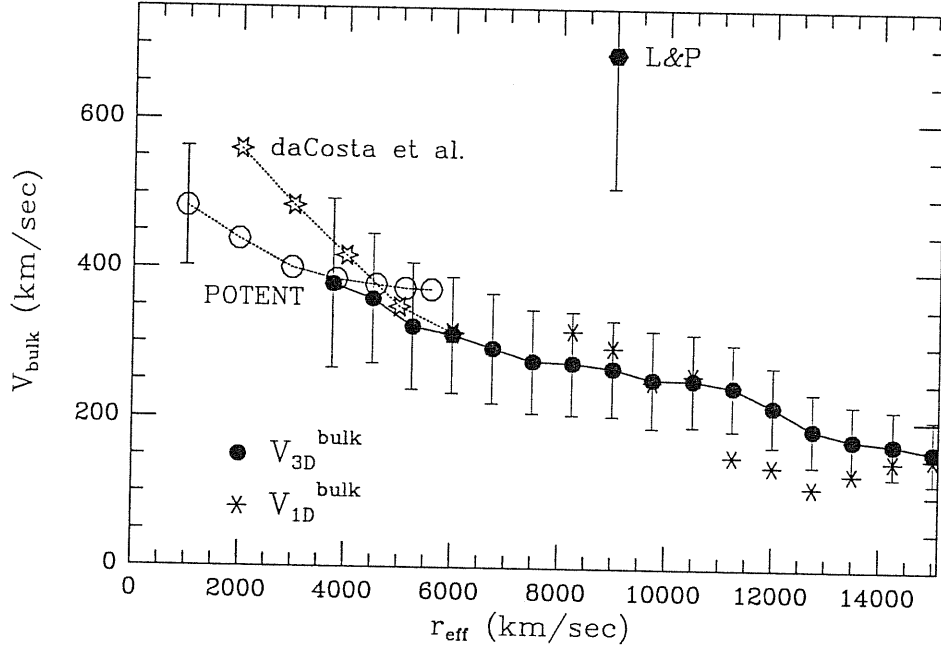
Figure 3.18: The cluster bulk velocity as estimated by the two methods described in the text together with the galaxy based *POTENT* and da Costa et al. (1995) values.

Here x_1 and x_2 are the position vectors of two objects having peculiar velocities $v(x_1)$ and $v(x_2)$ respectively (see, e.g., Górski 1988; Górski et al. 1989) and the average is over the sampled volume. In practice what one estimates is the scalar velocity correlation function $\xi_v(r)$ which is defined as the trace of the velocity correlation tensor,

$$\xi_v = \sum_i \Psi_{ii} = \langle v(x_1) \cdot v(x_2) \rangle. \tag{3.59}$$

One can show that this quantity is related to the power spectrum $P(k)$ via the relationship

$$\xi_v = \frac{(H_o f)^2}{2\pi^2} \int_o^\infty P(k) \frac{\sin(kr)}{kr} dk. \tag{3.60}$$

According to its definition, ξ_v is a measure of the coherence of the velocity field: if at some scale a bulk flow coherence dominates the velocity field, ξ_v will be positive, while both infall and outflow velocities result in negative ξ_v values.

We estimated the scalar velocity correlation function of our reconstructed cluster velocity field, considering only real clusters within a $200\,h^{-1}$Mpc sphere about the LG. The results are shown in Fig. (3.19) for two different smoothing radii. Errorbars represent $1-\sigma$ total uncertainties. The velocity correlation function has a monotonic decreasing behaviour,
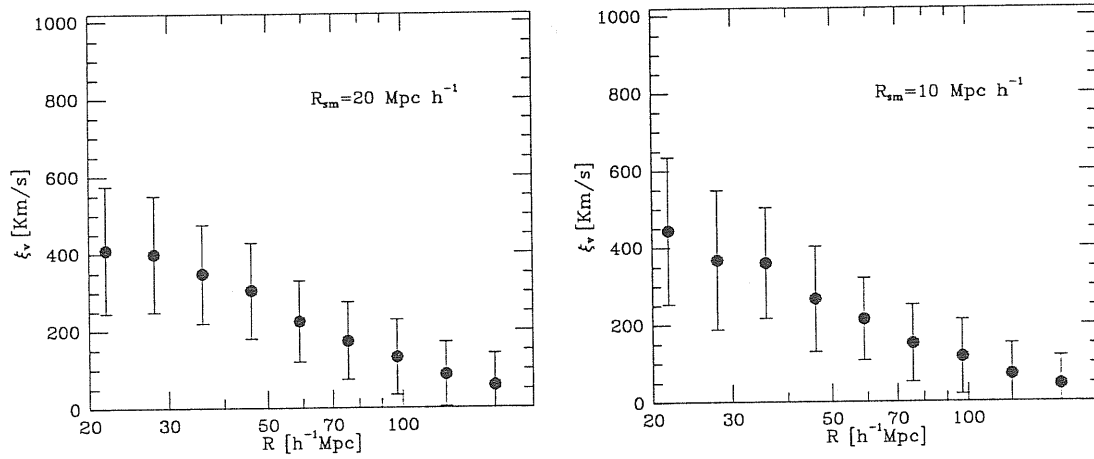
Figure 3.19: The scalar velocity correlation function of the 3D cluster velocities. Two cases corresponding to two smoothing radii ($R_{sm} = 10$ and $R_{sm} = 20\,h^{-1}$Mpc) are shown.

indicating that the velocity field is dominated by a coherent bulk motion on small scales. The correlation between the behaviour of the bulk flow and that of the velocity correlation function suggests that the bulk flow is the main feature of the velocity field. This is in part expected since, besides the bulk flow, the other sources of systematic motions typically originate from non–linear dynamics on small scales (e.g. the infall) which, in our analysis, have been smoothed out in order for linear theory to apply.

3.3.5   The Simulated Cluster Velocity Field and its Reliability

The simulations we consider here mimic the gravitational dynamics through the Zel'dovich approximation (ZA; Zel'dovich 1970; Shandarin & Zel'dovich 1989):

$$\mathbf{x}(\mathbf{q}, t) = \mathbf{q} + D(t)\nabla_{\mathbf{q}}\Phi(\mathbf{q}). \tag{3.61}$$

The simulations have been throughly described in B95 to which we refer for more details. Here we just remind that the initial power spectrum is convolved with a Gaussian window, $P(k) \to P(k)e^{-k^2 R_f^2}$, in order to suppress the shell crossing at small scales (e.g. Coles, Melott & Shandarin 1993; Melott, Pellman & Shandarin 1994). The filtering radius R_f is chosen in such a way that the average number of streams at each Eulerian point (Kofman et al. 1994) is $N_s = 1.1$. After assigning the linear potential on a grid, particles are moved from their initial grid positions according to eq. (3.61). The density and potential fields are then reassigned on the grid and clusters are selected as the highest local density maxima, so as

to reproduce the observed Abell/ACO cluster number density, $n_c \simeq 2 \times 10^{-5} h^3$ Mpc^{-3}.

The velocity of clusters is computed through the gradient on the grid of the evolved density field (see also Tini Brunozzi et al. 1995). This amounts to assume that, although the density field has undergone a substantial non–linear evolution, velocities and density fluctuations are still connected by the linear relation

$$\mathbf{v} \propto -\nabla\phi. \tag{3.62}$$

A detailed analysis of the Zel'dovich simulation reliability for describing the large scale dynamics in different cosmological scenarios is given in Moscardini et al. (1995). Here we just present some results aimed at assessing in a quantitative way the reliability of this approach by comparing the Zel'dovich velocity field with that obtained from an N–body simulation. In particular we consider the same Particle–Mesh simulation used by B95 for a similar comparison. The initial spectrum corresponds to the hybrid Cold+Hot DM (CHDM) model with $\Omega_{hot} = 0.3$; for simplicity we do not distinguish between hot and cold particles. The box size is $320\,h^{-1}$Mpc (with $h = 0.5$) and the number of grid points and particles is 128^3. In the N–body simulation clusters are identified as local maxima on the grid, following the same prescription outlined in the previous section. In order to define the cluster velocity, we follow a standard procedure (e.g. Kofman et al. 1994).

Starting from the same initial conditions and adopting the same number of particles and grid points, we run for comparison a Zel'dovich simulation in which the peculiar velocities of the evolved field were computed using eq. (3.62) (ZEL) and a simulation based on the pure Zel'dovich approximation in which peculiar velocity were computed by applying eq. (3.62) to the initial Lagrangian density field (LIN). We show the results at two different evolutionary stages, corresponding to $\sigma_8 = 0.67$ and $\sigma_8 = 1$. In Fig. (3.20) we compare the cluster velocity fields within a slice $60\,h^{-1}$Mpc thick for PM, ZEL and LIN simulations.

At the first stage ($\sigma_8 = 0.67$) there is a strong correspondence between the velocity fields recovered in the different simulations: all main figures are reproduced in the correct locations. The situation at $\sigma_8 = 1$ is slightly different: even if the main stream lines are roughly individuated, there is a tendency for both ZEL and LIN to overestimate the amplitude. In order to have a more quantitative assessment of the reliability of the Zel'dovich approach, we have applied the same statistical tests on the simulated data. The tests are: the 3D velocity probability function, the velocity correlation function and the bulk flow. Figure (3.21) summarizes the results at both evolutionary stages for PM, ZEL and LIN simulations.

At early times the PM and ZEL approximations give almost identical results, while

PM $\sigma_8=0.67$
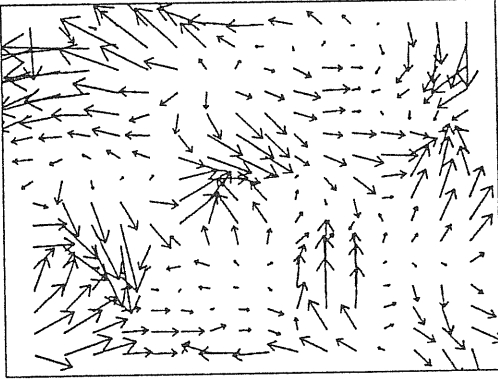
PM $\sigma_8=1.$
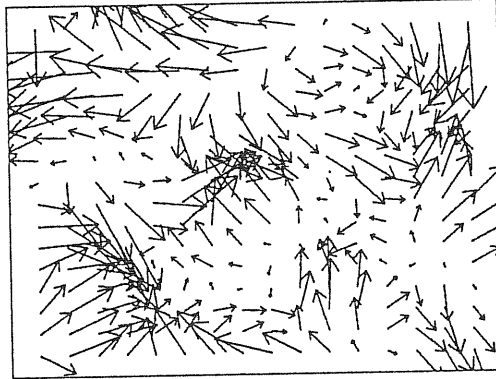
ZEL $\sigma_8=0.67$
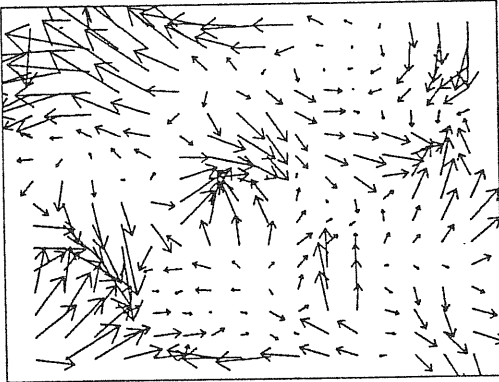
ZEL $\sigma_8=1.$
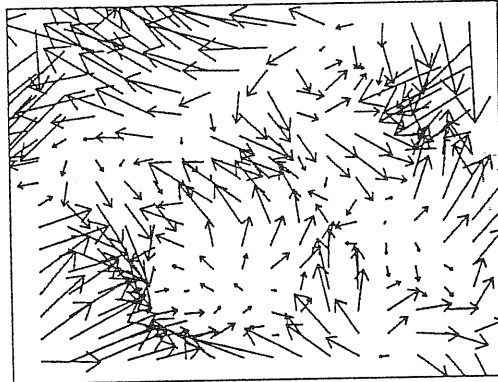
LIN $\sigma_8=0.67$
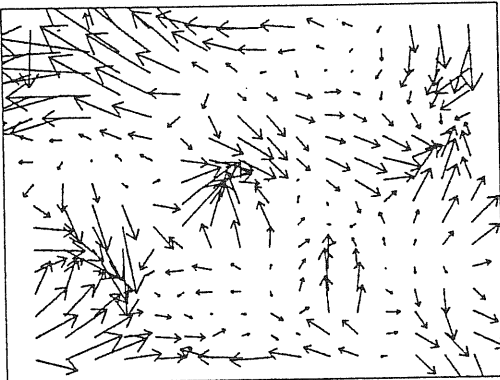
LIN $\sigma_8=1.$
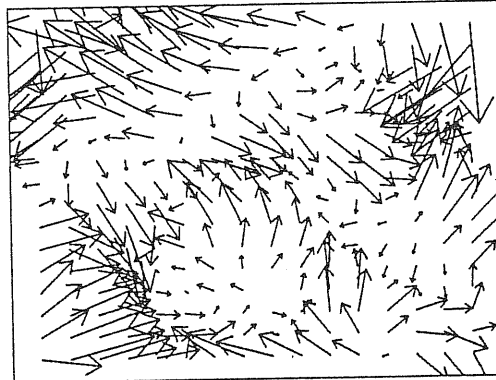
Figure 3.20: Comparison between the two approximation used (LIN) and (ZEL) and a PM N-body experiment. The cluster velocity fields produced in the three cases within a slice $60\,h^{-1}$Mpc are displayed at two different evolutionary epochs ($\sigma_8 = 0.67$ and $\sigma_8 = 1$).
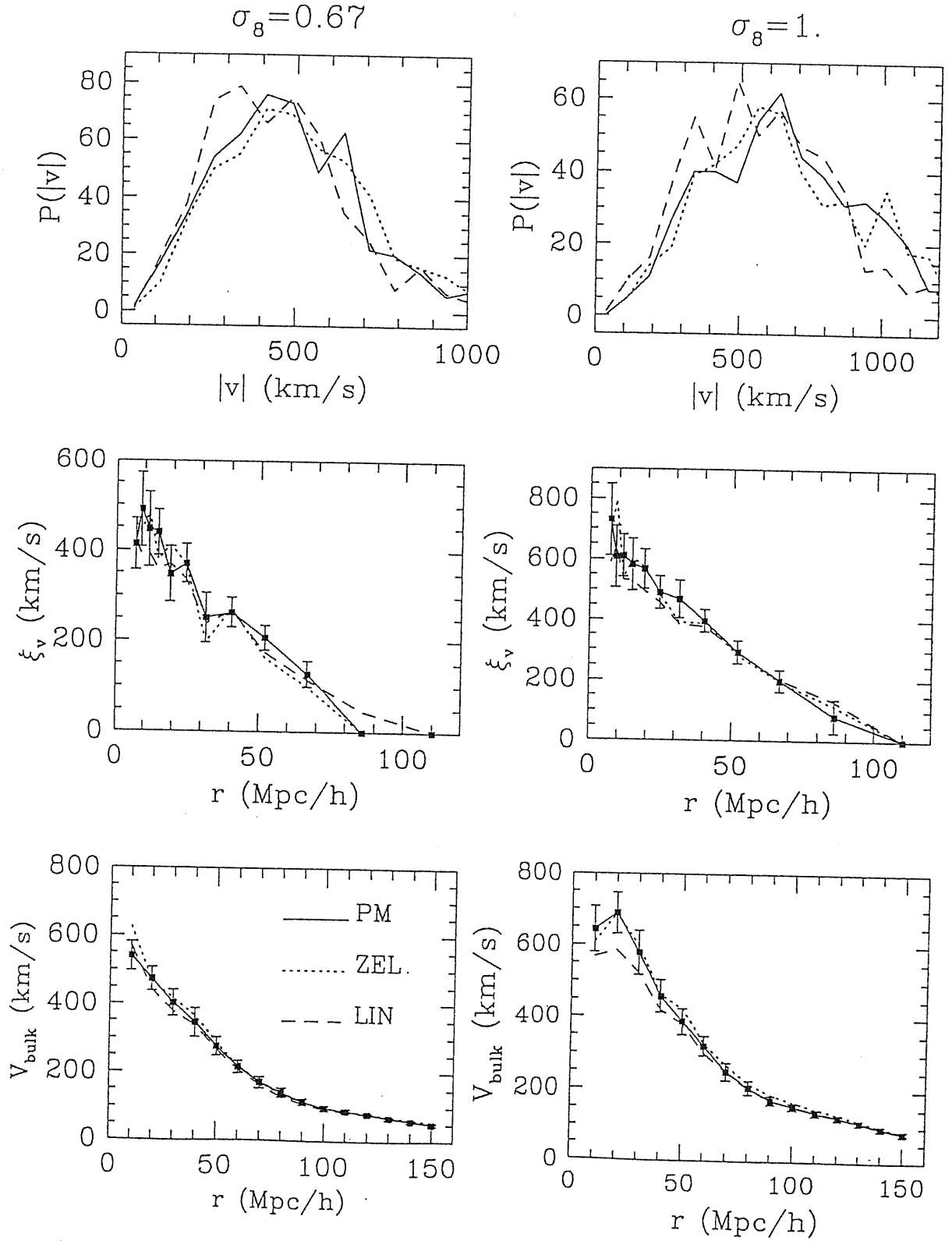
Figure 3.21: 3D probability velocity function, P(|V|), velocity correlation function, ξ_v, and the bulk flow velocity, V_{bulk}, for the LIN, ZEL and PM approximation at $\sigma_8 = 0.67$ and $\sigma_8 = 1$.

Model	Ω_o	Ω_Λ	h	σ_8	R_f
OCDM02	0.2	0.0	0.70	0.31	0.5
OCDM03	0.3	0.0	0.65	0.50	1.6
OCDM04	0.4	0.0	0.65	0.75	3.1
OCDM06	0.6	0.0	0.60	1.10	4.9
OCDM08	0.8	0.0	0.55	1.30	5.8
ΛCDM02	0.2	0.8	0.87	1.20	5.8
ΛCDM03	0.3	0.7	0.78	1.44	6.9
ΛCDM04	0.4	0.6	0.72	1.54	7.2
ΛCDM06	0.6	0.4	0.64	1.47	6.6
ΛCDM08	0.8	0.2	0.58	1.43	6.3
SCDM	1.0	0.0	0.50	1.36	6.0
CHDM	1.0	0.0	0.50	0.78	3.3

Table 3.7: The models. Column 2: the density parameter Ω_0; Column 3: the cosmological constant term Ω_Λ; Column 4: the Hubble parameter h; Column 5: the linear r.m.s. fluctuation amplitude at $8\,h^{-1}$Mpc σ_8; Column 6: the filtering radius R_f (in h^{-1}Mpc).

LIN produces a small excess of objects with low velocity and a slightly larger amplitude for the two–point correlation function at large separations. When $\sigma_8 = 1$ LIN is still producing an excess of small velocity objects and a lack of high velocity clusters. The two–point correlation function for PM and ZEL are quite similar at all separations while the linear ξ_v has a smaller amplitude when $r < 40\,h^{-1}$Mpc. Similarly PM and ZEL produce the same bulk velocity on all scales, while LIN produces a slightly lower amplitude for the bulk flow at small radii ($\leq 30\,h^{-1}$Mpc).

We can conclude from this analysis that our Zel'dovich approach gives a very good representation of velocity cluster field as far as the particular tests are concerned when we consider suitable scales even at $\sigma_8 = 1$.

Using the above Zel'dovich simulation we have explored several different cosmological scenarios in the framework of CDM models. In Table (3.7) the value of the cosmological parameter Ω_o is reported for each of the 12 model explored.

The CHDM model has a 30% of hot component. The cosmological term Ω_Λ, when present, is chosen in order to have a flat geometry: $\Omega_\Lambda = 1 - \Omega_o$ We refer to the Moscardini et al. (1995) work for a complete description of the normalization used; here we only list in

Table (3.7) the values of σ_8 for all the models considered together with the filtering radii R_f of the $P(k)$ used to suppress the shell crossing in the ZA. For each pair of $(\Omega_o, \Omega_\Lambda)$ values, we choose the Hubble parameter h in such a way that the age of the universe

$$t_o = H_o^{-1} \int_1^\infty \frac{dx}{x\sqrt{\Omega_o x^3 + (1 - \Omega_o - \Omega_\Lambda)x^2 + \Omega_\Lambda}} \tag{3.63}$$

(see e.g. Peebles 1993) is $t_o = 12\,$Gyr for all the models, except for SCDM and CHDM, for which we assume $h = 0.5$, giving $t_o = 13\,$Gyr.

For each model we run a single realization within a box of $960\,h^{-1}$Mpc aside, using 256^3 grid points and particles. The very large size of the box ensures that: *(a)* no appreciable box–to–box variance is present in the final results (we verified this by running two realizations for ΛCDM02 and CHDM); *(b)* fluctuation modes with wavelength larger than the box size provide a negligible contribution to bulk flows and velocity correlations, whose analysis is anyway confined within $180\,h^{-1}$Mpc.

The aim of these simulations is twofold. The first is that of comparing the cluster velocity fields produced in different cosmological scenarios. The second is to constrain the cosmological models by comparing the output of the numerical experiments with real data that, in our case, are provided by the reconstruction procedure. This second step is less trivial since to properly test numerical simulations against observations requires the knowledge of the observational biases and their effect on the statistic one wishes to use. This concern is greatly alleviated in our case since we will compare a simulated velocity field with a reconstructed one, i.e. with a full 3D field in which selection effects have been minimized.

To perform a proper comparison with our reconstructed cluster velocities one should substitute the simulated peculiar velocities, evaluated from eq. (3.62), with those obtained from the local cluster dipole assuming linear theory and a linear biasing scheme. This procedure uses a *local* bias parameter which need not be the same for different clusters. We have used the simulations to measure the value of the local bias defined as the ratio between the dipole velocity [eq. (3.13)] and the Zel'dovich velocity. We found that the distribution of the local biases has a large scatter (see also Tini Brunozzi et al. (1995) for a similar discussion in the study of the dipole structure). This scatter is a non trivial problem if one want to study the velocity fields, especially when using *local* statistics, like the probability velocity function. This scatter would be probably reduced by selecting observers more carefully (for example by requiring them to reproduce the observed large scale coherence of the LG dipole and of the observed streaming motion), and we hope to explore this point in the near future. For the time being and to be conservative we will compare the simulated and the

reconstructed velocity fields using average or integral statistics, like the two point velocity correlation function and the bulk flow.

The Bulk Velocity as a Cosmological Test:

The simulated bulk flow is measured from the full 3D velocity field which allows a direct comparison with the reconstructed cluster bulk flow computed in the previous section. The simulated cluster bulk velocity has been computed as follows: for each numerical experiment we selected 2000 observers randomly placed in the simulation box. Then we measured the bulk velocity in spheres of increasing radius around the observer's position, using eq. (3.53). Due to the large intercluster separation we started with a sphere of 50 h^{-1} Mpc to gather enough clusters. A limiting depth of 180 h^{-1} Mpc has been fixed to allow a meaningful comparison with real data. The cumulative bulk velocity, averaged over the 2000 observers, is displayed in Fig. (3.22) for each cosmological model. The two thick lines represent the 1−σ strip of the reconstructed cluster bulk flow. Note that the quantity displayed in the abscissa is the limiting depth and not the effective one. A simple visual analysis reveals that the only models we can rule out at a level > 1−σ are the OCDM ones with Ω_0 < 0.4. Flat models with non-vanishing cosmological constant but with Ω_0 < 0.4 together with the CHDM one are in good agreement with data on scales larger than $\simeq$ 10000 km/sec, while the SCDM model predicts a too large bulk velocity on small scales.

A more quantitative analysis has been performed as well. For each model we measured the fraction of the observers that measure a bulk flow with certain specified properties. The relative probability of observing that particular feature is reported in Table (3.8). In the third and fourth columns we listed the probability of measuring a bulk flow at 5000 km/sec within 1 and 2−σ from our reconstructed value, $P_{50}^{1\sigma}$ and $P_{50}^{2\sigma}$ respectively. We have chosen this depth since it is still within the range spanned by galaxy catalogues where cluster bulk velocity overlaps with that obtained from the $POTENT$ analysis (Dekel 1994) and with that measured using the recent the da Costa et al. (1995) data. Similarly, columns 5 and 6 contain the same probabilities measured at 15000 km/sec ($P_{150}^{1\sigma}$ and $P_{150}^{2\sigma}$). This is the limiting depth of the LP sample. The probabilities of observing a bulk flow within 1 and 2−σ from the LP one is listed in columns 7 and 8 ($P_{LP}^{1\sigma}$ and $P_{LP}^{2\sigma}$). Finally, we measured the fraction of observers whose cumulative bulk velocity is within the 1 and 2−σ strip throughout the whole range (5000 to 15000 km/sec) covered by the data (columns 9 and 10, $P_{all}^{1\sigma}$ and $P_{all}^{2\sigma}$, respectively). Comparisons with the data at 5000 and 15000 km/sec confirm the visual impression: the only disfavoured models are the OCDM ones with Ω_0 = 0.2 and 0.3 and,
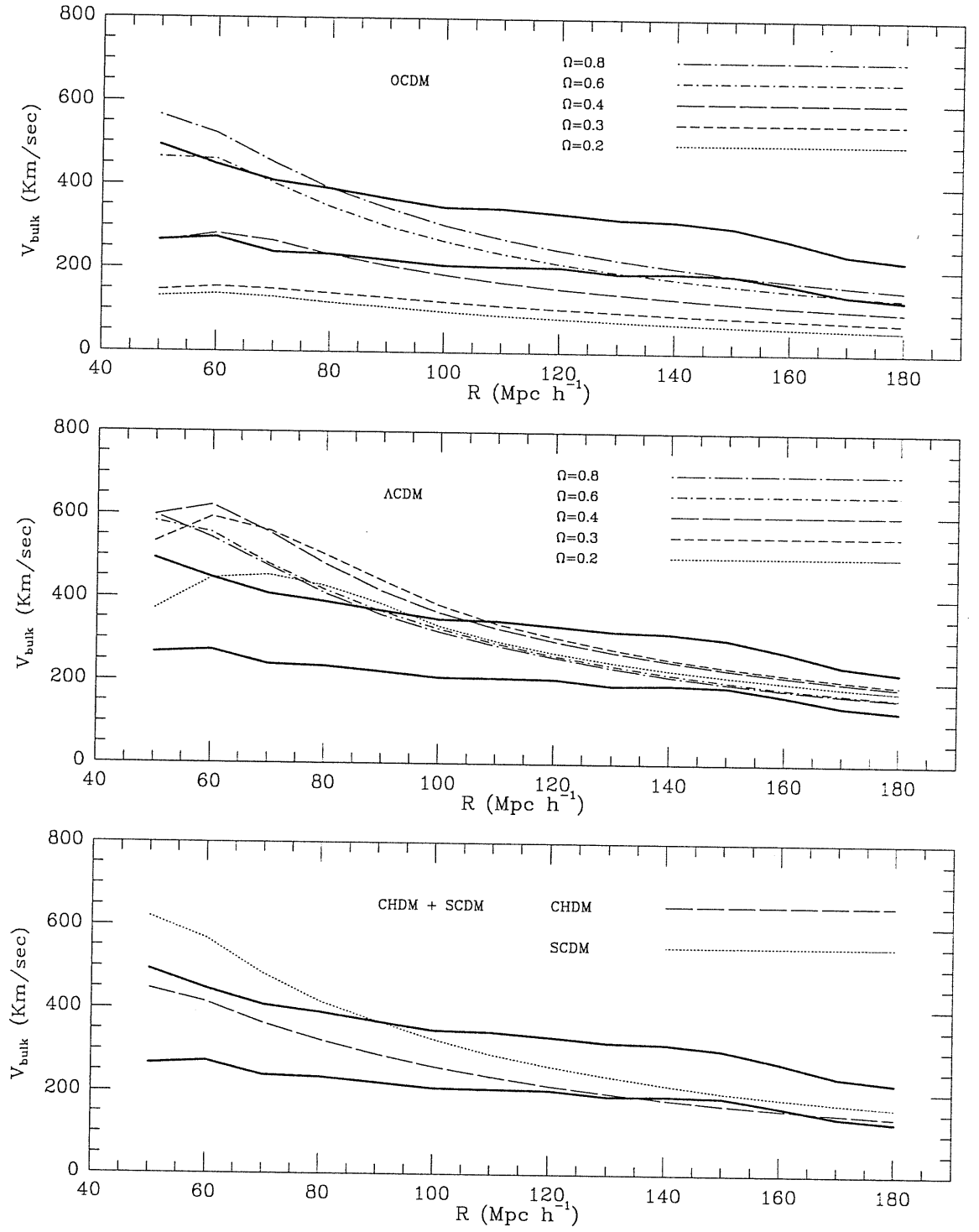
Figure 3.22: The simulated cluster bulk velocity predicted by different cosmological model is compared with the real cluster bulk flows (thick lines).

Model	Ω_o	$P_{50}^{1\sigma}$	$P_{50}^{2\sigma}$	$P_{150}^{1\sigma}$	$P_{150}^{2\sigma}$	$P_{LP}^{1\sigma}$	$P_{LP}^{2\sigma}$	$P_{all}^{1\sigma}$	$P_{all}^{2\sigma}$
ΛCDM	0.2	0.396	0.678	0.385	0.735	0.003	0.051	0.038	0.278
ΛCDM	0.3	0.299	0.531	0.403	0.715	0.004	0.072	0.012	0.161
ΛCDM	0.4	0.274	0.495	0.418	0.727	0.006	0.063	0.009	0.141
ΛCDM	0.6	0.312	0.547	0.375	0.721	0.001	0.034	0.004	0.135
ΛCDM	0.8	0.310	0.532	0.382	0.739	0.001	0.009	0.006	0.119
OCDM	0.2	0.017	0.307	$\leq 10^{-4}$	0.028	$\leq 10^{-4}$	$\leq 10^{-4}$	$\leq 10^{-4}$	0.019
OCDM	0.3	0.046	0.413	0.013	0.129	$\leq 10^{-4}$	$\leq 10^{-4}$	0.009	0.094
OCDM	0.4	0.383	0.783	0.108	0.379	$\leq 10^{-4}$	$\leq 10^{-4}$	0.023	0.228
OCDM	0.6	0.409	0.681	0.300	0.631	$\leq 10^{-4}$	0.004	0.010	0.187
OCDM	0.8	0.343	0.609	0.379	0.712	$\leq 10^{-4}$	0.013	0.006	0.151
SCDM	1.0	0.293	0.508	0.365	0.705	$\leq 10^{-4}$	0.023	0.015	0.109
CHDM	1.0	0.437	0.704	0.315	0.653	$\leq 10^{-4}$	0.015	0.018	0.237

Table 3.8: Bulk flow probabilities in different cosmological scenarios.

more marginally, the $\Omega_o = 0.4$ case. Moreover for all the models the LP result is a very low probability event. Finally, a small fraction of observers measure a cumulative bulk velocity in accordance with the data throughout the whole range of spanned scales. Even this test, however, lacks of discriminant power since only open CDM models with $\Omega_o = 0.2$ and 0.3 perform significantly worse than the others.

It is interesting to note that very similar results are obtained if, instead of selecting observers at random, we would have chosen the observers such that their properties are similar to those of the LG region (i.e. those with $-0.2 < \delta < 1$ density peaks having a peculiar velocity $600 < |\mathbf{v}_{LG}| < 650 \ km/sec.$).

The Velocity Correlation Function as a Cosmological Test:

In this analysis we use the whole simulation box. This has the effect of minimizing the box–to–box variance which should, however, be accounted for if one wants to compare simulations with our velocity field reconstructed within a $200 \, h^{-1}$Mpc sphere.

In Fig. (3.23) we plot $\xi_v(r)$ for the cosmological models explored at scales $r \geq 20 \, h^{-1}$Mpc, where the ZA description of the velocity correlations has been shown to be reliable. OCDM models are characterized by a progressively larger $\xi_v(r)$ as Ω_o increases. A quite evident discrimination between different Ω_o models is possible up to scales $r \simeq 60 \, h^{-1}$Mpc, while above $100 \, h^{-1}$Mpc all these models converge to a similar value rather quickly. Among
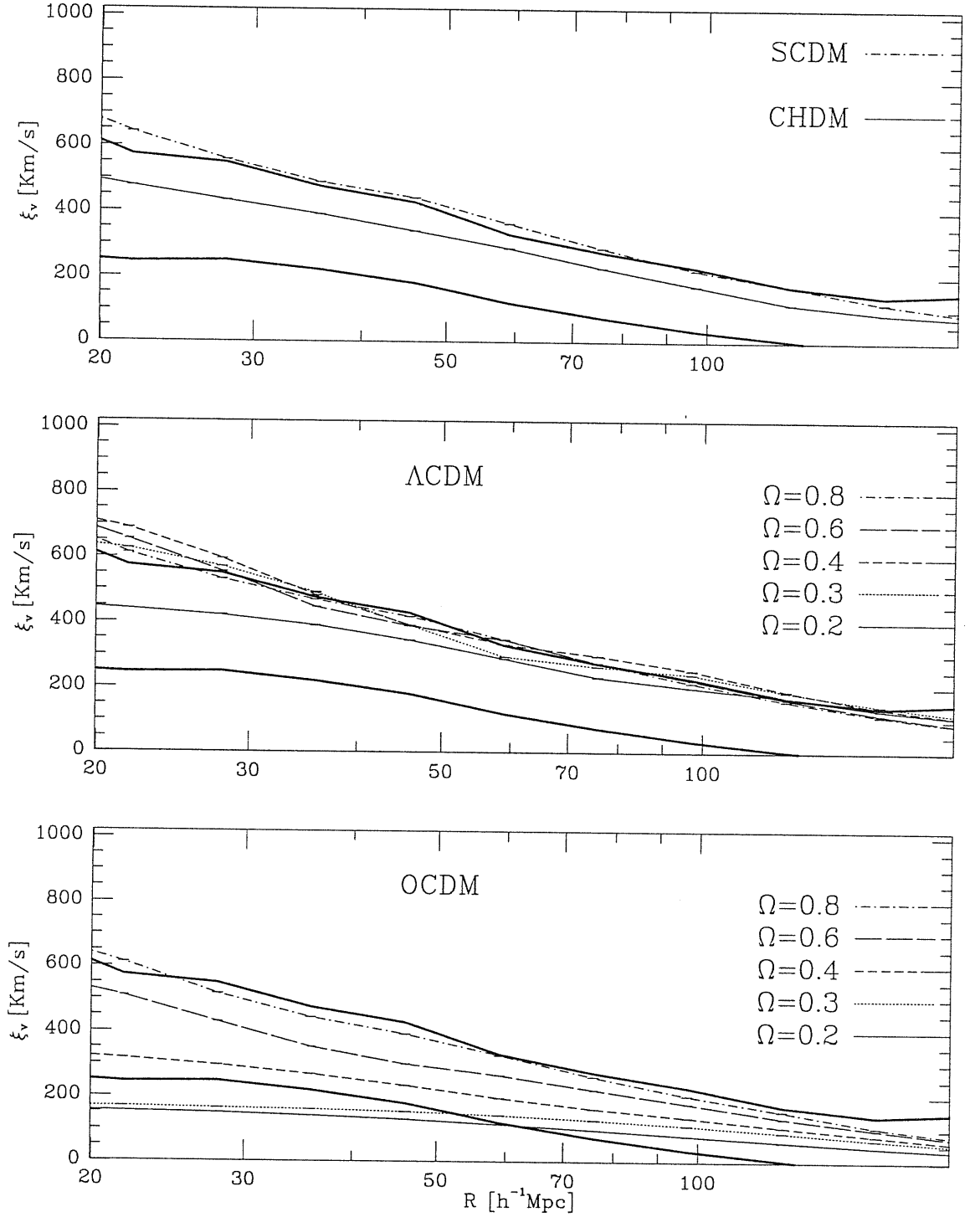
Figure 3.23: The scalar velocity correlation function of the simulated velocity fields for the different models explored. The two thick continuous lines delimitate the 1 σ strip relative to the ξ_v of the reconstructed cluster velocities.

the ΛCDM models, instead, the only model that have a quite different behaviour is ΛCDM02: all the other spectra provide almost indistinguishable velocity correlations. As we have verified the large simulation box keeps the cosmic variance at a very low level: we analysed two different realization of CHDM and ΛCDM02 models finding only a few percent of difference in their $\xi_v(r)$.

In Fig. (3.23) we also plot the $1-\sigma$ confidence strip relative to the reconstructed velocity correlation function (only the $R_{sm} = 20\,h^{-1}$Mpc case is considered). It is evident that the ξ_v does not put stringent constraints on the cosmological models. As in the bulk flow analysis, the only disfavoured models are the open CDM ones with $\Omega_o < 0.4$, for which the ξ_v exhibits a too low amplitude on scales smaller than $50\,h^{-1}$Mpc. For all the other models ξ_v lies within the $1-\sigma$ strip except on scales smaller than $30\,h^{-1}$Mpc. This consistency, however, is only marginal since all the remaining models but the SCDM and the $\Lambda = 0.2$ CDM ones, predict a velocity correlation with an amplitude very close tho the upper edge of the $1-\sigma$ strip.

3.3.6 Comparison with Observations: an Ω_o–Test

We have already evaluated the β_c parameter by matching the asymptotic amplitude of the gravitational acceleration induced on the LG by the Abell/ACO clusters distribution to the amplitude of the CMB dipole. Another method we used was that of equating the amplitude of the CMB dipole to the LG velocity obtained from the minimization procedure described in section (3.2.5). These comparisons give a reliable β_c estimate only if the cluster dipole has converged within the sample depth. Several different effects, however, makes this β_c estimate very noisy. In section (3.2.5) we obtained

$$\beta_c = 0.21^{+0.09}_{-0.11}\, f(V_{in})\,, \qquad f(V_{in}) \equiv \left[\frac{622 - V_{in}\cos\delta\vartheta}{622 - 180\cos\delta\vartheta}\right]\,, \qquad (3.64)$$

where most of the quoted scatter is due to the cosmic variance reflecting the fact that we are dealing with a single β_c measurement. An effective way to reduce the scatter upon β_c is therefore that of making several independent comparisons between the reconstructed and the observed peculiar velocities of different 'observers'.

In what follows we achieve this purpose by using two different categories of objects: first we consider those Abell/ACO clusters for which a reliable distance estimate is available and we compare their observed peculiar velocities to those reconstructed by our iterative method. A second analysis has been performed as well: we selected a subsample of objects

from the grouped version of the Mark II catalogue (Tormen et al. 1993) and we compared their velocities with that obtained from our reconstruction at the MKII objects' locations.

Abell/ACO Clusters:

The dataset we use is composed by three cluster subsamples:

- Abell clusters with IRTF distances extracted from the Giovanelli et al. (1994) sample (GTF). Amongst the 8 Abell/ACO clusters they list we exclude A262 because of its discrepant $T - F$ and $D_n - \sigma$ distances, A3526 (Cen 30), whose dynamics is known to be affected by non–linear effects and A1060 (Hydra) which has 4 Abell neighbours within 30 h^{-1}Mpc. Similarly, A2199 is excluded from the present–analysis since in our catalogue it has been collapsed in a unique object with its close Abell neighbour. Finally, to be conservative we double the uncertainty on the A1367 velocity, that in the Giovanelli et al. (1994) catalogue was very small.

- Abell clusters with IRTF distances extracted from the Hudson (1994) work, with distances corrected for inhomogeneous Malmquist bias (HTF). Excluding A3526, A1060 and A3742 (again discrepant $T - F$ and $D_n - \sigma$ distances) reduces the number of listed Abell/ACO clusters to 4 objects.

- Abell clusters with $D_n - \sigma$ distances extracted from the Hudson (1994) catalogue (HDN). The Abell/ACO subsample contain 6 objects and does not include Cen 30 and the Hydra cluster.

After scaling the reconstructed peculiar velocity to $\beta_c = 1$ we looked for a linear relationship between the observed u_{obs} and the line of sight component of the reconstructed peculiar velocity, $(\mathbf{v}_{rec} \cdot \hat{\mathbf{x}})$:

$$u_{obs} = A + \beta_c \, (\mathbf{v}_{rec} \cdot \hat{\mathbf{x}}), \qquad (3.65)$$

where $\hat{\mathbf{x}}$ is the unit position vector of the generic cluster. We expect a value of A consistent with zero. We already quantified the magnitude of the errors in the reconstructed velocities $(\sigma_T = \sigma_{vr})$ and we discussed their origin. However, in our case we must also account for errors in the observed velocities (σ_{vo}) whose amplitude increases with the object's distance and it is typically larger than σ_{vr}. To do so we use a linear fit to the data by minimizing the χ^2 merit function

$$\chi^2 = \sum_{i=1}^{N} \frac{[u_{obs,i} - A - \beta_c \cdot |\mathbf{v}_{rec,i} \cdot \hat{\mathbf{x}}|]^2}{\sigma_{vo,i}^2 + \beta_c^2 \sigma_{vr,i}^2}. \qquad (3.66)$$
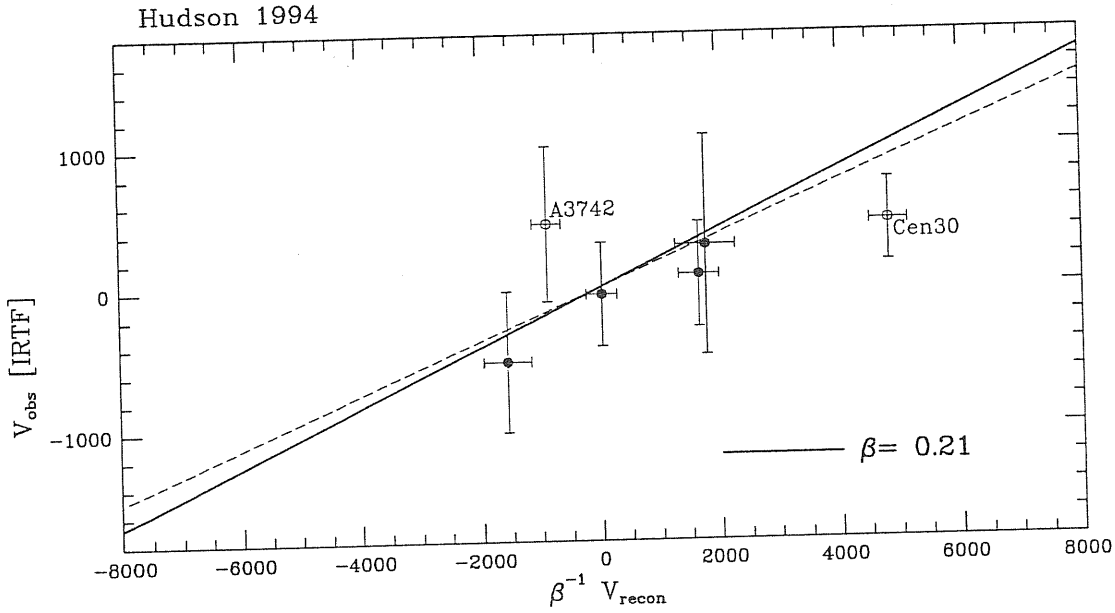
Figure 3.24: χ^2 fit to the GTF cluster peculiar velocities. A262 and Cen30 are excluded from the minimization procedure and are shown for reference only. Dashed line represents the best fit line while continuous line refers to the $\beta_c = 0.21$ slope.

The major drawback of this method is that it assumes that datapoints are statistically independent which is not true for the peculiar velocities because of the large coherence scale of the velocity field.

Figures (3.24) and (3.25) show the results of the fit to the GTF and HTF data in the case of $R_{sm} = 10\,h^{-1}\mathrm{Mpc}$. All the reconstructed velocities are normalized to $\beta_c = 1$. A simple visual inspection already reveals the most important result: predicted and observed peculiar velocities are linearly correlated, which constitutes a non trivial success for the GI model. From a more quantitative point of view it is clear that, due to the large uncertainties in the peculiar velocities, a large number of clusters (presently not available) should be used for determining the parameters' fit with a good precision. In fact, the small number of clusters generates a large uncertainty in the β_c value. In Table (3.9) we report the values of A and β_c (and their relative errors σA and $\sigma \beta_c$) together with the χ^2 value, the number of clusters selected, N_c, and the Q parameter (quantifying the probability that a value of χ^2 as poor as the listed value should occur by chance). The different entries correspond to the different cases we have explored which are characterized by the different smoothing applied. Both GTF and HTF samples give a β_c value somewhat smaller than that obtained from the cluster dipole analysis but still compatible with it due to the large scatter: a result that does
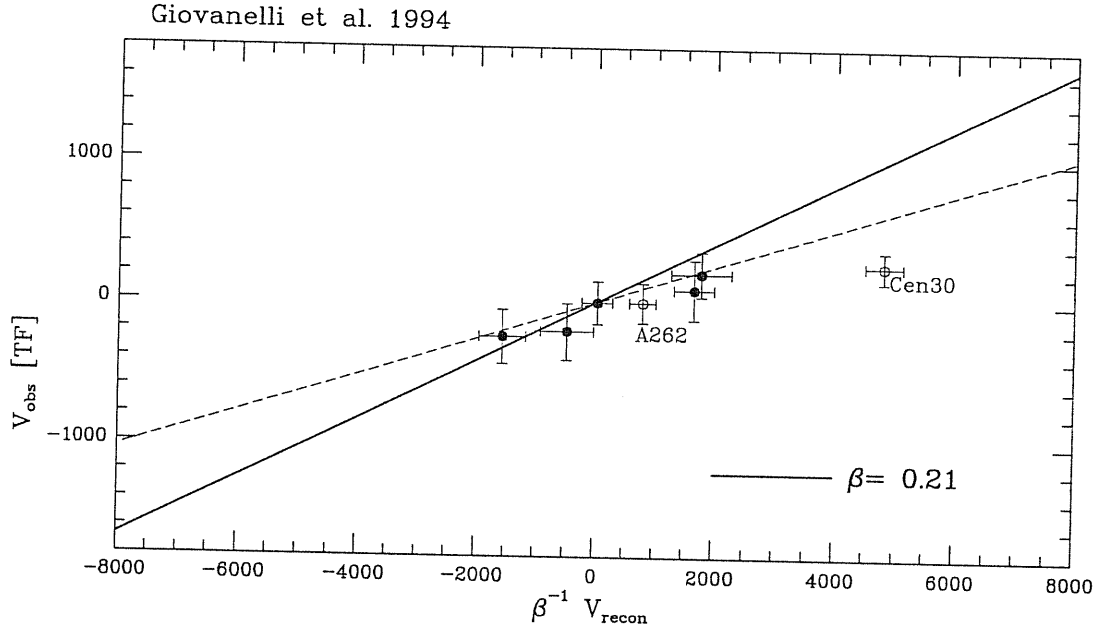
Figure 3.25: χ^2 fit to the HTF cluster peculiar velocities. A3742 and Cen30 are excluded from the minimization procedure and are shown for reference only.

Sample	R_{sm}	N_{cl}	A	σA	B	β_c	$\chi^2/$d.f.	Q
GTF	10	5	-23	100	0.14	0.08	0.5	0.89
GTF	20	5	-51	100	0.13	0.07	0.9	0.92
GTF	30	5	-78	100	0.13	0.07	0.3	0.96
HTF	10	4	-130	250	0.19	0.20	0.3	0.89
HTF	20	4	-149	300	0.19	0.22	0.3	0.93
HTF	30	4	-180	270	0.20	0.21	0.2	0.98
HDN	10	7	-90	180	-0.15	0.16	4.6	0.56

Table 3.9: Parameters for the linear fit to the v_{obs} versus $v_{rec} \cdot \hat{x}$ relation. Abell/ACO clusters from Hudson (1994) with IRTF and $D_n - \sigma$ distances (HTF and HDN, respectively) and Giovanelli et al. (1994) (GTF) are considered.

not depend on the smoothing adopted. Including A262, Cen30 and A3742 further lowers the β_c value, while the inclusion of the Hydra cluster does not appreciably affect the results of the minimization. Although the scatter is too large to put stringent constraints on the β_c parameter, this results is particularly significant since it is consistent with the cluster dipole analysis.

Using the HDN dataset, however, gives completely different results. From Table (3.9) we see that the fit, which is worse than in the previous cases, formally gives a *negative* value of β_c, although it is consistent with zero at a $1\ \sigma$ level. The consistency amongst the dipole analysis, the results of the minimization applied to IRTF clusters and that one applied to MKII objects (see below), however, make us confident that this discrepancy arises from some unknown bias in the $D_n - \sigma$ distances of the clusters we have analysed or to a statistical fluke ascribed to the small number of clusters used for the minimization.

MarkII Objects:

To evaluate β_c one can compare the predicted peculiar velocity at the generic location where a test particle with measured peculiar velocity is placed. In principle any luminous object can be used for this purpose. In practice, however, one must keep in mind that the reconstructed peculiar velocity field, has been obtained by heavily smoothing the non–linear contribution on small scale in order to apply linear theory. Therefore, to perform a self consistent comparison between the observed and predicted peculiar velocities one should either properly treat the observational data or select a subsample of objects having some special attributes.

One possibility is to smooth the observed peculiar velocities on a specified scale to allow a homogeneous comparison with the predicted smoothed velocity field: a way out similar to that adopted in the *POTENT* analysis (Bertschinger & Dekel 1989, Bertschinger et al. 1990). Another method, less rigorous but considerably easier to implement, is that of restricting the analysis to a class of objects for which non–linear contributions to the peculiar velocities are thought to be negligible (i.e. isolated objects for which the predicted peculiar velocity weakly depends on the smoothing adopted). In this work we use this second strategy. Its major drawback is that the amount of useful information is heavily reduced after the selection procedure.

The sample we consider here is the Mark II catalogue where galaxies have been grouped together by Tormen et. al. (1993) following the rules in the original papers (Lynden–Bell et al. 1988, Faber et al. 1989) and considering the Aaronson clusters of spirals as single

objects. The total number of galaxies in the catalogue is 1184, grouped into 704 objects [for the content of this grouped MKII catalogue see Table (1) in Tormen et al. (1993)]

As a first step towards the selection of the best subsample for our analysis, we compute the difference between the observed and the predicted peculiar velocity for each MKII object (ΔV). We found a strong nearly–linear correlation between ΔV and the absolute value of the observed peculiar velocity $|V_{obs}|$. This is not surprising since objects with large peculiar velocity typically reside in high density region where non–linear effects increase the galaxy velocities. More interesting is the behaviour of ΔV versus the number of MKII galaxies grouped in each MKII object, N_{MK}: ΔV is nearly constant for $N_{MK} > 1$ but is appreciably larger when $N_{MK} = 1$. These indications allow us to select a first subsample from the original grouped MKII catalogue; from now on we consider only those objects with $N_{MK} > 1$ and $|V_{obs}| < V_{Lim}$, where V_{Lim} is of few thousands km/sec (i.e. the typical velocity of a galaxy located in dense cluster).

Theoretical arguments provide further constraints forcing us to reduce the size of the sample even further.

- To minimize non–linear effect we exclude from the analysis those MKII objects with a MKII neighbor closer than a minimum distance, d_{MK}. The tests we performed have revealed that, in order to keep the results stable, we have to impose $d_{MK} > 1\,h^{-1}$Mpc. An upper limit to d_{MK} has been imposed as well since the isolation is likely an artifact due to the fact that the MKII catalogue is incomplete and some nearby galaxy not listed in the catalogue is probably present that may affect the local dynamics. For this reason we set $d_{MK} < 5\,h^{-1}$Mpc.

- For the same reason we should not consider those MKII objects too close to an Abell/ACO clusters. However, the non–linear effects generated by close clusters are already minimized by the smoothing procedure and we do not need to set any further constraint but, for the sake of consistency, when we consider 'models' characterized by a given R_{sm} we will exclude from the analysis all the MKII objects having an Abell/ACO cluster closer than R_{sm}.

- Errors on the observed peculiar velocities increase with the distance and thus to avoid large uncertainties we will consider only objects within a given distance d_{max}. In practice we found that including distant objects does not affect appreciably the results.

- Also MKII objects close to the LG should be excluded from the analysis since, as

R_{sm}	d_{min}	d_{max}	V_{min}	V_{max}	N_{MK}	d_{MK}	N_{tot}	A	σA	β_c	$\sigma\beta_c$	χ^2/d.f.	Q	r
10	**20**	∞	**-2000**	**2000**	**5**	**2**	**6**	**20**	**160**	**0.18**	**0.06**	**2.2**	10^{-2}	**0.53**
10	20	∞	-1000	1000	5	2	5	100	180	0.20	0.06	2	$1.5 \cdot 10^{-2}$	0.71
10	20	∞	$-\infty$	$+\infty$	5	2	7	65	180	0.21	0.07	3.3	$3 \cdot 10^{-3}$	0.33
10	20	∞	-2000	2000	5	1	8	-130	170	0.16	0.06	2.3	$4 \cdot 10^{-3}$	0.51
10	20	∞	-2000	2000	3	2	14	-40	90	0.19	0.05	2.6	$2 \cdot 10^{-3}$	0.52
10	0	∞	-2000	2000	3	2	15	-120	80	0.19	0.05	2.7	$4 \cdot 10^{-4}$	0.51
10	0	40	-2000	2000	3	2	9	-500	300	0.17	0.07	1.2	10^{-1}	0.54
5	20	∞	-2000	2000	5	2	10	180	130	0.17	0.07	1.7	$2 \cdot 10^{-2}$	0.47

Table 3.10: MKII subsample characteristics and parameters for the linear fit to the V_{obs} versus $\mathbf{V}_{rec} \cdot \hat{\mathbf{x}}$ relation.

we have seen, the exclusion of nearby clusters from the Abell/ACO sample causes the local dynamics to be ill reconstructed. For this purpose we have considered only objects beyond a minimum distance d_{min}. Even in this case, however, this bound is quite ineffective since including nearby objects has a very little effects mainly because most of the nearby MKII objects are close to some other MKII object and thus are already excluded from the analysis.

- We found that in order to keep the significance of the fit at an acceptable level we need to set a more stringent limit on N_{MK}. A reasonable value for Q is achieved by imposing $N_{MK} \geq 3$.

The above constraints allow us to define a 'standard' MKII subsample (whose characterizing parameters are shown in Table (3.10) as boldface quantities) to which we applied the χ^2 minimization procedure. This standard sample has been subsequently modified to assess the robustness of the analysis. The results are listed in Table (3.10). The first column contains R_{sm}, the minimum and maximum distances from the LG are listed in columns 2 and 3 while columns 4 and 5 contain the minimum and maximum allowed values for V_{obs}. Columns 6, 7 and 8 display the minimum N_{MK}, d_{MK} and the number of MKII objects selected for the χ^2 minimization N_{tot}, respectively. The remaining columns list $A \pm \sigma A$, $\beta_c \pm \sigma\beta_c$, χ^2, Q and the correlation coefficient, r.

The main feature is the stability of the results when the standard subsample is slightly modified, provided that $N_{MK} > 3$ and $d_{MK} > 1\,h^{-1}\mathrm{Mpc}$. The offset A is always compatible with zero while the β_c parameter stabilizes around 0.18 although with a large
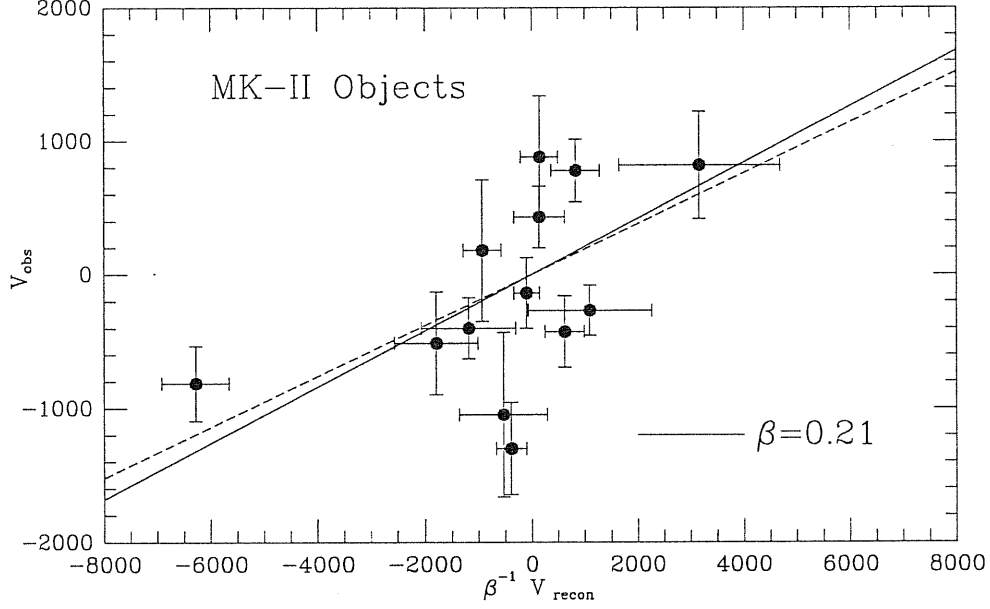
Figure 3.26: χ^2 fit to a MKII subsample. Continuous line represents the linear fit while dashed line refers to the case of $\beta_c = 0.21$.

scatter which, however, is smaller than that obtained from the previous minimization that used Abell/ACO clusters observed velocities. The small value of Q, however, tells us that the fit is not very good. This fact may indicates that the errors are underestimated or that they are not Gaussian distributed. Errors on V_{obs} come directly from the MKII catalogue while errors on V_{rec} have been computed by adding in quadrature σ_i to σ_o.

Figure (3.26) displays V_{obs} versus $(\mathbf{v}_{rec} \cdot \hat{\mathbf{x}})$ for the MKII objects. This plot refers to case listed in the fifth row of Table (3.10) for which the largest number of MKII objects is available. It is interesting to note that adding in quadrature the shot–noise error (which we know to overestimate the true error) improve the significance of the fit ($Q \sim 0.2$) increasing the value of β_c to 0.22, very close to the outcome of the dipole analysis, and leaving unaltered the value of A. This indicates that using a more reasonable shot–noise error, larger than zero but smaller than σ_{sn} would result in a better fit and a value of β_c larger than those listed in Table (3.10).

Contrary to the case of GTF and HTF samples analyses, varying the smoothing radius R_{sm} has a non negligible effect on the final results since β_c decreases as R_{sm} increases. This is not very evident from Table (3.10) but we verified that this is the case by exploring more extensively the space of parameters when R_{sm} is kept fixed. For $R_{sm} = 5h^{-1}$ Mpc we found $\beta_c \sim 0.15 \pm 0.8$, while for $R_{sm} = 20h^{-1}$ Mpc $\beta_c \simeq 2 \pm 2$. These results are not surprising since, as indicated by the Baugh and Efstathiou (1994) analysis, $R_{sm} = 5h^{-1}$ Mpc is not

sufficient small to wash out non–linear effects. On the other side increasing the smoothing radius to $R_{sm} = 20h^{-1}$ Mpc increases β_c and its variance. To explain the second effect one must keep in mind that we are selecting very few isolated objects (the smoothing radius in this analysis coincides with the minimum allowed distance from another Abell/ACO cluster) for which the dynamics is likely to be dominated by nearby objects not listed in the MKII catalogue.

It is clear from Table (3.10) that we are not able to put stringent constraints on β_c. However, as we outlined in the previous section, the present–analysis is remarkably consistent with the previous one and with the cluster dipole, making us confident that our reconstructed velocity field reproduces the true one. The large errors in β_c probably arise from the sparse sampling of the velocity field when using Abell/ACO clusters or the incomplete MKII catalogue.

3.4 CONCLUSIONS

We have applied the *RSCM* and the *LIRM* to a heirnearly volume limited sample of Abell/ACO clusters with the aim of recovering their true spatial distribution and velocities. Our analysis is very powerful and allows us to obtain an enormous amount of information that can be used, in principle, to put constraints on the cosmological models, to estimate the value of the β_c parameter, to assess the validity of the GI picture up to very large scales and to make prediction on the large scale structure and dynamics. In practice, however, the large uncertainties limit the strength of part of the analysis. The origin of the errors does not reside in the reconstruction method but mainly originate from the sparsness of the sampling which lead to a twofold problem. On one side the relatively small number of clusters causes a large scatter in the statistical analyses of the velocity field, allowing only to weakly constrain different cosmological models. On the other side the coarness of the reconstructed density and velocity fields makes a comparison with the observed peculiar velocities very noisy.

Among the many outcomes of the reconstruction procedure and of the analyses performed on the cluster density and velocity fields some are particularly worth stressing:

- The reconstruction algorithm proved to be very reliable, keeping the intrinsic errors of the reconstructed cluster position sat a very low level which are typically to within 1.6 %, while usual observational errors are of the order of 10%.

- From a cosmographic point of view the underlying density field appears to be dom-

inated by few extended prominent structures (the Shapley Concentration, Great At-tractor, Perseus–Pisces supercluster, the Coma, the Ursa Major and the Grus–Indus regions). The large scale high density regions are not isolated but seem to be inter-connected, suggesting a large coherence of the density fluctuation field. Furthermore, the smoothed cluster density field is consistent with that of galaxies (MARK III and optical) at least within the survey limits of the galaxy samples.

- The qualitative analysis of the peculiar velocity field reveals the existence of a large coherent motion in the general direction of the CMB dipole, towards the Shapley region, involving the Perseus–Pisces, the LG, the Great Attractor and the Shapley concentration itself, where a large back infall is observed.

- Redshift–space distortions have a non negligible effect on the cluster dipole amplitude. Removing them results in a $\sim 23\%$ decrease of the dipole amplitude, while its direction remains unaffected. The extent of this effect does not seem to depend on the details of the reconstruction procedure.

- We estimated β_c using two semi–independent procedures: (a) we equate the CMB dipole amplitude with that of the 3D cluster dipole and (b) we minimize the recon-structed cluster peculiar velocity residuals in the LG frame. The results depend rather weakly on the value assumed for the Virgo infall and on the smoothing applied. Vary-ing these parameters in a plausible range and taking into account the various sources of errors we obtained

$$0.18 \leq \beta_c \leq 0.23.$$

This β_c value is larger than what found by previous cluster dipole analyses which is due mostly to the fact that we have taken into account z–space distortions. Assuming $\Omega_o = 1$ we obtain $b_c \simeq 4.8$, in good agreement with other independent estimates. This β_c determination is based on one point in space (the LG) and thus its uncertainty is largely affected by the cosmic variance which we found to be ~ 0.07, clearly too large to put useful constraints on the Ω_o value.

- With the aim of better determining the β_c value, we compared the observed TF or $D_n - \sigma$ cluster peculiar velocities with our reconstructed ones, also extending the analysis to the velocities of the Mark II objects. The main feature is that our predicted and observed velocities velocities linearly correlate which constitutes an evidence in favour of the GI hypothesis. Unfortunately the available dataset is so small that it

turned out very difficult to set stringent constraints on β_c, although its central value was found consistent with that obtained from the cluster 3D dipole analysis.

- We measured the bulk velocity of galaxy clusters using two independent methods, obtaining very similar results. Using $\beta_c = 0.21$ the cluster bulk flow turned out to match that of galaxies in the region in which the two samples significantly overlap (50–60 h^{-1}Mpc) then it decreases with its amplitude becoming very small beyond 100 h^{-1}Mpc, in accordance with most of the commonly accepted cosmological models and in strong disagreement with the LP result.

- We compared the cluster reconstructed velocity field with that produced by numerical simulations of different cosmological scenarios. The comparison, aimed at constraining the various cosmological models, was made using low order statistics such as the bulk flow and the velocity correlation function. It turned out that these tests lack of discriminative power since the only models ruled out at a confidence level $> 1-\sigma$ were the Open CDM ones with $\Omega_o \leq 0.4$ and to a lesser degree the flat CDM models with $\Lambda > 0.6$ (note that the best models as far as these tests are concerned are the CHDM and the ΛCDM with $\Lambda = 0.2$).

Finally, there are a number of possible ways that may improve the strength of this procedure some of which have been already outlined by Scaramella (1994):

- Use other cluster catalogues containing more clusters objectively defined like those from APM and COSMOS, and merge them with the Abell/ACO sample in a homogeneous way. This would allow to increase the number of clusters available. Also, unlike the Abell/ACO catalogue that on large scales ($\sim 200\,h^{-1}$Mpc) starts suffering of statistical inhomogeneity problems, the automated catalogue would provide us with homogeneous cluster samples suited for statistical analysis.

- Merge the cluster catalogue with a shallower galaxy sample. A self consistent merging of these two datasets would allow to trace the local velocity and density fields with higher precision while galaxy clusters would certainly improve the modeling of the external gravitational field. With this strategy it is still possible to trace the dynamics on large scales without, however, loosing information on local scales. Applying the reconstruction procedure to such a hybrid catalogue would allow a more effective comparison with Mark II velocities and would naturally alleviate the zero–point uncertainty of the dipole determination (not only at the LG location).

- Improve the *LIRM* to account for non–linear effects: an upgrade that is necessary when dealing with galaxy catalogues which are typically smoothed on smaller scales.

- Gather more cluster redshift to reliably extend the depth of the sample.

- Measure the distance of a larger number of Abell/ACO sample using TF or $D_n - \sigma$ to reduce the uncertainty on the β_c determination when comparing the observed and the reconstructed cluster velocities.

- Improve the treatment of the ZoA taking into account the newly discovered clusters (e.g. Puppis).

- Automatically account for the shot–noise errors by properly Wiener filtering the density field.

We plan to develop the present–work along some of the above directions.

3.5 APPENDIX: The Shot–Noise Error

As in SYDHF92 we assume that luminous objects trace the density field. In this case the shot–noise arises from selection effects and from the unknown mass of the objects. In an ideal system of $\hat{N}_T$ clusters contained in a volume V, the peculiar velocity at the origin due to the clusters within the shell $[s, s + \Delta s]$ is

$$\mathbf{v}_T = \frac{\beta_c \langle M_i \rangle}{4\pi \rho_c} W(s) \sum_{i=1}^{N_T} \frac{M_i}{\langle M_i \rangle} \frac{\mathbf{s}_i}{|\mathbf{s}_i|^3}, \quad (A.1)$$

where M_i is the mass of the ith. cluster, $\langle M_i \rangle$ is the average cluster mass, $\rho_c = \frac{\sum_i^{N_t} M_i}{V}$ is the cluster mass density, $W(s)$ the window function and N_T the number of clusters within the shell. In the reconstructed cluster distribution we have $\hat{N}_1$ real clusters and $\hat{N}_2$ synthetic objects generated to account for selection effects. By averaging over several different reconstructions, we have $\hat{N}_T = \hat{N}_1 + \hat{N}_2$ (a relationship valid also in the generic shell: $N_T = N_1 + N_2$). For the reconstructed cluster distribution we can express the velocity at the origin as

$$\mathbf{v}_{rec} = \frac{\beta_c \langle \mu_i \rangle}{4\pi \bar{\rho}_c} W(s) \left[\sum_{i=1}^{N_1} \frac{\mu_i}{\langle \mu_i \rangle} \frac{\mathbf{s}_i}{|\mathbf{s}_i|^3} + \sum_{j=1}^{N_2} \frac{\mathbf{s}_j}{|\mathbf{s}_j|^3} \right], \quad (A.2)$$

where we have assumed that the cluster masses in the reconstructed distribution (μ_i) is proportional to the Abell–listed galaxy number and we have set each synthetic cluster mass equal to $\langle \mu_i \rangle$. With the above assumptions we can rewrite $R = \frac{W(s)\beta_c \langle \mu_i \rangle}{4\pi \bar{\rho}_c} = \frac{W(s)\beta_c \langle M_i \rangle}{4\pi \rho_c}$. We will not consider the case in which Abell/ACO clusters are weighted in different ways (i.e. when $\mathcal{W}_{rel} \neq 1$) since this more general case, which is more complicate to work out, leads to very similar results.

We can compute now the velocity difference $\mathbf{v}_{rec} - \mathbf{v}_T$ by splitting eq. $(A.2)$ in two parts each of them containing a sum over N_1 and N_2 clusters respectively.

$$\mathbf{v}_{rec} - \mathbf{v}_T = R \left[\sum_{i=1}^{N_1} (\tilde{m}_i - \bar{m}_i) \frac{\mathbf{s}_i}{|\mathbf{s}_i|^3} + \sum_{j=1}^{N_2} (1 - \bar{m}_j) \frac{\mathbf{s}_j}{|\mathbf{s}_j|^3} \right], \quad (A.3)$$

where $\tilde{m}_i = \frac{\mu_i}{\langle \mu_i \rangle}$ and $\bar{m}_i = \frac{M_i}{\langle M_i \rangle}$. By construction $\langle \mathbf{v}_{rec} - \mathbf{v}_T \rangle = 0$. The variance in the velocity difference, to which we refers to as shot–noise, can be computed as the expectation value of the square of the velocity difference. Since the expectation value of the cross terms is zero then the variance in the shell is

$$\sigma_s^2 = \langle |\mathbf{v}_{rec} - \mathbf{v}_T|^2 \rangle = \frac{R^2}{|\mathbf{s}|^4} \left[\sum_{i=1}^{N_1} \langle (\delta m_i)^2 \rangle + \sum_{j=1}^{N_2} \langle (1 - \bar{m}_j)^2 \rangle \right], \quad (A.4)$$

where $\langle (\delta m_i)^2 \rangle = \langle (\tilde{m}_i - \bar{m}_i)^2 \rangle \approx 0$ being a second order term.

Since our notation the generalized selection function is $P(b)P(z)$. We have that $N_1 = 4\pi n_c \frac{\rho_c(s)}{\rho_c} [P(b)P(z)]$ and $N_2 = 4\pi n_c \frac{\rho_c(s)}{\rho_c} [(1 - P(b)P(z))]$, where $\rho_c(s)$ is the cluster mass density within the shell and n_c is the cluster number density within the volume V. The global variance can be computed by summing over shells containing $N_2 = 1$ or $N_2 = 0$ objects giving

$$\sigma^2 = \left[\frac{\beta_c}{4\pi n_c} \right]^2 \left[\sum_{i=1}^{\hat{N}_2} \frac{W(s_i)^2}{|\mathbf{s}_i|^4} \frac{[1 - P(b)P(z)]}{P(b)P(z)} \langle (1 - \bar{m}_i)^2 \rangle \right], \quad (A.5)$$

where $\langle (1 - \bar{m}_i)^2 \rangle = \langle \bar{m}_i{}^2 \rangle - 1 = K$ that can be evaluated from real data assuming $\langle \bar{m}_i{}^2 \rangle = \langle \tilde{m}_i{}^2 \rangle$ (which naturally follows from the assumption that the mass of real clusters is proportional to the Abell listed galaxy number). We then obtain

$$\sigma^2 = \left[\frac{\beta_c}{4\pi n_c} \right]^2 \sum_{i=1}^{\hat{N}_2} \frac{W(s_i)^2}{|\mathbf{s}_i|^4} K \left[\frac{1}{P(b)P(z)} - 1 \right], \quad (A.6)$$

which is eq. (3.42).

Chapter 4

THE NUMERICAL ACTION METHOD

In this chapter we describe in detail a method introduced by Peebles (1989 [P1], 1990 [P2]) for reconstructing the orbits of luminous objects back in time and the associated mass density distribution.

The orbit reconstruction within the GI framework and the related growth of density fluctuations are mixed boundary condition problems, some of which are specified at the present–epoch and some at early times, in which one predicts the present–time velocity field given the density field or, vice–versa, the density field that can be obtained from the observed peculiar velocities. The boundary conditions are obtained by specifying the present–time galaxy positions and by requiring negligible peculiar velocities at early epochs (a condition contained in the GI hypotheses). One possible way of reconstructing galaxy orbits is to integrate the motions back in time using an N–body code. Despite the time reversibility of gravity this strategy would be completely hopeless when applied to virialized systems where memory of the initial condition has been erased, but it would also be ineffective in linear systems since the use of N–body codes is restricted to initial value problems. Within the GI framework, in fact, one finds the motions of particles under the hypothesis that their physical separations vanish at early times. This requirement makes generic backward N–body solutions unacceptable since the resulting primordial peculiar velocities are unbound, representing an unphysical evolution from chaos towards order in an expanding universe. A further difficulty is the presence of decaying modes that, having left no detectable presence at the present–time, would amplify the noise at early epochs. P1 and P2 noticed that mixed boundary conditions in the GI picture naturally lead themselves to an application of the

Hamilton's principle in which solutions represent stationary points of an action subject to fixed boundary condition at both the initial (vanishing peculiar velocities) and final (either observed present–time positions or redshifts) time.

The Least Action Principle (LAP) can be numerically implemented as a fully non–linear Lagrangian method to reconstruct the orbits of luminous objects from their present–time positions (or redshifts) or, when the distribution of objects is properly smoothed, to recover the primordial density field from the present–time one. When applied to the linear or quasi–linear regime, in which there is a smooth one–to–one correspondence between the final and initial positions, the solutions are minima for the action. In the non–linear regime, i.e. when considering systems with crossing time shorter than the age of the universe, the method find multiple solutions which represent stationary points that are not minima for the action, and one is left with the problem of deciding which is the 'true' solution. This is why the method is difficult to apply in the highly non–linear regime, but, as we will see, it can be useful in the mildly non–linear regime in which multiple orbits exist only for few objects in the system. As we will discuss in what follows, the numerical LAP implementation relies on the GI hypothesis and assumes a biasing scheme in which all the mass is associated to visible objects that are treated as pointlike massive particles having the same M/L ratio. Despite this simplified mass model, the method is able to account for the dynamics on a quite wide range of scales (from 200 Kpc up to $30\,h^{-1}\mathrm{Mpc}$).

Since the original Peebles' work (P1), the LAP method has been applied for many purposes:

- It can be used to determine the trajectories for the galaxies of the system considered. This allows us to study how the external masses influence the system's dynamics (e.g. whether the system is gravitationally bound or unbound), to which extent the system can be considered isolated and if tidal torques generate spin angular momenta comparable with observations (Peebles 1994 [P3], 1995 [P4], Dunn & Laflamme 1993 [DL1]).

- When this method is applied to redshift catalogues it allows us to reconstruct peculiar velocities and 3D positions. With this respect the LAP is an improvement over the iterative reconstruction methods since it naturally accounts for non–linear effects. In practice, to avoid multiple solutions, this LAP implementation has been restricted to system large enough for non–linear effects to be minimized (Shaya, Peebles & Tully 1993, Shaya, Peebles & Tully 1995 [SPT]).

- The LAP method is suitable to study the character of the primeval mass fluctuations needed to produce the present galaxy distribution and motions. This gives a useful measures of the primeval density contrast from which small systems have evolved or, on larger scales, to explore the statistical character of the primeval mass fluctuations (P2 and P3).

- Finally, with the LAP method one can recover the value of the density parameter, Ω_o, the Hubble constant and the M/L ratio of the system considered. In the LAP implementation these quantities play the role of free parameters that can be fixed by matching the observed redshifts (P1, P2, P3, P4, SPT).

Because of its intrinsically non–linear nature, the LAP method can be applied to systems with different sizes in which the dynamical regime ranges from the quasi–linear to mildly non–linear. It has been successfully applied for reproducing the dynamics of the spheroidal companions of the Milky Way (i.e. to a system with size $r < 300$ Kpc, P4), to recover the dynamical history of the LG galaxies and of its neighbouring groups within $r < 3$ Mpc (P1, P2, P3, P4, DL1) and to reconstruct the present–time positions of luminous galaxies within $30\,h^{-1}$Mpc from their observed redshift (Shaya, Peebles & Tully 1993 and SPT).

The LAP method is also an Ω–test that gives the unique possibility to evaluate the Ω_o value on very different scales using the same method. This issue is particularly important for the present debate about the Ω_o value since the dynamical estimates of the density parameter show an apparent contradiction:

- On scales $\leq 100\ h^{-1}$ Kpc the Milky Way satellites' dynamics (Faber & Ghallagher 1979; Little & Tremaine 1987; Zatrisky et al. 1989), the timing argument (Khan & Woltjer 1959; Gunn 1975; Gott & Thuan 1978; Mishra 1985; Einasto & Lynden-Bell 1982; Raychaudury & Lynden-Bell 1989) and the internal dynamics of spiral galaxies (Salucci et al. 1993), all agree with a density parameter value well below 1. Similar indications come from larger scale density determination based on the application of the Cosmic Virial Theorem (Peebles 1976), on the pairwise velocity dispersion of galaxies (Bean et al. 1983; Davis & Peebles 1983; Hale-Sutton et al. 1989), on the virial estimation of galaxy clusters' mass and on analyses of the galaxy groups' dynamics (Huchra & Geller 1982). The bulk of the evidence indicates a low Ω_o value (≤ 0.35) on scales $< 10\,h^{-1}$Mpc.

- Dynamical analyses based on the large scale velocity field give different results. The comparisons of the radial peculiar velocity field with the predicted velocities obtained from the observed galaxy number density (Strauss & Davis 1988; Kaiser et al. 1991), the IRAS/POTENT method (e.g. Dekel et al. 1993, Dekel 1994, Hudson et al. 1995), redshift–space distortions (PD, Fisher 1994) and the analysis of the outflows in voids (Dekel & Rees 1994) are consistent with an $\Omega_o = 1$ universe. Similarly, dipole estimates based on IRAS galaxies (Rowan-Robinson et al. 1990; SDHYF92 but see Plionis et al. 1993) are consistent with $\Omega_o = 1$. Finally, previous discrepancies arising from the cluster dipole analyses that seemed to indicate a low Ω_o universe disappear when, as we have seen in the previous Chapter, z–space distortions effects are minimized, allowing us to reconcile the cluster dipole amplitude with $\Omega_o = 1$.

If true, these observations indicate that $\sim 90\%$ of the mass in the universe clusters only on scales larger than $10\,h^{-1}\mathrm{Mpc}$. Alternatively, one may think that some systematic bias affects the dynamical Ω_o estimate either on large or small scales. For example the velocity bias detected in a number of numerical experiments (Carlberg & Dubinski 1991; Katz & White 1993; Carlberg 1993 Carlberg & Couchman 1989; Carlberg, Couchman & Thomas 1990; Carlberg 1991; Couchman & Carlberg 1992) together with hydrodynamical effects (Cen & Ostriker 1992) may reconcile the density determination on scales dominated by non–linear dynamics with an Einstein–De Sitter universe. On the other side the large spread that characterizes the measurements of Ω_o on large scales does not allow to rule out a low Ω_o universe. Finally, a possible cause of this dichotomy may originate from the use of different measurement techniques, a problem that can be solved by using the same technique over the largest possible range of scales. The LAP method is flexible enough to be applied over a large range of scale ($[0.1 - 30]\ h^{-1}\mathrm{Mpc}$), allowing a homogeneous analysis over different dynamical regimes and scales. To accomplish this task, however, the LAP technique needs to be carefully tested to identify and eliminate the possible biases. In particular the major concern is that the LAP assumes that luminous objects can be considered pointlike also at high redshifts where the overdensities from which galaxies form overlap in a quasi-homogeneous density field.

In this chapter we describe in detail the LAP technique and we implement its 'standard' numerical version (P1 and P2). To test our LAP code we have reproduced the P1 and P2 results, which also allows to discuss with more details the LG dynamics and the local Ω_o value. In the last part we will address the problem of the LAP reliability. More precisely we will use N–body simulations to appreciate the existence of possible mass biases.

4.1   THE LEAST ACTION PRINCIPLE METHOD

In this section we implement the LAP in a Friedmann expanding universe, assuming the GI picture. We describe the 'standard' P1 and P2 technique and the modifications that have been proposed in the literature.

4.1.1   The Least Action Principle: Basics

The Least Action Principle (also known as integral Hamilton's Principle) describes the motion of those mechanical systems for which all forces are derivable from scalar potential that may be function of the coordinates, velocities and time.

The principle can be stated as: *The motion of the system from time t_1 to time t_2 is such that the line integral*

$$S = \int_{t_1}^{t_2} L dt, \tag{4.1}$$

where L is the Lagrangian of the system, has a stationary value for the correct path of the motion.

The quantity S is referred to as the action of the system. That is, out of all possible paths by which the system's point could travel from its position at time t_1 to its position at time t_2, it will actually travel along that path for which the value of the integral (4.1) is stationary. The term "stationary value" for a line integral means that the integral along the given path has the same value to within first–order infinitesimals as that along all neighbouring paths. The notion of stationary value for a line integral thus correspond in ordinary function theory to the vanishing of the first derivative.

It is possible to summarize the LAP principle by saying that the motion is such that the *variation* of the line integral S for fixed t_1 and t_2 is zero:

$$\delta S = \delta \int_{t_1}^{t_2} L(x_1, ..., x_n, \dot{x}_1, ..., \dot{x}_n) dt = 0, \tag{4.2}$$

where x_i is the position of the i–th particle and $\dot{x}_i$ its time derivative.

Let us consider now a system of N particles interacting by the potential V. The action of the system is

$$S = \int_{t_1}^{t_2} dt \left[\sum_{i}^{N} \frac{m_i}{2} \left(\frac{d\mathbf{x}_i}{dt} \right)^2 - V \right], \tag{4.3}$$

where m_i is the particle mass. Under the infinitesimal change of orbits $\mathbf{x}_i \rightarrow \mathbf{x}_i + \delta\mathbf{x}_i(t)$, the action changes by the amount

$$\delta S = \int_{t_1}^{t_2} dt \delta\mathbf{x}_i \cdot \left[-m_i \frac{d^2\mathbf{x}_i}{dt^2} - \frac{\partial V}{\partial \mathbf{x}_i} \right] + \left[m_i \delta\mathbf{x}_i \cdot \frac{d\mathbf{x}_i}{dt} \right]_{t_1}^{t_2}. \tag{4.4}$$

If the last term vanishes, then the orbits satisfy the Euler–Lagrange equations. This condition is usually satisfied by fixing the positions, so $\delta x_i = 0$ at $t = t_1$ and $t = t_2$; but note that the principle also applies if dx_i/dt vanishes at the extrema; it is thus suitable for dealing with mixed boundary values problems.

4.1.2 Implementing the LAP in an Expanding Universe

Peebles' implementation of the LAP assumes that the peculiar gravitational acceleration of a galaxy can be estimated by concentrating the mass of the system around the visible galaxies. The gravitating system can therefore be regarded as a system of pointlike objects labelled by i, with masses m_i at the comoving position $x_i(t)$ at the time t. In the GI+hierarchical clustering framework the above picture can be questioned at high redshift, when the mass distribution must be nearly homogeneous, and at present–epoch for most of the cosmological models with $\Omega_o = 1$, in which galaxies are surrounded by extended overlapping haloes.

This simplistic mass assignment scheme, however, is not so unphysical if one supposes that at early epochs the masses of the protogalaxies were in regions with simple boundaries so that it is possible to concentrate the mass within each region in such a way that the gravitational field at the neighboring positions approximates that of the true mass distribution. In practice, one assumes that each pointmass traces the motion of the mass component out of which it is assembled, and it is assumed that the gravitational effect of these components on the motions of the other mass elements at high redshifts is well approximated by replacing the distributed mass with a single particle at the center of mass. This assumption is realistic provided that the clustering is not strong so that galaxies develop most of their motion at low redshifts, when there is ample room for the existence of galaxies as well defined mass concentrations. We will discuss the limits of this assumption and the possible biases that it can generate in the next section.

In an expanding universe it is convenient to write the proper separations between two particles $r(t)$ as

$$r(t) = a(t)x(t), \tag{4.5}$$

where $x(t)$ is the separation expressed in comoving coordinates and $a(t)$ is the expansion factor. In these coordinates the proper velocity of a particles u is

$$u = a\dot{x} + \dot{a}x, \tag{4.6}$$

where $a\dot{\mathbf{x}}$ is the peculiar velocity, and $\dot{a}\mathbf{x}$ is the recession velocity. The Lagrangian for the particle's motions is

$$L = \frac{1}{2}m(a\dot{\mathbf{x}} + \dot{a}\mathbf{x})^2 - m\Phi(\mathbf{x}, t), \tag{4.7}$$

where $\Phi(\mathbf{x}, t)$ is the gravitational potential. After the canonical transformation (Peebles 1980)

$$L' \to L - \frac{d\psi}{dt}, \qquad \psi = \frac{1}{2}ma\dot{a}x^2, \tag{4.8}$$

the Lagrangian for a systems of N particles becomes

$$L' = \sum \frac{m_i a^2}{2}\left(\frac{d\mathbf{x}_i}{dt}\right)^2 + \frac{G}{a}\sum_{i \neq j}\frac{m_i m_j}{|\mathbf{x}_i - \mathbf{x}_j|} + \frac{2}{3}\pi G\rho_b a^2 \sum m_i \mathbf{x}_i^2, \tag{4.9}$$

where $\rho_b(t)$ is the mean background density. The action S in comoving coordinates is therefore

$$S = \int_0^{t_o} dt \left[\sum \frac{m_i a^2}{2}\left(\frac{d\mathbf{x}_i}{dt}\right)^2 + \frac{G}{a}\sum_{i \neq j}\frac{m_i m_j}{|\mathbf{x}_i - \mathbf{x}_j|} + \frac{2}{3}\pi G\rho_b a^2 \sum m_i \mathbf{x}_i^2\right], \tag{4.10}$$

where the integration limits formally correspond to the present–epoch, t_o, and to the Big Bang epoch in the Friedmann universe.

The variation of the action after an infinitesimal change δS of an orbit is

$$\delta S = \int_0^{t_o} dt\,\delta\mathbf{x}_i \cdot \left(-\frac{d}{dt}m_i a^2 \frac{d\mathbf{x}_i}{dt} + m_i a\mathbf{g}_i\right) + \left[m_i a^2 \delta\mathbf{x}_i \cdot \frac{d\mathbf{x}_i}{dt}\right]_0^{t_o} \tag{4.11}$$

where the peculiar acceleration $\mathbf{g}_i$ is

$$\mathbf{g}_i = \frac{4}{3}\pi G\rho_b a\mathbf{x}_i + \frac{G}{a^2}\sum_j m_j \frac{\mathbf{x}_j - \mathbf{x}_i}{|\mathbf{x}_j - \mathbf{x}_i|^3}. \tag{4.12}$$

The last term on the r.h.s. of eq. (4.11) comes from integration by parts. To satisfy the Lagrange–Euler equations of motion the last term must vanish, implying

$$\delta\mathbf{x}_i = 0 \qquad \text{or} \qquad a^2 \frac{d\mathbf{x}_i}{dt} = 0 \tag{4.13}$$

at $t = 0$ or at $t = t_o$. The above requirements constitute the mixed boundary conditions that the LAP orbits must satisfy. The condition $\delta\mathbf{x}_i = 0$ at $t = t_o$ can be fulfilled if we can measure the position of the luminous objects within the system. The second bound is automatically satisfied when assuming the GI framework in which the primeval peculiar velocities vanish at early epochs:

$$a\frac{d\mathbf{x}_i}{dt} \to 0 \quad \text{when} \quad a \to 0,$$

which is more stringent than the second condition in eq. (4.13). Therefore, assuming the GI picture and provided that we know the positions of the galaxies, $\delta S = 0$ (that is the action is at a stationary point) when the orbits satisfy the equations of motion.

To implement the LAP we need to model the orbits using some trial functions:

$$x_i^\alpha(t) = x_i^\alpha(t_o) + \sum_n C_{i,n}^\alpha f_n(t), \qquad (4.14)$$

where $\alpha = 1, 2, 3$ are the components of the orbits, $f_n(t)$ are functions satisfying the boundary conditions in eq. (4.13) and $x_i^\alpha(t_o)$ represent the initial positions of the galaxies. In this work we use the same P1 set of 'standard' trial functions $f_n = a^n(1 - a)$, $n = 0, 1, 2, 3, 4$. As already pointed out by P1, the final results weakly depend on the choice of f_n. For example very similar results are obtained with the set of trigonometric functions $f_n = \sin(n\pi a/2)$. A judicious choice of the trial functions, however, depends on the problem considered, as discussed below.

The derivative of the action with respect to an expansion coefficient $C_{i,n}^\alpha$ is

$$\frac{\partial S}{\partial C_{i,n}^\alpha} = m_i \int_0^{t_o} dt f_n(t) \left[-\frac{d}{dt} a^2 \frac{dx_i^\alpha}{dt} + \frac{4}{3}\pi G\rho_b a^2 x_i^\alpha(t) + \frac{G}{a}\sum_j m_j \frac{x_j^\alpha - x_i^\alpha}{|\mathbf{x}_i - \mathbf{x}_j|^3} \right]. \qquad (4.15)$$

The orbits that are minima for the action satisfy the set of equations

$$\frac{\partial S}{\partial C_{i,n}^\alpha} = 0. \qquad (4.16)$$

Here we consider a cosmologically flat universe with a non–vanishing cosmological constant, thus the time interval is

$$H_o dt = \frac{a^{1/2}da}{[\Omega_o + a^l(1 - \Omega_o)]^{1/2}}, \qquad (4.17)$$

where $l = 1$ if $\Lambda = 0$ and $l = 3$ if the model is cosmologically flat. In the present implementation we will just consider the case in which $l = 3$ since open models with vanishing cosmological constant give similar results as the cosmologically flat ones with smaller expansion times. Using (4.15) and (4.17), it is easy to show that orbits satisfying (4.16) also satisfy the cosmological equations of motion

$$a^{1/2}\frac{d}{da} a^{3/2}\frac{d\mathbf{x}_i}{da} + \frac{3(1 - \Omega_o)a^4}{2F}\frac{d\mathbf{x}_i}{da} = \frac{\Omega_o}{2F}\left[\mathbf{x}_i + \frac{R_o^3}{M_T}\sum_j \frac{m_j(\mathbf{x}_j - \mathbf{x}_i)}{|\mathbf{x}_j - \mathbf{x}_i|^3} \right], \qquad (4.18)$$

where $F = \Omega_o + (1 - \Omega_o)a^3$ and R_o is the radius of the sphere that would contain the LG total mass, M_T, in an homogeneous universe at the present–time.

The equation of motion for the particle orbits expressed in physical length units, $\mathbf{r}(t)$, is

$$\frac{d^2\mathbf{r}_i}{dt^2} = \sum_{i \neq j} \frac{Gm_j(\mathbf{r}_j - \mathbf{r}_i)}{|\mathbf{r}_j - \mathbf{r}_i|^3} + \frac{\Lambda}{3}\mathbf{r}_i - \frac{4}{3}\pi G(\rho_h + 3p_h/c^2)\mathbf{r}_i, \tag{4.19}$$

where the last term accounts for a mass component hot enough to resist clustering on the scale of the system considered, with a local density close to the local mean. Its gravitational effect is similar to that of a cosmological constant. From eq. (4.19) it is clear that if Λ vanishes and in the absence of a hot component, the physical orbits $\mathbf{r}_i(t)$ are independent of Ω_o for a given expansion time, while the peculiar motions depend on the background Cosmology. Furthermore, when the expansion time t_o is held fixed there is no large difference between the prediction of an open model and a cosmologically flat one with the same Ω_o value. Similar considerations hold in presence of a hot, diffuse mass component.

In the present LAP implementation we use the P1 scheme to find the minima of S, in other words we adjust the coefficient $C_{i,n}^\alpha$ by stepping down the gradient of S with increments

$$m_i \delta C_{i,n}^\alpha \propto -\frac{\partial S}{\partial C_{i,n}^\alpha} \tag{4.20}$$

starting from the trial set $\left\{C_{i,n}^\alpha\right\}_o = 0$. The action S and its derivatives have been numerically evaluated from the integrals (4.10) and (4.15) using 100 uniformly spaced steps in a.

Knowing positions, redshifts and luminosities of all the objects to which we assign the same M/L ratio, we obtain the LAP orbits following the procedure below:

1. Choose the initial set of unknown coefficients $\left\{C_{i,n}^\alpha\right\}_o$.

2. Assume a cosmological background [the (Ω_o, H_o, Λ) set].

3. Select a M/L value.

4. Minimize the action by following the gradient and find the final $\left\{C_{i,n}^\alpha\right\}$ set.

5. Compare the observed redshift of anyone object to its recession velocity found by the minimization procedure (the LAP–redshift). If the difference between the two quantities is larger than a tolerance fixed *a priori* then back to step 3.

6. Compare the observed and the LAP–redshift of all the objects. If their residual are too large then back to step 2.

7. If one wants to estimate how the choice of $\left\{C_{i,n}^{\alpha}\right\}_{o}$ affects the final results then back to step 1.

At the end of the whole procedure we are able to trace the galaxy orbits back in time, to constrain the M/L value within the system and to determine the preferred cosmological background.

Finding Multiple Solutions:

With our procedure one finds the $\left\{C_{i,n}^{\alpha}\right\}$ set that minimizes the action. As a consequence the related orbits will represent galaxies approaching each other for the first time. This configuration is plausible for dynamically young systems for which the crossing time is larger than the typical evolutionary timescale (the expansion time in our case). When the clustering is large enough for the crossing time to be smaller than the Hubble time, other solutions representing stationary points that are not minima for the action, appear. In this case the LAP method finds multiple solutions and one has to decide which one describes the true dynamical history of the system. In practice this means than the LAP is not useful in the strongly non–linear regime when the number of solutions is very high, but it can be successfully employed in the mildly non–linear regime when the number of possible configurations is small enough to make a decision possible.

A convenient way to find multiple solutions at stationary points has been proposed by P2. In this case the increments $\delta C_{j,m}^{\beta}$ can be obtained by solving the equation

$$\frac{\partial S}{\partial C_{i,n}^{\alpha}} = \sum \delta C_{j,m}^{\beta} \frac{\partial^{2} S}{\partial C_{i,n}^{\alpha} \partial C_{j,m}^{\beta}}, \tag{4.21}$$

where the sum is over repeated index and

$$\frac{\partial^{2} S}{\partial C_{i,n}^{\alpha} \partial C_{j,m}^{\beta}} = m_{i} \int_{0}^{t_{o}} dt \left[\delta_{ij}\delta_{\alpha\beta} \left(a^{2}\frac{df_{n}}{dt}\frac{df_{m}}{dt} + \frac{4}{3}\pi G\rho_{b}a^{2}f_{n}f_{m} \right) + \frac{G}{a}T_{ij}^{\alpha\beta} \right], \tag{4.22}$$

with

$$T_{ij}^{\alpha\beta} = m_{i} \left[\frac{3x_{ij}^{\alpha}x_{ij}^{\beta}}{x_{ij}^{5}} - \frac{\delta_{\alpha\beta}}{x_{ij}^{5}} \right], \quad \text{for} \quad i \neq j$$

$$= \sum_{i\neq k} m_{i} \left[\frac{3x_{ik}^{\alpha}x_{ik}^{\beta}}{x_{k}^{5}} - \frac{\delta_{\alpha\beta}}{x_{ik}^{5}} \right], \quad \text{for} \quad i = j, \tag{4.23}$$

and $\mathbf{x}_{ij} = \mathbf{x}_{i} - \mathbf{x}_{j}$.

This matrix inversion method has been applied by Peebles to study in detail the orbits of the local group's members (P2 and P3). The problem of deciding among the sets

of possible solutions is not easy to solve since very often different configurations reproduce the observed galaxy recession velocities equally well.

The existence of multiple orbits does not affect very much the reliability of the LAP as a cosmological test since the different acceptable solutions find similar M/L ratios and (Ω_o, H_o, Λ) sets. The number of solutions increases with the clustering; a first attempt of using the LAP in these conditions has been recently performed by P4 who modified the standard LAP method to study the dynamics of the dwarf spheroidal companions of the Milky Way (Fornax, Leo I and Leo II). The approach used in that case is to parametrize the orbits of the companions by their positions at a discrete set of world times. The solutions are found by iteratively relaxing random orbits. The procedure is similar to the Feynman path integral formulation of quantum mechanics and the hope is to assign a probability to the different orbits to quantify the likelyhood of the different possible system configurations.

Parametrizing the Orbits:

The choice of trial orbits is not completely free but it should depend on the problem studied. For example, the simple trial orbits $f_n = a^n(1-a)$ satisfies the boundary conditions eq. (4.13) so that they have to be modified if, instead of distances, the orbits are constrained to observed redshifts. Furthermore, to avoid unphysical oscillations a necessary requirement is that the set of trial orbits $f_n(t)$ sample in a continuous way the time axis. This constraint comes from the fact that orbits have to be such that the integral in eq. (4.15) vanishes, which means that the LAP orbits must satisfy the equations of motion in a time average sense, the trial functions f_n being the temporal weights. To avoid unphysical solutions the orbits have to satisfy the equations of motion at any time and thus $f_n(t)$ must overlap to evenly sample the interval of integration.

A judicious choice of f_n should also account for the dynamical status of the system considered. In the mildly non–linear regime P3 showed that it is better to iterate to solutions starting from a random set of trial orbits, $\left\{ C_{i,n}^{\alpha} \right\}_o$, that twist around each other with the further requirement that the present–time position is approached with relatively small velocity. On the other extreme when dealing with quasi linear systems composed by thousand of particles one is not interested in studying the single orbits. The main requirement in that case a rapid convergence of the sum (4.14) which should also reproduce linear theory in the limit of small perturbation. Giavalisco et al. (1993) proposed the following set of orbits:

$$x_i^{\alpha}(t) = x_i^{\alpha}(t_o) + C_{i,1}^{\alpha}[D(t) - D_o] + C_{i,2}^{\alpha}[D(t) - D_o]^2 ....., \qquad (4.24)$$

where $D(t)$ is the growth function of linear modes and D_o its value at the present–epoch. Clearly (4.24) generalizes the Zel'dovich approximation (Zel'dovich 1970) to which it reduces in the limit of small displacements.

Applying the LAP to Redshift Survey:

A homogeneous and complete sampling of the dynamically relevant mass tracers is required to properly apply the LAP. Our 'standard' LAP implementation uses observed distances to predict recession velocities. Unfortunately reliable distance estimates are available for a very limited number of galaxies and the further requirement of complete sampling put very stringent limits on the dimension of the system to which the LAP can be applied. In practice, using the standard 'distance scheme' one cannot hope to study the dynamics on scales much larger than those of the LG. To extend the LAP analysis to larger scales one has to implement the so called 'redshift scheme' in which, starting from observed redshifts, the LAP is used to predict present–time galaxy positions, similarly to the iterative reconstruction we presented in the previous Chapter.

As outlined by Giavalisco et al. (1993) and by P3, when one uses the 'redshift scheme' the matrix of the second derivatives, $\partial^2 S/\partial C_{i,n}^{\alpha} \partial C_{j,m}^{\beta}$, in general cannot be derived from a scalar function of the unknown coefficients $\{C_{in}^{\alpha}\}$. To overcome this problem SPT have proposed an iterative scheme in which the objects are initially placed at trial positions, then the LAP orbits are found by following the gradient and, after having compared the observed and the LAP–redshifts, the points are replaced at new starting positions. The final orbits are found by iterating the whole procedure.

4.2   A LAP APPLICATION: THE LOCAL GROUP'S DYNAMICS

The LG is essentially an isolated binary system composed by two nearly equally massive galaxies (Milky Way and M31) surrounded by dwarf companions (N6882, I1613, WLM, Sex A, N1309 and N300). The characteristics of the LG member galaxies are summarized in Table (4.1).

The line–of–sight velocity of M31 with respect to MW is -125 km/sec. This is an unexpected result, since most galaxies are moving apart with the general Hubble expansion. One possible explanation is that M31 and MW have a random velocity dispersion relative to

Name	r_g	l	b	M_r	v_g
MW	-	-	-	0.7	-
M31	0.72	121.2	-21.6	1.0	-125
NGC 6822	0.49	25.3	-18.4	0.025	44
IC 1613	0.72	129.7	-60.6	0.025	-159
WLM	0.96	75.9	-73.7	0.025	-67
Sextans A	1.6	246.2	39.9	0.025	164
NGC 3109	1.6	262.1	23.1	0.1	193
NGC 300	1.8	299.2	-79.4	0.1	102
Sculptor	$2.66h^{-1}$	105.8	-85.8	2.0	219
Maffei	$2.66h^{-1}$	136.4	-0.4	2.0	168

Table 4.1: LG Galaxy Parameters. Column 1: Galaxy Name, Column 2: Distance to MW (Mpc), Column 3: Galactic Longitude, Column 4: Galactic Latitude, Column 5: Mass relative to M31 mass, Column 6: Radial velocity in the MW frame (km/sec).

the Hubble flow. In this case, the LG would be an accidental and temporary superposition. However, the probability of having such a superposition is quite low (5% ÷ 10% according to van den Bergh 1971). Moreover, according to the gravitational instability picture, in which galaxies have developed from small amplitude perturbations of the primordial density field, random velocities are expected to decay with time as $t^{2/3}$, and the present peculiar velocities would require a much higher velocity dispersion in the past, which can hardly be generated by any plausible physical mechanism.

It seems, therefore, that M31 and MW constitute a self–gravitating system. In this case, the Hubble flow has been locally halted and reversed by the mutual gravitational interaction. Classical Mechanics predicts the relative motion of these two objects: their relative separation r evolves with time according to Kepler's equation

$$r = a(1 - \cos\eta) \quad ; \quad t = \sqrt{\frac{a^3}{GM}}(\eta - e\sin\eta) + c, \tag{4.25}$$

where c is a constant, M is the LG mass, a, e and η are respectively the semi–major axis, the eccentricity, and the eccentric anomaly of the orbit. At high redshifts $r \to 0$ and $t \to 0$, therefore $e = 1$ and $c = 0$.

Their relative radial velocity can be written as

$$\frac{dr}{dt} = \frac{dr/d\eta}{d\eta/dt} = \sqrt{\frac{GM}{a}}\frac{\sin\eta}{1 - \cos\eta} = \frac{r}{t}\frac{\sin\eta(\eta - \sin\eta)}{(1 - \cos\eta)^2}. \tag{4.26}$$

At the present-epoch t_0, $r_0 \simeq 0.75$ Mpc and $\left(\frac{dr}{dt}\right)_0 \simeq 125$ km/sec. From eq. (4.26) it is possible to evaluate η by constraining the age of the universe t_0 in the range of the

commonly accepted values. If we suppose that M31 and MW are approaching for the first time ($\pi < \eta < 2\pi$), as confirmed by the successful LG formation model proposed by Peebles et al. (1989), then it is possible to determine the LG mass. The first value, obtained by Khan and Woltjer in 1959 ($\simeq 1.8 \times 10^{12}\ M_\odot$), has been enhanced by a factor ~ 2 in subsequent analyses.

Furthermore, dynamical influences of external groups cause the orbit of the binary system to be inevitably subjected to torques. The timing mass for orbits with angular momentum has been evaluated by Einasto & Lynden–Bell (1982): the LG mass turned out to be in the range $3 \div 6 \times 10^{12}\ M_\odot$. A different analysis carried out by Raychaudury & Lynden–Bell (1989) yielded that the effect of neighbouring galaxies on the M31–MW orbit does not greatly affect the radial–orbit timing mass estimate of the LG.

Even though we are considering an infalling system, in which the dark component and the galaxies are expected to have the same velocity (Carlberg 1991), these measures can only show that the Ω_o value on scales < 100 Kpc is far below unity and, therefore, that the mass in an $\Omega_o = 1$ universe cannot be concentrated around visible galaxies. As shown by Kroeker and Carlberg (1991) in their analysis based on N–body data, the timing argument for M31 and MW is consistent with the existence of extended galactic haloes in an $\Omega_o = 1$ universe.

Since the LG is thought to be a dynamically–young system composed by galaxies with known distances, it is a a good candidate for applying our numerical LAP code. In order to minimize the action we need to know positions, masses and peculiar velocities of the member galaxies. The masses of the objects are unknown, but all we actually need is their relative masses, i.e. the masses normalized to the mass of an arbitrarily fixed galaxy, under the assumption of constant M/L ratio for all the LG members. The reference mass is that of M31. As we have seen, one has to specify also the set cosmological parameters (Ω_o, h, Λ). Since we will consider only flat universes, the cosmological constant Λ is simply $1 - \Omega_o$. Orbital parameters, masses and a reliability estimates for the set of cosmological parameters are then obtained by minimizing the action under the condition that the line–of–sight peculiar velocity of M31 is reproduced. P1 and P2 found that the preferred cosmological model to reproduce the LG dynamics is ($\Omega_o = 0.1$, $h = 0.75$, $\Lambda = 0.9$). In what follows we use our LAP code to look at this result in detail.

To eliminate the singularity in the gravitational acceleration at zero separation, P1

modified the last term in eq. (4.12)

$$\frac{x_i - x_j}{[x_i - x_j + \epsilon_{ij}]^{3/2}},$$

(4.27)

with corresponding changes in the derivatives of the action. The softening parameter, ϵ_{ij}, has been imposed to be the same for each galaxy ($\epsilon = \epsilon_{ij}$) and has been set equal to 3 % of R_o. This large softening is not unrealistic because, according to the methods described previously, observations indicate that the large mass detected is distributed in halos, even in a low–density universe. However, as we have verified, quite similar results are obtained with $\epsilon = 0$ because the derived LG–galaxies' orbits are seldom close.

The LG galaxies considered in the standard P1 solution are listed in Table (4.1) in which the neighbouring Sculptor and Maffei groups are considered as well. Their distances, however, are based on the infra–red Tully–Fisher relation, calibrated to the redshift of more distant galaxies. The Hubble parameter enters therefore in two ways: by fixing the distance of the two external groups and by determining the present–epoch t_o. A cosmologically flat universe with $\Omega_o = 0.1$, gives $t_o = 12.6$ Gyr. In this model $h = 0.75$, therefore $t_o = 17$ Gyr, which is in the range of the acceptable values.

Figures (4.1a) and (4.1b) show the orbits found with the standard solution both in comoving and physical coordinates, respectively. The orbits are traced back in time up to an expansion factor of 0.1.

Figure (4.2) shows the LAP–redshifts against the observed redshift corrected to the center of MW, relative to the solution in Fig. (4.1a). The results are fully consistent with those obtained by P1, constituting a consistency check for the numerical code we have developed. In the standard solution NGC 6882 is approaching the MW for the first time, but its peculiar velocity is too negative. According to P2 this probably means that the actual orbit can be found at a stationary point that is not a minimum for S. NGC 6882 is in fact close enough to MW to have already completed an orbit, in which case now would be falling toward MW for the second time. In this case the $\delta S = 0$ solution is not unique and the matrix inversion method need to be applied. Starting with a particular set of initial condition, P2 found this stationary solution which closely reproduces the observed recession velocity of NGC 6882. The lack of this solution in the our analysis is not a serious concern since NGC 6882 has a low mass and its orbit does not affect final velocities of the other galaxies but only their initial positions. In other words one finds nearly the same mass for M31 irrespectively of the NGC6882 orbit.

The total mass of the LG turns out to be 6.4×10^{12} $M_\odot$, with MW having a mass

x (Mpc)
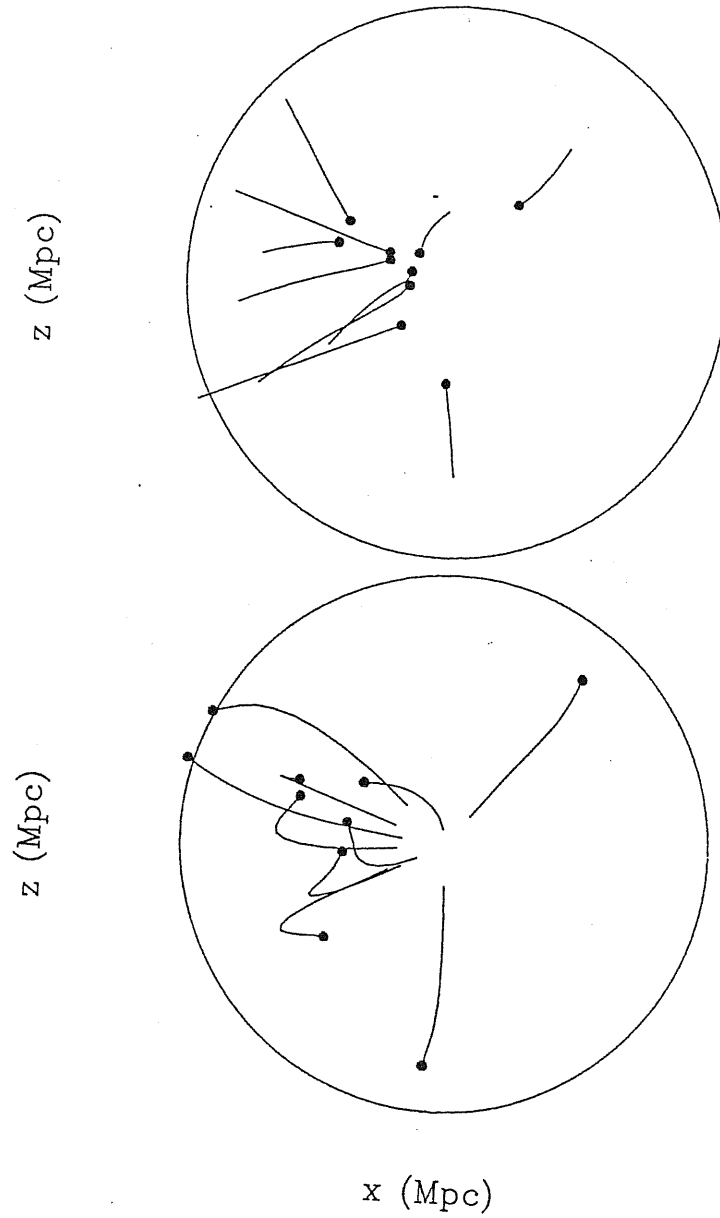
Figure 4.1: The local group LAP–reconstructed orbits for the $\Omega_o = 0.1$, $h = 0.75$ case. Black dots represent the present time galaxy positions. The radius of the sphere (= 6.77 Mpc) is the radius of that sphere that would contain the total mass of the system if the universe were homogeneous. The orbits are plotted in (a) co–moving coordinates and (b) physical coordinates.
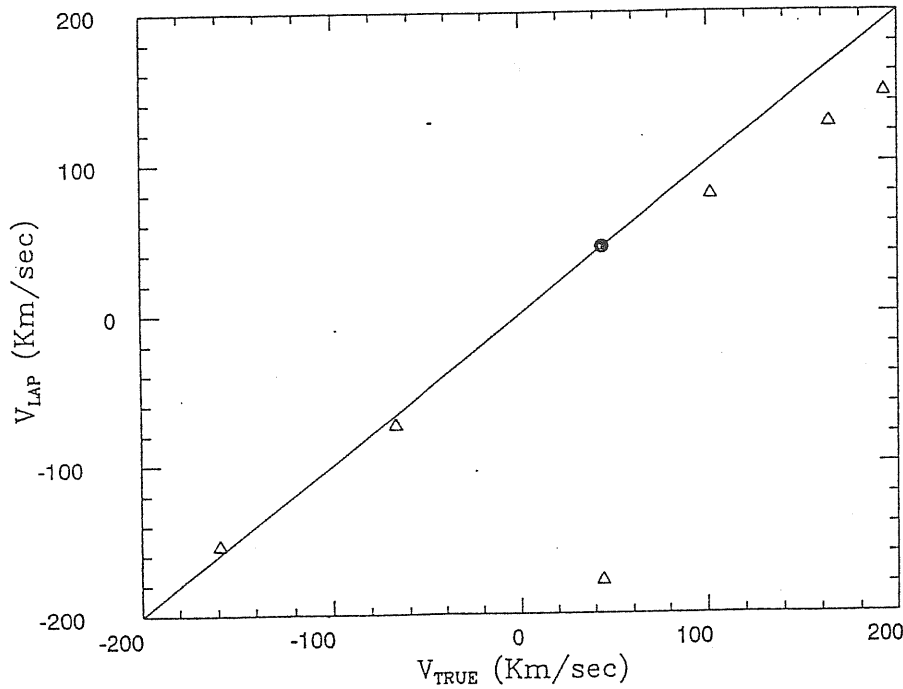
Figure 4.2: Peculiar velocities found using the LAP technique versus the true peculiar velocities. The same experiment as in fig. (4.1a) and (4.1b) The large discrepancy refers to the galaxy NGC 6882.

of 4.8×10^{12} $M_\odot$. The radius of the sphere that would contain the LG total mass in a homogeneous universe is $R_o = 6.7$ Mpc

The LAP method also allows us to estimate the transverse peculiar velocity v_t of M31 relative to MW. This is an important issue since it allows us to understand whether the MW–M31 system is gravitationally bound or not. The standard solution with Maffei and Sculptor group yields $v_t = 110$ km/sec but this result is very sensitive to the presence of external mass distribution: if the Maffei and Sculptor groups are ignored it would decrease to $v_t = 20$ km/sec while a larger transverse velocity is found when more distant galaxies are taken into account (DL1). This problem is closely related to the mechanism through which M31 and MW acquire their angular momenta. The study of the M31 and MW dynamics, however, is a difficult one since, as shown by P3, different LAP solutions exist in which M31 and MW reach their present–time positions following very different orbits. Once more the central problem is to select the 'true' solution from the set of plausible ones.

Starting from our 'standard' solution, it is now possible to explore the effect of changing the cosmological parameters h and Ω_o.
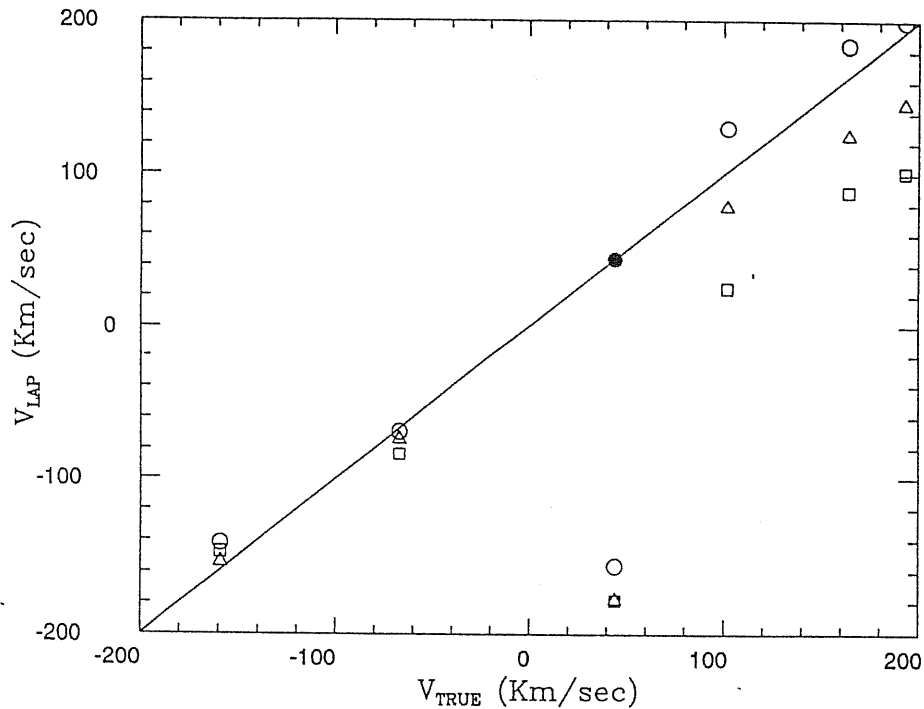
Figure 4.3: The same as in fig. (4.2). Open circles refer to the LAP experiment with $\Omega_0 = 0.1$, $h = 1.0$; open triangles represents the $\Omega_0 = 0.1$, $h = 0.75$ case, and open squares are the $\Omega_0 = 0.1$, $h = 0.5$ galaxies.

The effect of varying h

The value of the Hubble constant affects the solution through the timescale t_0 and determines the distance of the Sculptor and Maffei groups. We have ran three LAP simulations with $h = 0.5, 0.75, 1$. The predicted peculiar velocities for the three cases are plotted in Fig. (4.3).

For all the galaxies but NGC 6822 (for which P2 found that the passing solution does not exist when $h = 1$) good fits are obtained for $h = 1$ and $h = 0.75$. When $h = 0.5$ the age of the universe is $t_0 = 25$ Gyr., which means that in this model galaxies had a lot of time to experience gravitational interaction. As a result the velocities of NGC 300, Sextans A and NGC 3109 are systematically underestimated.

The Effect of Varying Ω_0

Besides the low Ω_0 model, we have considered an Einstein–De Sitter universe with $h = 0.5$ to obtain an acceptable time scale $t_0 = 13$ Gy. Fig. (4.4) shows the LAP orbits in comoving coordinates relative to Ω_0. The orbits are qualitatively different from the standard case, the main difference being in the relative motion of the three groups, that will be discussed in the next section. For the Einstein–de Sitter case the mass of the LG turned out

z (Mpc)

x (Mpc)
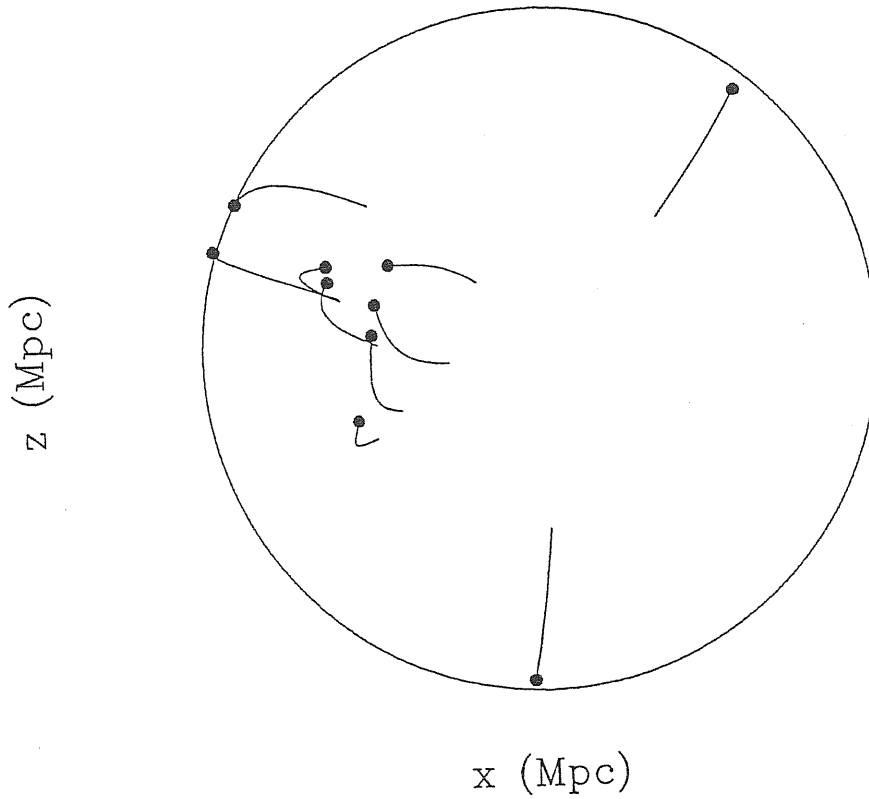
Figure 4.4: The The local group LAP–reconstructed orbits in physical moving coordinates for the $\Omega_o = 1$, $h = 0.5$ case. Black dots represent the present time galaxy positions. The radius of the sphere ($= 3.9$ Mpc), is that one that would contain now the total mass of the system if the universe were homogeneous.

to be $M_{LG} = 5.3 \times 10^{12}$ $M_\odot$ and $R_o = 3.9$ Mpc.

Despite of the different orbits, as shown in Fig. (4.5), the predicted peculiar velocities of the LG members match the observed velocities almost as well as in the standard case. Varying Ω_o does not affect appreciably the motions within the LG. Since, as we have seen, this is also true for the Hubble parameter and for the cosmological constant (P3) it is possible to generalize this statement by claiming that the background cosmology weakly affects the dynamics within the LG.

The Dynamical Influence of the Sculptor and Maffei Groups.

As for the background cosmological model, Sculptor and Maffei groups do not influence appreciably the dynamics of the LG galaxies. The Sculptor and Maffei groups' motion, relative to the LG can be used, however, to discriminate among different cosmological

Figure 4.5: LAP peculiar velocities versus true peculiar velocities. The open triangles represent the standard $\Omega_o = 0.1$, $h = 0.75$ solution while open circles refer to $\Omega_o = 1$, $h = 0.5$.
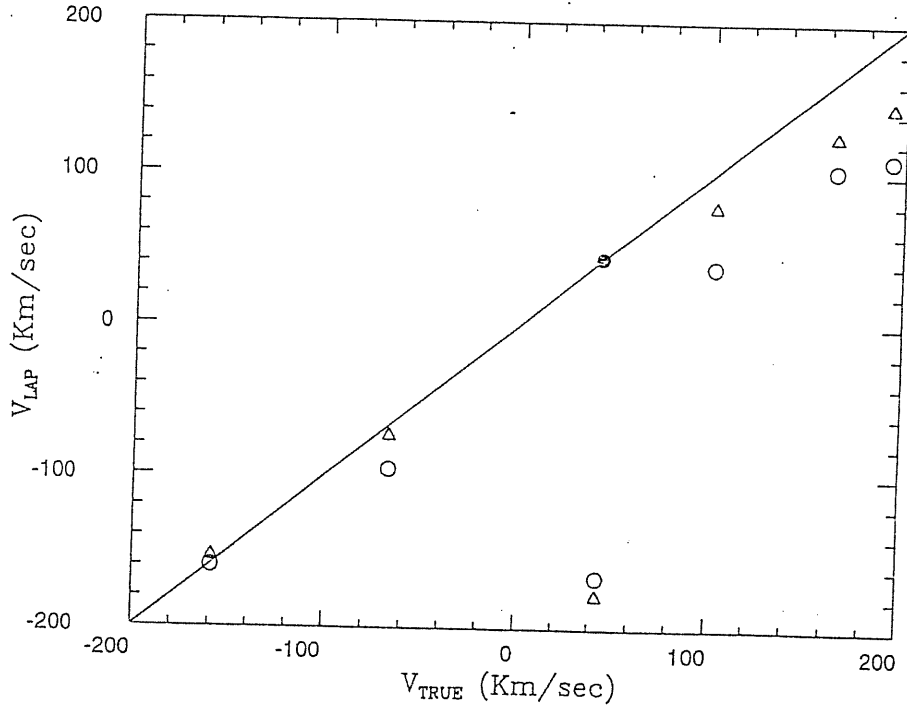
models.

As reported in Table (4.2), the standard solution yields a negative line–of–sight velocity for the Sculptor group which is reasonably close to the observed one, though an even better agreement is achieved with $h = 0.5$. In the Einstein–de Sitter solution, however, the two groups are receding from the LG, contrary to the observations. This difference can be easily understood: in the low–density solution, the three groups are in an overdense region, causing them to approach each other, while in an Einstein De-Sitter universe these groups are in a local underdensity. This is the reason why, when $\Omega_o = 1$ the Sculptor's recession velocity found by the LAP is larger than $H_o r$ as reported in Table (4.2). Given the present observational uncertainties, however, it is difficult to decide if this is a significant discrepancy.

The situation for the Maffei group is more complicated. In the low density model the LG is in an overdense region, so that the peculiar relative velocity of Maffei group is negative, indicating an inward motion. This result is in accordance with the Maffei distance assumed by P2, but it is inconsistent with the Mc Call's (1989) distance estimate of IC342 which is a likely member of the Maffei group, placed at ~ 1.5 Mpc. If true, this measure would imply a positive peculiar velocity of IC342 that could be explained only with the existence of

Name	v_g	v_1	v_2	v_3	v_4
NGC 6822	44	-178	-169	-155	-165
IC 1613	-159	-146	-153	-141	-159
WLM	-67	-83	-74	-69	-95
Sextans A	164	88	125	184	103
NGC 3109	193	101	145	199	110
NGC 300	102	25	78	130	38
Sculptor	219	189	147	105	290
Maffei	168	167	130	69	260

Table 4.2: Peculiar velocity. Column 1: Galaxy Name, Column 2: Observed v_g, Column 3: v_1 ($\Omega_o = 0.1$, $h = 0.5$), Column 4: v_2 ($\Omega_o = 0.1$, $h = 0.75$), Column 5: v_3 ($\Omega_o = 0.1$, $h = 1.0$), Column 6: v_4 ($\Omega_o = 1.0$, $h = 0.5$).

a massive system which is hidden by the ZoA. When $\Omega_o = 1$ the Maffei group has a positive relative peculiar velocity, according to Mc Call's distance determination. However, in the solution shown in Fig. (4.4), the relative peculiar velocity of Maffei group is close to zero and adopting the Mc Call's distance instead of the P2 one, would cause a reduction of the peculiar velocity, contrary to the observations. Thus, it appears that the Maffei group's motion when using the McCall distance , is anomalous both in high– and low–density universe.

Finally, although the motion of Sculptor and Maffei groups depends on the value of the density parameter, it is not a very discriminant test because of the presence of external masses which we have not accounted for.

4.3 Ω_o from the Local Group's Dynamics

We have seen that, until the uncertainties on the distance of the Maffei group is not reduced and external masses are not properly accounted for, the motion of the Maffei and Sculptor groups will constitute a rather weak evidence for a low Ω_o universe. Such a case, however, is supported by two other arguments.

- The first one is closely related to the recent LAP applications (P4 and SPT): a value of $M/L = 150$ allows the LAP method to reproduce the observed redshifts on a wide range of scales. Locally, it recovers the observed recession velocities of the Milky Way dwarf companions and the motion of the LG galaxies (P4). On large scales, besides the motion of the neighbouring groups, a low Ω_o universe turns out to be the best

model for reproducing galaxy and group redshifts up to 3000 km/sec (SPT). If true this last result is particularly important since, as discussed in section (4.3.1), it should be unaffected by the mass bias. Moreover, it would indicate that if we live in an Einstein–de Sitter universe then the mass clusters on scales larger than $30\,h^{-1}$Mpc.

- A second argument for a low Ω_o value comes from the observed local galaxy distribution. The LG is located near a region empty of galaxies with a size of $\sim 8\,h^{-1}$Mpc. Since we can survey the galaxies in our neighbourhood considerably further down the luminosity function, we can exclude the presence of faint galaxies in this local void. The straightforward interpretation of this depletion is that gravity has pulled out the matter from the local void to the local concentration. This is possible in a low–density universe in which the material to form the groups is gathered from a region of radius $R_o = 6.7$ Mpc, a size comparable to that of the local void, but seems to be implausible in an $\Omega_o = 1$ universe since, in that case, $R_o = 3.9$ Mpc.

4.4 LAP N–BODY TESTS

According to most of the commonly accepted cosmological scenarios, in an Einstein–de Sitter universe galaxies are surrounded by extended overlapping haloes. As we have seen we implemented the LAP under the hypotheses that the mass in the universe is now concentrated around visible galaxies and that, at early epochs, protogalaxy masses were in regions with simple boundaries: an assumption that can be questioned in an $\Omega_o = 1$ universe. In this section we test the goodness of this assumption, and thus the reliability of the method when $\Omega_o = 1$, by comparing the galaxy masses and orbits found by the LAP with the analogous quantities measured in $\Omega_o = 1$ CDM N–body simulations. In practice we will apply our numerical LAP code to the data extracted from N–body simulations as if they were real data. We start by identifying galaxies using a minimal spanning tree technique and then we characterize the galaxies belonging to a group by their center of mass positions, velocities and masses. The LAP method is then applied to mock galaxy groups and we recover both the absolute masses and the orbits of galaxies by matching the relative velocities of the two largest bodies in the system.

In section (4.3.1) we analyse the simulation of a single galaxy cluster. The galaxies in the simulation are identified at the peaks of the density field and contain a number of particles large enough to make a direct comparison between LAP and N–body orbits possible.

A second test aimed at improving the statistical significance of the previous analysis is presented in section (4.3.2). In this second case the LAP is applied to a mock catalogue of LG candidates extracted from a CDM cosmological simulation.

4.4.1 High Resolution N-Body Test

The data are obtained from the Carlberg (1993) collisionless N-body simulation designed to mimic the evolution of a galaxy cluster with enough particles to resolve galaxy scales.

A sphere of $12.5\,h^{-1}$Mpc comoving radius containing a peak extracted from a CDM $\Omega_{\rm o} = 1$ universe realization was initialized with $N = 10^6$ particles each having a mass $2.27 \times 10^9\,h^{-1}\,M_{\odot}$. The gravitational evolution of the system has been followed using a multistep quadrupole TREECODE (Barnes & Hut 1986, Dubinski 1988), taking into account the effect of an external quadrupole tidal field. The experiment was evolved using a softening length $\epsilon_1 = 3.9\,h^{-1}$Mpc and a minimum timestep of 0.025 time units. The inverse of the (linearly estrapolated) mass variance at $8\,h^{-1}$Mpc, b_8, was unity at $z = 0$. The problem of galaxy identification in this simulation is greatly simplified by the existence of dense pieces of long–lasting self–gravitating substructures with a velocity dispersion of $\sim 100\,km/sec$. This feature guaranteed the stability of the results when different galaxy identification procedures were used.

At the final epoch the cluster is a virialized triaxial anisotropic object with half mass radius $r_{1/2} = 1.13\,h^{-1}$Mpc and a one dimensional RMS velocity dispersion of 1080 km/sec.

Since our 'standard' LAP method applies only to dynamically young systems we adopted the following rescaling of the original N-body data:

- First of all we applied a time transformation such that in the new final epoch the system is composed of galaxies approaching each other for the first time that, in this case, means that we have to consider the N-body simulation at an earlier epoch. It turned out that at $t = 17.8$ the simulated cluster is composed by infalling galaxies, The first transformation to apply is therefore:

  Length transformation: $l \longrightarrow l' = l/a$

  Time transformation: $t \longrightarrow t' = t/a^{3/2}$

  Mass transformation: $m \longrightarrow m' = m$

Where a is the expansion parameter at $t = 17.8$. assuming $a = 1$ at $t = 31.6$.

- Then the new system must be scaled to the LG dimensions. Therefore a second transformation of the comoving coordinates is applied:

Length transformation: $l' \longrightarrow l'' = l'\beta = l\beta/a$

Time transformation: $t' \longrightarrow t'' = t' = t/a^{3/2}$

Mass transformation: $m' \longrightarrow m'' = m'\beta^3 = m\beta^3$

The complete set of transformations preserves the form of the equations of motion and the $\Omega_\circ$–value

The new system is still composed by 10^6 particles and has a comoving radius of $2.5\,h^{-1}$Mpc. The total mass contained in the simulation, M_T, turns out to be $1.8 \times 10^{13}\,h^{-1}\,M_\odot$ which we consider as the total mass of the group. This rescaling, however, introduces two inconsistencies.

1. The original quadrupole tidal field is computed by considering a sphere with a comoving radius of $12.5\,h^{-1}$Mpc, while the size of the transformed system is a factor of 5 smaller. As a consequence the tidal field applied is slightly smaller than the true–one.

2. The second more serious incongruity refers to the galaxies' haloes. The size of the system has been modified by transforming the comoving coordinates of the points which implies an unwanted reduction of the galactic haloes' extension. In practice we obtain a group of galaxies surrounded by haloes having the typical extension of those expected in a low $\Omega_\circ$ CDM universe while the background Cosmology is the standard CDM. Since the effect we are exploring are presumably caused by the existence of extended haloes, the rescaling we applied is expected to artificially improve the LAP reliability. To avoid this unwanted bias different analysis with no rescaling has been performed, as described in the next section.

To identify the galaxies we used two procedures. In the first one we selected all the groups at a percolation length $\alpha\overline{d}(t)$, where $\overline{d}(t)$ is the mean interparticle separation at time t. The overdensity associated with the corresponding peaks is $\frac{\delta\rho}{\rho} \propto (\alpha\overline{d}(t))^{-3}$. All the peaks above this threshold and containing a specified minimum number of points are then recognized as galaxies. We applied this procedure using several different overdensity

#	$\delta\rho/\rho$	N	M_T/M_{LAP}
1	45	9	1.47
2	125	13	1.25
3	1000	13	2.11
4	2500	9	1.60
5	6000	14	1.60
6	43000	9	1.77
7	125000	10	1.30
8^a	8000	10	1.76

Table 4.3: N–body test parameters. Column 1: Identification Number, Column 2: Overdensity threshold, Column 3: Number of selected peaks, Column 4: M_r/L_{LAP} ratio.

thresholds in order to test the dependence of the LAP solution on the $\frac{\delta\rho}{\rho}$ used. A second two–step procedure was also applied. In this case we identified the protogalaxies at $t = 6$ with groups containing at least 10 particles, found at a percolation length of $0.2 \times \bar{d}(t)$. These particles are then relinked at $t = 17.8$ (the final epoch) using a percolation length of $0.05 \times \bar{d}(t)$, corresponding to a minimum $\frac{\delta\rho}{\rho} = 8000$ (see Carlberg & Dubinski 1991 for more details on the link algorithm). The aim here was to test the possible dependence of the results on the adopted galaxy identification procedure. Finally, the LAP technique was applied to reconstruct the orbits of the largest selected galaxies. In Table (4.3) we report, for each experiment, the overdensity threshold $\frac{\delta\rho}{\rho}$, the number N of peaks considered , and the ratio between M_T and the group's mass found using the LAP technique (M_{LAP}). To be consistent with the N–body background cosmology we used $\Omega_o = 1$ and $h = 0.5$

Figure (4.6) shows the time evolution of a typical peak identified at a $\frac{\delta\rho}{\rho} = 8000$ overdensity threshold using the two–steps procedure. The high merging rate causes the motion of the center of mass to poorly describe the history of a galaxy orbit within the system. Peaks identified using different criteria evolve in a similar way.

In Fig. (4.7) (a) and (b) the orbits of galaxies with $\frac{\delta\rho}{\rho} = 128$ and $\frac{\delta\rho}{\rho} = 8000$ respectively, are compared with their true center of mass trajectories obtained from N–body data. In both cases a general qualitative agreement is found, but there are exceptions.

The LAP orbits for bodies 6 and 7 in Fig. (4.7a), as well as for body 12 in Fig. (4.7b), are significantly different from the true trajectories. Moreover the orbits of bodies 3 and 4 in Fig. (4.7a) are exchanged (although in this case we recovered the correct solution by slightly varying the density threshold). Probably in these cases the correct orbits represent stationary points which are not minima of the action (analogously to the N6822 case in P2)
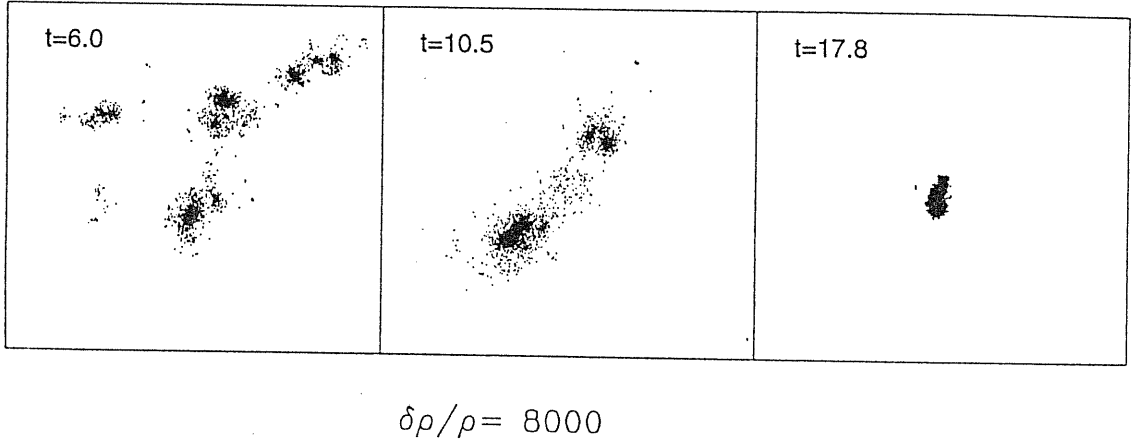
$\delta\rho/\rho = 8000$

Figure 4.6: Time evolution of a density peak identified at $t = 17.8$. The X-Y projections at times $t = 6.0$, 10.5, and 17.8 are displayed. The merging processes clearly characterize its dynamical evolution.

that could be found by using the more sophisticated matrix inversion scheme.

The second main result, shown in Table (4.3), is that M_{LAP} is systematically lower than M_T. The average M_T/M_{LAP} value is 1.6 with $\sigma = 0.27$. The stability of the mass ratio in all the different experiments indicates that this result depends neither on the galaxy identification procedure, nor on the overdensity threshold chosen. The magnitude of the mass discrepancy depends on definition of the system's mass. In this case the quoted M_T/M_{LAP} value should be regarded as a lower limit since, as we have already pointed out, the adopted rescaling artificially truncates galaxy haloes, hiding possible LAP failing which would otherwise occur in this case.

Figures Fig. (4.8a) and (4.8b) compare the true peak velocity v_{TRUE} from the N-body data with the same quantity found as a LAP solution (v_{LAP}). The same experiments as in Fig. (4.7a) and (4.7b) are considered. The underestimation of the mass causes v_{LAP} to be larger than v_{TRUE}. Interestingly the mass needed to match the peculiar velocity of the outer galaxies turned out to be very similar to M_T.

The Effect of Varying the Number of Galaxies, N_g:

After considering the peaks selected at an overdensity threshold $\frac{\delta\rho}{\rho} = 8000$ with the two–step procedure, we have applied the LAP technique using four different values of
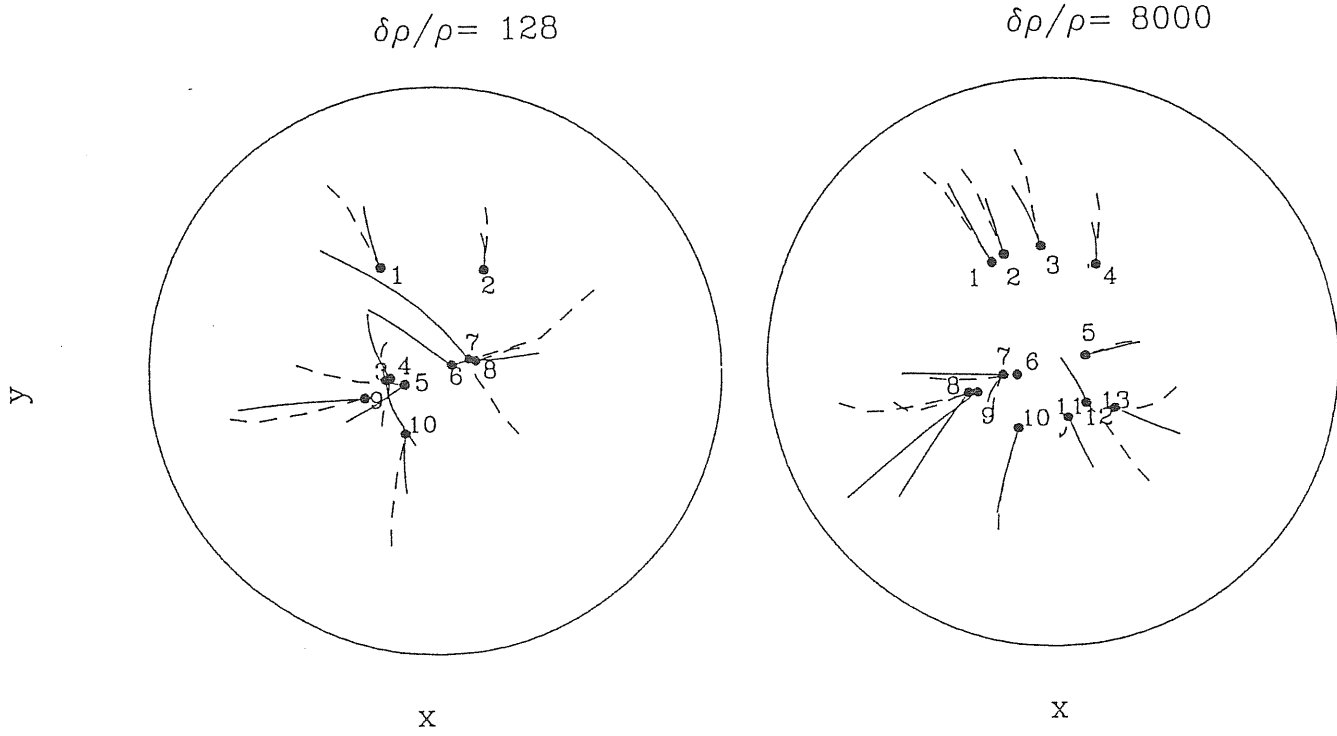
Figure 4.7: X-Y projections of the orbits for galaxies selected at $\frac{\delta\rho}{\rho} = 125$ and $\frac{\delta\rho}{\rho} = 8000$ respectively. Dashed lines represent the true orbits from the N–body experiment. Continuous lines are the orbits found by the LAP method. Black dots are the final positions of the galaxies. The orbits are traced back to a redshift 7. The circles have a radius of 5 Mpc. LAP orbits are quite similar to the true orbits. Significant differences in the orbits of bodies 6 and 7 (fig. 4.7a) and 12 (fig. (4.7b) probably indicate that true orbits represent stationary points which are not minima of the action.

Figure 4.8: Peculiar velocity found using LAP method vs. true peculiar velocity. The numbers refer to the galaxies in fig. (4.7) (a) and (b) The LAP method causes external galaxies to be less bound.

N_g: 8, 10, 14 and 17. The solution is not affected by changing this parameter: the same qualitative agreement between the LAP and the N-body orbits is found, and no significant variations in t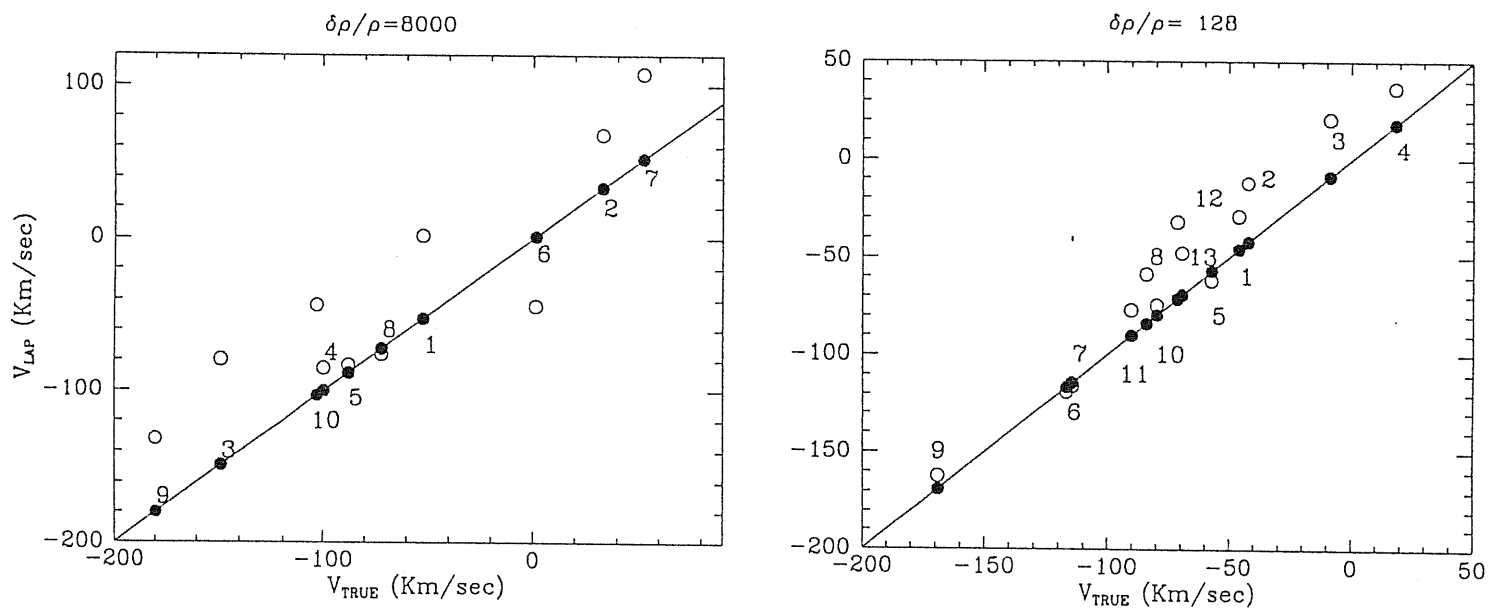he ratio M_T/M_{LAP} are observed ($= 1.75 \pm 0.02$). This N_g-independence arise since most of the system mass resides in the three largest bodies and thus variations in the number of light bodies considered do not appreciably affect the dynamics of the system.

The Effect of Varying the Final Epoch:

Since the two largest galaxies in the simulation are surrounded by extended overlapping haloes, one might suspect that their relative velocity is biased with respect to the dark component, even if they are approaching for the first time. The mass determination procedure would thus underestimate the total mass of the group. To test this hypothesis we considered the system at an earlier epoch ($t = 10.5$), when the velocity bias is expected to be negligible, or at least smaller than at $t = 17.8$. An overdensity threshold $\frac{\delta\rho}{\rho} = 8000$ was considered to identify galaxies at $t = 10.5$. We found that $M_T/M_{LAP} = 1.45$, only a factor 1.1 smaller than the average of values reported in Table (4.3). Thus, the velocity bias in the relative motion of the two largest bodies at $t = 17.8$, if present, has to be very small and cannot be the cause of the observed mass underestimation.

The Effect of Varying the Cosmological Parameters h and Ω_o:

P2 has shown that the LG dynamics is almost independent of Ω_o. As the density parameter, however, strongly influences the motion of the neighbouring groups, the LAP method was used to constrain the value of Ω_o. In this dynamical Ω_o test a hidden h-dependence is present because the distance of external galaxies is based on the infrared Tully–Fisher relation which is calibrated to the redshift of more distant galaxies (Peebles 1988). In practice this causes the LAP–Ω_o determination to be model dependent. As we have seen P2 chose (Ω_o, h) by constraining the expansion timescale, t_o, in the range of currently accepted values and he allowed for a non vanishing cosmological constant to obtain $t_o = 17$ Gyr in his $\Omega_o = 0.1$ $h = 0.75$ preferred cosmological model. In our case the cosmological background is known since we are considering N-body data. Nevertheless, as shown in Fig. (4.7) (a) and (b), the LAP method fails to reproduce the correct peculiar velocities. An interesting test is to apply the LAP method varying (Ω_o, h), in order to explore if a wrong cosmological model can bring the peculiar velocities closer to the correct values. We considered the 10 largest galaxies selected at a $\frac{\delta\rho}{\rho} = 8000$ threshold and we added six peaks containing more than 100 particles and having a distance from the center of mass of the group

in the range $4.2 - 4.8 \, h^{-1}$Mpc. To reproduce the observational uncertainties we introduced an h dependence in the outer peaks' distances. Using the correct cosmological parameters ($h = 0.5$ and $\Omega_o = 1$) we found that the average v_{LAP}/v_{TRUE} value for these peaks is 1.45. We analysed again the same N–body data, but considering it to be an $\Omega_o = 0.1$, $h = 0.75$ flat universe (with $\Lambda = 0.9$). The presence of a cosmological constant weakly influences the dynamics within the group but there is no appreciable difference between the predictions of an open model and a cosmological flat one with the same values of Ω_o and t_0 (P3). Analogously, the dynamics of the central part of the group was not appreciably influenced by introducing small external objects, or by changing the Ω_o–value. However, in the low density flat model, the value v_{LAP}/v_{TRUE} averaged over the outer galaxies turned out to be 0.83. Thus, paradoxically, the LAP method gives similar or even better results when an incorrect cosmological model is used. This suggests that, if $\Omega_o = 1$, the LAP technique cannot reliably determine the density parameter value in the LG neighborhood. A better proof that this is in fact the case will be given by the N–body test presented in section (4.3.2).

The Effect of Varying the Softening Parameter ϵ_i:

Extended galactic halos can be partially modelled by altering the $1/r$ potential to $1/\sqrt{r^2 + \epsilon_i^2}$, where ϵ_i is a softening parameter. After taking galaxies selected at a $\frac{\delta \rho}{\rho} = 8000$ threshold, we applied the LAP technique using several different ϵ_i–values. The original $\epsilon_i = 0.03 \times R_o$, corresponding to a value of 200 Kpc, was chosen in previous works (P1 and P2) to take into account the mass distributed in the halos. We increased the softening by a factor 2 and found that neither the orbits nor the M_T/M_{LAP} ratio were greatly changed. Very similar results were obtained when ϵ_i was set equal to 0, i.e., point–like galaxies. As already pointed out by P2, the observed ϵ–independence for ϵ_i in the range $0 - 400$ Kpc, derives from the fact that the softening parameters has a local effect, while the galaxy orbits found in the LAP solution are seldom close.

In an $\Omega_o = 1$ universe galaxy halos can be larger ($1 - 2 \, h^{-1}$Mpc). It is interesting to explore if the LAP method can take such extended halos into account. Since in the LAP implementation the galaxy extension is quantified by the softening parameter, the question can be modified as follows: how large should the softening parameter be in order to reproduce the dynamical effect of extended halos ? To answer this question we ran again the same LAP simulation with several different softening parameters until we obtained $M_T/M_{LAP} = 1$. The N–body experiment indicated that galaxy halos have a constant extension in physical coordinates back to $z = 1.15$. Since ϵ_i is expressed in comoving coordinates, we modeled

a time–dependent softening parameter $\epsilon_i(t)$ to keep its value constant in physical coordinates back to $z = 1.15$. At earlier times the softening was fixed equal to $\epsilon_i(z = 1.15)$. The present–time ϵ_i–value for which $M_T = M_{LAP}$ was ~ 1 Mpc. This large time–dependent softening parameter causes the external bodies to be more bound, resulting in a better match to their N–body peculiar velocities. However, the LAP–orbits of all the galaxies become shorter than the true ones. In spite of the larger, time dependent softening parameter, the LAP solution is still different from the N–body. These results can be accounted for if, as we will verify in the next section, galaxies are embedded in extended haloes which act as a hot mass component on the scale of the galaxy group. In this scenario the peculiar gravitational acceleration of galaxies within the group is determined by the mass concentrated around visible objects. A small softening parameter is therefore sufficient to reproduce the motion of inner galaxies. However, a large fraction of the mass is distributed in a weakly clustered intragroup background which causes the outer galaxies to have systematically smaller peculiar velocities, as observed. Therefore it is not surprising that a large softening parameter cannot both alleviate the missing mass problem and reproduce the motion of galaxies within the group.

4.4.2 Low Resolution N–Body Test

In this test the data were obtained from Couchman and Carlberg's (1992) cosmological N–body simulations. In this case the background Cosmology is also an $\Omega_o = 1$, $h = 0.5$, CDM model. Two computational cubes with sizes of 100 and 200 h^{-1}Mpc respectively, were considered. The total number of particles in each simulation is 128^3. Here we analyse the 100 h^{-1}Mpc cube data, thus the particle's mass is 2.65×10^{11} $M_\odot$ ($h = 0.5$). The mass variance at $8\,h^{-1}$Mpc is unity after 305 equal timesteps. The equivalent softening parameter for a Plummer potential corresponds to 15 h^{-1} Kpc, constant in physical units. Since no rescaling has been applied to the data, we avoid tidal field and halo–extension problems discussed in Section (4.3.1).

We adopted the galaxy identification procedures described in the previous section. In the first analysis we selected all the peaks at the final epoch, using the previous link method, at three different overdensity thresholds ($\frac{\delta\rho}{\rho} = 125$, 8000 and 64000) containing at least 5 particles. The second two–step procedure identified, after 50 timesteps, all the peaks having $\frac{\delta\rho}{\rho} \geq 125$, and then relinked the selected objects at the final epoch, using the same criteria followed in the former selection.

The next step was to consider binary galaxies resembling the Milky Way–M31 system to construct fictitious catalogues. We started by considering only objects having masses in the range $1.32 - 3.97 \times 10^{12}$ $M_\odot$ (i.e. peaks containing $5 - 15$ points). This is approximately the mass of our Galaxy when determined within a radius of ~ 100 Kpc, which turned out to be the typical radius of the sphere containing a $5 - 15$ points peak in the $\frac{\delta\rho}{\rho} = 8000$ threshold experiment.

The algorithm for finding binaries was: for each galaxy;

1. Find the closest neighbor and its distance r_1.

2. Find the next closest galaxy to the center of mass of the binary system and its distance r_2.

3. Compute the ratio r_2/r_1.

At this point the following constraints were applied:

- $0.3 < r_1 < 2$ (in Mpc units). The lower limit was imposed to avoid interacting galaxies in the sample. The upper limit was required to obtain a system similar to LG.

- $r_2 \geq 5$ Mpc, since the observed nearest groups are at a distance of 5.32 Mpc ($h = 0.5$) from the LG.

- Only approaching binaries were considered.

- $r_2/r_1 \geq 2.5$, in order to eliminate binaries which are members of a cluster.

One more condition, based on the total energy of the system, was applied. The sign of the energy can be calculated using the formula for a two–body system

$$\frac{E}{M_1 M_2} = \frac{v^2}{2M} - \frac{G}{r_1}, \tag{4.28}$$

where E is the total energy of the system, M_1 and M_2 are the masses of the individual galaxies, M is the total mass of the system, whose definition is given below, and v is the total relative velocity. Our purpose was to select LG candidates, but the question of whether the Milky Way–M31 system is bound or not does not have a clear answer because of the lack of information on the relative transverse velocity v_t. For example, according to P2 and the DL1 results, the Milky Way and M31 fail to be bound because of the influence of the external groups. However, if v_t were zero then the system would be bound. Therefore, we replaced v with the radial velocity v_r in eq. (4.28), and we required the l.h.s. to be negative.

As in the previous analysis, the magnitude of the possible discrepancy between M_{LAP} and the true mass depends on the definition adopted for the total mass of the system. We know from the work of Kroeker & Carlberg (1991) that the timing mass for approaching isolated binaries is well approximated (in an $\Omega_o = 1$ CDM N–body simulation) by the mass contained into two spheres centered on the galaxy positions and with radius equal to $r_1/2$ $(= M_K)$. Moreover, for first–approach binary systems, the LAP method gives a similar result to the timing argument $(M_K \sim M_{LAP})$. Here we use two different definitions for the total mass of the system:

i) M_5 is the mass contained within a sphere of 5 Mpc radius centered on the center of mass of the binary system, as measured from the N–body data. This is analogous to the M_T definition previously adopted.

ii) M_r is the mass contained within a sphere of radius $r = r_2 - 0.5$ Mpc, centered on the center of mass of the system. The 0.5 Mpc gap between r and r_2 has been introduced to avoid possible contamination from the outer objects' halos.

If the mass of the system was actually concentrated around the seen galaxies, then M_K, M_{LAP}, M_5 and M_r would coincide.

For each binary we computed the crossing time and the free fall crossing time t_{ffc},

$$t_c = \frac{r_1}{|v_r|}, \qquad t_{ffc} = \frac{\pi}{2}\sqrt{\frac{r^3}{2GM}}, \qquad (4.29)$$

where M can be either M_5 or M_r. Then, we divided the selected binaries into three different categories.

- The first one contains "wide" binaries, defined as those systems having both t_c and t_{ffc} larger than t_o.

- In the second category are the "quasi–wide" systems having

$$\frac{t_o}{2} < t_c < t_o \qquad \text{and} \qquad \frac{t_o}{4} < t_{ffc} < \frac{t_o}{2}. \qquad (4.30)$$

- All other binaries have been included in the third category.

Since these last systems are likely to have already completed at least one orbit, the relative LAP solution could not be unique. Therefore they will be included only for reference. Finally, we applied the LAP method to find the masses of the selected binaries. Results of LAP experiments performed using the different binary catalogues are summarized in Table (4.4).

| #	$\delta\rho/\rho$	N_1	Mean$_1$	σ_1	N_2	Mean$_2$	σ_2	N_{LG}	Mean$_3$	Mean$_4$
1^{t1}		32	0.5	0.2	24	0.5	0.2			
2^{t2}	125^a	47	1.0	0.5	46	1.0	0.5	3	0.6	0.7
3^{t3}		49	1.6	1.0	49	1.7	1.0			
4^{t1}		19	0.4	0.2	12	0.4	0.2			
5^{t2}	8000^a	31	0.8	0.4	29	0.8	0.4	4	0.7	0.9
6^{t3}		38	1.3	0.7	39	1.4	0.7			
7^{t1}		2	0.4	0.4	1	0.8	-			
8^{t2}	64000^a	11	0.8	0.3	8	0.9	0.3	1	1.4	1.44
9^{t3}		18	1.3	0.7	20	1.3	0.6			
10^{t1}		17	0.4	0.2	12	0.5	0.2			
11^{t2}	125^b	33	0.7	0.4	32	0.8	0.4	2	0.65	0.87
12^{t3}		39	1.1	0.7	40	1.3	0.7			
13^{t1}		5	0.3	0.2	2	0.5	0.2			
14^{t2}	8000^b	13	0.6	0.3	11	0.8	0.4	0	-	-
15^{t3}		17	1.1	0.7	18	1.2	0.7			
16^{t1}		1	0.6	-	1	0.7	-			
17^{t2}	64000^b	4	0.6	0.2	4	0.6	0.3	0	-	-
18^{t3}		11	0.7	0.3	18	0.7	0.3			

Table 4.4: N–Body test parameters.

The first column contains the experiment reference number and the second the overdensity threshold. In the remaining columns each row is divided in three subrows to take into account the three different categories defined above. The first subrow contains the parameters of "wide" binaries only. In the second, data from the first two categories are listed, while in the last all the objects are included. Columns 3, 4 and 5 contain the number of binaries found, the average value of $\log(M_5/M_{LAP})$ and the relative standard deviation respectively for the M_5 case. Columns 6 to 8 contain the same parameters for the M_r definition. The last three columns contain the number of best LG candidates and the corresponding average values of $\log(M_5/M_{LAP})$ and $\log(M_r/M_{LAP})$. The best LG candidates are constrained to have r_1 and $|v_r|$ in the range $600 - 850$ Kpc and $100 - 150$ km/sec respectively.

In this analysis the results depended slightly on both the galaxy identification procedure and the overdensity threshold. We mainly considered results from the catalogues containing galaxies selected at $\frac{\delta\rho}{\rho} = 8000$ since it was found that peaks above this overdensity threshold are good galaxy tracers (Carlberg & Dubinski 1991; Couchman & Carlberg 1992). In all the performed experiments the LAP method underestimated the system's mass. The average M_5/M_{LAP} ratio is ~ 5, significantly larger than in the previous analysis. As in the last section this mass underestimate suggests an intrinsic failure of the LAP method, presumabably related to the assumption that mass is concentrated around galaxies. To test whether mass is strongly clustered around density peaks or distributed in extended halos, we measured the mass contained in spheres of increasing radius centered on the midpoint of the binary system, normalized to the mass contained in a sphere of radius $r_{min} = r_1/2 + 0.2$ Mpc. The same procedure was repeated for each binary in the catalogue considered. Though the details depend on the selection criteria, we have found a result which is common to all catalogues considered: the mass is preferentially located on extended halos weakly clustered around the binary system. This is clearly shown in Fig. (4.9a) and (4.9b), in which we have plotted the quantity $M(< R) = \frac{\int_o^R (\rho(r) - \rho_b) d^3 r}{\int_o^{r_{min}} (\rho(r) - \rho_b) d^3 r}$ averaged over all the binaries of the two different catalogues. This is the mass distribution one would expect to find in a biased galaxy formation scenario.

The Effect of Varying the Softening Parameter ϵ:

Analogously to the previous section, we have looked for a softening parameter value which would give $M_T/M_{LAP} = 1$. If we select binaries at $\frac{\delta\rho}{\rho} = 8000$ using the two-steps procedure, and the softening is kept constant in physical coordinates up to $a = 10$, then

$\delta\rho/\rho= 8000 - $ One$-$Step Selection $\delta\rho/\rho= 8000 - $ Two$-$Steps Selection
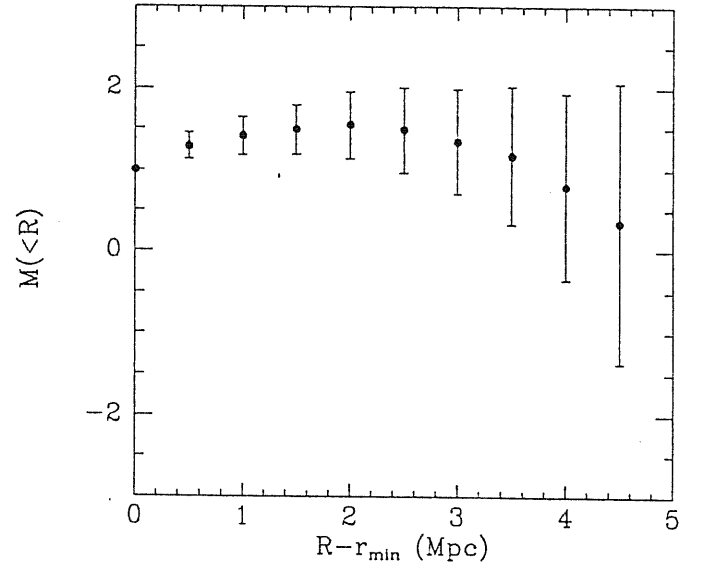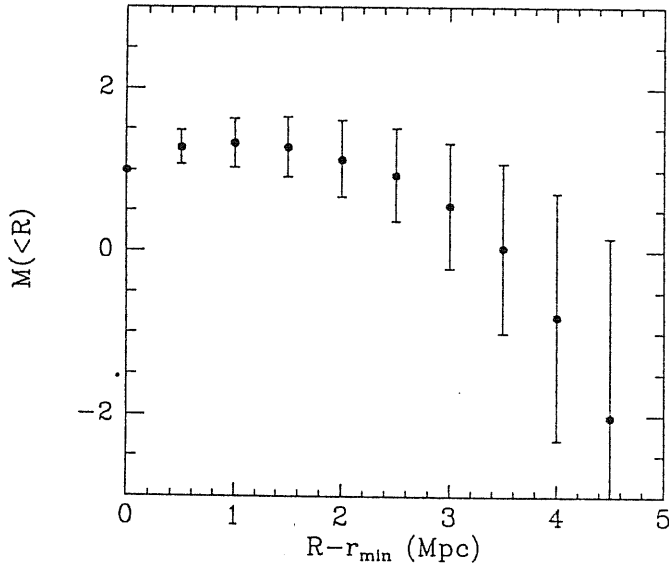
Figure 4.9: $M(< R)$ averaged over all the binaries vs. $R - r_{min}$ (in Mpc units). Binary galaxies selected at an overdensity threshold $\frac{\delta\rho}{\rho} = 8000$ using two different selection criteria are shown. The existence of extended haloes surrounding the binaries is inferred.

we find $\epsilon = 1.4$ Mpc. As expected, this value is higher than the previous one since in this simulation the haloes' extension have not been spuriously reduced by the transformations described in the last section.

Dynamical Influence of the Outer Galaxies:

Using N–body data we can study the effect of the tidal field induced by the outer galaxies on the binary dynamics by increasing the size of the system, centered around the LG candidate, to which the LAP method is applied. Thus, using the sample of the binaries selected at $\frac{\delta\rho}{\rho} = 8000$ we consider all the galaxies within a sphere centered in the center of mass of the binary system with radius $1.5 \times r_2$.

We have computed the new mass of the system M_{TID} finding that $M_{TID}/M_{LAP} = 1.3 \pm 0.2$; this indicates that the dynamics of the binary is only mildly affected by external galaxies and that its contribution to the LAP mass underestimate is quite small.

4.5   DISCUSSION AND CONCLUSION

The two different analyses carried out in Sections (4.3.1) and (4.3.2) indicate a substantial failure of the LAP method to describe the dynamics on LG scales in an $\Omega_\circ = 1$ universe. In section (4.3.1). we applied the LAP method to a group of galaxies obtained by transforming the data from a high resolution N–body simulation. Inconsistencies related with rescaling N–body data to reproduce the LG characteristics, reduce the extension of the haloes associated with the member galaxies and therefore this test will not reveal the full extent of the problem of using the LAP technique in an $\Omega_\circ = 1$ universe. There are two main outcomes from this first N–body test:

- The LAP method succeeds in qualitatively reconstructing the galaxy trajectories. A not obvious result since the high merging rate and the presence of large halos surrounding the objects cause the center of mass displacement to be a poor tracer of the group's dynamics.

- The mass of the system determined using the LAP method turns out to be systematically underestimated. The quoted M_T/M_{LAP} ratio is 1.6 ± 0.23. Although the magnitude of the discrepancy depends on the definition adopted for the mass of the system, the effect is undoubtedly real as indicated by the motion of external members of the group.

The above results do not depend on the peak identification procedure: Table (4.3) shows that varying the overdensity threshold by a factor 10^4 does not seriously affect the M_T/M_{LAP} ratio. This stability should have been, at least in part, expected since the peaks in the simulation analysed constitute a well–defined, long–lasting population of objects, easily identified by linking algorithms using different linking lengths. Tests performed to find the origin of this discrepancy indicate that the LAP solution depends neither on the number of peaks considered nor on the softening parameter chosen. Similarly we have found that the velocity bias in the simulation is very small and does not appreciably influence the M_{LAP} determination.

In section (4.3.2) we applied the LAP method to fictitious catalogues of binary galaxies extracted from a large volume N–body experiment. No rescaling was applied to the data. From this second test we confirm the above result since *the mass discrepancy was found to be even larger than in the previous test.*

The bulk of the evidence indicates that the origin of the Ω_o underestimate has to be found in the LAP method itself and it is not an artifact due to some systematic bias in the LAP–N–body comparison. One of the key assumptions of the LAP method's implementation is that all the matter in the universe is concentrated around visible galaxies. This approximation is well justified in an $\Omega_o = 0.1$ universe, in which the galaxies are surrounded by halos extending up to 200 Kpc. However, as we have verified, our $\Omega_o = 1$ CDM N–body simulation is characterized by the presence of much more extended overlapping halos weakly clustered around the peaks of the density field, as expected in a biased galaxy formation picture. Since the LAP technique can only reveal the mass clustered around visible objects, a dependence of the mass discrepancy on the relative separation of galaxies would be expected. In Fig. (4.10a) and (4.10b) we have plotted the mass discrepancy $\log(M_5/M_{LAP})$ versus the galaxy separation r_1 for binaries of two different catalogues. Even if a large scatter is present, *the mass discrepancy anti–correlates with the relative separation of the galaxies.* Moreover, this trend does not depend on the adopted galaxy identification procedure.

In a standard CDM cosmogony the resulting LAP mass at ~ 1 Mpc is $\sim 20\%$ of M_5, while at 2 Mpc M_{LAP} is close to M_5. Although these numbers depend on the shape of the power spectrum and on its normalization, it is reasonable to think that this effect is common to all the hierarchical clustering scenarios in which galaxies form in correspondence to the peaks of the density field and then accrete extended halos from the pressureless dark matter. We have verified that the quasi–homogeneous mass component missed by the LAP cannot be modeled by simply softening the gravitational force. According to the above evidence we conclude that:
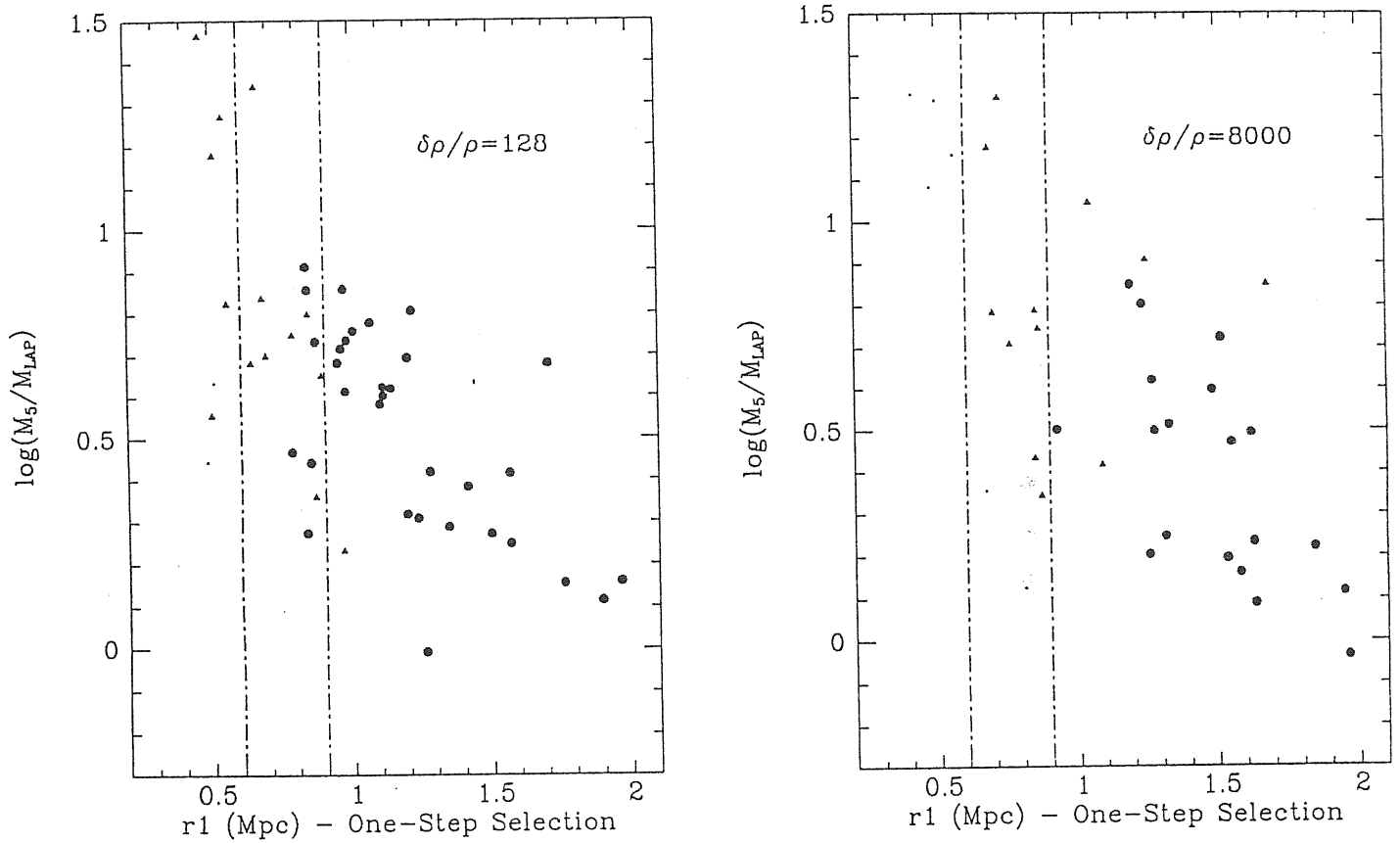
Figure 4.10: $\log(M_5/M_{LAP})$ vs. r_1. Binaries selected using two different overdensity threshold are shown. Black dots refers to 'wide' binary systems, filled triangles are for the binary included in the second category and small dots refers to bodies belonging to the third category (see text). The best LG candidates are contained in the region delimitate by two vertical lines. In both case the mass underestimate anti–correlates with the relative separation of the galaxies.

- The LAP technique reliably measures the clustered mass inside the system's orbits, which are qualitatively well reconstructed.

- The LAP method applied to the LG cannot rule out an $\Omega_o = 1$ value on the LG scales.

- In an $\Omega_o = 1$ universe the LAP can be safely applied to systems in which the average relative separations between objects is larger than ~ 2 Mpc, that is, much larger than the size of the collapsed galaxies.

The LAP method, however, is a powerful Ω-test when applied to systems large compared to the collapse radius of galaxies. If this picture is correct then the SPT result, who used the LAP to analyse the motion of groups and isolated galaxies on scales of $30 \, h^{-1}$Mpc, is free from mass biases and thus it would constitute an important evidence for a low Ω_o universe.

The above interpretation of the LAP mass underestimate has been recently challenged by DL2. They analysed an $\Omega_o = 0.2$ CDM N-body simulation and found that

- The LAP orbits are very discrepant from the N-body ones.

- The LAP underestimates the value of Ω_o by a factor 4–5.

- The discrepancy between the N-body and LAP line–of–sight galaxy peculiar velocities is due to the presence of CDM particles which are not linked to halos (the so called 'orphans')

It is quite difficult to reconcile these results with ours. In particular it is not easy to understand why we found a good agreement between the LAP and the N-body orbits in an $\Omega_o = 1$ universe while DL2, who analysed a low Ω_o CDM simulation in which haloes should be more concentrated, found very discrepant LAP orbits. Similarly, it is difficult to understand how the results shown in Fig. (4.10a) and $\log(M_S/M_{LAP}b)$ may be accounted for in the 'orphans' picture. The DL2 analysis is based on a large N-body simulation in which the LG candidates are 15 Mpc systems composed by ~ 10 galaxies (two of which form a central MW–M31 system–like pair). They identify galaxies by linking haloes of 2 Mpc that, due to the limited resolution of the N-body simulation, contain ~ 200 particles. In our high resolution N-body analysis we verified that to reliably trace a galaxy orbit back in time one has to consider systems like that one shown in Fig. (4.6), i.e systems that contain a similar number of particles within a much more concentrated region. Tracing back in time the motion of a more diluted system may be quite misleading, especially in a low Ω universe

where a 2 Mpc region surrounding a density peak sampled with low resolution, is an ill defined dynamical system.

To reach a definitive estimate of the LAP reliability, the DL2 and our analyses should be repeated using a high resolution low Ω_o N–body simulation like that one presented in section (4.3.2) with which it will be possible to evaluate the influence of the 'orphans' and to test the unexplored role of mergers through which a significant fraction of the total kinetic energy of the system might be dissipated.

REFERENCES

Abell G.O., 1958, ApJ, 3, 211

Abell G.O., Corwin H.G. & Olowin R.P., 1989, ApJS, 70, 1

Adams F. C., Bond J. R., Freese K., Frieman J. A. & Olinto A. V., 1993, Phys. Rew., D47, 426

Babul A. & White S. D. M., 1991, MNRAS, 253, 31P

Babul A., Weinberg, D., Dekel, D. & Ostriker, J.P., 1994, ApJ, 427, 1

Bagla J. S. & Padmamanabhan T., 1994, MNRAS, 266, 227

Bahcall N.A. & Soneira R.M., 1983, ApJ, 270, 20

Bachall N.A., Gramman M. & Cen, R., 1994, ApJ, 436, 23

Balkowsky C. & Kraan–Kortweg R. C. eds. 1994, it Unveiling the Large Scale Structure Behind the Milky Way, ASP Conference Series 67 (San Francisco: ASP)

Barrow J. & Tipler F. J., 1986, it The Anthropic Cosmological Principle, Clarendon Press, Oxford.

Batuski D.J., Bahcall N.A., Olowin R.P. & Burns J.O., 1989, ApJ, 341, 599

Baumgart D. J. & Fry J., 1991, ApJ, 375, 25

Bernardeau F., 1992, ApJ, 390, L61

Bertschinger E. & Dekel A., 1989, ApJ, 336, L5

Bertschinger E., Dekel A., Faber S., M., Dressler A. & Burstein D., 1990, ApJ, 354, 370

Bondi H. & Gold T., 1948, MNRAS, 108, 252

Borgani S., Coles, P. & Moscardini, L., 1994, MNRAS, 271, 223

Borgani S., Plionis, M., Moscardini, L. & Coles, P., 1995, MNRAS, in press [B95]

Bouchet F. R., Strauss M., Davis M., Fisher K. B. Yahil A. & Huchra J., 1993, ApJ, 417, 36

Bower R. G., Coles P., Frenk C. S. & White S. D. M., 1993, ApJ, 405, 403

Branchini E., Guzzo L. & Valdarnini R., 1994, ApJ, 424, L5

Branchini E. & Carlberg R. G., 1994, ApJ, 434, 37

Branchini E. & Plionis M., 1995, ApJ, submitted

Branchini E., Plionis M. & Sciama D.W., 1995, ApJ, submitted

Burstein D., 1990, Observational Astrophysics, p. 289, eds Tayler, R. J., White, R. E., Institute of Physics Publishing Bristol and Philadelphia.

Carlberg R. G. & Couchman H. M. P., 1989, ApJ, 340, 47

Carlberg R. G., Couchman H. M. P. & Thomas P. A., 1990, ApJ, 352, L29

Carlberg R. G., 1991, ApJ, 367, 385

Carlberg R. G. & Dubinski J., 1991, ApJ, 369, 13

Carlberg R. G., 1993, ApJ, 433, 468

Catelan P., Coles P., Matarrese S. & Moscardini L., 1994, MNRAS, 268, 966

Cen R. Y., Ostriker J. P., Spergel D. N. & Turok N., 1991, ApJ, 383, 1

Cen R. & Ostriker J. P., 1992, ApJ, 399, L113

Coles P., 1986, MNRAS, 222, 9P

Coles P. & Barrow J. D., 1987, MNRAS, 228, 407

Coles P., 1989, MNRAS, 238, 319

Coles P. & Jones B. J. T., 1991, MNRAS, 298, 1

Coles P., 1993, MNRAS, 262, 1065

Coles P., Melott A.L. & Shandarin S.F., 1993, MNRAS, 260, 765

Coles P. & Lucchin F., 1995, *Cosmology: The Origin and Evolution of Cosmic Structures*, John Wiley & Sons, Chicago.

Couchman H. M. P. & Carlberg R. G., 1992, ApJ, 389, 453

Courteau S., 1992, Ph.D. Thesis, UCSC

Courteau S., Faber S.M., Dressler A. & Willick J.A., 1993, ApJ, 412, L51

Croft R.A.C. & Efstathiou G., 1994, *Large Scale Structure in the Universe*, ed. Mücket J. P., et al., World Scientific, In press

da Costa L. N., Pellegrini P., Davis M., Meiksin A., Sargent W. & Tonry J., 1991, ApJS, 75, 935

da Costa L. N., et al., 1994, ApJ, 424 L1

da Costa L. N., et al. 1995, *Proceedings of the XXXth Moriond Astrophysics Meeting, in press*

Davis M. & Peebles P. J. E., 1983, ApJ, 267, 465

Dekel A. & Rees M. J., 1987, Nature, 326, 455

Dekel A., Bertschinger E. & Faber S., 1990, ApJ, 364, 349

Dekel A., Bertschinger E., Yahil A. Strauss M. A., Davis M. & Huchra J. P., 1993, ApJ, 412, 1

Dekel A., 1994, ARA&A, 32, 99

de Lapparent V., Geller M. J. & Huchra J. P., 1986, ApJ, 302, L1

de Lapparent V., Geller M. J. & Huchra J. P., 1986, ApJ, 332, 44

Dressler A. & Faber S.M., 1990, ApJ, 354, 13

Dunn A. M. & Laflamme. R., 1993, MNRAS, 264, 865 [DL1]

Dunn A. M. & Laflamme. R., 1995, ApJ, 442, L1 [DL2]

Efstathiou G., 1995, *Proceedings of the XXXth Moriond Astrophysics Meeting*, *in press*

Einasto J. & Lynden-Bell D., 1982, MNRAS, 199, 67

Faber S. M. & Ghallagher J. S., 1979, ARA&A, 17, 35

Faber S.M. & Jackson R.E., 1976, ApJ, 204, 668

Faber S.M. & Burstein D., 1988, *Large Scale Motions in the universe: A Vatican Study Week*, p. 115, eds Rubin V.C., Coyne G., Princeton Univ. Press.

Feldman H.A. & Watkins R., 1994, 430, L17

Feldman H., Kaiser N. & Peacock J., 1994, ApJ, 426, 23

Fisher, K. B., Davis, M., Strauss M. A., Yahil A. & Huchra J. P., 1993, ApJ, 402, 42

Fisher, K. B., Lahav O., Hoffman Y., Lynden–Bell D. & Zaroubi S., 1995, MNRAS, *in press*

Freudling W., da Costa N. L. & Pellegrini P. S., 1994, MNRAS, 268, 493

Giavalisco M., Mancinelli B., Mancinelli P.J. & Yahil A., 1993, ApJ, 411, 9

Giovanelli R. & Haynes M. P., 1991, ARA&A, 29, 499

Giovanelli R., Haynes M. P., Chamaraux P., daCosta L.N., Freudling W., Salzer J.J. & Wegner G., 1994 *Proceedings of the IAU symposium 168: Examining the Big Bang and Diffuse Background Radiation*, ed. M. Kafatos, *in press*

Gott III J. R. & Thuan T. X., 1978, ApJ, 223, 426

Gooding A. K., Park C., Spergel D. N., Turok N. & Gott III J. R., 1991, ApJ, 393, 42

Górski K., 1988, ApJ, 332, L7

Górski K., Davis M., Strauss M.A., White S.D.M. & Yahil A., 1989, ApJ, 344, 1

Górsky K. M., Hinshaw G., Bonday A. J., Bennet C. L., Wright E. C., Kogut A., Smmot G. F. & Lubin P., 1994, 430, L89

Gramman M., 1993, ApJ, 405, 449

Groth E. & Peebles P. J. E., 1977, ApJ, 217, 385

Gull S. & Daniell X., 1978, Nature, 272, 686

Gunn J. E., 1975, Comm. Ap.Space, Phys., 6, 7

Hamilton A. J. S., Kumar P., Lu E. & Matthews A., 1991, ApJ, 374, L1

Hale-Sutton D., Fang R., Metcalfe N. & Shanks T., 1989, MNRAS, 237, 569

Han M. & Mould J., 1990, ApJ, 360, 448

Harrison E. R., 1970, Phys. Rev., D1, 2726

Hoffman Y., 1994, *Cosmic Velocity Fields* (IAP, Paris), eds. Bouchet F. & Lachieze–Rey, p. 357

Hoyle F., 1948, MNRAS, 108, 372

Hubble E., 1934, ApJ, 79, 8

Hubble E., 1934, *The Realm of The Nebulae*, Yale Observatory Press, Yale

Huchra J. & Geller M., 1982, ApJ, 257, 423

Huchra J. P., Davis M., Latham D. & Tonry J., 1983, ApJS, 52, 89

Hudson M. J., 1992, Ph.D. thesis, Cambridge Univ.

Hudson M. J., 1993a, MNRAS, 265, 43

Hudson M. J., 1993b, MNRAS, 265, 72

Hudson M. J., 1994, MNRAS, 266, 475

Hudson M. J., Dekel A., Courteau S., Faber S.M. & Willick J.A. 1995, MNRAS, 274, 305

Jaffe A.H. & Kaiser N., 1994, *CITA Preprint*

Jerjen H, & Tamman G. A., 1993, A&A, 276, 1

Jing Y.P., Plionis M. & Valdarnini R., 1992, ApJ, 389, 499

Jing Y.P. & Valdarnini R., 1993, ApJ, 406, 6

Juskiewicz R., Vittorio N. & Wyse R.F.G., 1990, ApJ, 349, 408

Kahn F. D. & Woltjer L., 1959, ApJ, 130, 705

Kaiser N., 1984, ApJ, 284, L9

Kaiser N., 1987, MNRAS, 227, 1

Kaiser N., 1988, MNRAS, 231, 149

Kaiser N. & Lahav O., 1988, *Large Scale Motions in the universe: A Vatican Study Week*, p. 339, eds Rubin V.C., Coyne G., Princeton Univ. Press, Princeton.

Kaiser N. & Stebbins A., 1991, *Large–Scale Structure and Peculiar Motions in the Universe*, eds. Latham D. W. & L. N. da Costa, ASP, San Francisco, p. 111

Kaiser N., Efstathiou G., Ellis R., Frenk C., Lawrence A., Rowan–Robinson M. & Saunders, W., 1991, MNRAS, 252, 1

Katz N. & White S. D. M., 1993, ApJ. 412, 455

Klypin A. A. & Kopylov A. I., 1983, Sov. Astr. Lett., 9, 75

Kofman L., Bertschinger E., Gelb J.M., Nusser A. & Dekel A., 1994, ApJ, 420, 44

Koffman L., Bertschinger E., Gelb J., Nusser A. & Dekel A., 1994, ApJ, *in press*

Kogut A., Lineweaver C., Smoot G.F., Bennet C.L., Banday A., Bogges N.W., Cheng E.S., De Amici G., Fixsen D.J., Hinshaw G., Jackson P.D., Janssen H., Keegstra P., Lowenstein K., Lubin P., Mather J.C., Tenorio L., Weiss R., Wilkinson D.T. & Wright E.L., 1993, ApJ, 419, 1

Kolb E. W. & Turner M. S., 1990, *The Early Universe*, Addison–Wesley, Redwood City, California.

Kroeker T. L. & Carlberg R. G., 1991, ApJ, 376, 1

Lahav O., 1987, MNRAS, 225, 213

Lahav O., Rowan-Robinson, M. & Lynden-Bell, D., 1988, MNRAS, 234, 677

Lahav O., Edge A.C., Fabian A.C. & Putnet A., 1989, MNRAS, 238, 881

Lahav O., Fisher K. B., Hoffman Y., Scharf C. A. & Zaroubi S., 1994, ApJ, 423, L93

Lauer T.R. & Postman M., 1994, ApJ, 425, 418 [LP]

Lin H., 1995, PhD. Thesis, Harvard University.

Little B. & Tremaine S., 1987, ApJ, 320, 493

Loveday J., Maddox S. J., Efstathiou G. & Peterson P. A., 1994, ApJ, *submitted*

Lubin P. & Villela., 1986, Ann NY Acad. Sci., 470, 383

Lucchin F., Matarrese S. & Vittorio N., 1988, ApJ, 330,L21

Lucchin F., 1990, *Introduzione alla Cosmologia*, Zanichelli

Lynden–Bell D., Faber S.M., Burstein D., Davies R.L., Dressler A., Terlevich R.J. & Wegner G., 1988, ApJ, 326, 19

Lynden-Bell D., Lahav, O. & Burstein, D., 1989, MNRAS, 241, 321

Mancinelli P. J., Yahil A., Ganon G. & Dekel A., 1994, *Cosmic Velocity Fields* (IAP, Paris), eds. Bouchet F. & Lachieze–Rey, p. 215

Maddox S. J., Efstathiou G., Sutherland W. J. & Loveday J., 1990, MNRAS, 242, 43P

Matarrese S., Lucchin F., Messina A. & Moscardini L., 1991, MNRAS, 253, 35

Matarrese S., Lucchin F., Moscardini L. & Saez D., 1992, MNRAS, 259, 437

Mathewson D.S. & Ford V.L., 1994, ApJ, 434, L39

Mc Call M., 1989, ApJS, 97, 1341

Meiksin A. & Davis M., 1986, AJ, 91, 191

Melott A.L., Pellman T.F. & Shandarin S.F., 1994, MNRAS, 269, 626

Messina A., Moscardini L., Lucchin F. & Matarrese S. 1990, MNRAS, 254, 244

Messina A., Lucchin F., Matarrese S. & Moscardini L., 1992, Astropart. Phys., 1, 99

Mishra R., 1985, MNRAS, 212, 163

Miyaji T. & Boldt E., 1990, ApJ, 353, L3

Moscardini L., Matarrese S., Lucchin F. & Messina A., 1991, MNRAS, 248, 424

Moscardini L., Branchini, E., Tini Brunozzi, P., Borgani S., Plionis M. & Coles P., 1995, MNRAS *submitted*

Mould J.R., Staveley–Smith L., Schommer R.A., Bothun G.D., Hall O.J., Han M., Huchra J.P., Roth J., Walsh W. & Wright A.E., 1991, ApJ, 383, 476

Mukhanov V.F., Feldman H.A. $ Brandemberger R., 1992, Phys. Rep., 215, Nos. 5 & 6, 203

Narlikar J. V., 1993, *Introduction to Cosmology*, Cambridge University Press, Cambridge

Nusser A., Dekel A., Bertshinger E. & Blumenthal G. R., 1991, ApJ, 391, 16

Nusser A. & Dekel A., 1992, ApJ, 391, 443

Nusser A. & Dekel A., 1993, ApJ, 405, 437

Nusser A. & Davis M., 1994, ApJ, 421, L1

Padmamanabhan T. 1993, *Structure Formation in the Universe*, Canmbridge University Press, Cambridge

Park C., Vogeley M. S., Geller M. J. & Huchra J. P., 1994, ApJ, 431, 569

Peacok J. A., 1991, MNRAS, 253, 1P

Peacock J.A. & Nicholson D., 1991, MNRAS, 253, 307

Peacok J. A. 1992, in Martinez V., Portilla M., Saez., eds. *New insight into the Universe*, Proc. Valencia Summer School, Sringer, Berlin, p.1

Peacock J.A. & Dodds, S.J., MNRAS, 267, 1020

Peebles P.J.E. & Yu J. Y., 1970, ApJ, 162, 815

Peebles P.J.E. 1971, *Physical Cosmology*, Princeton University Press, Princeton

Peebles P. J. E., 1976, ApJ, 205, L109

Peebles P. J. E., 1980, it The Large Scale Structure of The Universe, (Princeton: Princeton University Press)

Peebles P. J. E., 1989, ApJ, 332, 17

Peebles P. J. E., Melott A. K., Holmes M. R. & Jiang L. R., 1989, ApJ, 345, 108

Peebles. P. J. E., 1989 ApJ, 344, L53 [P1]

Peebles P. J. E., 1990, ApJ, 362, 1 [P2]

Peebles P. J. E. 1993, *Principles of Physical Cosmology* (Princeton: Princeton University Press)

Peebles P. J. E., 1994, ApJ, 429, 43 [P3]

Peebles P. J. E., 1995, Preprint [P4]

Penzias A. A. & Wilson R. W., 1965, ApJ, 142, 419

Plionis M., 1988, MNRAS, 234, 401

Plionis M., 1988, MNRAS, 238, 417

Plionis M. & Valdarnini R., 1991, MNRAS, 249, 46 [PV91]

Plionis M., Valdarnini R. & Jing Y.P., 1992, ApJ, 398, 12

Plionis M., Coles, P. & Catelan, P., 1993, MNRAS, 262, 465

Plionis M., 1995, *Proceedings of the XXXth Moriond Astrophysics Meeting, in press*

Postman M., Huchra, J.P. & Geller, M.J., 1992, ApJ, 384, 407

Postman M., Spergel D.N., Satin B. & Juskiewicz R., 1989, ApJ, 346, 588

Primack J., 1984, *Proc. of International School of Physics Enrico Fermi*, Varenna, SLAC-PUB 3387.

Raychaudhury S. & Lynden-Bell D., 1989, MNRAS, 240, 195

Regös E. & Szalay A.S., 1989, ApJ, 345, 627

Rowan-Robinson M., Lawrence A., Saunders W., Crawford J., Ellis R., Frenk C.S., Parry I., Xiaoiang X., Allington-Smith. J., Efstathiou G. & Kaiser N., 1990, MNRAS, 247, 1

Rubin V. C., Thonnard N., Ford W. K. Jr. & Roberts S. M., 1976, AJ, 81, 719

Rybicki G. B. & Press W. H., 1992, ApJ, 398, 169

Sahni V. & Coles P. 1995, Phys. Rep. *in press*

Salucci P., Persic M. & Borgani S., 1993, ApJ, 405, 459

Scaramella R., Zamorani G., Vettolani G. & Chincarini G., 1990, AJ, 101, 342

Scaramella R., Vettolani G. & Zamorani G., 1991, ApJ, 376, L1 [SVZ91]

Scaramella R., Vettolani G. & Zamorani G., 1994, ApJ, 422, 1 [SVZ94]

Scaramella R., 1995, Astr. Lett. & Comm. *in press*

Scaramella R., 1995, *Proceedings of the XXXth Moriond Astrophysics Meeting, in press*

Scharf C., Hoffman Y., Lahav O. & Lynden-Bell D., 1992, MNRAS, 256, 229

Shanks T., Bean A. J., Ellis R., Fong R., Efstathiou G. & Peterson B. A., 1983, ApJ, 274, 529

Shaya E. J., Peebles P.J.E. & Tully B.R., 1993 1988, in Cosmic Velocity Fields IAP 1993, ed. Bouchet F.R. & Lachieze-Rey M., (Editions Frontieres)

Shaya E. J. & Peebles P.J.E., & Tully B.R. 1995, Preprint. [SPT]

Shandarin S.F. & Zel'dovich Ya.B., 1989, Rev. Mod. Phys., 61, 185

Simmons J. F. L., Newsam A. & Hendry M. A. 1994, *Cosmic Velocity Fields* (IAP, Paris), eds. Bouchet F. & Lachieze-Rey. p. 253

Smoot, G. F., Gorenstein, M. V. & Muller, R. A., 1977, Phis. Rev. Lett., 39, 898

Smoot G. F., et al. 1991, ApJ, 371, L1

Smoot G. F., et al. 1992, ApJ, 396, L1

Soifer B. T., Sanders D. B., Madore B., Neugebauer G., Danielson G. E., Elias J. H., Persson C. J. & Rice W. L., 1987, ApJ, 320, 238

Stebbins A., 1994, *Cosmic Velocity Fields* (IAP, Paris), eds. Bouchet F. & Lachieze-Rey, p. 253

Strauss M.A. & Davis, M., 1988, *Large Scale Motions in the universe: A Vatican Study Week*, p. 255, eds Rubin V.C., Coyne G., Princeton Univ. Press, Princeton.

Strauss M.A., Davis M. Yahil A. & Huchra J.P., 1990, ApJ, 361, 49

Strauss M.A., Davis M., Yahil A. & Huchra J.P., 1992, ApJ, 385, 421

Strauss M.A., Yahil A., Davis M., Huchra J.P. & Fisher K., 1992, ApJ, 397, 395 [SYDHF92]

Strauss M., Cen R., Ostriker J.P., Lauer T.R. & Postman M., 1994, ApJ, 444, 507

Strauss M.A. & Willick J.A., 1995, Physics Reports, *in press*

Szalay A. S., 1988, *Large Scale Motions in the universe: A Vatican Study Week*, p. 323, eds Rubin V.C., Coyne G., Princeton Univ. Press.

Taylor A. N. & Rowan–Robinson M. R., 1994, MNRAS, 265, 289

Tini Brunozzi P., Borgani, S., Plionis M., Moscardini L. & Coles P., 1995, MNRAS, *in press*

Tormen G., Moscardini L., Lucchin F. & Matarrese S., 1993, ApJ, 411, 16

Torres S., Fabbri R., & Ruffini R., 1994, A&A, 287,15

Tully R.B. & Fisher J.R., 1977, A&A, 54, 661

Tully R.B., 1987, ApJ, 323, 1

Tully R.B., Scaramella, R., Vettolani, G. & Zamorani, G., 1992, ApJ, 388, 9

van den Berg S., 1971, A&A, 11, 154

Vilenkin A., 1981, Phys. Rew., D24, 2082

Villumsen J.V. & Strauss M.A., 1987, ApJ, 322, 37

Vittorio N. & Juskiewicz, R., 1987, *Nearly Normal Galaxies*, p.451, ed Faber S.M., Springer–Verlag

Vogeley M. S., Park C., Geller M. J. & Huchra J. P., 1992, ApJ, 391, L5

Wagoner R. V., 1973, ApJ, 322, 37

Walker T. P., Steigman G., Schramm D.N., Olive K. A. & Kang H-S., 1991, ApJ, 376, 51

Walsh W. & Wright A.E., 1991, ApJ, 383, 476

Weinberg S., 1972, *Gravitation and Cosmology: Principles and Applications of the General Theory of Relativity*, John Wiley & Sons, Chicago.

Weinberg D. H., 1989, MNRAS, PhD. Thesis, Princeton University

Weinberg D. H., 1991, MNRAS, 254, 315

Weinberg D. H. & Cole S., 1992, MNRAS, 259, 652

Willick J. A., 1990, ApJ, 351, L45

Yahil A., Sandage A. & Tamman G.A., 1980, ApJ, 242, 448

Yahil A., Walker D. & Rowan–Robinson M., 1986, ApJ, 301, L1

Yahil A., Strauss M.A., Davis M. & Huchra J.P., 1991, ApJ, 372, 380

Yahil A. 1995, *Proceedings of the XXXth Moriond Astrophysics Meeting*, in press

Zel'dovich Ya. B., 1970, A& A, 5, 20

Zel'dovich Ya. B., 1972, MNRAS, 160, 1P

Zel'dovich Ya. B. & Novikov I. D., 1983, *The Structure and the Evolution of the Universe*, University of Chicago Press, Chicago.

Zatrisky D., Olszewski W., Shommer A. R., Peterson R. C. & Aaronson M., 1989, ApJ, 345, 759